Year : 2022

Characterizing conodont bioapatite from the Early-Triassic: an analytical and palaeoclimatological approach

Luz Zoneibe Augusto Silva

Faculté de Géosciences et de l'Environnement
Institut des Dynamiques de la Surface Terrestre
Université de Lausanne

CHARACTERIZING CONODONT BIOAPATITE FROM THE EARLY-TRIASSIC: AN ANALYTICAL AND PALAEOCLIMATOLOGICAL APPROACH

Thèse de Doctorat
Présentée à la
Faculté de Géosciences et de l'Environnement de l'Université de Lausanne

Pour l'obtention du grade de
Docteur en Sciences de la Terre

par
Zoneibe Augusto Silva LUZ
Maître ès Sciences de l'Environnement à l'Universidade Federal do Pará (UFPA), Belém, Pará

Directeur de thèse
Prof. Dr. Torsten Vennemann

Jury

Prof. Dr. Torsten Vennemann	Directeur
Prof. Dr. Marie-Elodie Perga	Président/Rapporteur
Prof. Dr. Hugo Bucher	Expert
Prof. Dr. Lukas Baumgartner	Expert
Dr. László Kocsis	Expert
Prof. Dr. Thomas Tütken	Expert

Université de Lausanne
2022

La Reprographie – UNIL
Lausanne
2022

Faculty de Geosciences and Environment
Institute of Earth Surface Dynamics
University of Lausanne

CHARACTERIZING CONODONT BIOAPATITE FROM THE EARLY-TRIASSIC: AN ANALYTICAL AND PALAEOCLIMATOLOGICAL APPROACH

Ph.D. thesis
Presented at the
Faculty of Geosciences and Environment of the University of Lausanne

To obtain the grade of
Ph.D. in Earth Sciences

by
Zoneibe Augusto Silva LUZ
M. Sc. of Environmental Sciences at the Universidade Federal do Pará (UFPA), Belém, Pará

Thesis director
Prof. Dr. Torsten Vennemann

Jury

Prof. Dr. Torsten Vennemann	Director
Prof. Dr. Marie-Elodie Perga	President/Rapporteur
Prof. Dr. Hugo Bucher	Expert
Prof. Dr. Lukas Baumgartner	Expert
Dr. László Kocsis	Expert
Prof. Dr. Thomas Tütken	Expert

Université de Lausanne
2022

La Reprographie – UNIL
Lausanne
2022

IMPRIMATUR

Vu le rapport présenté par le jury d'examen, composé de

Présidente de la séance publique :	Mme la Professeure Marie-Elodie Perga
Présidente du colloque :	Mme la Professeure Marie-Elodie Perga
Directeur de thèse :	M. le Professeur Torsten Vennemann
Expert interne :	M. le Docteur Laszlo Kocsis
Expert interne :	M. le Professeur Lukas Baumgartner
Expert externe :	M. le Professeur Hugo Bucher
Expert externe :	M. le Professeur Thomas Tütken

Le Doyen de la Faculté des géosciences et de l'environnement autorise l'impression de la thèse de

Monsieur Zoneibe Augusto SILVA LUZ

Titulaire d'un
Master in Environmental Sciences from Universidade Federal do Para (UFPA), Brazil

intitulée

CHARACTERIZING CONODONT BIOAPATITE FROM THE EARLY-TRIASSIC: AN ANALYTICAL AND PALAEOCLIMATOLOGICAL APPROACH

Lausanne, le 29 juin 2022

Pour le Doyen de la Faculté des géosciences et de l'environnement

Professeur Marie-Elodie Perga

2022

Characterizing conodont bioapatite from the Early-Triassic: an analytical and palaeoclimatological approach

Zoneibe Augusto Silva LUZ

"Podem ser encontrados aspectos positivos até nas situações negativas e é possível utilizar tudo isso como experiência para o futuro, seja como piloto, seja como homem."

- Ayrton Senna

Table of contents

Summaries

Characterizing conodont bioapatite from the Early-Triassic: an analytical and palaeoclimatological approach

Keywords: Conodonts. Early-Triassic. Fossil Geochemistry. Phosphate. Oxygen isotopes.

Caractérisation de la bioapatite de conodontes du Trias inférieur : une approche analytique et paléoclimatique

Mots-clés: Conodontes. Trias inférieur. Géochimie des fossiles. Phosphate. Isotopes de l'oxygène.

ABSTRACT

The Early Triassic (252 to 247 Ma) was a dramatic period for life on Earth. This time range follows the Permian-Triassic boundary mass extinction (PTBME), the most catastrophic biotic crisis on Earth. This episode is thought to have been triggered by the consequences of magmatic activity associated with the Siberian Traps volcanism, which added significant levels of greenhouse gases into the atmosphere. For this reason, early assumptions were that the ecological recovery during the Early Triassic was delayed for all organisms. However, recent contributions have characterized it as a succession of short-term recovery-extinctions cycles, controlled by climatic oscillations as well as regional environmental variations. A major intra-Triassic extinction at the Smithian–Spathian boundary (SSB) was noted to be even larger in magnitude for secondary consumers compared to the PTBME. Studies of biotic crises in the geological past are important to understand, such that we can also better estimate the impacts that Earth's natural system may be facing in view of future climatic and environmental changes. To complement the palaeoclimatic perspective about this period, this thesis investigated conodont bioapatites through stable oxygen isotope measurements ($\delta^{18}O$), used as proxies to estimate palaeoenvironmental conditions and relative sea water temperature changes.

While conodonts are widely used biogenic archives for tracing changes in palaeoclimatic/ environmental conditions, they are sadly very small in size and often only occur in low abundances in some critical sections that might be useful for palaeoclimatic/environmental interpretations. Hence, this thesis examined the possibility of using only a few conodonts for a representative analysis of their oxygen isotope composition. In particular, the SIMS (Secondary Ion Mass Spectrometry) analytical approach was critically examined for biogenic phosphates in general. Questions on the microstructure and chemical distribution in conodonts and shark teeth were studied to establish routine analytical protocols that would aim at ultimately using only a number of individual specimens in order to get representative and precise analysis. Through micro-analytical techniques, we noted the influence of sample preparation and of analysing different bioapatite tissues in the SIMS results. As such this first part then opened up the possibility of studying specimens also from sections that only contain rare conodonts but that are of critical importance for an improved, global interpretation of changing climatic and environmental conditions in the past.

The second part of this thesis involves *in-situ* $\delta^{18}O$ analysis in Omani conodonts from two exotic carbonate blocks: one from a condensed section with low sedimentation rates and abundant specimens recovered per layer; and one from a time-equivalent, well-preserved extended section, where conodonts are only rarely found. The new oxygen isotope measurements from these two comparative sections did improve our knowledge about the progression of the climatic upheavals covering the Smithian–Spathian Boundary (SSB).

In the third part, results from different sections around the globe are compared, ranging from low to high palaeolatitudes and from both palaeo-oceans of the Early Triassic: the Tethys and Panthalassa. The findings of this chapter highlight differences in conodont oxygen isotope compositions recovered from distinct settings, and enhance the knowledge about the palaeo-oceanography and -circulation, the palaeosalinity and the local controls on different sections studied in the comparison, allowing for a more detailed view on global changes in palaeoenvironmental conditions and changes thereof.

Being part of a major SNF-funded project, the Mid-Early Triassic Extreme Climatic Oscillation (METECO) project, the products of this thesis should both complement future interpretations about the Early Triassic climatic context and contribute with quantifications of climatic changes.

RÉSUMÉ

Le Trias inférieur (252 à 247 Ma) a été une période dramatique pour la vie sur Terre. Cette période suit l'extinction de masse de la limite Permien-Trias (PTBME), la crise biotique la plus catastrophique de l'histoire de la Terre. Cet épisode est supposé avoir été déclenché par les conséquences de l'activité magmatique associée au volcanisme des Trappes de Sibérie, qui a ajouté des niveaux importants de gaz à effet de serre dans l'atmosphère. Pour cette raison, les premières hypothèses émises étaient que la récupération écologique au cours du Trias inférieur ait été retardée pour tous les organismes. Cependant, des contributions récentes l'ont caractérisée comme une succession de cycles de récupérations-extinctions à court terme qui étaient contrôlés par des oscillations climatiques ainsi que par des variations environnementales régionales. Une extinction majeure intra-Trias à la limite du Smithian–Spathian (SSB) a été notée comme étant encore plus importante en magnitude pour les consommateurs secondaires par rapport à celle de la limite Permien-Trias.

Les études des crises biotiques dans le passé géologique sont importantes à comprendre, de sorte que nous puissions également mieux estimer les impacts auxquels le système naturel de la Terre pourrait être confronté en vue des changements climatiques et environnementaux futurs. Afin de compléter la perspective paléoclimatique de cette période, cette thèse a étudié les bioapatites de conodontes par des mesures d'isotopes stables de l'oxygène ($\delta^{18}O$), utilisées comme un indicateur pour estimer les conditions paléoenvironnementales et les changements de températures relatives de l'eau de mer.

Bien que les conodontes soient des archives biogènes pour tracer des changements des conditions paléoclimatiques/environnementales, ils sont malheureusement de très petite taille et ne sont souvent présents qu'en faible abondance dans certaines sections critiques qui pourraient être utiles pour les interprétations paléoclimatiques/environnementales. Ainsi, cette thèse a examiné la possibilité d'utiliser seulement quelques conodontes pour une analyse représentative de leur composition isotopique en oxygène. Dans un premier temps, l'approche analytique SIMS (Secondary Ion Mass Spectrometry) a été examinée de manière critique pour les phosphates biogènes en général. Les questions sur la microstructure et la distribution des éléments dans les dents de conodontes et de requins ont été étudiés afin d'établir des protocoles analytiques de routine visant à utiliser uniquement des spécimens individuels afin d'obtenir une analyse représentative et précise. De plus, cette étape était essentielle pour établir les principes de base de l'étude des spécimens rares provenant d'autres sections géologiques. Par des techniques de micro-analyse, nous avons noté l'influence de la préparation des échantillons et de l'analyse de différents tissus des bioapatites sur les résultats SIMS. En tant que telle, cette première partie a ouvert la possibilité d'étudier des spécimens provenant également de sections qui ne contiennent que de rares conodontes mais qui sont d'une importance critique pour une interprétation améliorée et globale de l'évolution des conditions climatiques et environnementales dans le passé.

La deuxième partie de cette thèse implique l'analyse *in-situ* de $\delta^{18}O$ dans les conodontes d'Oman provenant de deux blocs carbonatés exotiques : l'un provenant d'une section condensée avec de faibles taux de sédimentation et d'abondants spécimens récupérés par couche ; et l'autre d'une section étendue équivalente dans le temps et bien préservée, où les conodontes sont rarement trouvés. Les nouvelles mesures des isotopes de l'oxygène provenant de ces deux sections comparables ont permis d'améliorer nos connaissances sur la progression des bouleversements climatiques qui couvrent le SSB.

Dans la troisième partie, les résultats des différentes sections du globe sont comparés, allant

des basses aux hautes paléolatitudes et des deux paléo-océans du Trias précoce : la Téthys et le Panthalassa. Les achèvements de ce chapitre soulignent les différences dans les compositions isotopiques de l'oxygène des conodontes récupérés dans des environnements distincts, et améliorent les connaissances sur la paléo-océanographie et la -circulation, la paléosalinité et les contrôles locaux sur les différentes sections étudiées dans la comparaison, ce qui permet de porter une vue plus détaillée sur les changements globaux dans les conditions paléoenvironnementales et leurs modifications.

Faisant partie d'un projet majeur financé par le FNS, le projet Mid-Early Triassic Extreme Climatic Oscillation (METECO), les résultats de cette thèse devraient à la fois complémenter les interprétations futures sur le contexte climatique du Trias inférieur et contribuer aux quantifications des changements climatiques.

INTRODUCTION

1. Introduction

1.1 Climate change and mass extinctions

The effects and impacts caused by climate change are currently one of the most demanded areas in scientific research (Hull and Darrock, 2013). Since the Industrial Revolution, anthropogenically derived emissions of greenhouse gases (e.g., CO_2, CH_4) are increasing continuously, putting the stability of Earth natural systems to such conditions under pressure (Passow and Carlson, 2012; IPCC, 2019). In the marine realm, imminent impacts that are estimated comprise an increase in sea surface temperatures of more than 1.5 °C by the end of the century, a global decline in ocean oxygen content, ocean acidification and changes in the thermohaline circulation (e.g., Latif et al., 2006; Guinotte and Fabry, 2008; Hofmann and Schellnhuber, 2009; Schmidtko et al., 2017). Organisms that can act as climate change mitigators are also being affected by such consequences, will further strain the survival of life in general. For instance, calcifying marine plankton organisms (e.g., coccolithophores and foraminifera) are important carbon sinks for counterbalancing the atmospheric CO_2 (e.g., Wolf-Gladrow et al., 1999; Riebesell et al., 2000). The functioning of such organisms at their normal, steady state is already compromised, threatening the stability of the carbon cycle in marine systems (Boyd, 2015). Consequently, it became a priority to study Earth's natural systems to better understand the natural variation of the chemical elements with time and how these interact with living organisms (e.g., via biomineralization processes, Kocsis, 2011). As of the 1950's to 1960's, a number of scientific and technical developments allowed for improved oceanographic and geologic studies that can now help 'quantifying' Earth's elemental distribution and the fluxes thereof in natural systems (e.g., Michener and Lajtha, 2007; Pereira and Benedito, 2007). These investigations study not only the modern context (including the Holocene), but also the geological past. With these developments it is now possible to assess data from extreme climatic conditions in Earth's history, which may be comparable to nowadays, such as mass extinction events. These are of particular interest as they may represent periods of relatively rapid environmental changes, similar to those that can be expected for future changes in climate (e.g., intervals with relatively rapid changes in CO_2 concentrations). These environmental changes are recorded by geochemical proxies (Hull and Darroch, 2013). Moreover, the study of biotic crises can help to better constrain prediction models, which need to compile the diverse data reflected in abiotic and biotic association, such that the elaboration of mitigation plans by the responsible governments and global authorities can be improved.

The research developed here has a focus on the Early Triassic (252 to 247 Ma., Widmann, 2019), a period of major climatic oscillations for Earth's ecosystems (e.g., Goudemand et al.,

2019). This interval follows the greatest extinction event in the Phanerozoic Era: the Permian–Triassic boundary mass extinction (PTBME), where more than 90 % of all marine species on Earth went extinct (MacLeod, 2014) (Figure 1).

Current common thinking is that this crisis was closely related to the consequences of the magmatic activity associated with the Siberian Traps volcanism, which may have added significant levels of greenhouse gases to the atmosphere (e.g., MacLeod, 2013). Additionally, the extreme climatic conditions (Figure 2A.1) triggered anoxic events in the marine realm, represented by black shales in the geological record at a number of localities around the globe (e.g., Wignall and Twitchett, 2002; Knoll et al., 2007; Bottjer, 2012; Joachimski et al., 2012; Sun et al., 2012; Grasby et al., 2013; Zhang et al., 2018) (Figure 2A). Due to these critical circumstances, earlier interpretations considered that the ecological recovery during the Early Triassic was delayed as it was for the marine benthic fauna (Isozaki, 1997; Wignall and Twitchett, 2002; Meyer et al., 2011; Joachimski et al., 2012).
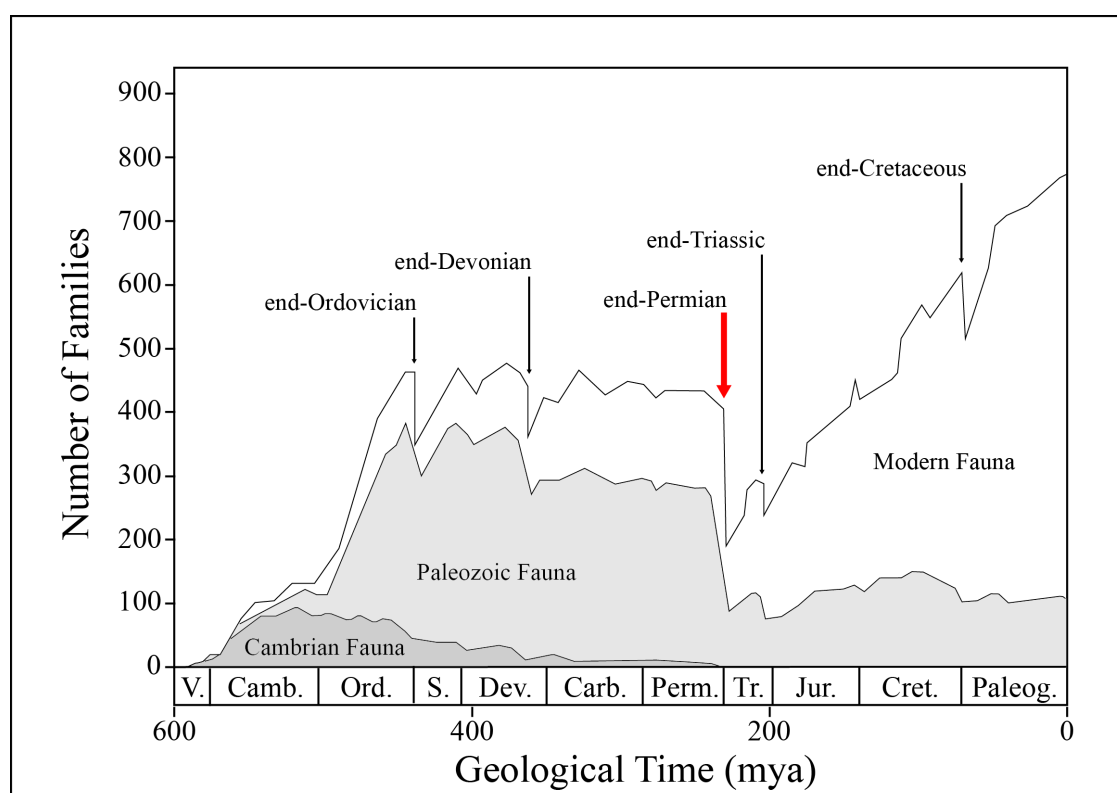
Figure 1. The Phanerozoic timeline and the variations of the marine faunal biodiversity, correlated to the five main mass extinction events (arrows). Modified from: MacLeod (2014).

However, recent palaeontological and geochemical research suggest that conditions were not uniformly adverse in the aftermath of the PTBME. While the benthos lingered to recover after the PTBME, secondary consumers (ammonoids, conodonts) had short-term cycles of diversification-extinction periods (Orchard, 2007; Galfetti et al., 2007a, 2008; Brühwiler et al., 2010; Ware et al., 2011; Romano et al., 2013; Hautmann et al., 2015; Jattiot et al.,

2018; Leu et al., 2019; Zhang et al., 2019; Goudemand et al., 2019; Widmann et al., 2020). These cycles were likely controlled by equally short-term climatic oscillations with regionally variable environmental impacts (e.g., bottom-water anoxia) (Song et al., 2011; Leu et al., 2019; Goudemand et al., 2019; Widmann et al., 2020). Another critical life crisis eventuated at the Smithian–Spathian boundary (249.29 to 249.11 Ma, Widmann et al., 2020) (Figure 2A.2, B.1).
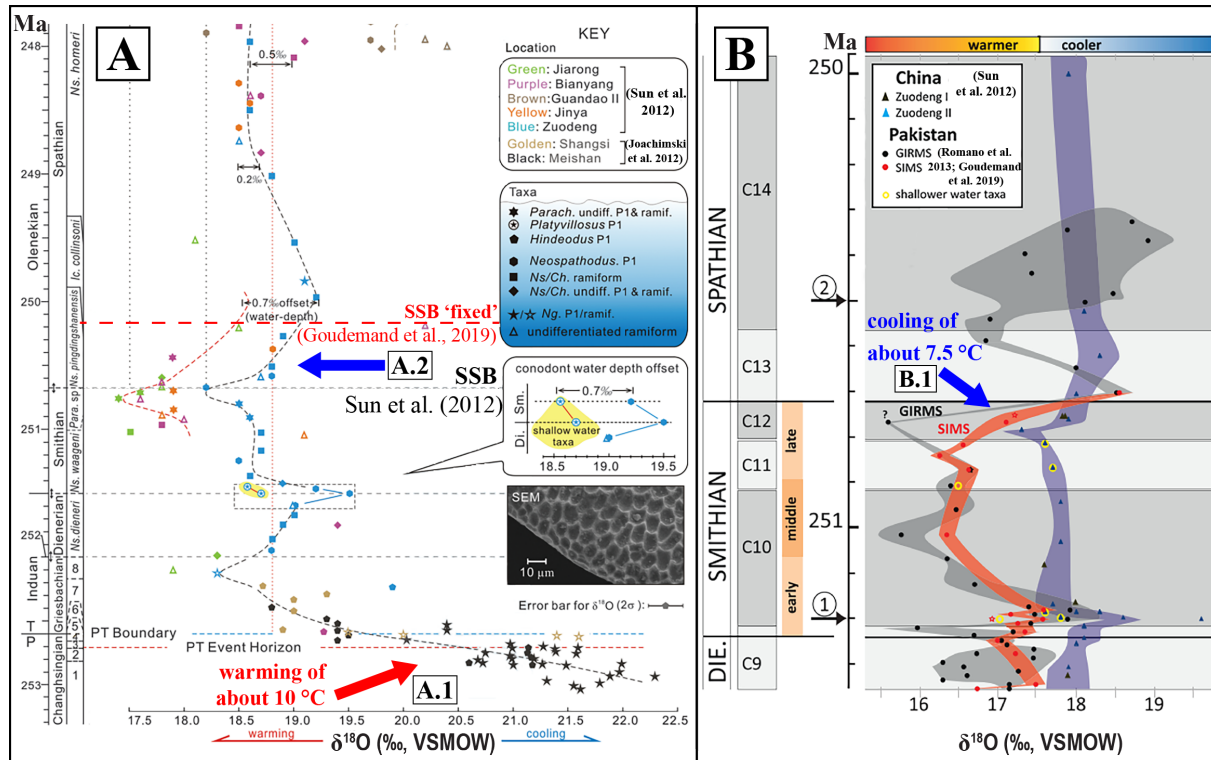
Figure 2. Oxygen isotope compositions from South China and Pakistani conodonts, measured by Sun et al. (2012) (South China), Romano et al. (2013) and Goudemand et al. (2019) (Pakistan). 'Ma' stands for millions of years ago. The red arrow points to the PTBME. Details about the climatic upheavals of this biotic crisis and of its aftermath are reflected as oscillations of oxygen isotope compositions, a proxy to sea water temperatures, in **(A)** - (Sun et al., 2012) and **(B)** - (Goudemand et al., 2019). In **(A.1)**, the red arrow shows the PTBME warming event and in **(A.2)** and **(B.1)**, the blue arrow shows the Smithian–Spathian boundary (SSB) cooling event. Note that the SSB was wrongly placed by Sun et al. (2012) and this was corrected by Goudemand et al. (2019).

For conodonts and to some extent ammonoids, this intra-Triassic extinction was of greater magnitude than the PTBME (Orchard, 2007; Brühwiler et al., 2010). Numerous independent proxy archives (e.g., bioapatites, carbonate rocks, fossilised pollen) support cycles of rapid environmental changes at planetary level (e.g., Hermann et al., 2011; Romano et al., 2013; Hochuli et al., 2016; Goudemand et al., 2019; Hammer et al., 2019; Widmann et al., 2020). The reasons behind these intra-Triassic extinctions are still debated, but it has recently been suggested that volcanic and unilateral temperature cycles (warming/cooling) may have alternately been the main drivers for these cycles (e.g., Goudemand et al., 2019; Hammer et al., 2019; Widmann et al., 2020). Carbon isotope compositions of organic and inorganic carbon support global increases of atmospheric CO_2 and associated increase in the continental

weathering and erosion of silicates as a subsequent mitigation as a cause for this cyclicity (Zhang et al., 2018; Goudemand et al., 2019; Schneebeli-Hermann et al., 2020; Widmann et al., 2020). These processes suggest that eutrophication may have been common in coastal zones due to an increased nutrient input from the continents (Payne and Kump, 2007; Meyer et al., 2016; Goudemand et al., 2019). This is further corroborated by an abundance of black shales, typical geological indicators of bottom-water anoxia, in many continental sections worldwide over this period (Grasby et al., 2013; Wignall et al., 2016; Zhang et al., 2018; Song et al., 2014, 2019).

The Early Triassic has important climatic similarities with the situation expected by climatic change today. The first concerns that organisms were experiencing a relatively quick increase of sea surface temperatures during the Permian-Triassic transition (Figure 2A; Joachimski et al., 2012). From now to 2100, it is expected that life will have to adapt to a temperature increase of at least 1.5 °C (up to 4 °C, IPCC, 2019), and as in the Triassic, it seems that the benthic fauna is suffering critically the consequences of such temperature changes (e.g., corals, Marshall and Baird, 2000; Carpenter et al., 2008). A second analogy noted for the Triassic is related to the oceanic circulation and upwelling events. Upwelling zones is where deep cold waters ascend and boost the primary productivity at the surface and nutrients are introduced to support life (e.g., Mohan et al., 2018; Barlow et al., 2021; Narvekar et al., 2021). During the Early Triassic, it has been suggested that upwelling occurred in the Panthalassa Ocean at the western margin of Pangea, in a similar fashion to that of the modern Pacific Ocean at the western margin of North and South America (e.g., Martindale et al., 2014; Arnesen, 2017; Brookfield et al., 2020; Grasby et al., 2020). However, the functioning of such bioproductive zones is also uncertain with the given climatic change (García-Reyes et al., 2015).

With the aim to further understand the effects of rapid climatic oscillations on the Earth's natural systems and its associated living organisms, a geochemical study of the stable oxygen isotope compositions and major/minor chemical compositions was undertaken on conodonts. Conodonts were aquatic eel-like jawless vertebrates that were ubiquitous from the Cambrian to the Triassic, and their dental elements can be found in many geological deposits around the world (Barnes and Fahreus, 1975; Briggs et al., 1983; Jones, 1992; Orchard, 2007; Cardoso et al., 2015). Classical bulk sampling and *in-situ* stable isotope measurements of oxygen isotope compositions in phosphate ($\delta^{18}O$) in conodont dental parts can provide insights about the palaeoclimate and palaeoenvironmental conditions (e.g., Trotter et al., 2008; Sun et al., 2012; Joachimski et al., 2012; Romano et al., 2013; Goudemand et al., 2019) following the Permian-Triassic extinction. Chemical analysis may provide additional insights about the

structure, texture, and odontogenesis on the studied specimens (e.g., Katvala and Henderson, 2012; Zhang et al., 2017; Shirley et al., 2018; Leonhard et al., 2021) and shed light on analyses-specific instrumental fractionations for SIMS O-isotope measurements. This research was part of a bigger project entitled *'Mid-Early Triassic Extreme Climatic Oscillation'* (METECO), which addressed global abiotic forcing and biotic feedbacks in a multidisciplinary approach for estimating perspectives of the climate change (funding by the Swiss National Science Foundation SNF: 200020_160055/1 to Hugo Bucher and Torsten Vennemann). This major project also had as an objective the development of a more precise climatic model (the METECO model), considering altogether biotic and abiotic factors for this elaboration. The METECO project (2016–2021) was succeeded by a Sinergia project entitled *'Quantifying decamillennial changes in carbon cycling, climatic and biotic responses to Late Permian–Early Triassic volcanism'* (SNF project number CRSII5-180253). This new project also aims to build on the METECO research results to further constrain the environmental and climatic changes at and after the Permian-Triassic extinction events.

1.2 Research context: Conodonts

Conodonts are an important tool for palaeoclimatic studies due to a lack of alternative reliable paleo-proxy archives from pre-Cretaceous time ranges, as calcitic fossils are more prone to alteration (e.g., Luz et al., 1984). However, some aspects must be taken into consideration for using these fossils; the general biomineralogical characteristics of their bioapatite; the degree of sample preservation for conodonts is known as Conodont Alteration Index (CAI); the depositional setting of material provenance and a precise taxonomic identification. These features will be briefly discussed below.

1.2.1 General mineralogy and Conodont Alteration Index (CAI)

Conodont dental elements are predominantly composed of a carbonate fluorapatite and have a general formula of $Ca_5Na_{0.14}(CO_3)_{0.16}(PO_4)_{3.01}(H_2O)_{0.85}F_{0.73}$ (Sweet, 1988). This contrasts with mammal teeth where the mineralized matrix is primarily hydroxylapatite (Francillon-Vieillot et al., 1990; Vennemann et al., 2001; Zhang et al., 2017). Fluorapatite is less soluble and more resistant to post-mortem alteration compared to the more common hydroxylapatite or dahllite as bioapatite (Posner et al., 1984). Conodonts are known not to vary substantially in chemical composition relative to their different mineralogical structures (e.g., Trotter and Eggins, 2006; --, 2016b). Additionally, their bioapatite is subdivided in two structures: crown and basal body (Trotter et al., 2007). The crown is composed of a hyaline lamellar tissue that

is considered analogous to vertebrate 'enameloid' and a more porous complex denominated albid cancellate tissue, also known as 'white matter', an exclusive trait of conodonts (Figure 3) (Donoghue, 1998, 2001; Trotter et al., 2007). The basal body is porous and is often compared to the vertebrate 'dentine', but it is frequently absent due to its fragility during fossilization processes (Trotter et al., 2007; Wheeley et al., 2012). High-resolution imaging has shown that conodonts also present growth layers, better noted in the hyaline crown given the porous aspect of the white matter (e.g., Figure 3; Chen et al., 2016). It is suggested that their apatite crystals were being gradually synthetized, developing themselves in a similar way to the growing dentition of other vertebrates (Donoghue, 1998). If these animals were migrating through the water column, it is possible that distinct geochemical compositions are recorded in each individual growth band, which should correspond to the aqueous environment where they lived at the given period of tooth formation (Vennemann et al., 2001). Hyaline and albid tissues were investigated by geochemical *in-situ* approaches. Employing these techniques allowed to check if the growth layers of conodonts provide any systematic or variable range of geochemical results, as occur in accretionary growing hard tissues of modern organisms (e.g., fish otoliths, Sturrock et al., 2012).

Finally, the degree of sample preservation must be verified before any geochemical procedures and for conodonts this can be identified by the Conodont Alteration Index (CAI, Epstein et al., 1977). This scale was elaborated to indicate the extent of textural and compositional alteration in conodont bioapatite, and it correlates with burial temperatures of the specific conodonts. For example, the lower value in this classification (CAI 1) is taken to indicate temperatures of < 80 ºC, while the highest value (CAI 5) corresponds to temperatures of > 300 ºC (Epstein et al., 1977; Wheeley et al., 2012). The colour results from the pyrolysis of residual organic compounds trapped between hard tissue layers (Trotter et al., 2007; Wheeley et al., 2012). Due to the progressive and irreversible nature of the colours produced during burial heating, the CAI scale is often used as a preliminary indicator of preservation for conodont elements and the thermal alteration of the host rocks (Wheeley et al., 2012). In this research, all CAI ranges were used. Well-preserved elements (CAI 1) are thought to be a reliable base for palaeoclimatic and environmental interpretations and were used for calibrations established in this study. Samples with higher CAI (2 to 5) will be carefully interpreted. Previous studies of phosphate oxygen isotope compositions found consistent values from CAI > 1 samples (Joachimski et al., 2009; Zhang et al., 2017), but the opposite trend of higher variability with increasing CAI was also observed (Wheeley et al., 2012).
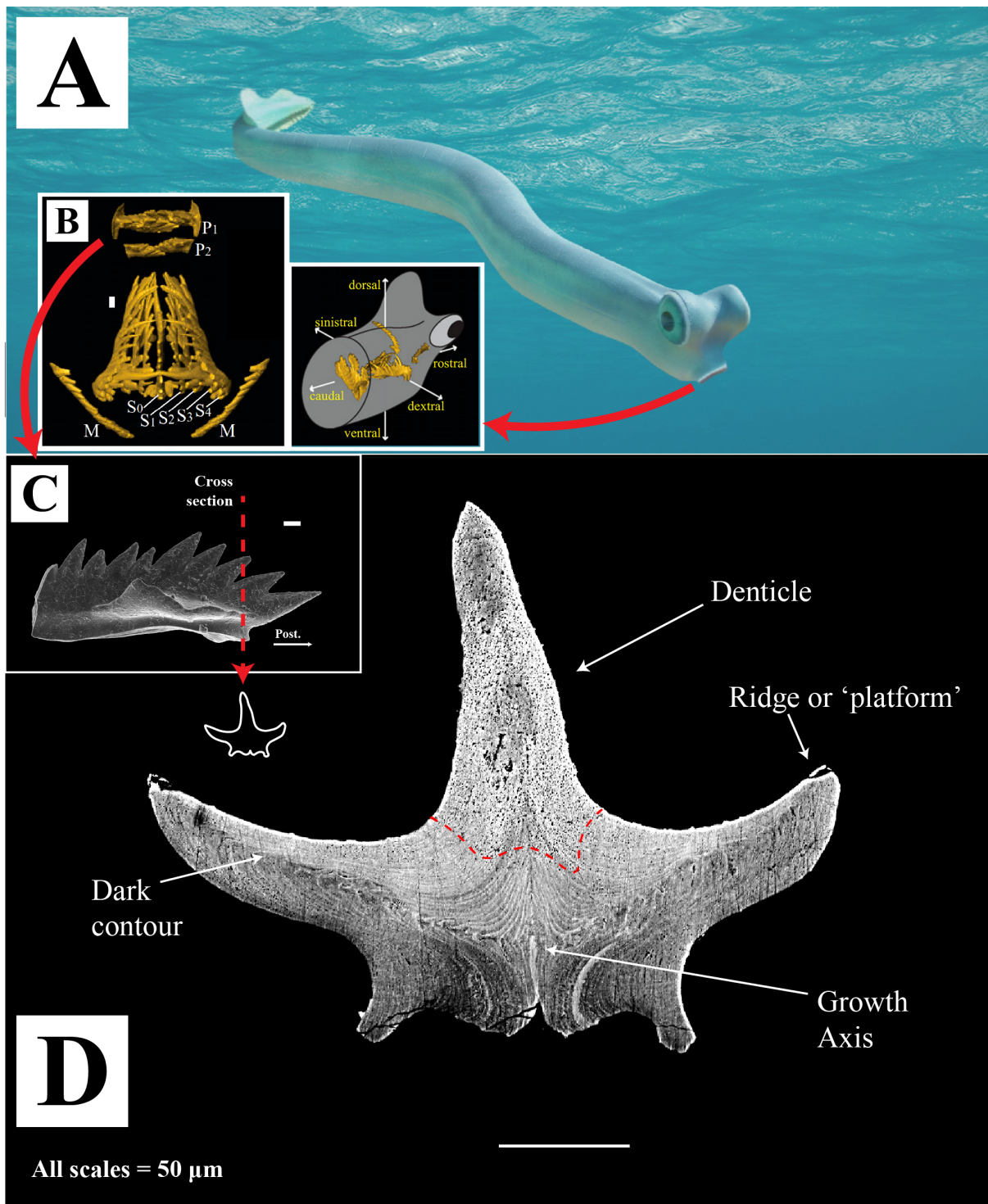
Figure 3. (A) Palaeoartistic interpretation of the conodont animal by © Beat Scheffold (PIMUZ Collection Assistant). The red arrow points towards a reconstruction of the conodont dental apparatus in dorsal view **(B)**, showing the different elements and their position (modified from Goudemand et al., 2011). Among these, P_1-elements **(C)** were selected as they are more diagnostic for accurate taxonomic identifications. Cross-sections of the conodont crown in posterior view **(D)** reveals the presence of patches of albid tissue (above the dashed red line) in the denticle. In the lower part, the hyaline tissue is dominant. At this same portion, a dark contour is noted from the ridges and extending laterally, just over the growth axis (details in Chapter I).

1.2.2 Conodont origin and identification

Samples used in this work were previously sampled by members of the palaeontological museum of the University of Zürich and are from different fossiliferous deposits around the world

(Figure 4). The sections from which samples have been chosen present different depositional features contrasting between coastal/marine settings, particular associated facies (e.g., adjacent levels containing organic matter) and are considered to be from distinct palaeolatitudes. All previous studies about the SSB dealing with $\delta^{18}O$ from conodonts were made of geological sections deposited on continental shelves and slopes. But in this study, samples recovered from carbonate blocks deposited on marine sea mounts in Oman and Timor are available (Baud et al., 2001; Brühwiler et al., 2012; Jattiot et al., 2015; Brosse et al., 2019). Sea mount-deposited sediments are valuable assets for palaeontological reconstructions (e.g., Orchard, 1995; Maekawa et al., 2018), since the depositional conditions are considered to represent open marine realm that are less prone to an influence from continental weathering and erosion and also freshwater runoff, which may have adverse effects on both primary compositions of the conodonts as well as their preservation potential (e.g., Zhang et al., 2018; Schneebeli-Hermann et al., 2020; Widmann et al., 2020). A local continental runoff may have an influence on the oxygen isotope composition of the seawater ($\delta^{18}O_{water}$) and consequently be reflected in the bioapatite of ectotherm animals (Kocsis et al., 2007; Klug et al., 2010; Fischer et al., 2012; Leuzinger et al., 2015; Carrillo-Briceño et al., 2019), including conodonts (e.g., Luz et al., 1984; Trotter et al., 2008). The stable oxygen isotope records from the marine sections are also thought to represent open marine conditions, hence complementing the understanding about Early Triassic climatic changes on a global perspective.

① **Spitsbergen** ② **United States** ③ **Oman**
🔴 Omani offshore seamount location ④ **Timor**
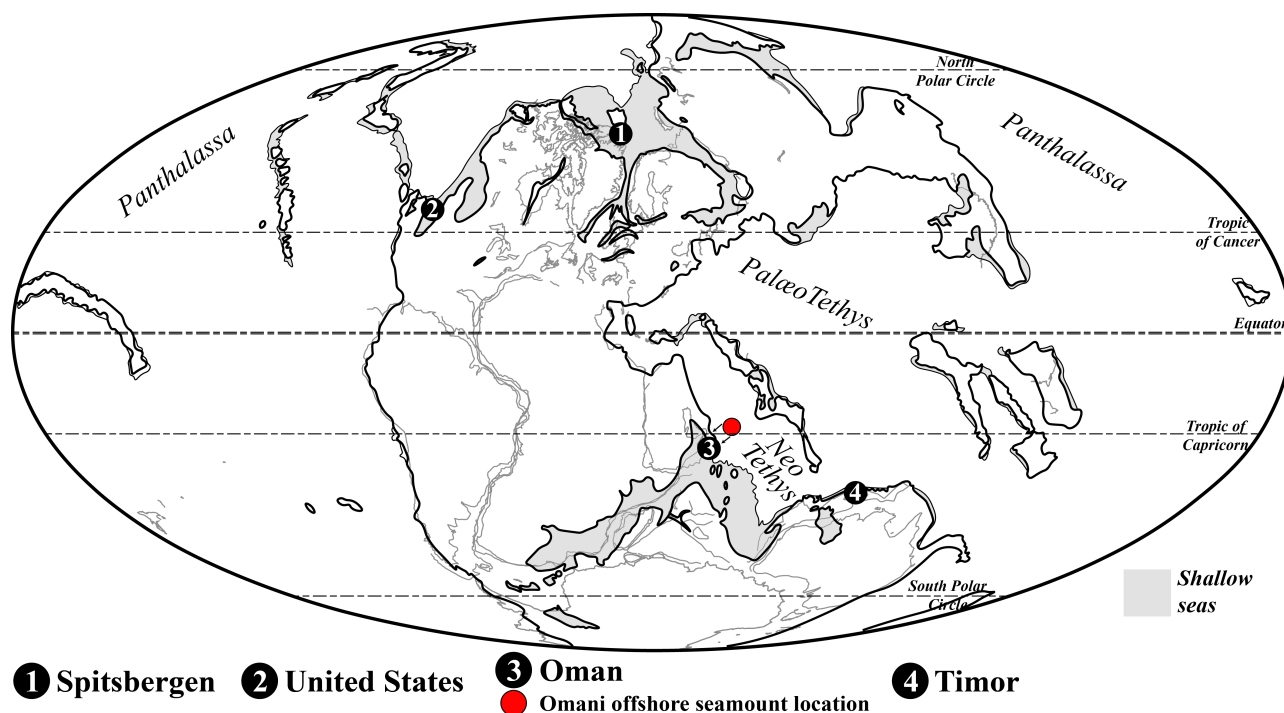
Figure 4. Simplified Early Triassic palaeogeography. Circles represent the palaeopositions of the sampled sections, while the grey shaded area indicates shallow seas. Stensiöfjellet in Spitsbergen **(1)**; Crittenden Springs, Georgetown and Palomino Ridge in United States **(2)**; Wadi Musjah and Jebel Aweri in Oman **(3)**, and Noe Tobe in Timor **(4)**. Modified from the preliminary PANALESIS map for the Early Triassic done by Vérard (2015), Vérard et al. (2019).

Introduction

The sections from which samples have been chosen present different depositional features contrasting between coastal/marine settings, particular associated facies (e.g., adjacent levels containing organic matter) and are considered to be from distinct palaeolatitudes (Figure 4). All previous studies about the SSB dealing with $\delta^{18}O$ from conodonts were made of geological sections deposited on continental shelves and slopes. But in this study, samples recovered from carbonate blocks deposited on marine sea mounts in Oman and Timor are available (Baud et al., 2001; Brühwiler et al., 2012; Jattiot et al., 2015; Brosse et al., 2019). Sea mount-deposited sediments are valuable assets for palaeontological reconstructions (e.g., Orchard, 1995; Maekawa et al., 2018), since the depositional conditions are considered to represent open marine realm that are less prone to an influence from continental weathering and erosion and also freshwater runoff, which may have adverse effects on both primary compositions of the conodonts as well as their preservation potential (e.g., Zhang et al., 2018; Schneebeli-Hermann et al., 2020; Widmann et al., 2020). A local continental runoff may have an influence on the oxygen isotope composition of the seawater ($\delta^{18}O_w$) and consequently be reflected in the bioapatite of ectotherm animals (Kocsis et al., 2007; Klug et al., 2010; Fischer et al., 2012; Leuzinger et al., 2015; Carrillo-Briceño et al., 2019), including conodonts (e.g., Luz et al., 1984; Trotter et al., 2008). The stable oxygen isotope records from the marine sections are also thought to represent open marine conditions, hence complementing the understanding about Early Triassic climatic changes on a global perspective.

Conodonts are also expected to live in different water depths and hence distinct habitats (e.g., pelagic or nektobenthic) as indicated by their ecological features (e.g., Joachimski et al., 2012; Trotter et al., 2015; Goudemand et al., 2019). The above is largely based on the distribution patterns of taxa within sedimentary facies (Barnes and Fahreus, 1975; Sweet and Bergström, 1984). A different school of thought suggests that the conodont biofacies distribution is mainly controlled by physico-chemical properties (e.g., salinity, nutrients, and dissolved oxygen levels) rather than by water depth, temperature or a relative stenohaline lifestyle (Carr et al., 1984; Orchard, 1996; Orchard, 2007; Purnell and Jones, 2012; Sun et al., 2012; Chen et al., 2015; Herrmann et al., 2015; Leu et al., 2019). Nonetheless, previous stable isotope investigations noted a $\delta^{18}O$ offset in species expected to have lived under distinct conditions (e.g., Joachimski et al., 2012; Trotter et al., 2015; Chen et al., 2021), while in other cases this heterogeneity between the isotopic compositions was not detected (e.g., Joachimski et al., 2009; Buggisch et al., 2010). Among the multi-elements known from Early-Triassic conodont dental apparatuses, P_1-elements are preferred for more accurate taxonomic identifications (Figure 3). These platform-like elements are less heterogeneous morphologically compared to ramiform

elements and therefore might be more suited for *in-situ* studies on individual conodont parts (Orchard, 1995, 2005, 2007; Maewaka et al., 2018).

1.3. Goals of the Ph.D.

For more than two decades, the research group of the PIMUZ has been studying the ecological recovery of the PTBME aftermath and the SSB crisis (e.g., Baud et al., 2001; Galfetti et al., 2008; Hermann et al., 2011; Ware et al., 2011; Brühwiler et al., 2010, 2012; Romano et al., 2013; Hautmann et al., 2015; Hochuli et al., 2016; Jattiot et al., 2015, 2018; Goudemand et al., 2019; Brosse et al., 2019; Hammer et al., 2019). In this scope, the Stable Isotope Laboratory group from the UNIL has been contributing with geochemical analyses in the last 15 years, done mainly in the form of carbon and oxygen stable isotope analysis of carbonate rocks. These have revealed in different sections the positive isotope excursion characteristic of the SSB crisis (e.g., Galfetti et al., 2007b; Brühwiler et al., 2009; Leu et al., 2019; Schneebeli-Hermann et al., 2020; Bagherpour et al., 2020; Widmann et al., 2020). More recently, this partnership was refined when phosphatic biominerals were included in the studies (e.g., Romano et al., 2013) and by the METECO investigation (this thesis), that had as one of its objectives to use bioapatites addressing the Early Triassic palaeo-climatic and -environmental changes.

Carbonate rocks and biominerals are more susceptible to physical destruction and/or chemical alteration during diagenesis and metamorphism, thus their use for studying pre-Cretaceous times is more limited (Luz and Kolodny, 1984; Kocsis, 2011). In contrast, bioapatites (i.e., bones and teeth) are thought to be more resistant to such diagenesis and inorganic alteration even over geologic time scales, as the P-O bonds of the phosphate molecule are considered to be less prone to reaction compared to the C-O bonds in carbonate ions (PO_4^{3-} *vs* CO_3^{2-}, Vennemann et al., 2001; Tütken and Vennemann, 2011; Kocsis, 2011). Hence, phosphates may be valuable assets for estimating the palaeo-climatic and -environmental changes. However, initial applications of stable isotope techniques using the conodont bioapatite were hindered due to sampling limitations (e.g., small size of conodonts, Trotter et al., 2008). Recent improvements that reduced the required sample quantity per analysis and new *in-situ* analytical techniques today allow for a study of sections with only few specimens recovered.

The main objective of this research is to investigate Early Triassic palaeoclimatic and environmental changes through stable isotope measurements of oxygen in phosphate from conodont bioapatite as a proxy.

This thesis is outlined in three chapters, written in manuscript format. The first work (Chapter I) is dedicated to improve the accuracy of our palaeoclimatic estimates by establishing

an analytical protocol for *in-situ* measurements of oxygen isotope compositions using SIMS techniques (Secondary Ion Mass Spectrometry). Two methods of stable oxygen isotope measurements were used: bulk sampling and high-temperature reduction (HTR) analysis, and *in-situ* measurements using a SIMS. Also, the microstructure and elemental distribution of conodonts was investigated using scanning electron microscopy (SEM) and an electron microprobe (EMPA), respectively. The analyses were focused on a single cosmopolitan species, *Scythogondolella* ex. gr. *milleri*, that was sampled from all studied sections (Figure 4). As an additional basis of comparison, the bioapatite of modern and fossil shark teeth was used. Like conodonts, sharks are one of the few vertebrate groups that have their bioapatite in the fluorapatite form (Vennemann et al., 2001), and they are commonly used for palaeoclimatic and – environmental studies, as well as being frequently used as a secondary apatite standard for $\delta^{18}O$ studies (e.g., Wheeley et al., 2012; Trotter et al., 2015). This chapter establishes guidelines in how to best analyse the often-scarce specimens of conodonts from important geological sections. This chapter have been submitted to *Geostandards and Geoanalytical Research*.

The second work (Chapter II) involves bulk sampling and *in-situ* $\delta^{18}O$ analysis of conodonts from marine carbonate exotic blocks from Oman. The $\delta^{18}O$ data from two geological units that recorded the Smithian and Spathian are compiled: the first one (Wadi Musjah) is abundant in fossils and analyses could be done by the two techniques of this study (HTR, SIMS); the second is an extended section (Jebel Awari) where the Smithian–Spathian boundary is well represented, but only few specimens could be recovered and thus were analysed by SIMS only. This is, to the best of our knowledge, the first time that conodonts from marine sections have been analysed for their $\delta^{18}O$ values. The $\delta^{18}O$ measurements from this extended section improved the knowledge about the progression of the climatic upheaval that happened during the SSB. In contrast to most of the research works so far where this interval was interpreted based on condensed sections that have shown sudden changes in temperature (Sun et al., 2012; Romano et al., 2013; Goudemand et al., 2019), the chosen profiles are considered to give more detailed records. Also, the $\delta^{18}O$ values are correlated to brachiopod clumped isotope analysis measured by the UNIL group (O. Edward and T. Vennemann), and which provided the $\delta^{18}O$ value of water (i.e., $\delta^{18}O_w$) that can be used to calculate conodont formation temperature. Additionally, recently Leu (2021 – PIMUZ) has done a multidisciplinary intercalibration that combined the Unitary Association Method (UAM), bio- and as well as chemostratigraphy of the Omani sections and those in the larger Tethyan realm (e.g., South China). By correlating these results with the recent U-Pb ages measured from a sequence of ash beds within the Chinese sections (Widmann, 2019 – UNIGE), the relative intensity, timing and also duration

of the cooling measured across the SSB could be estimated. This chapter will be submitted to *Palaeogeography, Palaeoclimatology, Palaeoecology*.

The third manuscript (Chapter III) relates conodonts already analysed from the two first papers as well as additional specimens in order to allow for a comparison between the $\delta^{18}O$ values of conodonts from different palaeolatitudes and different parts of the palaeoceans of the Early Triassic (Tethys and Panthalassa, Figure 4). The aim is to estimate palaeoceanic circulation patterns and possible temperature gradients. Because the samples from the Panthalassic sections are exclusively from coastal sections, they rather reflected palaeosalinity patterns from where conodont bioapatites precipitated, thus allowing us to estimate the palaeoenvironment. The compilation of this dataset with data already obtained from low-latitudes of the Tethys ocean contributed to a more global palaeoenvironmental interpretation of the Smithian-Spathian boundary biotic crisis. Additionally, our estimates will be correlated with results from numerical modelling that are being developed by the UNIGE research group. Preliminary climate simulations have shown contrasting palaeotemperatures and palaeosalinities between the Tethys and Panthalassa oceans (C. Ragon – UNIGE), hence an independent test of the validity of our results. This chapter will be submitted to *Palaeoceanography*.

"An understanding of the natural world and what's in it is a source of not only a great curiosity, but great fulfillment."

- Sir David Attenborough

CHAPTER I

New insights on micro-scale variations of chemical and oxygen isotope compositions in conodont and shark tooth bioapatite

Author contributions:

Zoneibe Luz, conceptualization, data curation, formal analysis and investigation, methodology, visualisation, original draft writing, review and editing.

Marc Leu, methodology, resources, validation, draft review and editing.

Lukas Baumgartner, formal analysis and investigation, methodology, resources, supervision, validation.

Anne-Sophia Bouvier, formal analysis and investigation, methodology, draft review and editing.

Hugo Bucher, conceptualisation, funding acquisition, methodology, resources, supervision.

Torsten Vennemann, conceptualisation, funding acquisition, methodology, resources, supervision, validation, draft review and editing.

New insights on micro-scale variations of geochemical and oxygen isotope compositions in conodont and shark tooth bioapatite

Zoneibe Luz[a,*], Marc Leu[b], Lukas Baumgartner[c], Anne-Sophie Bouvier[c], Hugo Bucher[b], Torsten Vennemann[a]

[a] *Institut des Dynamiques de la Surface Terrestre, Université de Lausanne, Rue de la Mouline, 1015 Lausanne, Switzerland*

[b] *Palaeontological Institute and Museum, University of Zürich, Karl-Schmid-Strasse 4, 8006 Zürich, Switzerland*

[c] *Institut des Sciences de la Terre, Université de Lausanne, Rue de la Mouline, 1015 Lausanne, Switzerland*

*Corresponding author: zoneibe.luz@gmail.com (Zoneibe Luz)

Abstract

Fossil bioapatite is widely used as a proxy archive to estimate palaeoclimatic and environmental conditions. However, well-preserved fossil teeth are often scarce in the geologic records, and they can be of a size that is too small for applications of classical analytical techniques in geochemistry. While new micro-scale *in-situ* methods now allow for studies of small specimens, it is important to understand the nature of bioapatite mineralisation, including the microstructure and the chemical and isotopic variations between structurally different parts of the fossil. To help understand the complexities of small-scale biomineralisation processes and their impact on possible O-isotope variations measured, this study used several different micro-analytical techniques (scanning electron microscopy, electron microprobe analysis, and secondary ion mass spectrometry - SIMS) to analyse the chemical and O-isotope compositions of bioapatites of distinct ages and states of preservation for both conodonts, as well as fossil and modern shark teeth. Stable oxygen isotope measurements in these biominerals were also made using a classical bulk sampling, chemical preparation, and high temperature reduction analysis (HTR). Quantitative analyses and chemical element distribution maps of segminiplanate conodont P_1-elements are often found to be heterogeneous in terms of their chemical compositions. The reason for this heterogeneity may be related to conodonts retracting their teeth during growth, a suggestion also supported by variations in Ca, F, Mg, S, and Na concentrations. Based on differences of sample preparation and $\delta^{18}O$ values, conodonts from Timor analysed by SIMS are separated into three groups. The $\delta^{18}O$ mean is lower and the values have a larger variation for samples transversally cross-sectioned (16 $\pm$1 ‰, n = 13) and for conodonts with a middle

longitudinal cross section (15.7 ±1.9 ‰, $n = 11$), where the albid and hyaline tissues are mixed. In contrast, the hyaline tissue of conodonts cross-sectioned longitudinally at the lower part of the crown had homogeneous $\delta^{18}O$ values of 17.1 ±0.2 ‰ ($n = 13$), similar to those of the HTR analysis (17.3 ±0.4 ‰, $n = 7$). Shark teeth also had a large range in their $\delta^{18}O$ for the *in-situ* technique. The $\delta^{18}O$ variance between distinct enameloid zones of the same tooth in modern sharks is up to 1.3 ‰. The heterogeneity in the chemical concentrations between the bioapatite structures does not influence the *in-situ* oxygen isotope measurements though. Instead, variations of $\delta^{18}O$ are sensitive to analytical artefacts related to sample texture, which are influenced by the preparation of the samples for analyses. Based on the isotopic homogeneity of the hyaline tissue from the lower part of the crown and similarity with analogous specimens sampled in bulk, the conodont sample set from Timor (*Scythogondolella* ex. gr. *milleri*) was selected to be an internal standard for the SwissSIMS laboratory. This new in-house standard can be used to normalise the oxygen isotope compositions and consequently help interpret variations in palaeo-climate and -environmental conditions for bioapatite based on individual conodont analyses.

Keywords: Phosphates, conodont, oxygen isotopes, SIMS, bioapatite

1. Introduction

Bioapatite mineralised in bones and teeth is an important proxy archive used in palaeontological research. Fossils of bones and teeth not only provide information about the past fauna and possible palaeo-ecological dynamics of geological records but can also be used to evaluate palaeo-environmental and -climatic conditions (e.g., Longinelli et al., 1973a, b; Kolodny et al., 1984; Kohn and Cerling, 2002). The general bioapatite formula with its most common anion substitutions is $Ca_5(PO_4, CO_3, SO_4)_3(OH, F, CO_3)$, and the PO_4^{3-} and CO_3^{2-} groups can have their oxygen isotope compositions measured individually (Vennemann et al., 2001). Oxygen isotope compositions of phosphate bound oxygen ($\delta^{18}O_{PO4}$) are an alternative to that of carbonates to help understand the palaeoenvironment of the Palaeozoic era (Wenzel et al., 2000; Joachimski et al., 2009; Trotter et al., 2008, 2016a), including studies of mass extinction events (e.g., Joachimski et al., 2012; Sun et al., 2012; Romano et al., 2013; Goudemand et al., 2019). During such periods reliable estimates of palaeotemperatures using calcite fossils may be more difficult to interpret, because of their susceptibility to physical destruction and chemical alteration during diagenesis and metamorphism. The strong P-O bond of the phosphate molecule is considered to be more resistant to diagenetic alteration than the CO_3^{2-} (e.g., Kohn and Cerling, 2002; Zazzo et al., 2004a). Oxygen isotope palaeothermometry based

on bioapatites is hence a valuable approach that can complement information for periods where estimates of the palaeoenvironment are more challenging (e.g., Luz et al., 1984; Kolodny and Luz, 1991; Iacumin et al., 1996; Lécuyer et al., 2003; Tütken and Vennemann, 2011).

However, the application of oxygen isotope techniques to Palaeozoic bioapatites is often limited by the small size of one of the major fossils used for this era: conodonts. These are eel-like, jawless vertebrates that were ubiquitous from the Cambrian to the Triassic (Luz et al., 1984). Conodont dental elements are composed of fluorapatite - the most resistant form of apatite (Posner et al., 1984) - and they are frequently used as index fossils (e.g., Orchard 2005, 2007). This allows them to be used as palaeoproxies for studies of climatic change (e.g., Trotter et al., 2008; Joachimski et al., 2012; Romano et al., 2013; Goudemand et al., 2019). Classical analyses for O-isotope compositions require a minimum amount of 1 to 5 mg of phosphate (e.g., Vennemann et al., 2002; Mine et al., 2017), which limits applications to conodonts given their small size (about 500 µm) and weight (< 100 µg). While bulk sampling is a valid approach for palaeo-climatic/ecologic interpretations (e.g., Wenzel et al., 2000; Joachimski et al., 2009, 2012; Sun et al., 2012; Romano et al., 2013), the measured $\delta^{18}O_{PO4}$ values may average possible intra-tissue differences as well as intra- and inter- specific taxon variations.

Over the last decade, the $\delta^{18}O$ values of individual conodonts were increasingly measured by secondary ion mass spectrometry (SIMS) (Rigo et al., 2012; Wheeley et al., 2012; Trotter et al., 2015, 2016a; Zhang et al., 2017; Goudemand et al., 2019). This *in-situ* technique uses a finely focused primary ion beam for sputtering the sample surface, producing secondary ions that are extracted and directly analysed for their oxygen isotope composition. The high spatial resolution of SIMS measurements can measure isotopic compositions with a depth of ablation by the ionised beam of about 1 to 6 µm, at a diameter of 10 to 30 µm (e.g., Wheeley et al., 2012). However, to obtain results on such small scales, the sample surface topography must be less than 5 µm (Marin-Carbonne et al., 2022). Surface topography is known to affect the $\delta^{18}O$ values measured by SIMS by creating tilted surfaces compared to the perpendicular incidence of the secondary ion beam (e.g., Kita et al., 2009). The analysis of distinct tilted surfaces can effectively deform the electrostatic field and modify the trajectory of the secondary ions (Kita et al., 2009), thus the differential sputtering of irregular sample textures can cause instrumental mass fractionations (IMF). This is an important factor to verify in bioapatites with different biomineralogical structures (e.g., Skinner and Jahren, 2007). Polishing of such different structures that may also include different forms of apatite because of different chemical compositions, may produce contrasting topographies between the structures and consequently irregular sample textures. In addition, the high intensity ablation by ion microprobe is a

disadvantage, as the sample sputtering releases oxygen from all oxygen-bearing sites in apatite (CO_3^{2-}, PO_4^{3-}, OH^-) and as such standardisation with samples of similar chemical composition and structural disposition becomes important for accurate measurements (e.g., Wheeley et al., 2012). This could compromise the reliability of this approach since these different O-bearing sites not only have different O-isotope compositions, but also have a different susceptibility to diagenetic changes compared to the oxygen bound to the phosphate ion (Iacumin et al., 1996; Lécuyer et al., 2010). However, because oxygen derived from the phosphate ion dominates in fossilised bioapatite (about 90 to 95 %) that is commonly a carbonate containing hydroxylapatite (also referred to as dahllite), compared to the carbonate oxygen (about 3 to 6 %) and hydroxyl oxygen (0 to 3 %), it is often assumed that the $\delta^{18}O$ values measured by SIMS are close to those of the phosphate molecule (e.g., Lécuyer et al., 2010; Wheeley et al., 2012; Zhang et al., 2017).

Another possible source of bias could be that data from bioapatites measured by SIMS is normalised and calibrated using the magmatic fluorapatite of Durango (c.f., Trotter et al., 2008; Wheeley et al., 2012; Sun et al., 2016; Zhang et al., 2017; Wudarska et al., 2022). Durango apatite is a distinctive fluorapatite from an open-pit iron ore mine at Cerro de Mercado, Durango City, Mexico (Chew et al., 2016). Besides having a high inter-crystal oxygen isotope variation (up to 4.4 ‰, Sun et al., 2016), the Durango apatite is compositionally different from conodont bioapatite and may have specific sources of isotopic bias when sputtered by an ion beam during *in-situ* analyses (e.g., Trotter et al., 2015, 2016a; Sun et al., 2016; Wudarska et al., 2022). To evaluate such matrix related effects, previous studies employed a second fluorapatite standard, for example a great white shark tooth, to be analysed in parallel with the Durango standard (Trotter et al., 2008; Rigo et al., 2012). The enameloid structure in shark teeth would be an optimal choice as a secondary standard, given the relative abundance of both modern and fossil specimens (Cappetta et al., 2012). They are also frequently used as palaeoproxies for palaeoclimate studies, and numerous contributions were done using the bulk method for the enameloid (e.g., Kocsis et al., 2014; Leuzinger et al., 2015; Carrilo-Briceno et al., 2018). Earlier investigations using bulk sampling noted that modern shark teeth were relatively homogeneous in their $\delta^{18}O$ (e.g., Vennemann et al., 2001; Kocsis et al., 2015), with minor variations only noted in inter- and intra- tooth tissue (dentine *vs* enameloid) analyses. In addition, the larger size of a shark tooth compared to conodonts allow a higher number of analyses such that is possible to use the same sample for different SIMS sessions. Despite the potential to serve as reference materials, a more recent SIMS study on shark teeth, obtained from sharks living under controlled environmental conditions, measured $\delta^{18}O$ variations of up to 4 ‰ in the same enameloid sub-structure (Žigaitė and Whitehouse, 2014). This highlights the necessity of further

studying shark teeth to test their feasibility to normalise $\delta^{18}O$ values.

Ideally, a conodont fluorapatite standard could be used for the measurements of conodonts. Some studies specifically addressed *in-situ* $\delta^{18}O$ variations in conodonts (Wheeley et al., 2012; Rigo et al., 2012; Trotter et al., 2008, 2015; Zhang et al., 2017), but there are contrasting conclusions about the best biomineralogical structure to be used (e.g., Trotter and Eggins, 2006; Trotter et al., 2007). It can also be challenging to characterise conodonts for *in-situ* investigations. The conodont crown is composed of hyaline and albid tissue (Donoghue, 1998), and a clear distinction between the two structures is only possible with high-resolution microscopy techniques such as scanning or transmission electron microscopy (Donoghue, 1998; Trotter et al., 2007). However, SIMS analyses are set using a light microscope, making it difficult to distinguish the conodont crown tissues. While not all previous *in-situ* oxygen isotope measurements note a systematic difference between hyaline and albid crown, overall O-isotopic variation may be higher if different tissues are sampled (e.g., Wheeley et al., 2012; Zhang et al., 2017). Progress related to the sampling protocol may ease the visualisation of one or another crown tissue, which could favour the positive decision of using rare conodont specimens for *in-situ* geochemical techniques.

Knowledge on the chemical composition of bioapatites is also important, both for paleo-environmental interpretations and to verify whether a "compositional" instrumental fractionation effect exists for bioapatite. Studies of calcite have noted such compositional 'matrix effects', where the instrumental mass fractionations are related to different Mg, Fe, and Mn content (Rollion-Bard and Marin-Carbonne, 2011; Śliwiński et al., 2018). For Mg variations in carbonates a standard deviation for $\delta^{18}O$ of about 0.3 ‰ per wt.% was noted (Rollion-Bard and Marin-Carbonne, 2011), and between the bioapatite structures the Mg typically has concentrations of less than 1.5 wt.% (e.g., Elliott, 2002; Skinner and Jahren, 2007), hence the effect of Mg can be expected to be minor. In contrast, even small contributions of the Fe as $FeCO_3$ (1-2 mol%, about 1 wt.%) can bias the $\delta^{18}O$ values by 2–3 ‰ (Śliwiński et al., 2018). This may be relevant to fossil bioapatites too, as they can be enriched in Fe by diagenetic processes (Raiswell, 1997; Trotter and Eggins, 2006). Although some quantitative and qualitative chemical analysis were monitored for conodonts and shark teeth (e.g., Trotter and Eggins, 2006; Kocsis et al., 2015; Zhang et al., 2017; Shirley et al., 2018), few contributions mapped their chemical distributions (Katvala and Henderson, 2012; Enax et al., 2014). Variations in the chemical composition of elements such as the F and Mg, are known to influence the degree of crystallinity (i.e., crystallite size and crystal class) of apatite (LeGeros, 1981; Elliott, 2002; Katvala and Henderson, 2012; Enax et al., 2014). Samples containing lower

F and higher Mg concentrations have a smaller crystal size and a higher strain of elements (i.e., more 'impurities' - trace elements in the bioapatite) (LeGeros, 1981; Elliott, 2002). Moreover, structures assumed to have only restricted pore spaces (e.g., shiny enameloid layer of sharks, Enax et al., 2014) have their chemical distribution somewhat similar to the dentine, which is known to be more susceptible to alteration processes (e.g., Vennemann et al., 2001).

To test for factors influencing the instrumental fractionation of bioapatites more rigorously, we prepared conodonts and shark teeth in different views (longitudinal and transversal cross sections), to verify which sample orientation and which tissue type and chemical composition is most advantageous for $\delta^{18}O$ studies. For calibration purposes, a comparison of the O-isotope analyses by SIMS is then made with the classical method of silver phosphate microprecipitation and analysis in bulk sampling by High Temperature Reduction (HTR). To evaluate structural variations, high-resolution scanning electron microscopy (SEM) as well as qualitative and quantitative measurements of their chemical composition by electron microprobe analyses (EMPA) were made. These may provide additional insights about the structure, texture, and odontogenesis on the studied specimens (e.g., Katvala and Henderson, 2012; Enax et al., 2012, 2014; Shirley et al., 2018, 2020), and may also shed light on analyses-specific instrumental mass fractionations (IMF) for SIMS O-isotope measurements of different apatites, including bioapatites such as shark teeth and conodonts.

A final objective of this study is to develop a secondary reference material for *in-situ* isotopic measurements of bioapatites such as conodonts, to be applied to future oxygen isotope analyses ($\delta^{18}O$) in phosphate for sites where single conodont analyses are required in order to gain a better understanding of past climatic oscillations. Ultimately, improvements in the accuracy of measuring $\delta^{18}O$ values from conodonts will refine the interpretation and understanding of palaeoclimatic changes, such as for example the climatic oscillations following the Permian–Triassic mass extinction (e.g., Goudemand et al., 2019).

2. Material and Methods

2.1 Study area and material

Conodonts from five Early Triassic sites were used (Figure 1.1). Each locality has its specific depositional features, a description of which is summarised in the Supplementary File S1.1.

Rock samples were treated in acetic acid (10 %), sieved and screen washed (0.5 mm, 1 mm, 2 mm) for subsequent picking of the conodonts using a binocular microscope. Taxonomic identification is based on references of Early Triassic species (e.g., Orchard, 2005, 2007, 2008;

Leu et al., 2019). Among the multi-elements known from Early Triassic conodont dental apparatus, platform-like elements (P_1 elements) were preferred for more accurate identifications, since they are taxonomically more diagnostic, with the highest morphological change during evolution compared to other elements. Segmiplanate P_1-elements of *Scythogondolella* ex gr. *milleri* were selected as our reference taxon as dental elements were available from all localities (Tables 1.1, 1.2). This species is widely used in the conodont biostratigraphic zonation and is commonly related to the *Wasatchites distractus/Anasibirites multiformis* ammonoid zone (Jattiot et al., 2015; Leu et al., 2019; Goudemand et al., 2019). *Sc.* ex gr. *milleri* has a relatively short fossil record (about 200 ky) and can be found in lower late Smithian deposits around the world (e.g., Orchard and Zonneveld, 2009; Leu et al., 2019). An important remark about the selected elements is that they do not have the basal body preserved, the structure more susceptible to diagenesis (Wheeley et al., 2012; Zhang et al., 2017). The maximum burial temperatures of the conodonts can be assessed by the Conodont Alteration Index (CAI; Epstein, 1977). In this study, most of the samples have a CAI of 1 (Table S1.1), the lowest and best-preserved following CAI classification (< 80 °C). In contrast, USA specimens from Crittenden Springs have a CAI of 2.5 to 3 (< 200 °C). One CAI 5 specimen (< 300 °C) from Guryul Ravine, Kashmir (Leu et al., 2019) was used for comparison purposes of their chemical compositions (Table S1.1).
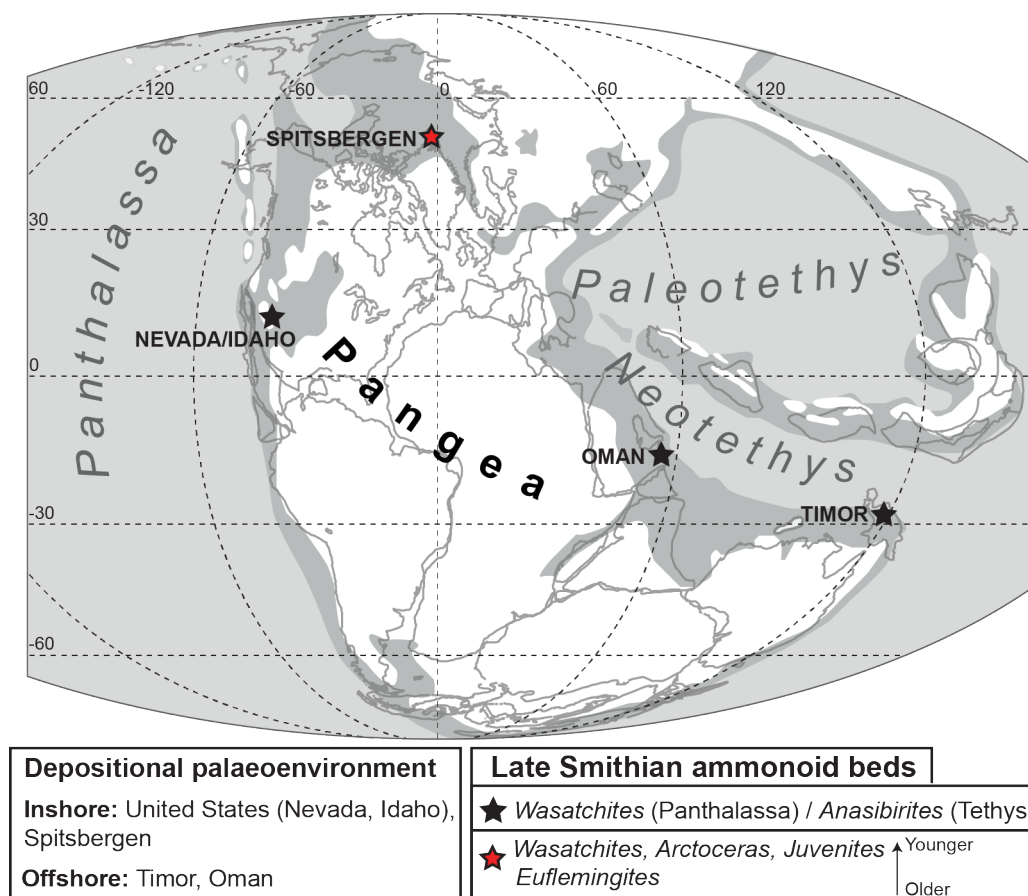
Figure 1.1. Simplified palaeogeographic reconstruction of the Early Triassic period. Stars represent the relative position of sampled sections, and their colours denote the ammonoid related beds in parenthesis. Modified after Leu et al. (2019).

26

Table 1.1. Conodont and shark teeth δ¹⁸O values analysed by SIMS. The *n* refers to the number of sample spots analysed for each specimen. Samples labelled with a 'b' (i.e., TM$_{mid\ longitudinal}$ group) are re-analysis in specimens of the TM$_{low\ longitudinal}$ group (TM2, TM5–TM12). Shark enameloid abbreviations are **SCED**: single crystallite enameloid edge; **SCE**: single crystallite enameloid; **PBE**: parallel bundled enameloid; **TBE**: tangled bundled enameloid.

Sample ID	Taxon	Origin	Age	Cross section	δ¹⁸O (VSMOW)	δ¹⁸O Std dev.	*n* (spots)
TM2	*Scythogondolella ex gr. milleri*	Noe Tobe/ West Timor	late Smithian	Low longitudinal (TM$_{low\ longitudinal}$)	17,0	0,2	10
TM5					17,0	0,2	4
TM6					17,0	0,2	4
TM7					16,9	0,3	4
TM8					17,3	0,2	3
TM9					16,9	0,2	4
TM10					17,0	0,2	3
TM11					17,4	0,5	4
TM12					17,4	0,1	4
TM15					17,3	0,4	7
TM16					16,5	0,3	7
TM17					17,1	0,3	8
TM18					17,3	0,4	8
TM2b				Middle longitudinal (TM$_{mid\ longitudinal}$)	10,8	2,1	8
TM5b					16,1	1,2	7
TM6b					16,1	0,3	8
TM7b					16,4	0,5	8
TM8b					16,7	0,3	8
TM9b					16,0	0,8	8
TM10b					16,9	0,4	8
TM11b					16,1	0,6	7
TM12b					16,6	0,3	6
TM19					16,8	0,4	6
TM20					13,6	0,9	8
TM1				Transversal (TM$_{transversal}$)	16,8	0,4	7
TM1b					16,8	0,3	8
TM3					16,4	0,1	2
TM4					16,3	0,7	4
TM13					15,4	0,6	4
TM14					15,5	0,4	7
TM21					17,1	0,4	8
TM22					16,9	0,4	8
TM23					16,9	0,3	8
TM24					15,1	1,6	2
TM25					15,0	1,0	4
TM26					13,6	1,2	3
TM27					15,8	0,6	3
CS1		Crittenden Springs/USA		Low longitudinal	15,0	0,6	4
CS2					15,4	0,3	4
CS3					15,9	0,3	4
CS4					15,6	0,1	4

ID	Species	Locality	Age	Structure		Value	SD	n
GT1		Georgetown/USA				15,4	0,2	3
GT2						15,0		1
SB1	*Scythogondolella mosheri*	Stensiöfjellet/Spitsbergen				14,4	0,2	2
SB2						14,4	0,2	4
SB3	*Scythogondolella ex gr. milleri*					14,5	0,2	3
SB4						14,5	0,1	2
SB5						14,4	0,2	4
SB6						14,4	0,3	2
SB7						14,2		1
				Specific shark structures				
GW1en	*Carcharodon carcharias*	South Africa	Modern	Enameloid total		22,4	0,5	9
				Enameloid structures	**SCED**	22,8	0,2	5
					PBE	21,9	0,3	4
GW2en				Enameloid total (PBE)		22,9	0,3	11
GW3en				Enameloid total		22,8	0,5	12
				Enameloid structures	**SCED**	23,2	0,1	4
					PBE	23,0	0,1	4
					TBE	22,2	0,5	4
GW3de				Dentine		10,8	0,2	2
GW4en				Enameloid total		22,9	0,6	10
				Enameloid structures	**SCED**	23,1	0,2	4
					SCE	23,6	0,4	2
					PBE	22,3	0,4	4
GW4de				Dentine		11,0	0,8	3
OD1en	*Odontaspis denticulata*	van der Hocht collection	Oligocene	Enameloid total		21,3	2,7	12
				Enameloid structures	**SCED**	17,8	1,0	4
					SCE	23,2	0,4	4
					PBE	23,0	0,2	4
OD1de						20,3	0,3	4
OD2en				Enameloid total		20,9	1,0	14
				Enameloid structures	**SCED**	22,2	0,2	4
					SCE	20,7	0,1	3
					PBE	20,2	0,5	4
					TBE	20,2	0,3	3
OD2de						20,2	0,3	4

Table 1.2. Conodont and shark teeth $\delta^{18}O_{PO4}$ values analysed by HTR (TC/EA). The *n* refers to the number of silver capsules analysed for each sample.

Sample ID	Taxon	Origin	Age	$\delta^{18}O_{PO4}$ (VSMOW)	$\delta^{18}O_{PO4}$ Std dev.	*n* (splits)
TM-HTR	*Scythogondolella* ex gr. *milleri*	Noe Tobe/West Timor	late Smithian	17,3	0,4	7
WMJ-SM		Wadi Musjah/Oman		16,9	0,2	3
GW1en	*Carcharodon carcharias*	South Africa	Modern	22,3	0,1	6
GW2en				22,4	0,1	6
GW3en				22,2	0,0	2
GW3de				22,7	0,0	2
GW4en				21,9	0,1	2
GW4de				22,0	0,1	2
OD1en	*Odontaspis denticulata*	van der Hocht collection	Oligocene	21,8	0,1	2
OD1de				21,6	0,1	2
OD2en				21,8	0,2	2
OD2de				21,0	0,0	2

Modern shark teeth that have been studied previously (Vennemann et al., 2001) and fossil shark teeth donated to T. Vennemann completed the sample set. Shark tooth samples are all from the Lamniformes order (a.k.a. mackerel sharks, Ebert et al., 2013): the modern representants are Great White sharks from waters of the East coast of South Africa (KwaZulu-Natal, Vennemann et al., 2001) and fossil teeth are from *Odontaspis denticulata*, *Anotodus* sp. and *Carcharias cuspidata*, recovered from Oligocene-Miocene marginal marine basin settings of the Molasse basin (Vennemann et al., 1998).

While ideally all samples would have been used for all geochemical techniques mentioned in the introduction, the complex preparation techniques for the small conodonts allowed us to use some specimens for one method only. Nonetheless, these samples help illustrate the structural and chemical variations found on μm-scales within conodont bioapatite. A detailed list the different techniques used, as well as the sample origin is summarised in the Supplementary Information (Table S1.1).

2.2 Methods

2.2.1 Sample selection and analytical protocol

At the University of Lausanne, the samples were cleaned in distilled, deionised water using an ultrasonic bath to reduce surface contamination prior to drying overnight at 70 °C. All modern shark teeth were also cleaned in boiling salt water to remove organic matter (Vennemann et al., 2001).

For the conodonts, only the Oman and Timor sites provided enough specimens to use for the bulk sampling method. Sites from the USA and Spitsbergen had few specimens for *in-situ* measurements only. Samples for individual analysis were mounted in an epoxy resin (EpoFix), polished, cleaned and dried overnight (60 °C) before coating with carbon (SEM, EMPA) or gold (SIMS) for sample conductivity. A large number of well-preserved (CAI 1) conodonts of *Scythogondolella* ex gr. *milleri* were collected from the exotic carbonate block from Noe Tobe (Timor) (Jattiot et al., 2015). Their preservation state and abundance represented a good opportunity to establish our analytical protocol for SIMS measurements. Conodonts from Timor were cross-sectioned to note their structurally different tissues (albid *vs* hyaline tissue). Initially, two main cross-sectioning strategies were adopted: a transversal cross section (Figure 1.2A); and a longitudinal cross section at the lower part of the crown (Figure 1.2B). Conodonts transversally cross-sectioned were positioned to expose the posterior side, where the basal body was located, a structure analogous to the vertebrate dentine (Donoghue, 1998). To verify that the samples were not influenced by remains of a broken basal body, some samples were transversally cross-sectioned at the anterior part (Table S1.1, Figure 1.3B). After some experiments, samples cross-sectioned longitudinally were repolished after a first analysis of oxygen isotopes (labelled with a 'b' in Table 1). However, these cross sections where the exposed portion was at the interior of the conodonts (Figure 1.2C), had unique characteristics and deserved more attention. Two more samples were prepared for this approach (TM19 and 20). In total, three main conodont groups are presented in the results and discussion: conodonts with a low longitudinal cross section; with a middle longitudinal cross section; and conodonts transversally cross-sectioned. SEM images helped to determine the predominant conodont tissue associated with these - hyaline, albid, or a mixture, thus helping in this classification and in the presentation of the results (more details in 3.1). Original output images and additional cross-sectioned specimens (Table S1.1) are presented in the Supplementary File S1.2. Based on preliminary $\delta^{18}O$ values (sections 3.4 and 4.3) in the three main conodont groups from Timor, specimens from Oman, USA and Spitsbergen were prepared with a low longitudinal cross section only.

For the shark teeth, the analyses focused on the tip of the teeth. This is a zone of convergence of the outer enameloid layer (Figure 1.4), offering a larger surface area for the analysis. Individual tooth tips were cross-sectioned to expose two views: a transversal cross section (Figure 1.4B, C) and a longitudinal cross section to expose both enameloid and dentine in different orientations (Figure 1.4A). An influence of the apatite crystal was noted for fluorine concentrations in EMPA measurements (e.g., Goldoff et al., 2012). However, no differences

were reported for oxygen isotope analysis of crystallographically different orientations of analyses (Li et al., 2021; Wudarska et al., 2022). The fluorine content was measured in shark teeth "parallel-bundled" enameloid tissue (PBE, Figure 1.4). In the transversal cross section, the PBE has its *c*-axis parallel to the EMPA and SIMS beams. In the longitudinal cross section, the *c*-axis of the PBE is perpendicular.
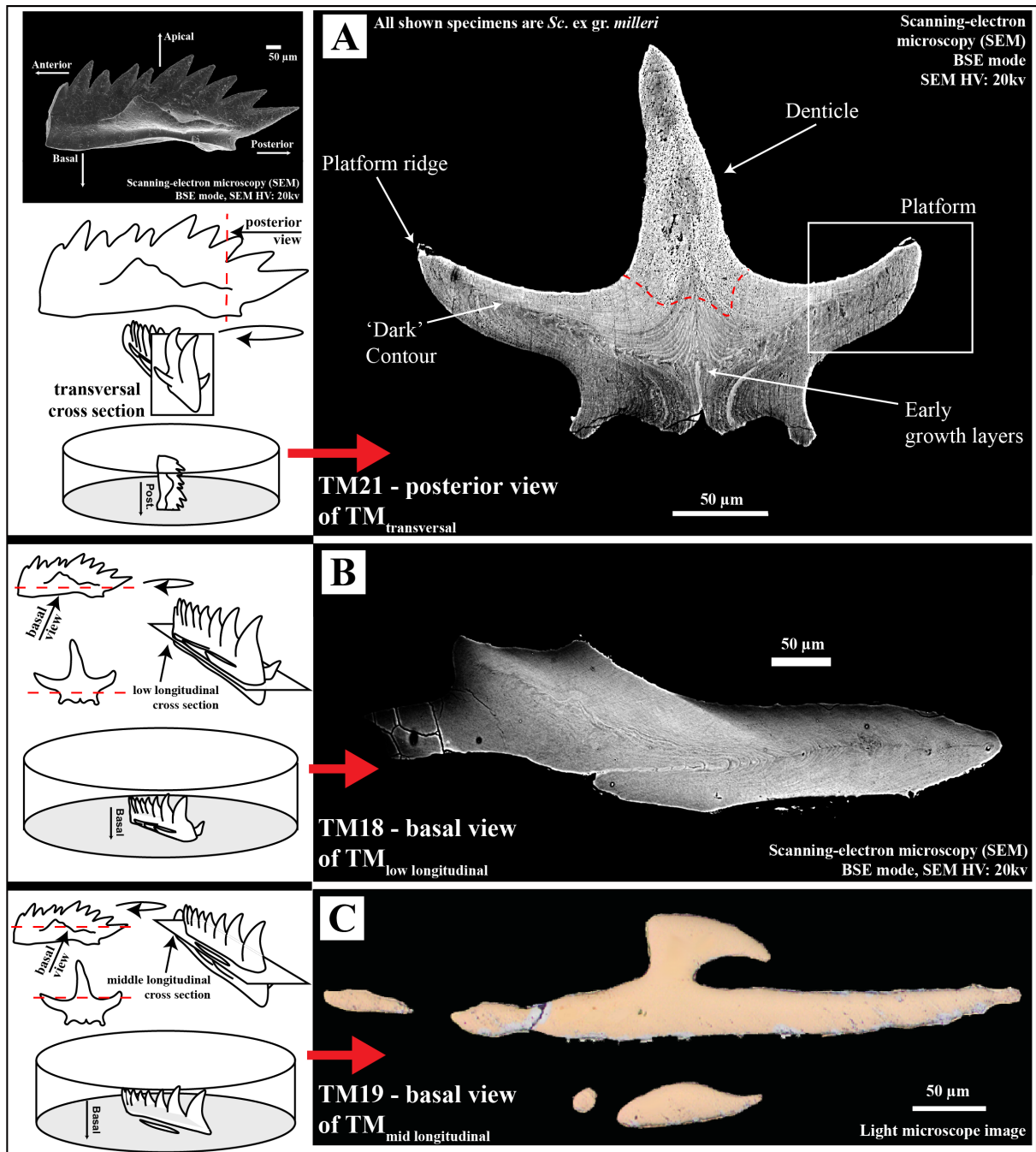
Figure 1.2. Schematic representation of the sampling protocol (upper-left) employed for *Sc.* ex gr. *milleri* conodonts and scanning-electron microscopy images (right) in back-scattered electron mode for two of the three main groups classified in this research. Specimens were prepared for visualisation of longitudinal (TM18, TM19) and transversal (TM21) cross sections. A transversal cross section (TM$_{transversal}$) of the posterior extremity **(A)** reveals the presence of patches of albid crown/tissue (above the dashed red line) in the denticle. The dark contour mentioned in the text is also indicated, starting in the ridges and extending laterally in the platforms, just over the growth axis. In the longitudinal cross section at the lower conodont crown (TM$_{low longitudinal}$), the lamellar hyaline crown is the predominant structure **(B)**. The third group comprises specimens also cross-sectioned longitudinally (TM$_{mid longitudinal}$) and polished until about the interiors of the conodont crown **(C)**.

31
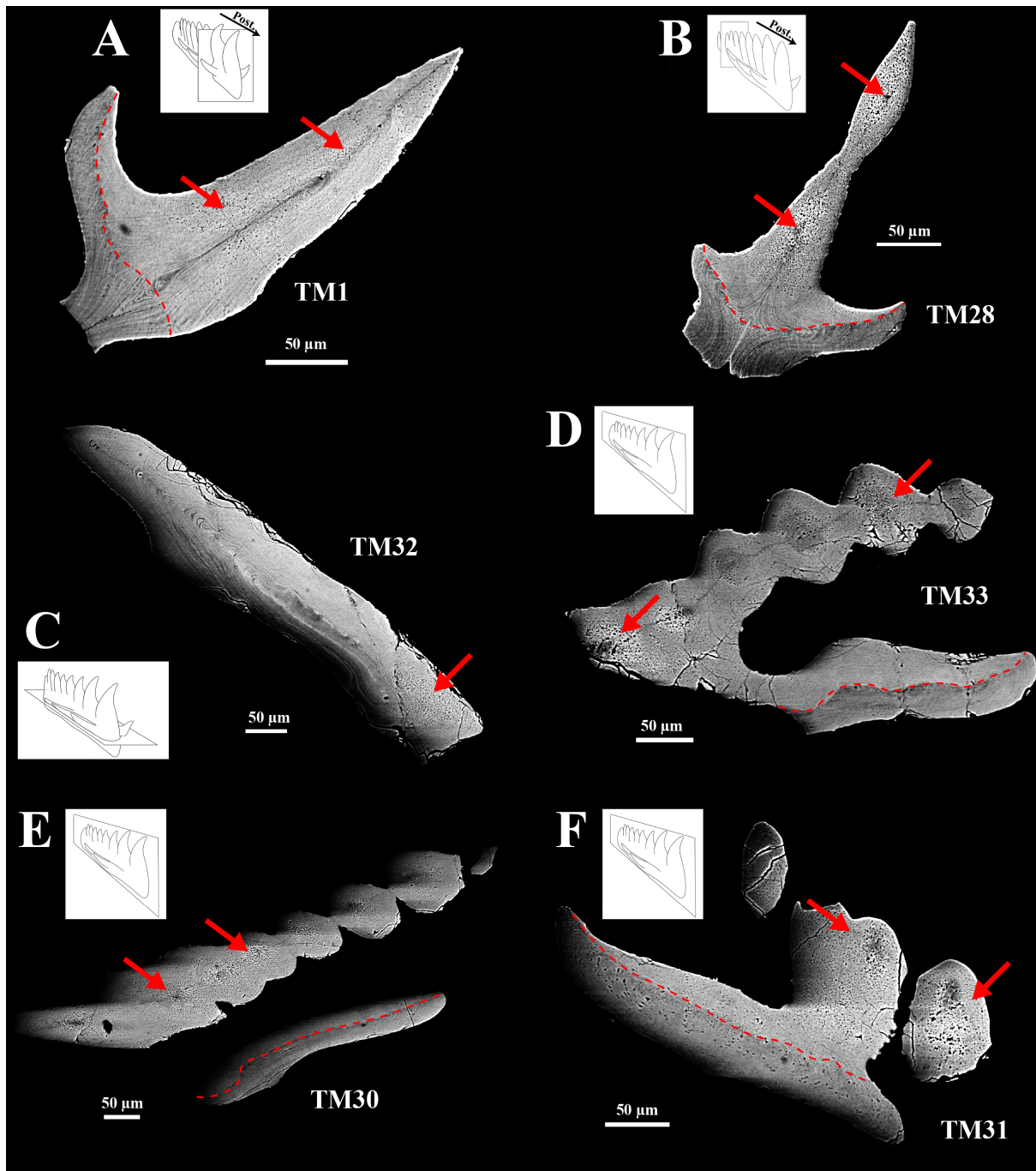
Figure 1.3. Additional *Sc.* ex gr. *milleri* specimens imaged by SEM in back-scattered electron mode (SEM-HV: 20 kV): transversal cross sections of the posterior **(A)**, and anterior extremities **(B)**; longitudinal cross section of the lower crown **(C)**, and vertical longitudinal cross sections of the conodonts for **(D)**, **(E)** and **(F)** (lateral view). The red arrows point towards more porous regions, which should indicate albid tissue presence. The dashed line remarks the reticulated dark contour at the lower conodont crown.

2.2.2 SEM, EMPA and SIMS preparation

For experimental purposes for the SEM, EMPA, and for the SIMS, eight teeth/conodont elements (GW1, GW5, TM1 to TM6) were pre-treated with 1 M Ca-buffered acetic acid (pH = 4.5, 2 h) to remove any exogenous carbonates, followed by several rinse cycles with distilled, deionised water (Koch et al., 1997). For some sessions the samples were analysed in the original resin where they were prepared, but for other sessions the resins were cut and placed into an indium mount. A summary about this preparation can be found in the SwissSIMS website

(https://swisssims.com/sample-preparation/).
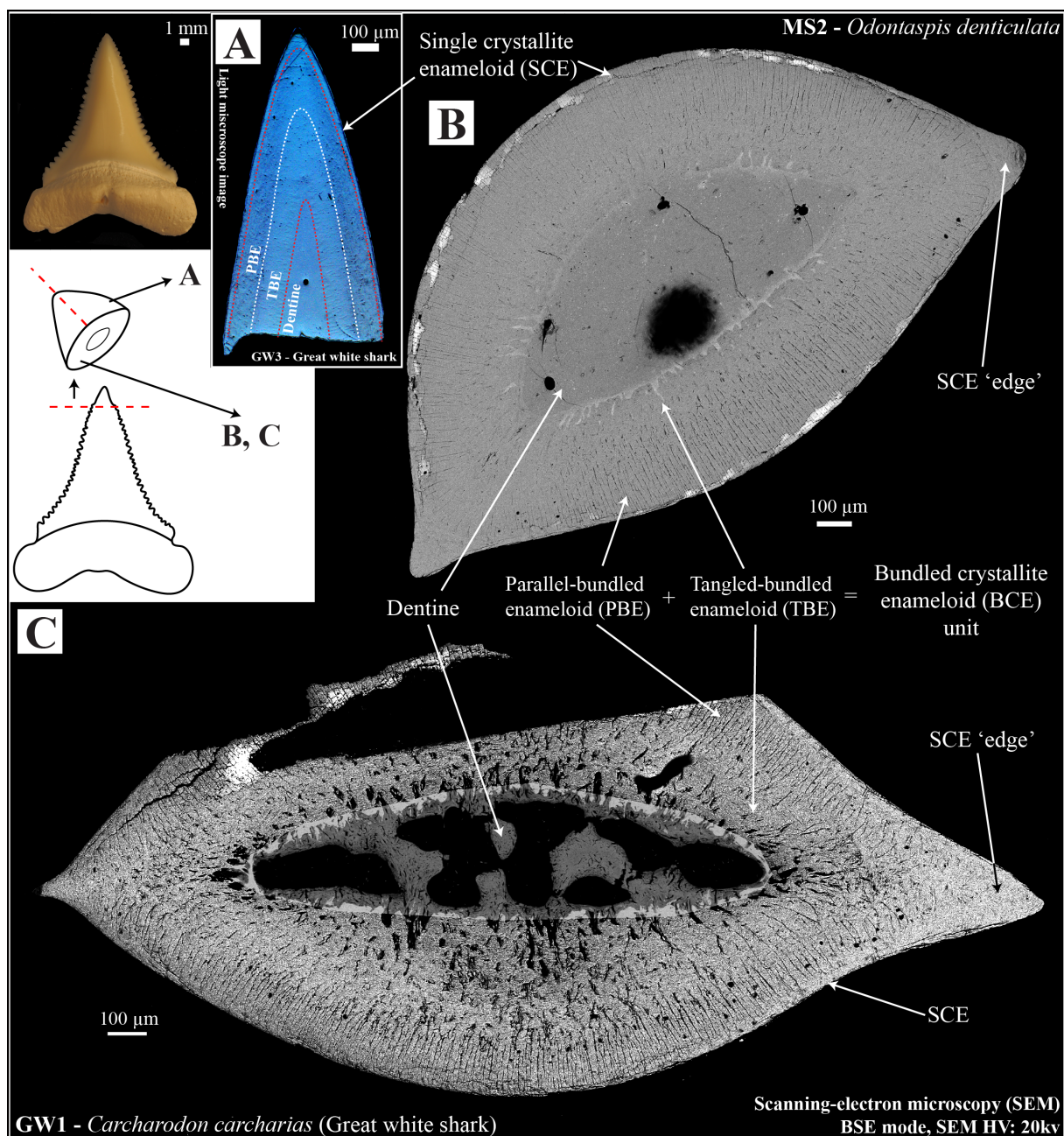
Figure 1.4. Schematic representation of the longitudinal and transversal cross sections prepared for modern (great white shark, *Carcharodon carcharias*) and fossil (*Odontaspis denticulata*) shark teeth. Shark biomineralised structures can be noted even in reflective light microscope images in longitudinally cross-sectioned teeth **(A)**. Scanning-electron microscopy images **(B)**, **(C)** of transversal cross sections have clearly shown such components: at the outer part the single crystallite enameloid (SCE); just below it the parallel bundled enameloid (PBE) can be identified, followed by the tangled bundled enameloid (TBE) surrounding the dentine. An irregular sample surface is identified in the dentine of the modern specimen (GW1).

New and used indium beads were melted into the mounts and pressed several times using a hydraulic press. The pressure was gradually increased (1000 to 5000 psi, 1–5 min per step) until a satisfactory surface topography was achieved. To avoid analytical artefacts related to sample geometry and topography, samples were prepared to be within 10 mm from the centre of the mount and to have less than 5 µm of surface topography relative to the standard

in the same mount (c.f., Kita et al., 2009). A good sample topography for analysis was readily obtained for the smaller conodonts (about 3 µm), but for the larger bioapatites of sharks this was more difficult (File S1.3). The topography varied within the enameloid zones (Figure S1.1) and in some samples, layers had more than 5 µm of relief compared to the standard in the mount (Durango). Although most parts of the dentine of modern sharks were within the 5 µm relief, dentine has a more irregular surface texture in modern compared to the fossilised teeth. This is more remarkable in samples pre-treated in the additional acetic acid step mentioned above (GW1 in Figure 1.4C, GW5 in File S1.2). Details about how this textural variation could have influenced the results are discussed below (4.1, 4.2).

Scanning electron microscopy (SEM)

Analyses were made using a Tescan Mira II LMU in backscattered electron emission (BSE) mode. Conodonts were examined for growth layers and albid/hyaline tissues in different orientations (Figures 1.2, 1.3, File S1.2). Only transversally cross-sectioned shark teeth were studied but it was enough to observe the enameloid components and the dentine, as well as to estimate the structural arrangement of samples longitudinally cross-sectioned (Figure 1.4, File S1.2). We used the terms and definitions of biomineralogical structures presented by Trotter and Eggins (2006), Orchard (2007) and Zhang et al. (2017) for conodonts and by Enault et al. (2015) and Wilmers et al. (2021) for sharks in the Results and Discussion (sections 3. and 4.).

Electron micro-probe analyses (EMPA)

Quantitative analyses were made on 7 bioapatites (3 conodonts, 4 sharks, Tables S1.1) and qualitative chemical distribution maps were prepared for 14 bioapatites (8 conodonts and 6 sharks, Table S1.1) in order to shed light on likely systematic zoning in conodonts and shark teeth (Figures 1.5, 1.6 and 1.7, Table S1.2, File S1.4). Chemical concentrations and distributions were determined using a JEOL JXA-8530F HyperProbe. For the quantitative analysis, longitudinal and transversal cross sections of shark and conodonts (Figure 1.5, Table S1.2) were selected. For the qualitative maps of sharks, the same bioapatite orientations were used (Figure 1.7, File S1.4), and for conodonts (Figure 1.6) we included a sample with the anterior part transversally cross-sectioned (Figure 1.3B, TM28 in File S1.4). Measurements were produced in four sessions. The accelerating voltage was between 10 to 15 kV with a current of 20 nA. The reason for using a lower voltage (10 kV) in some sessions was to reduce the sample damage and to be able to analyse the same specimens by SIMS in the same layers investigated by EMPA. For both sessions, the diameter of the beam was 5 µm and was slightly

defocused, also for reducing sample damage. Each sample point was analysed during 50 ms. For quantitative analyses, element selection includes major elements present in the conodont bioapatite (Ca, P, F) and minor and trace elements common in bioapatite (Na, S, Mg, Fe, Sr, Cl, Y, Al, K) (e.g., Trotter and Eggins, 2006; Katvala and Henderson, 2012; Enax et al., 2014; Zhang et al., 2017; Shirley et al., 2018). For the mapping, ten elements were analysed per counting cycles in a total of two cycles.

Sample	Structure/Tissue	P_2O_5	F	Al_2O_3	K_2O	CaO	SrO	Na_2O	MgO	Cl	SO_3	FeO	Y_2O_3	unmeasured portion	Total (%)	Sample ID and EMPA analysis spots spatial resolution: 5 µm
Odontaspis denticulata (Fossil sharks)	Enameloid	40.8 ±0.5	3.7 ±0.3	0.002 ±0.004	0.002 ±0.004	52.1 ±0.5	0.31 ±0.08	0.83 ±0.1	0.14 ±0.04	0.01 ±0.01	0.22 ±0.05	0.13 ±0.09	0.01 ±0.02	1.8 ±0.8	98.2 ±0.8	OD1 / OD2
	Dentine	34.1 ±0.7	2.8 ±0.1	0.003 ±0.003	0.003 ±0.005	50.2 ±0.8	0.44 ±0.07	0.84 ±0.03	0.29 ±0.03	0.05 ±0.03	2.74 ±1.4	1.65 ±0.8	0.02 ±0.02	7 ±1.9	93 ±1.9	
Carcharodon carcharias (Recent sharks)	Enameloid	41.5 ±0.4	3.8 ±0.2	0.003 ±0.004	0.005 ±0.006	52 ±0.8	0.24 ±0.07	0.87 ±0.1	0.2 ±0.08	0.006 ±0.01	0.08 ±0.02	0.02 ±0.03	0.009 ±0.02	1.3 ±1	98.7 ±1	GW3 / GW4
	Dentine	31.4 ±4.2	0.2 ±0.2	0.002 ±0.002	0.006 ±0.008	34.6 ±5.3	0.15 ±0.05	0.81 ±0.2	0.98 ±0.2	0.09 ±0.05	0.18 ±0.03	0.03 ±0.05	0.02 ±0.02	31.6 ±10	68.4 ±10	
Sc. ex gr. milleri (Conodonts)	Conodonts total average	40.7 ±0.6	4 ±0.4	0.002 ±0.004	0.005 ±0.006	52 ±0.8	0.19 ±0.07	1.04 ±0.1	0.13 ±0.08	0.03 ±0.02	0.16 ±0.09	0.02 ±0.04	0.006 ±0.01	1.9 ±1.3	98.1 ±1.3	
TM_{low} longitudinal	Hyaline	40.4 ±0.4	3.7 ±0.3	0.002 ±0.004	0.004 ±0.006	51.5 ±0.7	0.19 ±0.06	1.09 ±0.1	0.17 ±0.06	0.04 ±0.02	0.22 ±0.05	0.02 ±0.03	0.005 ±0.01	2.6 ±1	97.4 ±1	TM18
TM_{mid} longitudinal	Hyaline and albid	40.9 ±0.5	4.2 ±0.2	0.002 ±0.003	0.006 ±0.007	52.4 ±0.5	0.2 ±0.06	1 ±0.1	0.17 ±0.06	0.02 ±0.02	0.10 ±0.03	0.02 ±0.04	0.006 ±0.01	1 ±0.8	99 ±0.8	TM20
$TM_{transversal}$	Hyaline and albid, 'upper' crown	40.9 ±0.5	4.1 ±0.2	0.003 ±0.005	0.002 ±0.004	52 ±0.6	0.16 ±0.07	1 ±0.08	0.08 ±0.06	0.03 ±0.02	0.13 ±0.07	0.03 ±0.04	0.006 ±0.01	1.6 ±0.7	98.4 ±0.7	TM21
	Hyaline, 'lower' crown	39.2 ±0.8	3.2 ±0.2	0.0003 ±0.001	0.01 ±0.008	50.2 ±0.6	0.16 ±0.07	1.35 ±0.04	0.35 ±0.06	0.04 ±0.03	0.4 ±0.1	0.02 ±0.04	0.01 ±0.02	5.2 ±1.2	94.8 ±1.2	

Figure 1.5. Quantitative analyses of bioapatites studied by EMPA for major and minor elements. The "unmeasured portion" can be mainly considered as organic matter/CO_3^{2-} ions. Sample spots were increased for better visualisation, and they are drawn over vector illustrations of each sample. Precise sizes are available in the Supplementary Table S1.2.

The analytical criteria for data normalisation used were based on those described by Katvala and Henderson (2012). The "unmeasured" portion of our mass percentages is interpreted as carbonate, organic matter, or simply void space (resin) (Table S1.2). To minimise uncertainties related to the carbonate component, GasBench II-mass spectrometry carbonate in apatite isotope and concentration analysis of the shark teeth were made (details just below).

Data were selected based on an evaluation of edge effects, instrument error and analytical artefacts from sample preparation. Ca and P concentrations were constant throughout the bioapatite, but some data points near the edges had unusually low Ca and P concentrations and a lower total compared to adjacent sample spots. This edge effect suggests that the beam was not centred on a flat part of the sample. A total of two data points were excluded from our quantitative analysis calculations and details of this evaluation are given in the Table S1.2. Dark areas and areas depleted in major element concentrations (e.g., Ca, P) are due to traces of indium in void spaces that remained in the samples (verified using a reflected light microscope; see File S1.4).
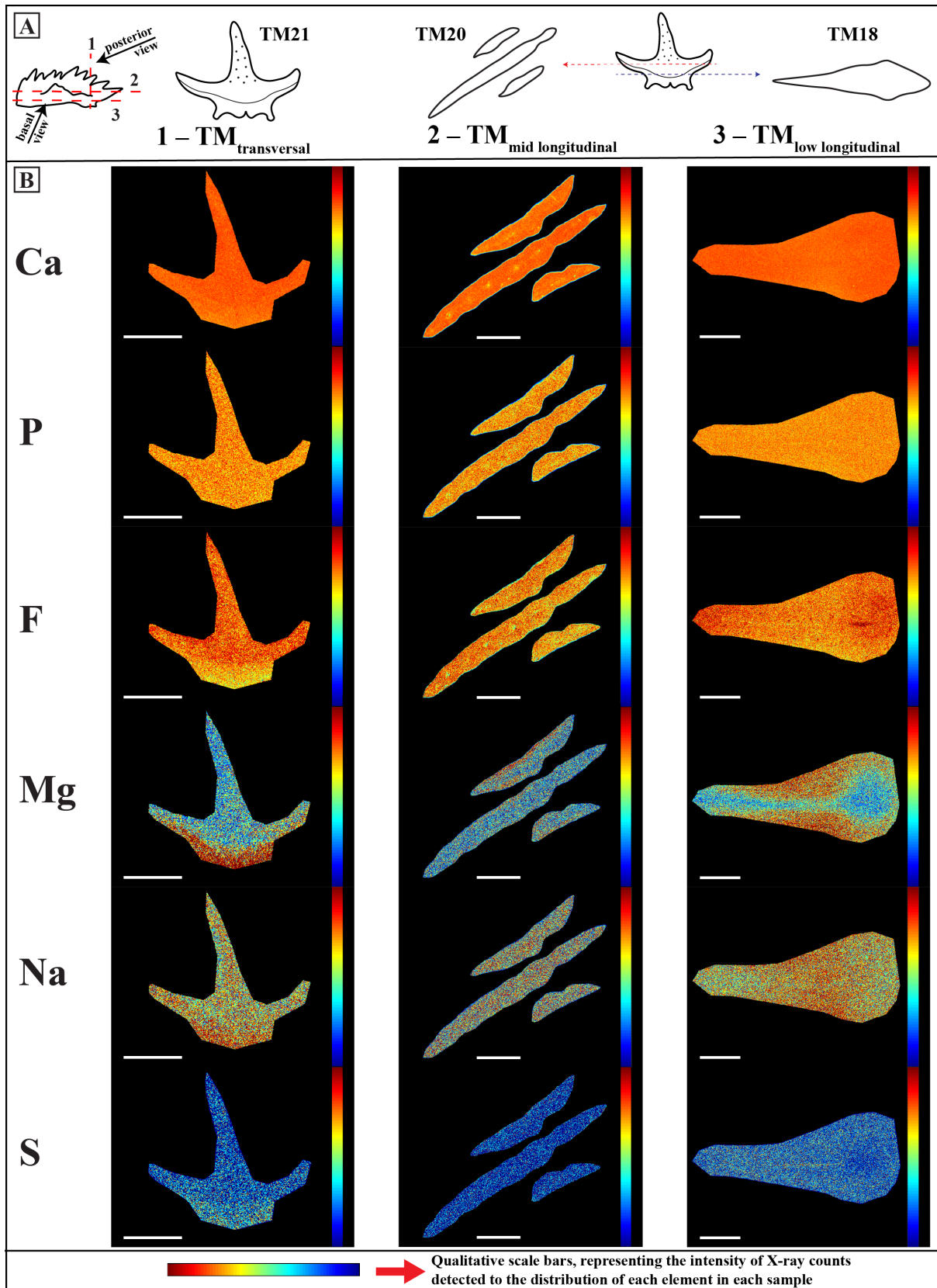
Figure 1.6. Qualitative EMPA chemical mapping of *Sc.* ex gr. *milleri* specimens showing the distribution of Ca, P, F, Mg, Na and S in the conodont crown. **(A)** The three conodont groups from Timor were evaluated by this technique and their respective results are presented below in **(B)**. Significant heterogeneity can be observed in the lower part of the crown of TM$_{transversal}$ (TM21) **(1)**. The TM$_{mid longitudinal}$ (TM20) is rather homogeneous **(2)**, and SIMS analysis spots are scarcely visible in the F and Ca chemical maps (only sample analysed after a SIMS session). The TM$_{low longitudinal}$ (TM18) also presents a degree of heterogeneity on its chemical distribution **(3)**, notable for the Mg. Scale bars: 50 μm.
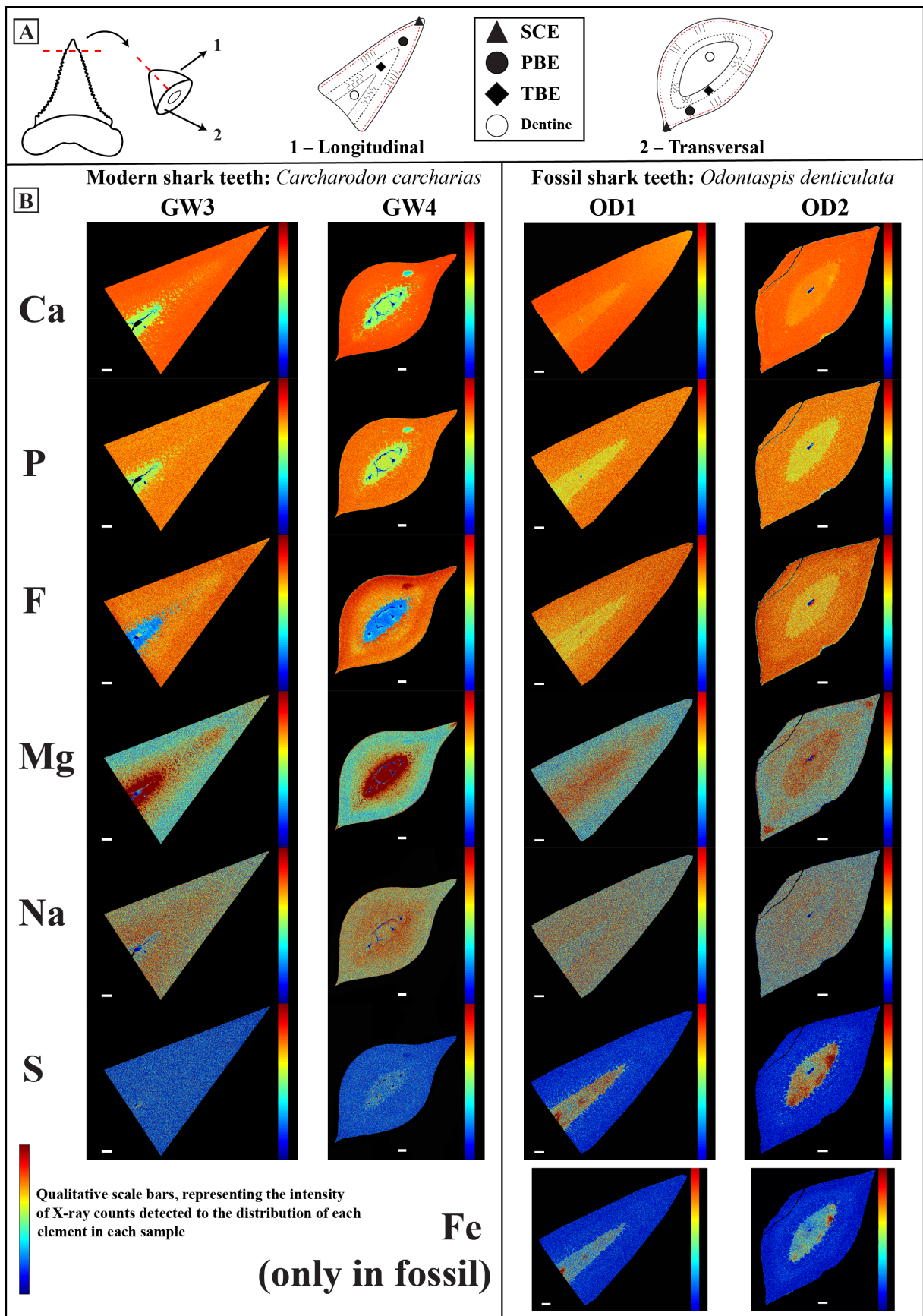
Figure 1.7. Qualitative EMPA chemical mapping of modern (*C. carcharias*) and fossil (*O. denticulata*) shark teeth showing the distribution of Ca, P, F, Mg, Na and S. **(A)** Longitudinal (GW3, OD1) and transversal (GW4, OD2) cross sections were prepared from teeth tips where enameloid tissues (SCE, PBE and TBE) and dentine are observed. **(B)** Enameloid and dentine had expected variations in their elemental concentrations and a relative chemical heterogeneity is observed between the PBE and TBE, layers that make up the bundled crystallite enameloid (BCE). Scale bars: 100 µm.

3.2.3 Oxygen isotope analysis (HTR, SIMS) and carbonate content estimates (GC-IRMS)

GasBench isotope ratio mass spectrometry (GasBench-IRMS)

Stable isotope measurements were done of the carbonate component of 4 shark teeth (2 modern and 2 fossil, Table S1.1) with the objective to estimate their carbonate content (Table S1.3). The enameloid and dentine surfaces were abrased with a micro drill to collect sample powders. About 10–15 μg of a pure in-house carbonate standard (CM – Carrara Marble) was weighed into glass vials. For the shark enameloid, this quantity corresponded to 800–1000 μg, while for the dentine 500–600 μg was used. Analyses were made following the procedures of Spötl and Vennemann (2003), adapted to use smaller sample quantities. The oxygen and carbon isotopic compositions were analysed using a GasBench II coupled to a Thermo Fisher Scientific Delta V mass spectrometer. In the GasBench II, the vials were flushed using helium and reacted with 99 % orthophosphoric acid to produce a CO_2 gas to be analysed by the mass spectrometer. The measured isotopic ratios were normalised to an in-house Carrara marble calcite standard calibrated against NBS-19.

High-Temperature Reduction (HTR) analysis

Oxygen isotopes were measured in 12 bioapatites (2 conodonts, 8 enameloid *vs* dentine pairs of sharks and 2 in the enameloid only, Table 1.2) to compare the results of the isolated phosphate component ($\delta^{18}O_{PO4}$) against the *in-situ* $\delta^{18}O$ values containing all oxygen-bearing sites (SIMS). To obtain the $\delta^{18}O_{PO4}$ values by HTR, the phosphate group in apatite was separated via precipitation as silver phosphate, following a method adapted after Mine et al. (2017). For this method, about 1 to 1.5 mg of original bioapatite is required. Enameloid and dentine of shark teeth was sampled by abrasion of the crown surface using a micro-drill or by fracturing small pieces of a tooth using an agate mortar and pestle. Conodonts were sampled in bulk and several specimens (60 to 100) were necessary for each sample, but the results should be a representation of the crown (albid and hyaline tissues) since no basal body is preserved. All samples were pre-treated in 1 M acetic acid-Ca acetate (pH = 4.5, 2 h) and rinsed several times in deionised water (Koch et al., 1997). International reference material (NIST SRM 120c) and in-house laboratory standards were prepared in parallel with each sequence of samples. Duplicates or triplicates of Ag_3PO_4 were analysed for each sample on a TC/EA (high-temperature conversion elemental analyser) coupled to a Finnigan MAT 253 mass spectrometer according to the method described in Vennemann et al. (2002), where silver phosphate is converted to CO at 1450 °C via reduction with graphite. The accepted error (1 sigma, σ) for this study is ±0.3 ‰ (1 standard

deviation, 1SD). Measurements were corrected to in-house (LK-2L: 12.1‰, LK-3L: 17.9‰) and international Ag_3PO_4 phosphate standards, (USGS80: 12.5 ‰, USGS81: 34.7 ‰) that had ±0.3‰ (1σ) standard deviations during measurements (File S1.5). The NIST SRM 120c phosphorite reference material had an average value of 21.8‰ ±0.3‰ (n = 17). The isotope compositions are expressed in the δ notation relative to Vienna Standard Mean Ocean Water (VSMOW).

Secondary-ion mass spectrometry (SIMS)

Sixty bioapatite samples (50 conodonts and 10 enameloid *vs* dentine of sharks, Table 1.1) were measured one to ten times (typically 4 sample spots, total: 330) *in-situ* ($\delta^{18}O$). Longitudinal and transversal cross sections of shark teeth (Figures 1.4, 1.8) and conodonts (Figures 1.2, 1.9, 1.10) were selected. About 50 sample spots were measured per mount (File S1.5). Oxygen isotope measurements were made using the IMS CAMECA 1280HR of the SwissSIMS national facility in three different sessions (December 2018, June 2019, November 2019). A 1.5nA Cs^+ ion beam (10 kV voltage) was focused into a spot of about 15 μm and with a depth resolution of about 1.5 μm (Figure 1.10). ^{16}O- and ^{18}O- secondary ions were detected on multi-collector Faraday cups, equipped with 10^{10} (L'2) and 10^{11} (H'2) ohms resistors, respectively. The analytical routine consists of calibration of the Faraday cups at the beginning of each day. Each analysis consists of 30 sec of pre-sputtering, automated centring of secondary ion beam, followed by 16 cycles of 4 seconds of secondary ion detection. In order to calibrate the measurements, two crystals of Durango standard were used for correction of $\delta^{18}O$ values. Their $\delta^{18}O_{PO4}$ values were determined by laser fluorination (first crystal: 8.7 ±0.1 ‰, n = 2; second crystal: 9.0 ±0.1 ‰, n = 4, File S1.1) (Vennemann et al., 2002). Each run was normalised with their respective Durango batch (File S1.5). Typical count rate on Durango was about 1.3×10^9 counts per second, similar to the unknowns.

A quartz standard (UNIL-Q1) was measured repeatedly during each session, in order to monitor the instrument stability. Typical reproducibility (in standard deviation, 1SD) is 0.15–0.2 ‰. Durango standards were also measured repeatedly, although less often as they reproduce less well (Sun et al., 2016; Wudarska et al., 2022; File S1.5). Indeed, typical error for Durango is 0.25 to 0.3 ‰. Results are reported as an average of the sample spots done per sample. The shark enameloid $\delta^{18}O$ values are given as an overall average as well as averages of each structural tissue (Table 1.1), to individually compare them with the $\delta^{18}O_{PO4}$ values measured by HTR (Table 1.2). The isotope ratios are expressed in the δ-notation relative to Vienna Standard Mean Ocean Water (VSMOW).
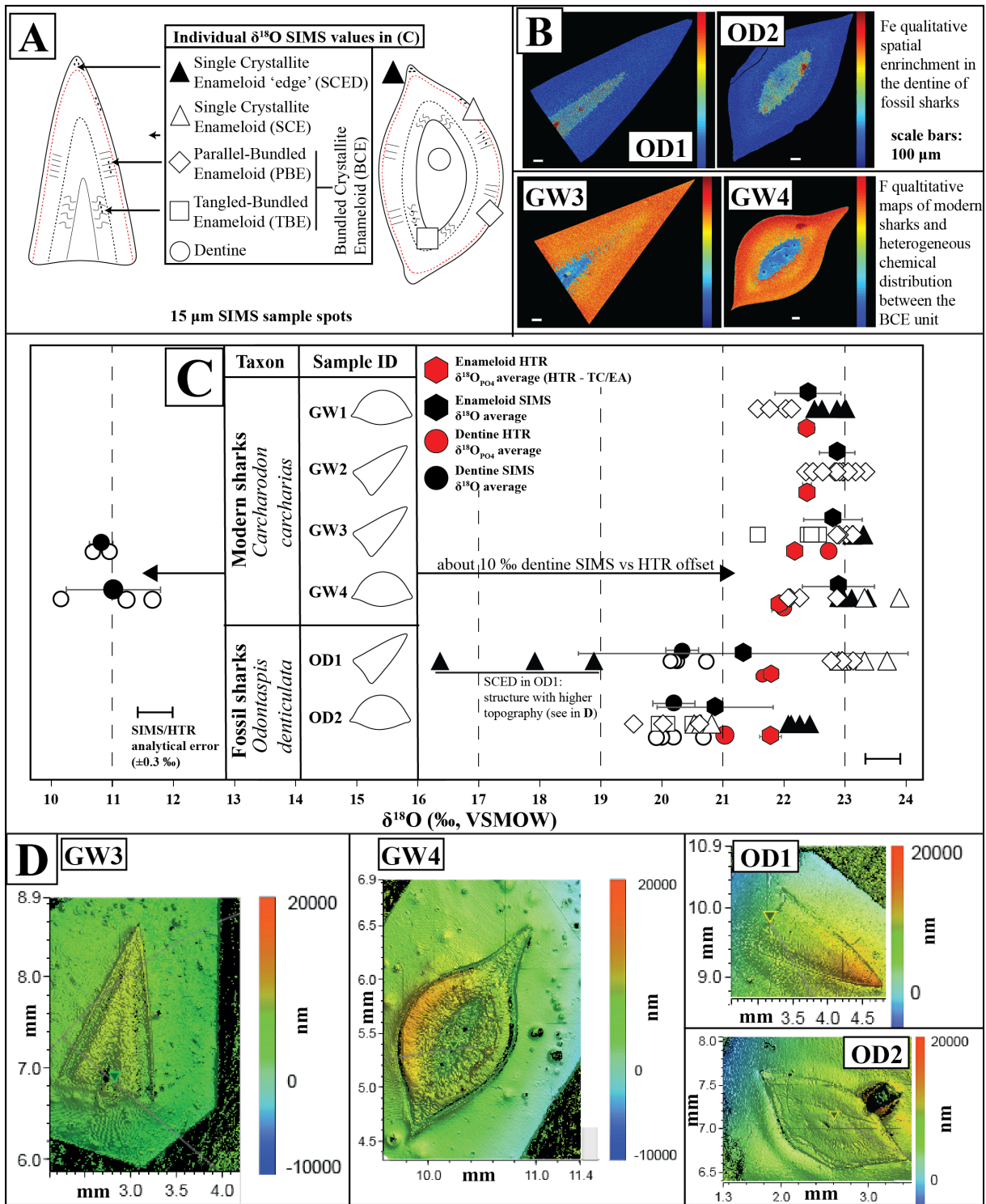
Figure 1.8. Modern and fossil shark bioapatite $\delta^{18}O$ values measured by SIMS and HTR (TC/EA). In **(A)**, a schematic representation of the cross sections and where sample spots were sputtered in each enameloid layer and in the dentine (symbols) are presented. Chemical distributions maps discussed to explain some $\delta^{18}O$ variations noted in modern and fossil specimens are shown **(B)**, and the qualitative scale for them is explained in Figure 1.7. To the modern we selected the F distribution map mainly to show the contrast between the TBE *vs* PBE. To the fossil, the Fe distribution map is given, which associated with the S suggests the presence of pyrite in the dentine. In **(C)**, SIMS $\delta^{18}O$ values of each layer are presented individually by white/black symbols (see A for tissue types represented by the different symbols), while the red symbols refer to the $\delta^{18}O$ values obtained by HTR. All enameloid structures were homogenized to the HTR analysis. Profilometer topographic profiles are given in **(D)**, and the irregular sample texture of the dentine can be better seen in the GW4 specimen.
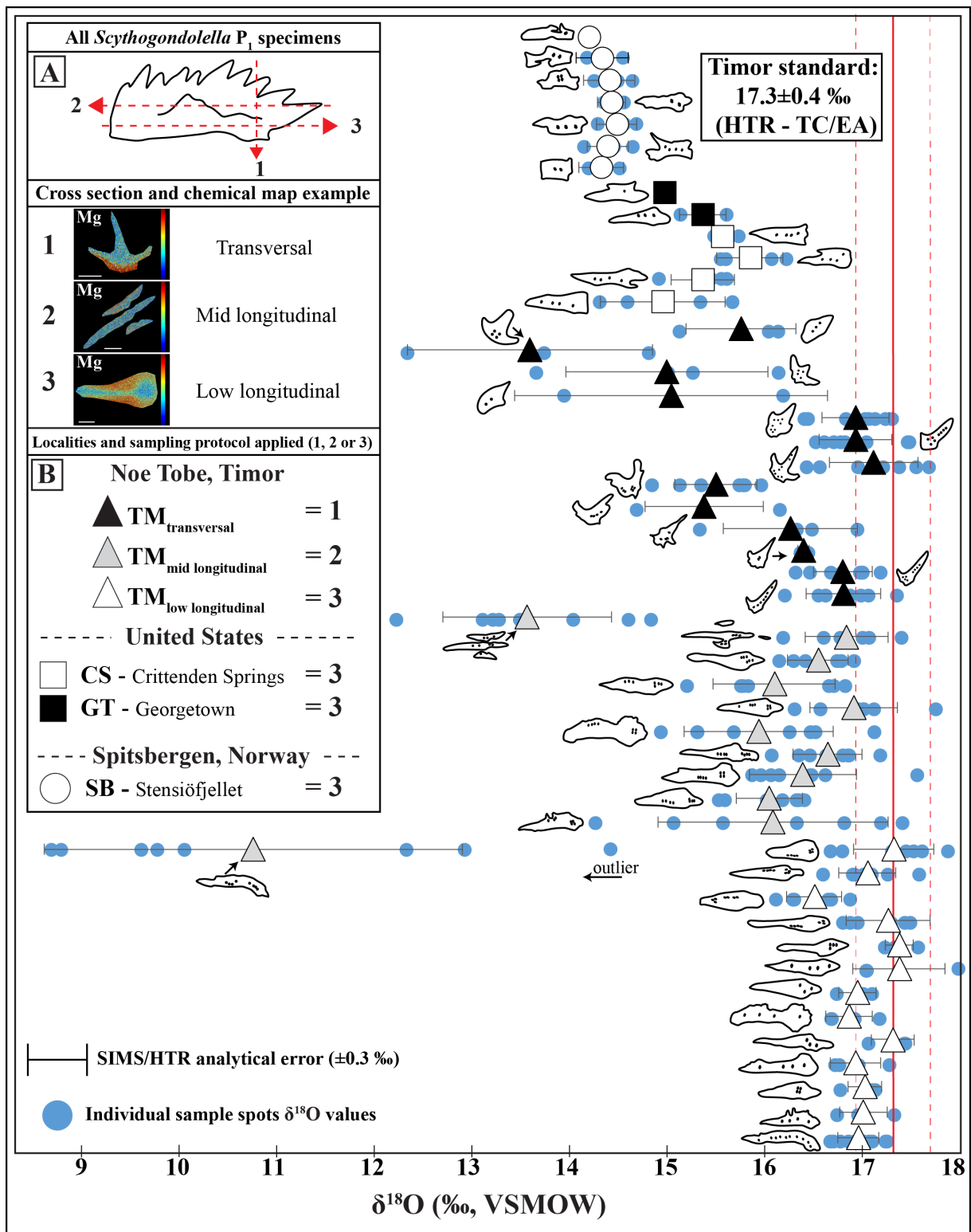
Figure 1.9. $\delta^{18}O$ mean values and standard deviations of *Sc.* ex. gr. *milleri* specimens analysed by SIMS. At the top left, **(A)** dashed arrows indicate the cross sections done on the three main conodont groups from Timor, and below examples of their respective qualitative maps for Mg are shown. We selected the Mg for better visualisation of the relative chemical heterogeneity (colour and scale bars in Figure 1.6). Based on the more homogeneous values, conodonts from USA and Spitsbergen were prepared similarly to the sample set **(3)**. Below the chemical maps, **(B)** symbols to each dataset are given. At the right, the red line and the marked range area correspond respectively to the $\delta^{18}O_{PO4}$ mean value of *Sc.* ex. gr. *milleri* from Timor obtained by HTR (TC/EA) and its standard deviation. Vector drawings of each sample and sample spots are illustrated at the side or close to their respective results, and blue circles represent individual $\delta^{18}O$ analysis. The sample order in Table 1.1 is plotted inversely upwards, hence, the lowest symbol in the figure is the first sample in the table (TM2).
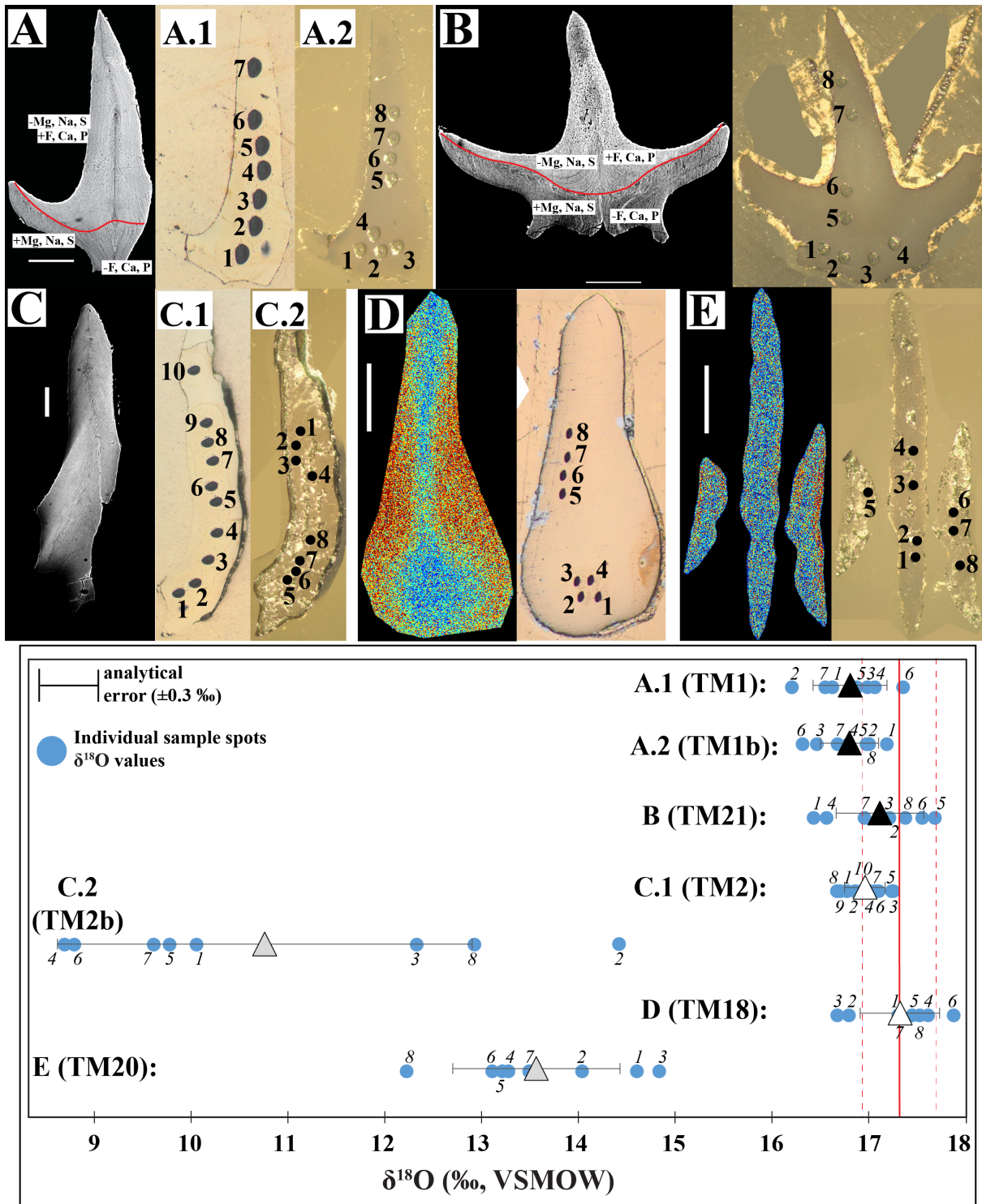
Figure 1.10. Example of conodonts from the three main sampled groups, with comparisons between their chemical patterns against the sample spots analysed by SIMS. **(A)**, **(B)** and **(C)** are SEM images done in BSE mode (details, Figures 1.2, 1.3), while **(D)** and **(E)** are chemical distribution maps for Mg (details, Figure 1.6). Again, Mg was selected for better visualisation. Sample spots over the visible porosity of the albid tissue still reproduced within the HTR reference $\delta^{18}O$ value **(A, B)**, as well as analysis on zones enriched chemically in minor components **(C.1, D)**. Analysis in conodonts more chemically homogeneous have more negative and scattered $\delta^{18}O$ values **(C.2, E)**. Thus, the chemical variations do not seem to relate with IMF to SIMS measurements. The samples **(C.2)** and **(E)** have visible roughness over the crown surface due to a quick polishing done after the SIMS analysis were made.

3. Results

3.1 Bioapatite microstructures

High resolution images were prepared for 14 bioapatites (9 conodonts and 5 sharks, Table S1.1) to distinguish their main biomineralogical structures and they are given in Figures 1.2, 1.3, 1.4 and in the Supplementary File S1.2. Conodont textures and albid and hyaline crown growth layers were observed. All growth laminae measure less than 10 μm across (Figures 1.2, 1.3), hence analyses by SIMS represent an average $\delta^{18}O$ of at least two growth layers. In the samples with a low longitudinal cross section, the predominant texture corresponds to the hyaline crown and there is a restricted degree of porosity near cracked portions (Figures 1.2B, 1.3C). In the transversally cross-sectioned conodonts, the hyaline crown is dominant, growing from the central axis and extending laterally to the platforms (Figures 1.2A, 1.3A, B, File S1.2); but in the upper part, the denticle presented a higher degree of porosity characteristic of the albid crown, mixed with layers of hyaline tissue. Longitudinal cross sections of the lateral conodont view also have a high porosity at the denticles when compared to the lower part (Figure 1.3D, E, F). Based on these observations and in the results explained below (sections 3.2 and 4.3), we concluded that repolished samples also have a mixed aspect of albid and hyaline tissue in their surface. Thus, the three set of conodont samples from Timor mentioned above (section 2.2.1) were classified as: hyaline tissue in a low longitudinal cross section - $TM_{low\ longitudinal}$; mixed tissue (i.e., hyaline and albid) in a middle longitudinal cross section - $TM_{mid\ longitudinal}$; and mixed tissue in a transversal cross section - $TM_{transversal}$.

SEM scans of shark teeth show the two types of textural/mineralogical units: the single crystallite enameloid (SCE, also referred to as ridge cutting edge layer – c.f. Wilmers et al., 2021) and the bundled crystallite enameloid (BCE) unit (Figure 1.4, File S1.2). These structures are also distinguishable using reflected light microscopy (Figure 1.4A). The single crystallite enameloid (SCE) parts cover the outer surface of the crown; and the random orientation of crystals occur at the edges of transversal cross sections and at the tip of the teeth in longitudinal sections. Chemical compositions may help to distinguish different layers too (see below). From the BCE unit, two of the three components can be seen: the parallel bundled enameloid (PBE) just adjacent to the SCE unit, with crystals arranged parallel to the crown surface; and the tangled bundled enameloid (TBE) that is observed between the PBE and the dentine from fossil teeth, with crystals of more random orientation but with a 'smooth' surface similar to the PBE. The dentine of recent shark teeth is less commonly exposed as it is readily damaged and even removed during sample preparation. This is related to the lower degree of porosity for the recrystallised dentine parts in fossil shark teeth compared to the recent shark teeth (Figures

1.4B, C, 1.8, File S1.2).

3.2 Chemical compositions

Quantitative analyses

One dental element from each of the three conodont groups was analysed: the TM18 for TM$_{low\ longitudinal}$ (sample spots $n = 27$), TM20 for TM$_{mid\ longitudinal}$ ($n = 29$) and TM21 for TM$_{transversal}$ ($n = 30$) (Figure 1.5, Table S1.2). Conodonts longitudinally cross-sectioned (TM$_{low\ longitudinal}$ and TM$_{mid\ longitudinal}$) are similar in major components (Ca, P and F), but with slightly lower average values were measured for the TM$_{low\ longitudinal}$ samples. The "unmeasured" concentrations are more contrasting, with 2.6 ±1 (TM$_{low\ longitudinal}$) and 1 ±0.8 % (TM$_{mid\ longitudinal}$, Figure 1.5) giving larger differences, albeit within error still. Samples transversally cross-sectioned (TM$_{transversal}$) clearly had a higher "unmeasured" content at the lower part of the crown (5.2 ±1.2 %) compared to the upper part (1.6 ±0.7 %). Mg, S, and Na concentrations are also higher in the lower part and the Ca, P, and F were lower (Figure 1.5). When excluding data points from the lower part of the crown ($n = 4$), the Ca and P concentrations of the TM$_{transversal}$ and the F content are within error the same as to those of the TM$_{mid\ longitudinal}$ sample.

Four shark teeth were examined by quantitative analysis: two fossil and two modern specimens prepared in transversal and longitudinal cross-sections (Figure 1.5, Table S1.2). The enameloid and dentine clearly have different compositions. In general, the fossil and modern enameloid are similar in their Ca, P and F concentrations (Figure 1.5), with only minor differences for Fe and S. However, larger differences are noted for their dentine parts (Figure 1.5). The most notable is in the "unmeasured content" that is high in the modern dentine (31.6 ±10 %), lower in the fossil dentine (7 ±1.9 %), and lowest in the enameloid parts (fossil: 1.8 ±0.8 %; modern: 1.3 ±1 %). The F content is also similar in the enameloid of modern and fossil teeth (about 3.8 %), while it is lower in the dentine parts (2.8 ±0.1 % in fossil and 0.2 ±0.2 % only in the modern parts; Figure 1.5). No significant difference is noted in the F content to the PBE, which has its *c*-axis distinctly oriented to the EMPA beam in the transversal (OD2 and GW4: *c*-axis parallel) and longitudinal (OD1 and GW3: *c*-axis perpendicular) cross sections. However, for the samples transversally cross-sectioned (OD2, GW4), the F concentration is higher in the PBE than in the TBE (3.9 ±0.2 *vs* 3.3 ±0.3%, Table S1.2). Not surprisingly, minor elements in bioapatite such as Na, Mg, Sr, Fe and S, have higher concentrations in the dentine than in the enameloid (Figure 1.5), with the fossilised dentine being enriched in some particular elements. For example, the Mg of the dentine in modern specimens is the highest amongst all apatite measured in this study (1 ±0.2 %), while Fe can only be found in trace amounts except

for the dentine of fossil shark teeth (1.7 ±0.8 %). Similarly to the latter, the S concentration of the fossil dentine is the highest among the bioapatites (2.7 ±1.4 %).

Zoning of major and trace elements

Qualitative chemical maps were produced of the same specimens presented above (Figure 1.6, 1.7), and for additional specimens shown in the Supplementary File S1.4. The chemical map for the sample TM19 (TM$_{mid\ longidutinal}$) is only presented in the Supplement (File S1.4) since it had a stain that could not be removed prior to chemical mapping. The TM$_{low\ longitudinal}$ conodont (TM18) shows slight compositional gradients in its elemental distribution (Figure 1.6B), with detectable zoning in both Ca, P and F contents, which have higher concentrations in the anterior and posterior parts of the conodont, decreasing towards the platform structures. For Mg and S, and to some degree Na, this zoning is reversed with higher concentrations at the platform structures, decreasing towards the inner parts (Figure 1.6B). Comparison with individual quantitative data points corroborate the chemical heterogeneity (Table S1.2). The TM$_{mid\ longidutinal}$ conodont (TM20) has a less exposed area and is more homogeneous in elemental distribution (Figure 1.6B), with only a minor change in the Mg distribution, increasing in the platform portions. The TM$_{transversal}$ sample also has a heterogeneous elemental distribution (TM21) (Figure 1.6B), also corroborating the quantitative measurements (Figure 1.5, Table S1.2). Ca and F distributions are homogeneous in the upper part of the conodont until the middle part/growth centre, but in the lower part there is a decrease in the concentration of these elements. Again, Mg, S, and Na compensate for Ca and F and have higher concentrations at the lower portion of the crown.

For the shark teeth the enameloid has higher Ca, P, and F and lower Mg and S content than the dentine (Figure 1.7B), while the SCE has higher concentration of Mg, comparable in amount to the dentine part (transversal sectioned specimens in Figure 1.7). In the BCE unit, the PBE unit has slightly higher Ca and F and lower Mg and Na concentrations than the TBE unit. The dentine chemical compositions and distributions vary between modern and fossil specimens, but in the latter group, Fe and S contents are higher (Figure 1.7B).

3.3 Carbonate content

The carbonate content measured for 4 shark teeth have a range from 1 to 6 wt.% (Table S1.3). The *n* refers to the number of vials analysed between the specimens. Shark enameloid have lower carbonate contents than the dentine. In the enameloid, the results were 0.6 wt.% (*n* = 2) for the modern shark and 1.0 wt.% (*n* = 2) for the fossil shark. In the dentine, the values were

2.3 ±0.6 wt.% (*n* = 4) and 5.2 ±0.9 wt.% (*n* = 2) for the modern and fossil shark, respectively.

3.4 Oxygen isotope analyses in phosphate

The $\delta^{18}O$ values of 72 bioapatites have a range from 10.8 ‰ to 22.9 ‰ (Tables 1.1, 1.2, File S1.5). Among the samples, 52 are from conodonts with a range from 10.8 ‰ to 19.5 ‰, and 20 are from shark teeth with a range from 10.8 ‰ to 22.9 ‰.

High-temperature reduction (HTR)

The $\delta^{18}O_{PO4}$ values from samples analysed by HTR (*n* = 12) have a range between 16.9 to 22.7 ‰ (Table 1.2). The conodont bulk samples from the same geochronological zone (*Wasatchites/Anasibirires* zone, late Smithian) had within their respective analytical error (1σ) the same $\delta^{18}O_{PO4}$ values: *Sc.* ex gr. *milleri*, from Timor have a mean $\delta^{18}O_{PO4}$ value of 17.3 ±0.4 ‰ (*n* = 7), while specimens from Wadi Musjah have an average $\delta^{18}O_{PO4}$ value of 16.9 ±0.2 ‰ (*n* = 3).

The $\delta^{18}O_{PO4}$ values from 6 shark teeth (4 modern and 2 fossil) have a range between 21 to 22.7 ‰. Two modern teeth had only their enameloid analysed, while the other four had their enameloid and dentine analysed (Table 1.2). All enameloid structures were homogenized and the $\delta^{18}O_{PO4}$ values should represent their average. Samples with both tissues analysed have within error the same $\delta^{18}O_{PO4}$ values, with the exception of one fossil shark tooth where the enameloid has somewhat higher values compared to dentine (OD2en: 21.8 ±0.2 ‰ *n* = 2 *vs* OD2de: 21.0 ±0.0 ‰, *n* = 2).

Secondary ion mass spectrometry (SIMS)

The $\delta^{18}O$ values from samples analysed by SIMS (*n* = 60) have a range between 10.8 ‰ and 22.9 ‰ (Table 1.1). Fifty conodonts have $\delta^{18}O$ values in a range from 10.8 ‰ to 17.4 ‰ with the standard deviation for most of them being of 0.3 ‰ (1σ) (*n* = 26), and specimens with a variation > 0.3 ‰ $\delta^{18}O$ (*n* = 22) are not necessarily samples where more analysis spots were done (c.f. Wheeley et al., 2012; Figure 1.9, Table 1.1). Pre-treated conodonts (TM1-TM6) had $\delta^{18}O$ values similar to those of non-pre-treated samples of the same group (Table 1.1). The three groups of Timor conodonts from different cuts have significant differences in their $\delta^{18}O$ values (ANOVA: *F* = 5.07, *p* = 0.01183, Table S1.4). For samples where the hyaline crown is mixed with the albid crown, variations in $\delta^{18}O$ values are larger (TM$_{transversal}$: 16 ±1 ‰, *n* = 13; TM$_{mid\ longitudinal}$: 15.7 ±1.9 ‰, *n* = 11) compared to only the hyaline crown (TM$_{low\ longitudinal}$: 17.1±0.2 ‰, *n* = 13). Furthermore, the $\delta^{18}O$ values from the hyaline crown are within error (1SD) the same

as the bulk samples from Timor analysed by HTR (17.3 ±0.4 ‰, $n = 7$).

Hyaline crown samples of *Sc.* ex gr. *milleri* from USA have a mean $\delta^{18}O$ value toof 15.4 ±0.3 ‰ ($n = 6$), higher than the average $\delta^{18}O$ value of *Scythogondolella* from Spitsbergen (14.4 ±0.1 ‰, $n = 7$) (Table 1.1, Figure 1.9). For the $TM_{low\ longitudinal}$ results, statistical tests One-way ANOVA, Tukey's pairwise for the three datasets of Timor, USA and Spitsbergen confirm that this same species has different average $\delta^{18}O$ values in the three localities (Table S1.4).

Ten shark teeth (6 recent and 4 fossil) analysed by SIMS have $\delta^{18}O$ values within a range from 10.8 ‰ to 22.9 ‰, and most of the individual enameloid $\delta^{18}O$ values are higher than dentine (Table 1.1, Figure 1.8, Figure S1.1). Averaging the results of the enameloid structures (i.e., SCE + PBE + TBE to total enameloid), the recent shark $\delta^{18}O$ values are between 10.8 ‰ to 22.9 ‰, and fossil shark $\delta^{18}O$ values are between 20.2 ‰ to 21.3 ‰. Among the enameloid layers, the edges of the SCE are shown separately (SCED, Figures 1.4, 1.8), in order to discuss the influence of a higher surface sample area for this component. The $\delta^{18}O$ values between enameloid zones in the same tooth can differ by up to 5.5 ‰, while the single tissue $\delta^{18}O$ differences are lower (up to 1 ‰ only in SCED of OD1 in Figure 1.8, Figure S1.1). The average $\delta^{18}O$ values of each enameloid component (SCED, SCE, PBE, TBE) was individually compared to the $\delta^{18}O_{PO4}$ values for the same tooth analysed by HTR (Figure 1.8C). $\delta^{18}O$ values from PBE, SCED and TBE are the same as measured for HTR, while values from the SCE may show some differences. All shark dentine results reproduced to within the 1σ error, with the exception of one sample of a recent tooth (GW4de, Table 1.1, Figure 1.8C), and $\delta^{18}O$ values from modern specimens are substantially lower (about 10 ‰) compared to those measured by HTR (GW3de: 10.7 ±0.2 ‰ and GW4de: 10.9 ±0.8 ‰ lower for the SIMS analyses).

4. Discussion

4.1 Major element compositions and mineralogy of bioapatite analysed

Ca and P are the major elements of all bioapatites analysed, making up about 95 wt.%, with the exception of the dentine of the recent shark tooth where the unmeasured fraction makes up about 32 wt.% (Figure 1.5). The major and minor element concentrations measured are all similar to those previously reported (Elliot, 2002; Skinner and Jahren, 2007; Katvala and Henderson, 2012; Enax et al., 2014; Kocsis et al., 2015; Zhang et al., 2017). The F concentrations in recent and fossil shark tooth enameloid as well as in the conodonts are all similar at close to 3.8 wt.%, which also corresponds to the ideal stoichiometric proportion of F in a pure fluorapatite $Ca_5(PO_4)_3F$ (Figure 1.5). While F is known to be readily incorporated into hydroxyl- or carbonate-apatite, such as represented by the dentine of the recent shark tooth, it

is unlikely to have been added to the enameloid of the shark teeth, nor to the conodonts during diagenesis, because the fluorapatite, the most stable form of apatite, already has Ca, P, and F concentrations at their stoichiometric concentrations (e.g., McConnell, 1973; Katvala and Henderson, 2012). During the fossilisation process of bioapatite, the pore spaces (unmeasured portion in Figure 1.5) left after decay of the organic matter are commonly filled by secondary phosphate and other minerals, allowing for the introduction of new elements but also for cation replacements on newly formed or recrystallised biophosphate (e.g., Kohn and Cerling, 2002; Tütken and Vennemann, 2011). Common cation replacements to the Ca site are Mg, Na, Sr, Ba, K, Rare Earth Elements (REE) and even U (Kohn and Cerling, 2002; Tütken and Vennemann, 2011; Kocsis, 2011; Hughes and Rakovan, 2015). Mg and Na have a contrasting distribution compared to Ca in all studied bioapatites, with higher concentrations in those parts that have or have had higher unmeasured portions (Figures 1.5, 1.6, 1.7), confirming previous findings that these elements concentrate in newly formed, secondary phosphate (Katvala and Henderson, 2012; Enax et al., 2014). S is correlated with the Mg and Na distributions, and the three additionally contrast with P and F contents, again with marginally higher concentrations in tissues with higher unmeasured portions. Using the data from quantitative analyses, the ionic formula for the apatite analysed was determined (carbonate *vs* hydroxyl *vs* fluor -apatite) (Deer et al., 1992). The bioapatite of conodonts had a calculated formula of $Ca_{4.7}Na_{0.17}(CO_3)_{0.22}(PO_4)_{2.88}F_{1.05}$ (Table S1.2), similar to shark enameloid, hence both can be classified as carbonate-fluorapatite.

4.2 Shark teeth chemical and oxygen isotope compositions

Chemical compositions of tissues analysed

In the enameloid, the unmeasured portion from fossil and modern specimens (about 1.5 %) are similar to the carbonate content of about 1 wt.% for both samples (Table S1.3), typical for enameloid (Figures 1.5) (Vennemann et al., 2001; Enax et al., 2012; Kocsis et al., 2014; Aguilera et al., 2017). As expected, the dentine in the fossil shark teeth has a much lower unmeasured portion (7 ±1.9 %, Figures 1.5) compared to the modern shark teeth (32 ±10 %), in part because of the recrystallisation and filling of pore spaces during fossilisation (Figure 1.4B). However, the high unmeasured concentration in the modern specimens does not represent only the collagen portion in the dentine structure but is also related to poor polishing for such porous material, notably for the material where a pre-treatment has removed much of the organic matrix in recent teeth (Figure 1.4C).

Ca and F have qualitatively higher concentrations in the outer layers of the enameloid (SCE and PBE), compared to the TBE and the dentine (Figure 1.7). Teeth transversally cross-

sectioned have differences between the SCE and PBE, notably for the F and Mg distributions. Similar patterns were measured by qualitative energy dispersive X-ray (EDX) maps in modern *Isurus oxyrinchus* (Enax et al., 2014), another lamniform shark. While the heterogeneity between the SCE and PBE are less noteworthy in our specimens compared to those in Enax et al. (2014), more details on structurally different tissues can be indicated when mapping the chemical compositions of the tissues. The chemical variations within the enameloid of the modern species can be explained by the microstructural differences between the components (i.e., SCE and TBE *vs* PBE). Based on observations of the enameloid of modern *Carcharias taurus* (also a lamniform taxon, Wilmers et al., 2021), as well as of *I. oxyrinchus* (Enax et al., 2014), the fluorapatite crystallite bundles forming the SCE and TBE are randomly oriented within the structures, whereas the PBE has its crystallite bundles arranged in parallel to the crown surface (e.g., Fig. 6 in Wilmers et al., 2021). The entangled aspect of the SCE and TBE crystallite bundles has pore spaces of about 1 μm, which are not seen in the densely packed bundles of the PBE. These characteristics favour diagenetic or surficial *in-vivo* remineralisation processes in the TBE and SCE, or even while the structures are precipitated originally in the tooth bed (Enax et al., 2014). Quantitative analyses from the OD2 and GW4 also give lower F concentrations for the TBE compared to the PBE. This may explain why the fossil enameloid has similar elemental distributions and concentrations compared to the modern teeth and thus may be expected to be less influenced during diagenesis and fossilisation (e.g., Trueman and Tuross, 2002; Kohn, 2008).

Fe and S were found in higher concentrations in fossilised shark tooth "dentine" tissues compared to all other bioapatites (Figure 1.5). Fe is an element usually incorporated into the bioapatite structure during diagenesis and, in its common association with S, suggests the secondary mineralisation of pyrite (FeS_2), a mineral frequently formed in sedimentary rocks and biominerals rich in organic matter (Raiswell, 1997; Van Dover, 2007). The large spatial enrichment of these two elements in the dentine of our fossil shark teeth (about 50 to 100 μm wide) supports the presence of secondary pyrite (Figures 1.5, 1.7). Such zones of secondary mineral enrichment are clearly to be avoided for SIMS $\delta^{18}O$ measurements.

Oxygen isotopes compositions of tissues analysed

All shark bioapatite tissues reproduced within 0.2 ‰ by HTR (1SD; Table 1.2). For any one tooth, the different tissue types also have the same oxygen isotope compositions. This contrasts with the $\delta^{18}O$ values measured using the SIMS (Table 1.1, Figure 1.8). While the dentine is known to be more prone to alteration and hence often excluded from analyses, this

tissue, notably that of the recent teeth was analysed by SIMS to test for matrix and textural effects. In the modern shark, the dentine had about 10 ‰ lower $\delta^{18}O$ values compared to the enameloid of the same tooth when measured by the SIMS but had identical $\delta^{18}O$ values to enameloid for the HTR method.

The low $\delta^{18}O$ value measured for the modern shark tooth using SIMS may, in part, be related to the presence of organic matter (e.g., Drewicz et al., 2020). While there are no collagen $\delta^{18}O$ values reported for sharks in the literature, the collagen $\delta^{18}O$ values of herbivore mammals was measured to be about 5 ‰ lower compared to that for enamel $\delta^{18}O_{PO4}$ values (Kirsanow et al., 2008; Drewicz et al., 2020). Assuming the same degree of isotopic ^{18}O depletion (i.e., $\Delta_{collagen-phosphate}$) for shark tooth collagen, and assuming that the complete unmeasured portion represents collagen only, such a contribution would decrease the $\delta^{18}O$ values by only 1.5 ‰ (Table 1.3). A speculative ^{18}O-depletion of 20 ‰ per weight percent for the collagen, hence four times the $\Delta_{collagen-phosphate}$, would lower the values by 7 ‰, again not enough to justify the low $\delta^{18}O$ of dentine measured here. Contributions of sputtered oxygen from organic matter are possible, but it is also unlikely that the teeth contain 30 wt.% of organic remnants after the pre-treatment procedure (boiling salt water) and hence this contribution will likely be small. In a similar comparison of different biogenic apatite tissues from sandbar shark teeth (*Carcharhinus plumbeus*), Žigaitė and Whitehouse (2014) noted about 2 to 3 ‰ lower $\delta^{18}O$ values compared to the enameloid. While this is a smaller difference compared to our measurements, other factors would need to be considered to explain the more than 10 ‰ lower SIMS $\delta^{18}O$ values of recent dentine compared their HTR values (Figure 1.8C).

Table 1.3. Conodont and shark teeth $\delta^{18}O_{PO4}$ values analysed by HTR (TC/EA). The *n* refers to the number of silver capsules analysed for each sample.

$\Delta_{carbonate-phosphate}$ (‰)	weight percentage (%)									
	1	2	3	4	5	6	7	8	9	10
7	0.07	0.14	0.21	0.28	0.35	0.42	0.49	0.56	0.63	0.7
8	0.08	0.16	0.24	0.32	0.4	0.48	0.56	0.64	0.72	0.8
9	0.09	0.18	0.27	0.36	0.45	0.54	0.63	0.72	0.81	0.9
$\Delta_{collagen-phosphate}$ (‰)										
-5	-0.05	-0.1	-0.15	-0.2	-0.25	-0.3	-0.35	-0.4	-0.45	-0.5
-13	-0.13	-0.26	-0.39	-0.52	-0.65	-0.78	-0.91	-1.04	-1.17	-1.3
-20	-0.2	-0.4	-0.6	-0.8	-1	-1.2	-1.4	-1.6	-1.8	-2

Another possibility to explain this discrepancy for this large difference in $\delta^{18}O_{enameloid}$ and $\delta^{18}O_{dentine}$ for the recent shark teeth may be related to sample texture, that is problems with irregular sample heights (pits) and/or tilted sample surfaces that may both be created during the

complex polishing procedures (e.g., Kita et al., 2009). We found that our even mild pre-treatment of the larger great white shark tooth resulted in an irregular sample surface that was difficult to polish prior to SIMS analyses (Figure 1.4C). This was not noted for the smaller sample chips nor the conodonts that were easier to polish leaving a flat surface without irregular heights nor tilted sample surfaces. Kita et al. (2009) noted that if samples have topographic differences of between 10 to 40 µm or more a bias for *in-situ* measurements of up to +4 ‰ may be obtained. Differences in sample height caused by pits that may have rather flat bottoms are expected to be less relevant as such height differences may be corrected for by refocussing the sample during a SIMS analysis. Similar problems were also noted for biogenic carbonates, which may have fine-grained and porous textures (Orland et al., 2015). SIMS $\delta^{18}O$ values measured on otoliths with high porosity were about 2 ‰ lower than values measured by conventional isotope ratio mass spectrometry (Helser et al., 2018). In ammonite shells, a depletion of 1 ‰ in the $\delta^{18}O$ values was noted for analyses near cracked portions of the biomineral surface (Linzmeier et al., 2020).

The tooth tip prepared by Žigaitė and Whitehouse (2014) was smaller than the great white shark tooth tip used in our study. Their sample also had a surface topography of less than 1 µm, including the dentine parts, and the surface was flat with no visible irregular heights. As their $\delta^{18}O$ offset is also lower compared to ours, this offset may indeed be related to the organic matter content and/or carbonate content of the dentine compared to much lower contents thereof in enameloid. In contrast, our higher offset of more than 10 ‰ may be attributed to a combination of a contribution of sputtered oxygen from the unmeasured portion of the dentine, in addition to an irregularly tilted surface texture that results from the small nano-meter size crystallites in modern dentine during polishing. Hence, this is considered to be an analytical artefact of the SIMS measurement.

The individual SIMS $\delta^{18}O$ values measured for the enameloid structures of the shark teeth (Figure 1.8, Figure S1.1) were also different. The larger $\delta^{18}O$ variations in the fossil tooth are likely the result of secondary alteration processes, as also suggested by the higher concentrations of Fe and S in these tissues too (Figure 1.8B, C). For the modern teeth, the individual $\delta^{18}O$ values for the different tissues have a variation of ±1.3 ‰ (Table 1.1, Figure 1.8C), similar to the inter-tissue $\delta^{18}O$ heterogeneity within the enameloid tissues noted for *C. plumbeus* teeth by Žigaitė and Whitehouse (2014). With the exception of the GW1, the modern enameloid $\delta^{18}O$ values appear to be 0.5–1 ‰ enriched in ^{18}O compared to the average $\delta^{18}O_{PO4}$ measured by HTR (Figure 1.8C). Comparable results were obtained for most of the SIMS investigations using bioapatites (e.g., Rigo et al., 2012; Trotter et al., 2015, 2016a; Goudemand et al., 2019), and the

δ^{18}O values had to be corrected in order to interpret values for past environmental conditions.

An enrichment in ^{18}O measured using SIMS analysis and compared to the classical silver phosphate preparation could potentially be related to a contribution of carbonate-ion sourced oxygen, as this is commonly noted to be enriched in ^{18}O compared to the phosphate group by about 9 ‰ (e.g., Iacumin et al., 1996; Vennemann et al., 2001; Lécuyer et al., 2010; Sisma-Ventura et al., 2019). Given the low unmeasured content of the shark enameloid (< 3 wt.%), mass balance estimates of the carbonate contribution to these analysed tissues would be limited to about 0.3 ‰ for the δ^{18}O values (Table 1.3). This suggests that for the majority of our fluorapatite dataset, contributions of oxygen ions from other oxygen-bearing sites (CO_3^{2-}, SO_4^{2-}, OH$^-$) that can bias the δ^{18}O values measured by SIMS are limited (e.g., Lécuyer et al., 2010; Wheeley et al., 2012; Zhang et al., 2017).

Given the low carbonate content as well as unmeasured portion for all enameloid tissues, modern as well as fossilised, the differences in δ^{18}O values for the structurally different enameloid tissues in the shark teeth are hence unlikely to be related to the carbonate content or unmeasured portions. By analogy to the study by Žigaitė and Whitehouse (2014), it is likely that the enameloid of the PBE is simply the best to analyse as it has simple crystal orientations, larger crystal size and, as for all enameloid layers, lesser matrix interferences due to carbonate content or unmeasured portions. Alternatively, this may well be an ontogenetic effect of the different enameloid tissues that can indeed only be detected with SIMS measurements. Analysis of more samples are required to address any patterns of specific enameloid structures that may cause IMF. Nonetheless, enameloid layers that have contrasting concentrations of Mg and F in their structures (SCE and TBE, Figures 1.7, 1.8B), had a good δ^{18}O reproducibility for most samples, with some of their results overlapping with the 'reference' HTR δ^{18}O$_{PO4}$ values (Figure 1.8C). Hence chemical matrix effects may be excluded.

4.3 Conodont chemical and oxygen isotope compositions

Chemical compositions of tissues analysed

For conodonts, the total unmeasured content is low (average of 1.9 ±1.3 %) but was higher for the lower part of the TM$_{transversal}$ specimen (5.2 ±1.2 %). Among the conodont biomineralogical tissues, the albid tissue is known to have a lower content of CO_3^{2-} compared to the hyaline tissue (Trotter and Eggins, 2006). A lamellar pattern characteristic of hyaline tissue is recognised for most of the crown in the TM$_{transversal}$ (Figure 1.2A). The unmeasured content (including CO_3^{2-}) was higher at the lowermost part of the crown (Figure 1.5). This part is also separated by a "dark" contour and darker lower zone that can be seen in specimens analysed

by SEM (Figure 1.2A, Figure 1.3A, B). The Mg, S and Na concentrations are also higher in this lower part of the conodont, similar to the unmeasured portion (Figures 1.5, 1.6) and at the cost of Ca, P, and F concentrations. The crown has a similar pattern of chemical distributions to the enameloid, whereas the lower part of the crown is comparable to the dentine of shark teeth (Figures 1.5, 1.6, 1.7). These observations are similar to those reported by Katvala and Henderson (2012) and Enax et al. (2014), but this is the first time that the chemical distribution of segmiplanate conodont P_1-elements is analysed. One could expect such chemical pattern at the posterior extremity of a conodont dental element, because this is where the basal body is originally located. However, one specimen with its anterior extremity cross-sectioned transversally shows a similar pattern to that of the $TM_{transversal}$ result (Figure 1.3B).

We analysed additional conodonts to test if this chemical distribution pattern is exclusive for our *Sc.* ex gr. *milleri* specimens from Timor, or if this pattern could still be detected in samples subjected to a relatively high temperature of fossilisation (300 °C, CAI 5) (specimens: WMJ1, WMJ2, GR1 in Table S1.1, File S1.4). Interestingly, a specimen of *Borinella* sp. from the early Spathian of Oman (WMJ1) also had a similar pattern at the lower part of the crown. The same can be said for an element of *Sc.* ex gr. *milleri* conodont from Kashmir (Guryul Ravine, Leu et al., 2019) with a CAI 5 (GR1), but the chemical zonation is less pronounced when compared to well-preserved conodonts.

A pristine or secondary elemental 'imprint' in the conodont bioapatite?

Major (Ca, P, F) and trace elements (Mg, S, Na) as well the unmeasured portion have complementary concentrations within the crown of the conodonts. Distinct chemical concentrations between albid and hyaline crown were expected as the latter tissue was reported to have a higher carbonate as well as and trace elemental content (e.g., Trotter and Eggins, 2006; Trotter et al., 2016b). However, the relative enrichment for Mg, S, Na and the unmeasured portion was only noted for the reticulated, "darker" areas situated at the lowermost part of the crown (Figure 1.2A, 1.5, 1.6B).

One suggestion that may explain this chemically distinct zone, already made by Katvala and Henderson (2012), is that the lower part of the conodont crown was periodically retracted into the epidermis for growth. In order to grow and to repair bioapatite crystals, modern and ancient vertebrates have the adaptability of retracting or even maintaining their teeth within the tooth bed, thus maximizing the contact with the organic matrix and consequently increasing the absorption of nutrients into the tissue (e.g., Jeppson, 1979; Donoghue, 1998; Rakovan, 2002). For conodonts, this suggestion was first based on microstructural studies that described regular

and irregular reticulate surfaces on some dental elements, thought to be a reflection of the cell pattern of the tissue that covered the crown (Donoghue, 1998; Donoghue and Purnell, 1999; Turner et al., 2010). However, recent geochemical investigations using Palaeozoic taxa have also corroborated the suggestion of retraction into a tooth bed (Katvala and Henderson, 2012; Shirley et al., 2018).

It is worth mentioning that in these studies and in our investigation, conodont species from the 'euconodonts' group were used, which are described as being more 'complex' and derivative forms of conodonts which appeared around the Late Cambrian and persisted until their disappearance during the Late Triassic (Donoghue, 1998; Orchard, 2007; Donoghue et al., 2008).

Na, as well as Mg and S, may be used to interpret if these trace elements were introduced during bioapatite diagenesis (e.g., Kohn et al., 1999; Dauphin and Williams, 2004).Given the lower Na, Mg, and S concentrations measured in the upper part of the crown, but relative enrichment in the lower conodont crown in parallel to the higher unmeasured portion, it is likely that these elements have a secondary origin in a tissue that may partially resemble that of dentine in shark teeth.

This discussion highlights the complexity of the conodont feeding apparatus as discussed by Katvala and Henderson (2012), that also advocated the usage of the terminology 'teeth' and not 'elements' when referring to conodont dental bioapatite as a more proper biological designation to this structure. Meanwhile, additional research of their microstructure has revealed more details about the diversity and functional ecology of these "tooth-like" structures (e.g., Jones et al., 2012; Murdock et al., 2013; Martínez-Pérez et al., 2016). More studies utilizing a higher number of samples are necessary to fully understand the nature of the various dental morphologies which these animals present between different taxa. However, at least from the Late Cambrian until the Early Triassic period, it is probable that the majority of euconodont species (a.k.a. "complex conodonts") presented the biological adaptation of retracting their teeth into the tooth bed for an eventual repair and regrowth of this tissue.

Oxygen isotope compositions of tissues analysed

Segmiplanate P_1-elements of *Sc.* ex gr. *milleri* from Early Triassic strata of Timor were of sufficient abundance to prepare three sample sets were prepared to test our analytical protocol. The $\delta^{18}O$ values for the $TM_{low\ longitudinal}$, representing largely the hyaline crown (Figure 1.2B), are the most homogeneous tissues analysed (17.1 ±0.2 ‰, $n = 13$, Figure 1.9). Their average $\delta^{18}O$ value is also within 1σ error the same as the reference value for Timor conodonts measured by

HTR (17.3 ±0.4 ‰, $n = 7$). In contrast, the TM$_{transversal}$ samples that may include denticles and/or albid crown tissues (Figure 1.2A), have a higher $\delta^{18}O$ variance with also lower average values (16 ±1 ‰, $n = 13$, Figure 1.9). The conodonts from the TM$_{mid\ longitudinal}$ group, polished at a higher level and measured towards the interior of the dental elements (Figure 1.2C) also have a higher variance and lower $\delta^{18}O$ values (15.7 ±1.9 ‰, $n = 11$, Figures 1.9, 1.10). The lower $\delta^{18}O$ values and higher variance in the albid tissue and in the interiors of conodonts is in line with previous SIMS measurements of conodonts (Wheeley et al., 2012; Zhang et al., 2017). The similarity of the TM$_{mid\ longitudinal}$ with the TM$_{transversal}$ $\delta^{18}O$ values, as well as the quantitative element analyses confirms that these sections indeed represent albid tissue in both conodont groups. For samples of *Scythogondolella* from USA and Spitsbergen, prepared also for a low longitudinal section, the measurements of $\delta^{18}O$ values also reproduced well with a low variance (1σ error of 0.3 ‰ or better; Figure 1.9), even though the absolute values are quite different and likely related to different palaeoenvironmental conditions.

For this study it is of interest to note that even for the TM$_{transversal}$ group and even more so for the TM$_{mid\ longitudinal}$ group have $\delta^{18}O$ values overlapping with the HTR reference value despite being clearly an albid tissue (Figures 1.9, 1.10A, B). Previous studies attributed the low $\delta^{18}O$ measured in the albid crown and in the interiors of conodonts to a higher susceptibility of these tissues to diagenetic alteration (e.g., Wheeley et al., 2012; Zhang et al., 2017). However, if both tissues were more susceptible and the values measured for these tissues are not affected by IMF's, one would expect the $\delta^{18}O$ values measured via HTR analysis that represents an average of 60 to 100 conodonts, to give average values between those of the albid and the hyaline crown, as the albid crown makes up an estimated 50 or more % of the conodont crown (e.g., Figures 1.2A, 1.3, 1.10A, B; Donoghue, 1998). Instead, the HTR results are rather similar to the $\delta^{18}O$ values measured in the hyaline tissue of the lower part of the crown (i.e., TM$_{low\ longitudinal}$, Figure 1.9). A possible factor involved decreasing the SIMS $\delta^{18}O$ values, related to the albid tissue, is to have an irregular sample texture for analysis because of porosity. Pore spaces within the albid crown can be up to 5 µm, but SEM or transmission electron microscopy (TEM) in thin sections are necessary for a more comprehensive perspective of these structures (e.g., Donoghue, 1998; Trotter et al., 2007). SIMS ablation pits in regions with underlying intracrystalline pores could have formed irregular sample surfaces, which may bias the $\delta^{18}O$ measurement. The hyaline crown, despite its lamellar crystal structure, has intracrystalline nanopores that provide less chance to create irregular surfaces after the secondary ion ablation. This suggestion may also explain why in some cases individual analysis on albid tissue overlap with the hyaline tissue (Rigo et al., 2012; Trotter et al., 2008, 2015), and in other cases the $\delta^{18}O$ values are different

(Wheeley et al., 2012; Zhang et al., 2017).

As described above for the shark teeth, an enrichment in ^{18}O measured using SIMS analysis and compared to the classical silver phosphate preparation could potentially be related to a contribution of carbonate-ion sourced oxygen, as this is commonly noted to be enriched in ^{18}O compared to the phosphate group by about 9 ‰ (e.g., Iacumin et al., 1996; Vennemann et al., 2001; Lécuyer et al., 2010; Sisma-Ventura et al., 2019). However, given the low unmeasured content of the conodonts, similar to that for the shark tooth enameloid (< 3 wt%), mass balance estimates of the carbonate contribution to these analysed tissues would be limited to about 0.3 ‰ for the δ^{18}O values (Table 1.3). Higher ^{18}O enrichments would be possible on *in-situ* measurements at the lower part of the conodont crown only (+0.5 ‰). This suggests that for most of our dataset, contributions of oxygen ions from other oxygen-bearing sites (CO_3^{2-}, SO_4^{2-}, OH^-) that can bias the δ^{18}O values measured by SIMS are also limited (e.g., Lécuyer et al., 2010; Wheeley et al., 2012; Zhang et al., 2017). This is also supported by the observation that the hyaline crown values for δ^{18}O are within error the same as those measured by the HTR method.

Traditionally, oxygen isotope contributions from organic remnants still present in the conodonts is considered minimal as conodonts preserve or even only contain very small amounts of organic matter (e.g., Wheeley et al., 2012), but well-preserved dental elements (i.e., CAI 1) could contain epithelial tissue within conodont tissues (Donoghue, 1998). Considering the quantitative estimate of only 2.6 ±1 wt.% of the unmeasured portion in $TM_{low\ longitudinal}$ that is hyaline tissue (Figure 1.5), mass balance calculations similar to those for the shark teeth above, would imply a depletion of ^{18}O of about 0.15 ‰ only, perhaps accounting for the small but consistent offset between the SIMS δ^{18}O (17.1 ‰) and the HTR $\delta^{18}O_{PO4}$ (17.3 ‰) averages.

The elemental concentrations and distributions measured in conodonts are similar to those noted to the fossil shark enameloid *vs* dentine: higher substituting cations and unmeasured portions in the dentine as well as the lower hyaline crown part that may have been embedded in the tooth, compared to the nearly stoichiometric Ca, P, and F concentrations for fluorapatite in the enameloid or upper albid and hyaline crown tissues. In parallel to the shark teeth, those parts with the higher unmeasured contents also have the highest variance for their δ^{18}O values and may also have lower average δ^{18}O values, although this difference in δ^{18}O is by far not as pronounced as that for the shark teeth dentine. However, the parts with the higher substituting trace element and unmeasured portions of the conodont tissues may still have similar absolute δ^{18}O values compared to those tissues of stoichiometric fluorapatite composition - upper hyaline crown and albid crown tissues too (Figure 1.10A, B). Furthermore, the analytically most homogeneous hyaline tissue of the $TM_{low\ longitudinal}$ zones that also has average δ^{18}O values

(17.1 ‰, ±0.2 ‰) identical to the bulk HTR values (17.3 ±0.3 ‰) does show some systematic differences in the elemental distributions of Ca, P, F, Mg, Na, and S (e.g., Figure 1.10C.1, D). Also, *in-situ* analyses in the interiors of conodonts on surfaces similar to the shark enameloid, with near-stoichiometric Ca, P and F and low Mg, Na and S concentrations (i.e., TM$_{mid\ longitudinal}$, Figures 1.5, 1.6) may have larger isotopic variations (Figures 1.9, 1.10C.2, E) and also lower average $\delta^{18}O$ values (15.7 ±1.9 ‰) compared to the HTR values. Collectively this suggests that the chemical variations of well-preserved conodonts do not cause IMF for the SIMS O-isotope measurements. Instead, the lower and more scattered $\delta^{18}O$ values may be related to an irregular texture of the conodonts, as most of the low $\delta^{18}O$ was measured in sample sets which included albid tissue in the analysis (i.e., for the TM$_{transversal}$ and TM$_{mid\ longitudinal}$ groups). Such irregularities may be produced during the sample preparation and/or may be inherent to the crystal size and orientation in the biogenic apatite of the conodonts. Hence, care has to be taken with the sample preparation and the choice of the final biogenic apatite tissue to be analysed.

As has been previously noted (c.f., Wheeley et al., 2012; Zhang et al., 2017), analysis of the albid tissue is prone to give lower and more variable $\delta^{18}O$ values for *in-situ* measurements. Just as for the recent shark dentine $\delta^{18}O$ values, we attribute the biased $\delta^{18}O$ values measured in conodonts to an irregular sample texture (for example a tilted analytical surface; Kita et al., 2009) for SIMS analysis. By analogy to the distinct shark teeth enameloid tissues (SCE and PBE, see above), the hyaline crown appears to be the most reliable conodont tissue for *in-situ* SIMS O-isotope analyses and longitudinal cross sections of this tissue can be readily prepared for microanalyses techniques. Sample texture is also a more relevant factor for reliable SIMS O-isotope measurements than specific tissue choices, hence ideally all analytical spots, whether in albid or hyaline crown portions should always be verified with subsequent or preceding SEM imaging to identify the analysed tissue, as well as an optical profilometer (c.f. Kita et al., 2009) to confirm the final analytical texture. The relatively small variations in chemical compositions for the conodont tissues do not, however, cause IMF for the SIMS O-isotope measurements (c.f. Wheeley et al., 2012; Zhang et al., 2017). Ideally also, one should concentrate the analysis spots in one area to avoid analyses of distinct growth zones and texturally different zones within the conodont tissue.

4.4 A new in-house SIMS standard

A principal objective of this research was to refine the SIMS measurements and its usefulness for different tissues in bioapatite, as well as to define a possible bioapatite standard to be used for future SIMS measurements, particularly of conodonts. The Durango apatite is

compositionally and structurally different compared to fossil bioapatite (Table S1.2), hence it is more appropriate to use a bioapatite standard, or at least to combine such a standard with the Durango standard for SIMS measurements and the data reduction. The selected bioapatite needs to be relatively homogeneous in its oxygen isotope composition, which can be difficult if different growth lines or structures of the studied biomineral are analysed during a SIMS session (beam diameter: 15 µm). However, the bulk analysis by HTR done in parallel provide a good basis for studying the possible variations in $\delta^{18}O$ by SIMS (Table 1.1, 1.2).

For the recent shark teeth, the variation in measured $\delta^{18}O$ values is clearly related to the type of tissue analysed with the SIMS, as no such differences were noted for the HTR measurements on these different tissue types (dentine and enameloid). The $\delta^{18}O$ differences for the dentine between HTR and SIMS are likely to be related to the irregular sample texture analysed *in-situ*, with possible minor contributions of sputtered oxygen released from the organic matrix, if present. The relatively high Fe and S contents in fossil specimens, suggestive of diagenetic alteration, can be used to justify the intra- and inter- tissue variations in $\delta^{18}O$ values measured as either primary or clearly secondary in nature. The variation in structure, texture and density of the shark teeth render them more complex than previously thought and not ideal as bioapatite standards, notably if used in cross-section to the structurally different tissue types. To minimise such analytical artefacts that can ultimately cause bias for *in-situ* microanalysis techniques, we recommend consulting a recent contribution by Shirley et al. (2020). It summarises common setbacks of phosphatic microfossils' sample preparation and the different solutions to solve them, which vary with the nature of the studied material. Nevertheless, given the larger size of shark teeth and the ease of exposing and hence polishing only the outer enameloid structure, there is still potential to use them as in-house standard material, or for an individual study where no alternative bioapatite standards are available. Sharks, for which their teeth were formed under controlled environmental conditions have potential as the chemical composition of the water can be controlled (e.g., Žigaitė and Whitehouse, 2014), though research in animals under stress conditions in captivity reported disrupted bone formation (e.g., Yirmiya et al., 2006).

For the conodonts, sample spots should focus on a single tissue, and while the albid tissue can provide reliable $\delta^{18}O$ values, it is more prone to present irregular sample textures given the larger pore spaces compared to hyaline tissue. Based on the oxygen isotope compositions measured, the *Sc.* ex gr. *milleri* from Timor, now named 'TM-SM', was hence selected as an internal standard for oxygen isotope analysis of conodonts for the SwissSIMS laboratory at the University of Lausanne (UNIL). A large number of specimens can still be recovered from the Timor sediments. Using the most reliable dataset ($TM_{low\ longitudinal}$), the $\delta^{18}O$ values measured by

SIMS are statistically undistinguishable from the TM-HTR $\delta^{18}O_{PO4}$ values (*t* test: p > 0.173, Table S1.4). The $\delta^{18}O$ average of all sample splits used for both methods (SIMS and HTR) for the *Sc.* ex gr. *milleri* from Timor is 17.1 ±0.3 ‰ (*n* = 20), and this value will be considered for the TM-SM in-house standard. This conodont standard is thus a good, high $\delta^{18}O$ standard, which can be used together with the low $\delta^{18}O$ standard of the Durango fluorapatite while a low $\delta^{18}O$ bioapatite standard has not been developed yet. Both TM-SM and Durango may provide a suitable basis for scaling the instrumental fractionations of SIMS measurements of bioapatite.

5. Conclusions

A detailed geochemical and oxygen isotope study of conodonts and shark teeth provides new insights for SIMS O-isotope measurements of bioapatites. Systematic and/or more random variations in chemical compositions that may occur within the different bioapatite-mineralised hard tissues can be used to discriminate the importance of primary versus secondary mineralisation processes and hence help select parts of the biogenic tissue that are of interest for subsequent O-isotope measurements and palaeoenvironmental interpretations. However, no systematic relations are noted between relatively small chemical variations in conodont or enameloid shark tooth biogenic tissues and variations of their SIMS oxygen isotope measurements. Conodont as well as shark tooth enameloid also have near-stoichiometric major element compositions of fluorapatite. The SIMS $\delta^{18}O$ variations measured in such tissues, when compared to conventional HTR measurements of the same material, are largely related to analytical artefacts relating to the different structures and textures of the phosphatic tissues. Adjacent tissues with different crystal size, densities of crystals or orientation, and with relatively large pore spaces ($\geq 1 \ \mu m$) are prone to give differences in texture during sample preparation. This is clearly evidenced by comparing results from the classical silver phosphate precipitation methods, which also isolate the PO_4^{3-} ion from other potential O-bearing sources, to the $\delta^{18}O$ measurements using SIMS. A single biomineralogical layer that is readily prepared with a minimal final sample topography and with a flat surface should be analysed. Outer fluorapatite enameloid layers from shark teeth or also fluorapatite of lower crown tissues from conodonts would both analytically, as well as in terms of minimisation of secondary mineralisation or remineralisation during diagenesis, be suitable tissues for SIMS analyses. While enameloid shark bioapatite is recommended to be used as a secondary standard for *in-situ* oxygen isotopic investigations in vertebrate dental tissues, the interpretation of its SIMS $\delta^{18}O$ values should be done with caution as the different "enameloid" layers can have contrasting $\delta^{18}O$ values. Regarding conodont bioapatite, the hyaline crown is confirmed as a reliable tissue for SIMS $\delta^{18}O$ analysis. Best results can be

obtained from cross sectioning longitudinal cuts of the lower crown of the conodonts. These sections are relatively easy to be prepared and also avoid albid tissue commonly mineralised within the denticles. Based on the present results, a conodont sample set from Timor (TM-SM) was selected to be used as an internal standard for stable isotope analyses of bioapatite for the SwissSIMS laboratory at the University of Lausanne. Additional material of this sample could be made available for cross-laboratory tests and potential standard calibration.

6. Research Data and Supplementary Material

Research data associated with this article can be found in the Supplementary Material. All suplements were uploaded to a Data Repository (https://doi.org/10.5281/zenodo.7301728). The Supplementary Material table of contents to the current chapter is:

File S1.1 Additional information on material and methods: general geological description for the sites from where conodonts were selected; and the Durango normalisation for SIMS measurements.

File S1.2 Original files and additional images made by Scanning Electron Microscopy (SEM)

File S1.3 Output files and screenshots of images taken using a profilometer to verify the sample topography.

File S1.4 Chemical distribution output files and additional maps.

File S1.5 Raw oxygen isotope data and normalisation.

Table S1.1 Complete list of all referred conodont bioapatites, Conodont Alteration Index (CAI) and oxygen isotope technique used.

Table S1.2 Quantitative analysis raw data and ionic calculations.

Table S1.3 Carbonate in bioapatite analysis raw data and estimates of the carbonate contents.

Table S1.4 Statistical tests of conodont oxygen isotope data.

Figure S1.1 Shark tooth enameloid δ^{18}O values analysed by SIMS and the relative topographic offset between each analysed layer with the standard (Durango).

[Silver Surfer, speaking to a Lion]:

"Unlike the humans, who call you beast, there is no violence in your heart. No hint of avarice, no smoldering hate! Yet man, who has won dominion over all this world, is a stranger to peace — a prisoner, caught in the web of his own nameless fears."

- Stan Lee

CHAPTER II

Climate cooling in the Early Triassic subtropics

Author contributions:

Zoneibe Luz, conceptualisation, data curation, formal analysis and investigation, methodology, visualisation, original draft writing, review and editing.

Marc Leu, methodology, resources, validation, visualisation, draft review and editing.

Oluwaseun Edward, data curation, formal analysis and investigation, methodology, validation, draft review and editing.

Aymon Baud, resources, validation, draft review and editing.

Hugo Bucher, conceptualisation, funding acquisition, methodology, resources, supervision, original draft writing, review and editing.

Torsten Vennemann, conceptualisation, funding acquisition, methodology, resources, supervision, validation, draft review and editing.

Climatic cooling in the Early Triassic subtropics

Zoneibe Luz[a,*], Marc Leu[b], Oluwaseun Edward[a], Aymon Baud[c], Hugo Bucher[b], Torsten Vennemann[a]

[a] *Institut des Dynamiques de la Surface Terrestre, Université de Lausanne, Rue de la Mouline, 1015 Lausanne, Switzerland*

[b] *Palaeontological Institute and Museum, University of Zürich, Karl-Schmid-Strasse 4, 8006 Zürich, Switzerland*

[c] *Institut des Sciences de la Terre, Université de Lausanne, Rue de la Mouline, 1015 Lausanne, Switzerland*

*Corresponding author: zoneibe.luz@gmail.com (Zoneibe Luz)

Abstract

In the aftermath of the largest mass extinction, the Early Triassic included a major environmental perturbation during which nektonic marine organisms (e.g., ammonoids, conodonts) underwent a series of extinction-origination cycles associated with eustatic sea-level changes, the ecological reorganisation of land plants and global fluctuations in the carbon cycle. Early Triassic palaeotemperatures were not invariably hot and varied along with carbon-budget cycles. The major and protracted Early Triassic extinction of nekton spanned the late Smithian (700 ky) and peaked at the Smithian–Spathian boundary (SSB), some 2.7 Ma after the end-Permian extinction event (252 Ma). Oxygen isotope values – a proxy for relative changes in sea-surface temperature – were analysed from best-preserved conodont bioapatite (Conodont Alteration Index CAI 1) to gain a better understanding of the role temperature played during the late Smithian extinction. Conodont $\delta^{18}O$ values were measured from two sections in Oman (Hawasina Nappes & Batain Mélange) representing pure carbonate settings deposited on marine seamounts, thus excluding abnormal salinity fluctuations that could influence the oxygen isotope compositions of the seawater. Combined with clumped isotope measurements (δ^{47}, Δ_{47}) from associated brachiopods, a $\delta^{18}O_w$ value of -1.7 ± 0.8 ‰ can be estimated for contemporary waters. Secondary ion mass spectrometric (SIMS) measurements on conodonts provided high-resolution $\delta^{18}O$ constraints on the evolution of sea-surface temperature changes across the extinction interval. The middle Smithian negative $\delta^{18}O$ anomaly extended into the early late Smithian, where it reached its lowest values. This nadir was followed by a protracted first order-positive trend representing a cooling by about 7.5 °C during the late Smithian and early Spathian. Thus, this first-order cooling trend confirms previous trends noted for shelf

sections in the northern Indian margin and South China. Conodont zone chronostratigraphy, calibrated by U-Pb ages, suggests this cooling trend lasted for about 400 ky (average cooling rate of 1 °C per 53 ky). This estimate confirms that the mid-late Smithian to earliest Spathian cooling recorded from the Tethyan realm was much too long to be accounted for by a volcanic winter, and was likely too slow to drive nektonic species directly to extinction. The highly resolved SIMS time series obtained from the expanded SSB Batain section suggests the presence of short-term temperature oscillations superimposed onto the first-order cooling trend. The middle Smithian and late early to middle Spathian first-order warming trend clearly postdates the negative C isotope peaks measured for carbonates by at least 200 to 300 ka. However, the intervening first-order cooling trend tracks the positive C isotope excursion with no detectable time offset. Pending further substantiation from coeval sections, these delayed and synchronous temperature responses may hold significant implications for constraining the mechanisms driving the Early Triassic C cycle and climate. Accordingly, Early Triassic climatic upheavals may differ from those associated directly with the PTBME by their typically slower pace rather than their amplitude. It is possible that Early Triassic climate changes and extinctions were driven by mechanisms unrelated to those associated with the PTBME and concurrent SLIP volcanism.

1. Introduction

Significant oscillations in climate are likely to affect the internal functioning and hence also interactions of biological life with the inorganic geochemical cycles in ecosystems. In recent years, climatic changes have been enhanced by anthropogenic activity (IPCC, 2019). In the marine realm, higher sea surface temperatures are expected for the coming years and imminent consequences include a global decline in ocean oxygen content and enhanced ocean acidification (Guinotte and Fabry, 2008; Hofmann and Schellnhuber, 2009; Schmidtko et al., 2017; IPCC, 2019). Both will severely compromise the survival of calcifying marine organisms (e.g., coccolithophores and foraminifera), important carbon sinks for the mitigation of CO_2 in the atmosphere. A good understanding of the magnitude and timing of past climatic changes and their effects on aquatic life are also essential to understand how and if these organisms can adapt to the changes in climatic conditions. With that in mind, it is also very instructive to study similar 'critical' conditions in Earth's history (i.e., mass extinction events), that is to use the past as a window to the future so as to estimate how nature for a given ecosystem reacts without the

anthropogenic influence (e.g., Kiessling et al., 2019).

Among the several biotic crises during the Phanerozoic, the Early Triassic (252 to 249 Ma) was studied in this work. This interval was a period of major climatic oscillations for Earth's ecosystems, following the most catastrophic of all known biotic crises: The Permian–Triassic boundary mass extinction (PTBME), an event when more than 90 % of all marine species went extinct around the globe (e.g., MacLeod, 2014). While still debated, one of the main reasons attributed to this life crisis could have been the release of greenhouse gases, likely to be derived from Siberian trap volcanism, which triggered a long-lasting global warming; associated with anoxic events in the deep marine realm and deposition of extensive black shales, as recorded in a number of localities worldwide (e.g., Bottjer, 2012; Joachimski et al., 2012; Sun et al., 2012; Zhang et al., 2019; Grasby et al., 2020; Widmann et al., 2020). Due to these adverse circumstances, it is often thought that the entire biological and ecological recovery during the Early Triassic was delayed (Meyer et al., 2011; Joachimski et al., 2012; Hautmann et al., 2015; Grasby et al., 2016). However, recent palaeontological and geochemical contributions suggest that conditions were not uniformly adverse in the aftermath of this extinction. Several minor series of extinction-origination cycles occurred within the Early-Triassic (Song et al., 2011). These are marked by shifts in the carbon and oxygen isotope compositions that coincided with a high diversification rate of some secondary marine consumers (conodonts and ammonoids) (Orchard, 2007; Galfetti et al., 2007a, 2008; Brühwiler et al., 2010; Romano et al., 2013; Jattiot et al., 2018; Leu et al., 2019; Zhang et al., 2019; Goudemand et al., 2019; Widmann et al., 2020). A more pronounced cycle occurred at the Smithian–Spathian boundary (249.29 to 249.11 Ma, Widmann et al., 2020). For conodonts, and to some extent ammonoids, this intra-Triassic extinction was of greater magnitude than the PTBME (Orchard, 2007; Brühwiler et al., 2010). The trigger for this biotic crisis is still a matter of debate (e.g., Goudemand et al., 2019), but several independent proxies have indicated environmental changes on a global scale (i.e., Widmann et al., 2020). Palynological data, notably fern spikes, have shown a change in the terrestrial vegetation from humid to arid conditions towards the end of the Smithian (Hermann et al., 2011; Hochuli et al., 2016). The carbon cycle also records a large positive carbon isotope excursion, which suggests a major change in the carbon budget (Payne et al., 2004; Galfetti et al., 2007a, b; Zhang et al., 2019; Leu et al., 2019; Goudemand et al., 2019; Widmann et al., 2020; Schneebeli-Hermann et al., 2020), with an associated positive oxygen isotope excursion that reflects a transition from warm to cooler sea surface temperatures (Romano et al., 2013; Goudemand et al., 2019). More recently, mercury anomalies (Hg/TOC) were also described for the middle Smithian to early late Smithian thermal maximum as noted by the O-isotope

compositions of conodonts (Shen et al., 2019). However, recent contributions have shown that these anomalies are rather 'weak' and non-synchronous with the thermal maximum at this interval (Hammer et al., 2019; Widmann et al., 2020).

This study complements the above-mentioned perspective with high-resolution oxygen isotope ($\delta^{18}O$) measurements in phosphate from well-preserved bioapatite of conodonts from Oman (Conodont Alteration Index – CAI – of 1; Figure 2.1). Conodonts were eel-like, jawless vertebrates that were ubiquitous from the Cambrian to the end of the Triassic and the oxygen isotope composition of their teeth is a well-known proxy to address questions on palaeoclimate (e.g., Wenzel et al., 2000; Trotter et al., 2008; Sun et al., 2012; Romano et al., 2013; Chen et al., 2021). Given size constraints for 'conventional' techniques of oxygen isotope analyses of conodonts, high time-resolution records, notably in sections with low conodont abundances are often difficult to obtain (conodonts are often about 500 μm in size, with a weight of less than 100 μg; Wenzel et al., 2000). However, recent analytical and technological improvements such as oxygen isotope analyses by Secondary Ion Mass Spectrometry (SIMS), now allow for *in-situ* analysis of individual conodonts (e.g., Rigo et al., 2012, Wheeley et al., 2012; Trotter et al., 2008, 2015; Zhang et al., 2017; Goudemand et al., 2019). With this *in-situ* technique, a higher spatial and temporal resolution of $\delta^{18}O$ measurements can be achieved, also allowing sections with a scarce occurrence of specimens to be analysed. For example, recent analyses of conodonts by Goudemand et al. (2019) from the Early Triassic of Pakistan (Nammal Gorge, Salt Range, see Romano et al., [2013] for the 'conventional technique' study), have indicated that neither extreme climatic warming nor cooling triggered the extinction at the SSB, contrasting previous interpretations of extreme high temperatures at the SSB causing the biotic crisis (e.g., Sun et al., 2012). For this study both a classical method that required batch sampling (about 1 mg of bioapatite) to precipitate silver phosphates and analysis by High Temperature Reduction (HTR), as well as *in-situ* measurements by secondary ion mass spectrometry (SIMS) were used to refine the interpretations at the SSB.

All previous O-isotope studies of conodonts at the SSB were made on geological sections deposited on continental shelves and slopes. In contrast, this study focusses on samples recovered from carbonate blocks deposited on marine sea mounts (Wadi Musjah and Jebel Aweri, Figures 2.2, 2.3) (Baud et al., 2001; Brühwiler et al., 2012; Brosse et al., 2019). Sea mount-deposited sediments are valuable assets for palaeontological reconstructions (e.g., Orchard, 1995; Maekawa et al., 2018), since the depositional conditions are less prone to an influence from processes such as burial of organic matter, continental weathering and freshwater runoff (Zhang et al., 2018; Schneebeli-Hermann et al., 2020; Widmann et al., 2020). The latter effect

may have an influence on the oxygen isotope composition of the water ($\delta^{18}O_w$) and consequently be reflected in the bioapatite of ectotherm animals (e.g., Kocsis et al., 2007; Fischer et al., 2013; Leuzinger et al., 2015; Carrillo-Briceño et al., 2019), including conodonts (e.g., Luz et al., 1984; Trotter et al., 2008). However, the block of Jebel Aweri, with a large build-up of the Ad Daffa sedimentary units (Hauser et al., 2001), reflects high sedimentation rates, and hence with a well-preserved and expanded geochronology of the SSB interval (Figure 2.3). This provides a unique opportunity to improve the temporal resolution of climatic/environmental changes across the SSB. The stable oxygen isotope records from the marine sections are also thought to represent open marine conditions, complementing the comprehension about Early Triassic climatic changes on a global perspective.
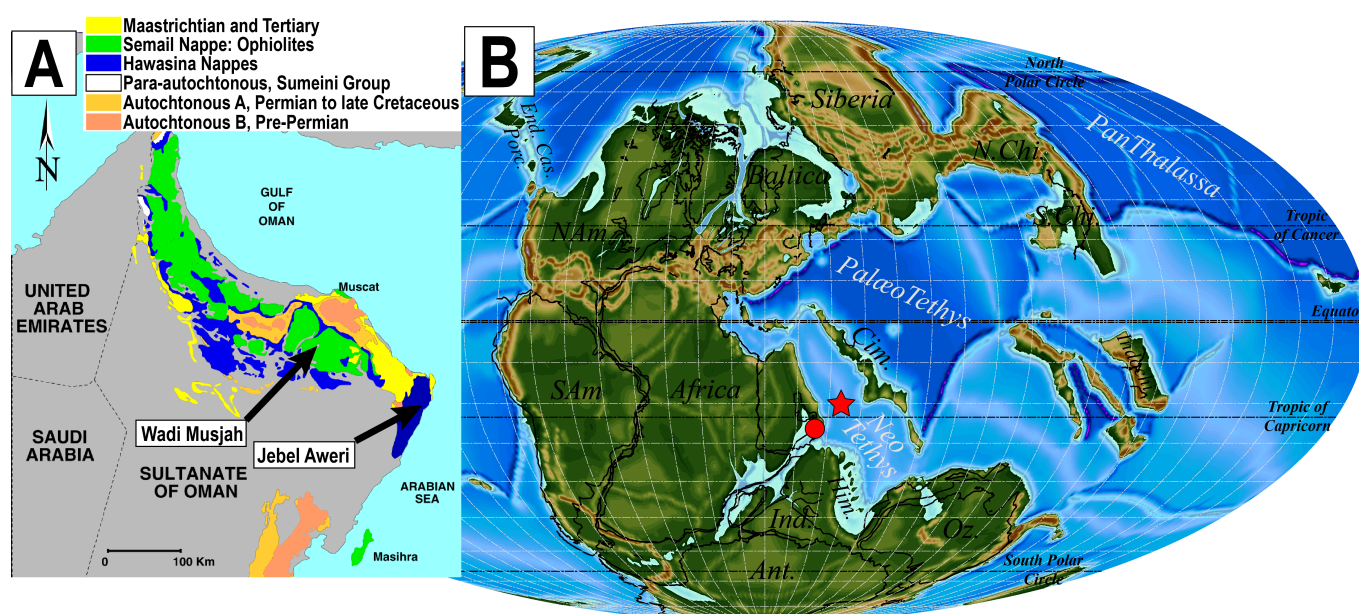
Figure 2.1. (A) The current positions of the Jebel Aweri and Wadi Musjah sites within the Arabian Peninsula; and **(B)** a palaeogeographic reconstruction of the Early Triassic with the relative location of the studied sections. The star is the location of the marine seamount during the Early Triassic, but samples were collected at where the circle is. Modified after Vérard (2019) and Leu (2021).

2. Geological Setting

The two studied localities are situated in the Arabian Peninsula (Figure 2.1A), and they have been selected from a number of sections in Oman that cover the PTBME and the Early Triassic recovery (Baud et al., 2001; 2012; Krystyn et al., 2003, Twitchet et al., 2004; Richoz, 2006; Baud and Bernecker, 2010; Richoz et al., 2005, 2010a, 2010b, 2014; Brühwiler et al., 2012; Clarkson et al., 2013, 2015, 2016; Brosse et al., 2019; Chen et al., 2019; Souquet and Goudemand, 2020; Leu, 2021). During the Early Triassic, these sections were part of the Northern Gondwana margin within the tropics (20 ºS), at the eastern part of the 'Pangea' supercontinent (Figure 2.1B and Ricou et al., 1994). Surrounded by Neotethys exotic carbonate

blocks of Permian–Triassic age, the sections were deposited on sea mounts inherited from a rifting phase and on marine plateaus, which belonged to tilted blocks of the Permian–Triassic continental margin (Leu, 2021). The blocks were later dismembered during a phase of oceanic convergence and redeposited in a proximal turbidite (olistostrome) of the Hawasina basin (for Wadi Musjah, Baud et al., 2001, 2012; Richoz et al., 2014) and of the Batain Basin (for Jebel Aweri, Baud et al., 2012; Brühwiler et al., 2012; Brosse et al., 2019). The studied sections are separated by approximately 160 km west-east and more detailed sedimentological/stratigraphic descriptions can be found in Brühwiler et al. (2012), Baud et al. (2018), Brosse et al. (2019) and Leu (2021).
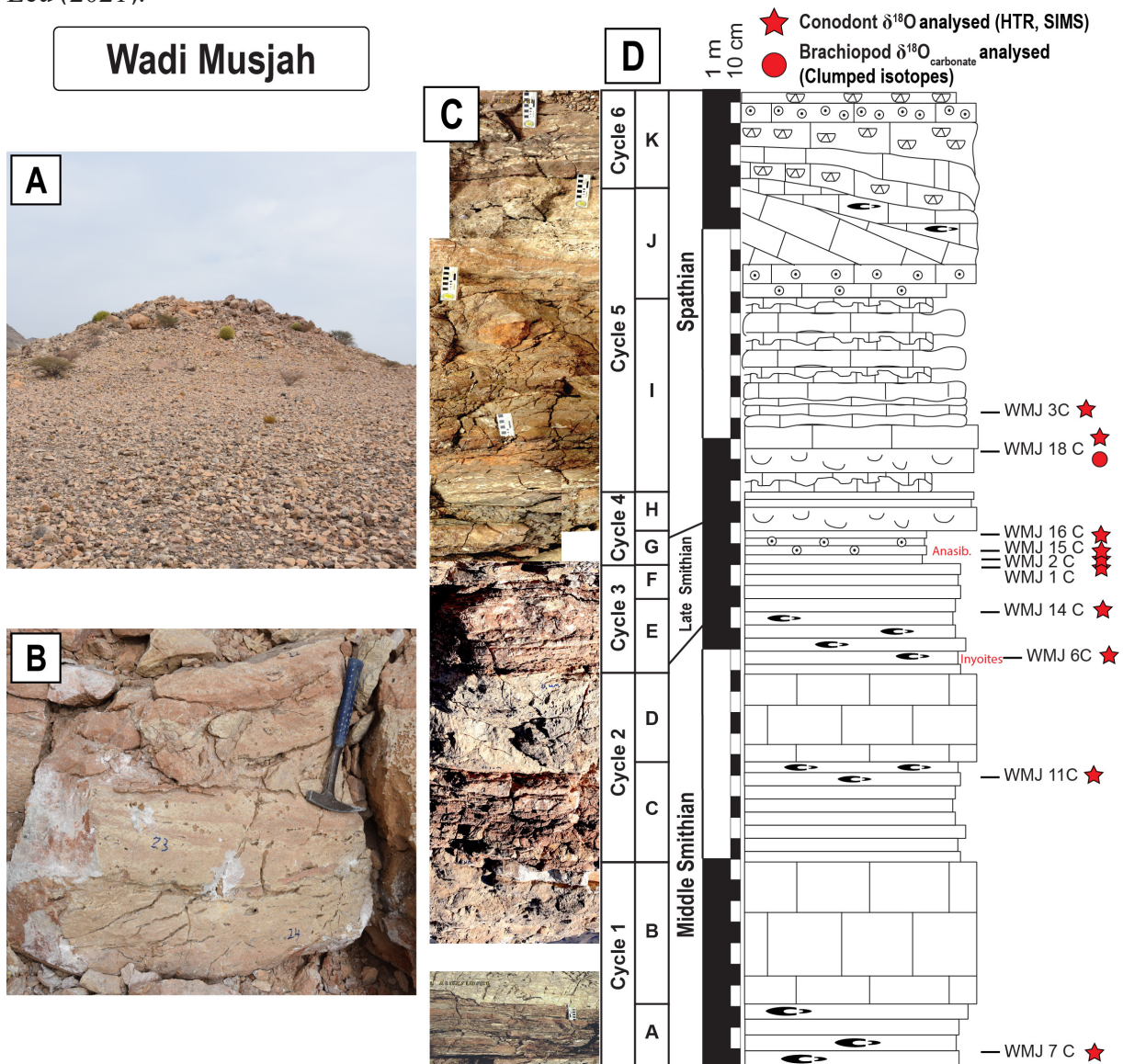
Figure 2.2. (A) Outcrop view of the Wadi Musjah site and **(B)** of the Smithian–Spathian boundary (SSB). In column **(C)** the images of the layers are given in succession. In column **(D)** a detailed stratigraphic log shows cycles and corresponding levels. Layers sampled for $\delta^{18}O$ and Δ_{47} analyses are marked as red stars or a circle, respectively. Modified from Leu (2021).

Figure 2.3. (A) West outcrop view of the Jebel Aweri build-up section, lower block of ca. 22 m thickness. White lines indicate layer boundaries as visible in the field. **(B)** Outcrop view of the upper block (ca. 8 m thick), with visible layer boundaries indicated. **(C)** Outcrop view (from East) of the top of the lower block with the erosive contact between the shell supported biostrome (level 8) and the overlying clast supported bioherm. **(D)** Outcrop view (from East) with the level 9 shown; side-view shows an erosive type of contact at this level with the underlying shell supported biostrome (level 8). **(E)** Detailed stratigraphic log with cycles and corresponding levels are shown. Layers sampled for $\delta^{18}O$ and Δ_{47} analyses are marked (red stars/circle). Modified from Leu (2021).

2.1 Wadi Musjah

Wadi Musjah exotic blocks (22°57'44.50"N, 58°16'1.40"E) outcrop about 75 km south of Muscat (Figure 2.1A, 2.2) and they are surrounded by the Semail Ophiolite Nappe

sediments, representing the kilometer-sized Hawasina window (Leu, 2021). The investigated carbonate block is a 4.6 m thick Hallstatt-type limestone unit that covers the middle Smithian to early Spathian. It represents about the same time interval as the about 30 m thick Jebel Aweri block, but with a lower resolution across the SSB due to the low sedimentation rate. This site is subdivided into 11 sedimentary levels, including six cycles of bioclastic lime-mud, reddish in colour, overlain by a calcite-cemented biostrome of light grey to beige colour, the latter differing in composition between the upper and lower parts. Additional information correlating the stratigraphic log is shown in Figure 2.2 with conodont taxonomy, local maximum horizons (LMHs) and unitary associations (UAZs) is given in Supplementary Figure S2.1.

2.2 Jebel Aweri

The Jebel Aweri reef block (22°21'24.85"N, 59°45'19.32"E) is located within the Batain Plain (Figure 2.1A, 2.3). Situated in the eastern part of Oman and southeast of the town of Sur, sediments of the Batain Plain extend about 40 km west-east and 130 km northeast-southeast where gravel deposits cover an extensive part. Earlier work described the geology of the Batain Plain as imbricated allochthonous units, with folded and faulted Permian to Late Cretaceous marine sediments and volcanic rocks belonging to the Hawasina nappes (Roger et al., 1991; Béchennec, 1992; Wyns et al., 1992; Leu, 2021). Later, a 'Batain Group' was defined (Immenhauser et al., 1998) with the description of four new formations (Sal, Guwayza, Wahrah and Fayah) and four units (Qarari, Aseelah, Ad Daffah and Ruwaydah) consisting of Permian to uppermost Maastrichtian sedimentary and magmatic rocks (Peters et al., 2001; Hauser et al., 2002). The Jebel Aweri exotic block is part of the Ad Daffah Unit within the Sal Formation (Triassic), and an outcrop gap subdivides the build-up block into two parts, a 22 m thick lower block and 8 m thick upper block. This Early Triassic reef succession consists mainly of microbially (dendrolitic stromatolite), cemented clasts and shelly biostromes. An early pervasive cementation of radiaxal, fibrous and botryoidal calcite largely makes up the block. Additional information correlating the stratigraphic log is shown in Figure 2.3 with conodont taxonomy, local maximum horizons (LMHs) and unitary associations (UAZs) is given in Supplementary Figure S2.2.

3. Material and Methods

3.1 Sample selection and evaluation methods

Conodonts were sampled from the collection of the Palaeontological Institute and Museum of the University of Zurich; the collection having been previously sampled in the field

by ML and HB (Tables 2.1, 2.2). About 3 to 4 kg of bulk sediment were collected per layer from Wadi Musjah, and 8 to 10 kg per layer from Jebel Awari. Crushed rock samples were treated in acetic acid (10 %), sieved and screen washed (0.5 mm, 1 mm, 2 mm) for subsequent picking of conodonts using a binocular microscope. Taxonomic identification is based on references of Early Triassic species (e.g., Orchard, 2005, 2007; Maekawa et al., 2018; Leu, 2021). Segminate (blade-like) and segmiplanate (platform-like) P_1 elements (family Gondolellidea [Lindström, 1970]) were preferred for more accurate taxonomic identifications, since they show relatively high evolutionary rates in morphological diversity and are morphologically less heterogeneous on the species level compared to other elements. Exceptions in using platform elements or blade-like for our investigation include more angulate-shaped P_1 specimens belonging to the family Ellisonidae (Clark, 1972) from Wadi Musjah and three specimens from Jebel Aweri (JA-18C, 19C, 1C), where coniform/ramiform dental elements were used (Table S2.1). All specimens were classified according to their Conodont Alteration Index (CAI) to estimate their degree of preservation (Epstein et al., 1977). This scale was elaborated to indicate the extent of textural and compositional alteration in conodont bioapatites, and it correlates with burial temperatures of the specific conodonts. Because of the progressive and irreversible nature of the colours produced during burial heating, the CAI scale is often used as a preliminary indicator of preservation for conodonts (Wheeley et al., 2012). Given the good preservation of the marine blocks sampled in this study, all selected elements for oxygen isotope measurements have a CAI of 1 (the lowest possible, diagenetic temperatures estimated at <50 to 80 ºC).

A large number of specimens could be recovered from Wadi Musjah (Figure 2.2), allowing both *in-situ* and bulk sampling analytical techniques to be used. In contrast, while a higher resolution was sampled from Jebel Aweri (Figure 2.3), only 1 to 3 specimens per layer could be recovered, limiting the analyses to SIMS. The relative age for each geological section used is based on the Unitary Association method (UAM) of biochronology applied to these sections by Leu (2021) (Figures S2.1, S2.2). The UAM uses a deterministic mathematical model that aims for a set of compatible species for an age estimate (Guex and Davaud, 1984). This allowed an optimal temporal correlation between Wadi Musjah, deposited under very low rates of sedimentation, and Jebel Aweri, which due to its high sedimentation rates has the best resolution for the SSB of the sections analysed. A complete list of samples analysed in this study is given in the Supplementary Table S2.1.

Table 2.1. Conodont $\delta^{18}O$ values analysed by HTR (TC/EA) (gray shaded background) and SIMS (no shading) from Wadi Musjah. For HTR analysis, the *n* refers to the number of silver capsules analysed for each sample. For SIMS analysis, the *n* refers to the number of sample spots per conodont. All specimens have a Conodont Alteration Index of 1. Palaeotemperatures are based on the equation of Lécuyer et al. (2013) [T (°C) = 117.4 - 4.5 x ($\delta^{18}O_{PO4}$ - $\delta^{18}O_{w}$)], using a $\delta^{18}O_{w}$ of -1.7 ‰.

Sample ID	Taxon	$\delta^{18}O_{PO4}$ (HTR) (VSMOW)	$\delta^{18}O_{PO4}$ Std dev.	*n*	$\delta^{18}O$ (SIMS) (VSMOW)	$\delta^{18}O$ Std dev.	*n*	Temperature (°C)
WMJ-7C 1	?*Hadrodontina* sp.	17.0	0.2	3				33.1
WMJ-7C 2					15.5	0.2	4	39.8
WMJ-7C 3					15.6	0.4	4	39.3
WMJ-7C 4					16.0	0.2	4	37.7
WMJ-11C 1		17.0	0.1	3				33.2
WMJ-11C 2					15.8	0.3	3	38.5
WMJ-11C 3					16.7		1	34.5
WMJ-11C 4					16.7	0.1	2	34.8
WMJ-6C 1		16.9	0.3	4				33.9
WMJ-6C 2					16.5	0.2	4	35.3
WMJ-6C 3					17.0	0.2	4	33.0
WMJ-6C 4					16.6	0.5	4	34.9
WMJ-6C 5					16.3	0.3	4	36.6
WMJ-14C 1		16.8	0.2	3				34.1
WMJ-14C 2					16.5	0.3	4	35.5
WMJ-1C 1		16.6	0.2	3				35.0
WMJ-1C 2					15.8	0.6	4	38.5
WMJ-1C 3					15.5	0.1	4	40.2
WMJ-2C 1		17.4	0.0	2				31.5
WMJ-2C 2					16.3	0.9	2	36.2
WMJ-2C 3					16.3	0.3	4	36.4
WMJ-2C 4	*Scythogondolella* ex gr. *milleri*	16.9	0.2	3				33.7
WMJ-2C 5					17.3	0.2	3	32.0
WMJ-2C 6					16.7	0.1	3	34.7
WMJ-2C 7					16.9	0.1	4	33.6
WMJ-15C 1	*Borinella* sp.	18.5	0.1	3				26.7
WMJ-15C 2					18.5	0.4	2	26.6
WMJ-15C 3					18.5	0.4	4	26.6
WMJ-15C 4					18.5	0.4	4	26.3
WMJ-16C 1	*Borinella* sp.	18.6	0.3	3				26.1
WMJ-16C 2					18.3	0.2	4	27.5
WMJ-16C 3					18.1	0.3	4	28.2
WMJ-16C 4					18.3	0.1	4	27.3
WMJ-16C 5					18.6	0.4	4	26.0
WMJ-18C 1		18.8	0.0	3				25.2
WMJ-18C 2					19.0	0.3	4	24.2
WMJ-18C 3					19.4	0.3	4	22.6
WMJ-18C 4	*Novispatodhus* sp.	18.5	0.2	3				26.7
WMJ-3C 1		18.4	0.3	3				27.1
WMJ-3C 2	*Borinella* sp.				19.0	0.3	4	24.4

Table 2.2. Conodont $\delta^{18}O$ values analysed by SIMS from Jebel Aweri. Results within the UAZ–3 are marked (gray-shaded). The *n* refers to the number of sample spots per conodont. Palaeotemperatures are based on the equation of Lécuyer et al. (2013) [T (°C) = 117.4 - 4.5 x ($\delta^{18}O_{PO4}$ - $\delta^{18}O_w$)], using a $\delta^{18}O_w$ of -1.7 ‰.

Sample ID	Taxon	$\delta^{18}O$ (SIMS) (VSMOW)	$\delta^{18}O$ Std dev.	*n*	Temperature (°C)
JA-17C	*Novispathodus pindingshanensis*	17.8	0.2	4	29.5
JA-18C		17.2		1	32.4
JA-19C		17.1	0.3	4	33.0
JA-1C		16.3	0.3	3	36.6
JA-21C		16.7	0.3	6	34.7
JA-22C		17.5	0.5	2	31.2
JA-11C		17.6		1	30.5
JA-24C		16.8	0.3	2	34.4
JA-25C		17.0		1	33.3
JA-26C		17.4	0.2	7	31.4
JA-27C		16.8	0.3	3	34.0
JA-2C		17.6	0.2	2	30.4
JA-28C		17.9	0.2	8	29.0
JA-29C		17.9	0.4	4	29.3
JA-13C		17.5	0.2	4	31.1
JA-3C	*Novispathodus* sp.	18.7	0.6	6	25.8
JA-30C	*Novispathodus* nov. sp.	18.0	0.4	4	28.9
JA-36C	*Novispathodus* sp.	18.9	0.4	4	24.7
JA-31C		19.1		1	24.0
JA-15C		18.6	0.1	4	26.0
JA-33C		19.6	0.2	4	21.8
JA-14C		18.5	0.2	4	26.4
JA-35C		18.7	0.4	4	25.7
JA-7C		19.0	0.1	4	24.1

3.2 Methods for stable oxygen isotope analyses

The methods used in this chapter to the HTR and SIMS measurements are the same described in the previous chapter (section 3.2.3). Only specific methods details and standards related to the conodonts investigated to this chapter are reported below. Additionally, the $\delta^{18}O$ values were compared to $\delta^{18}O$ of conodonts and $\delta^{18}O$ and $\delta^{13}C$ values of carbonates, from previous contributions, including: $\delta^{13}C$ from Wadi Musjah, Jebel Aweri (Leu, 2021); $\delta^{18}O$ and $\delta^{13}C$ from the additional Omani sections of Radio Tower, Wadi Bani Khalid (Chen et al., 2019, 2021); $\delta^{18}O$ and $\delta^{13}C$ from the South China sections Zuodeng, Jiarong, Bianyang and Jinya (Sun et al., 2012); $\delta^{18}O$ from the Pakistani section Nammal Gorge (Romano et al., 2013; Goudemand et al., 2019).

3.2.1 Bulk sampling and High-Temperature Reduction analysis (HTR)

The accepted error (1σ) for this study is of ±0.3 ‰ (standard deviation, 1SD, 95% confidence interval), representing a 1 °C temperature variation if the oxygen isotope values are converted for thermometry (Lécuyer et al., 2013). Measurements were corrected to the international Ag_3PO_4 phosphate standards (USGS80: 12.5 ‰, USGS81: 34.7 ‰) that had better than ±0.3‰ (1σ) standard deviations during measurements. The NIST SRM 120c phosphorite reference material had an average value of 21.5 ±0.2‰ ($n = 12$).

3.2.2 *In-situ* analysis by Secondary Ion Mass Spectrometry (SIMS)

Longitudinal sections of the lower part of the conodont crown (oriented to expose the basal view) were mounted into epoxy resins and the measurements were focused on the hyaline crown. In general, conodonts had a residual relief of ±2 µm after polishing (Supplementary File S2.1). Oxygen isotope measurements were made in three different sessions (February 2020, July 2020, and February 2021). A Durango apatite crystal and an in-house conodont standard (TM-SM) were used to normalise the $\delta^{18}O$ values. The standards were measured 1 to 6 times before, in the middle and at the end of each analytical cycle with about 50 sample spots analysed per cycle. The standard deviation was ±0.3 ‰ (1σ) for the Durango and ±0.2 to ±0.4 ‰ for the TM-SM (File S2). The Durango apatite $\delta^{18}O$ value was determined by laser fluorination to 9.0 ±0.1 ‰ ($n = 4$) (Vennemann et al., 2002), while the $\delta^{18}O$ value for the conodont standard (17.1 ‰) is based in HTR (TC/EA) measurements ($n = 7$, about 400 specimens in total) and SIMS analyses ($n = 13$) (Chapter I; File S2.2).

3.2.3 Clumped isotope measurements in brachiopods

Fossil brachiopod samples recovered from two beds (1 per locality) in the studied successions were analysed for their clumped isotope (Δ_{47}) compositions to estimate the temperature during carbonate precipitation, subsequently allowing for an estimate of the $\delta^{18}O$ value of the carbonate precursor fluid (seawater).

The carbonate clumped isotope technique for estimating temperature is based on the temperature-dependent bonding of the heavy isotopes (^{13}C and ^{18}O) in the carbonate mineral lattice (see Eiler, 2011 for a review). As this "clumping" of heavy isotopes is thermodynamically controlled and relates to temperature of crystallization but is independent of the oxygen isotope composition of the fluid, the temperature at which carbonate precipitation occurred can be determined (Eiler and Schauble, 2004; Ghosh, 2006, Stolper and Eiler, 2015). This can then be used to calculate the oxygen isotope composition of the precursor fluid using calcite-water

fractionation factors and carbonate $\delta^{18}O$ value (e.g., Epstein et al., 1953; Kim and O'Neill, 1997; Brand et al., 2013).

Material for clumped isotope analysis was extracted from texturally well-preserved fossil brachiopod shells along visible growth lines using a scalpel. In addition, samples were analysed from micritic carbonate of the host rocks in order to obtain the range of temperatures recorded in both the fossil brachiopods and host carbonate rock, as well as to assess the reliability of the brachiopod clumped isotope temperatures. Between 20 and 30 mg of shell material was extracted from each brachiopod sample. From each set of extracted material, about four replicates each (4000–4500 µg) were weighed into 2 ml vials for analyses. Clumped isotope measurements were conducted at the University of Lausanne using a NuCarb sample preparation device coupled to a Nu Perspective gas source mass spectrometer.

The protocol for the clumped isotope measurements at the University of Lausanne is similar to that used for conventional stable isotope measurements of carbonates. In a vacuum-based system the CO_2 produced at 70 ºC by automated injection of 110 µl of H_3PO_4 with a specific gravity of 1.95. Then, the gas is extracted via a water trap held at -80 ºC and cryofocussed with liquid nitrogen and two cold fingers into the inlet of the mass spectrometer. The gas is also passed over a PoraPakTM Q adsorption trap held at -30 ºC and degassed at temperatures of 150 ºC between sample extractions. Analyses take about 1.5 hrs/sample for the clumped isotope measurements. These analyses have a routine precision better than 0.02 and 0.04 ‰ for $\delta^{13}C$ and $\delta^{18}O$ values (1 SD), respectively, for our in-house Carrara Marble standard (CM2), as well as NBS-19 and -18 used for normalisation. Δ_{47} clumped isotope measurements of 300 to 800 µg sized samples have routine SE's of 0.007 to 0.012 ‰ and within-run external standard deviations for CM2, ETH-1, and ETH-3 of better than 0.015 ‰ ($n = 9$), or better than 0.020 for ETH-2 to -4 ($n = 3$), while for large samples of about 4 mg, the SD's are better than 0.008 ‰. A δ^{47} - Δ_{47} linearity correction as well as background or pressure correction has not been applied and the final values are normalised relative to the ETH-1, -2, and -3 standards analysed within each sequence (Bernasconi et al., 2021). Data reduction was manually carried out and final Δ_{47} values (Δ_{47} CDES) were calculated using the slope and intercept of the Δ_{47} values of ETH-1, ETH-2 and ETH-3 (Bernasconi et al., 2018) projected to 90 ºC by applying an acid fractionation correction of 0.092 ‰. Temperatures (T) were subsequently calculated using the Δ_{47} – T calibration of Bonifacie et al. (2017) as it is valid for a wide range of temperatures and chemical compositions of carbonates (-1 ºC to 300 ºC). Water oxygen isotope compositions were calculated by inserting the Δ_{47}-based temperatures and measured carbonate ^{18}O compositions into commonly used oxygen isotope thermometry equations (e.g., Kim and O'Neil, 1997;

Coplen, 2007).

3.2.4 Palaeotemperature equations

The $\delta^{18}O_{PO4}$ value of bioapatite is a well-known environmental proxy (e.g., Vennemann et al., 2001; Kohn and Cerling, 2002; Lécuyer, 2004; Zazzo et al., 2004a, b; Kocsis, 2011). Longinelli and Nuti (1973a, b) recognised that the $\delta^{18}O_{PO4}$ values of several ectothermic fish are related to two environmental parameters: water temperature (T) and the $\delta^{18}O$ value of the water ($\delta^{18}O_w$). Based on these studies, an equation that empirically represents the oxygen isotope fractionation between biogenic phosphate and water was calculated, which was later revised (Kolodny et al., 1983; Pucéat et al., 2010; Lécuyer et al., 2013). This equation or revised versions thereof are used as a palaeothermometer. It has been shown that different equations yield different values in the converted palaeotemperatures, and the variation is up to 8 ºC. We calculated our palaeotemperatures using the latest equation of Lécuyer et al. (2013) [T (ºC) =117.4 - 4.5 × ($\delta^{18}O_{PO4}$ - $\delta^{18}O_w$)]. A value for the seawater of -1.7 ‰ was used, supported by the clumped isotopes measurements on contemporaneous brachiopods sampled from the same sections (see section *4.3* below).

4. Results

The $\delta^{18}O$ values of 64 bioapatites have a range from 15.5 ‰ to 19.6 ‰ (Tables 2.1, 2.2, Figures 2.4, 2.5). Conodonts investigated by HTR ($n = 12$) have a ±2.2 ‰ variation and with better than ±0.3‰ (1σ) standard deviations during measurements. The range in $\delta^{18}O$ values measured for individual conodonts by SIMS ($n = 52$) is about 4.6 ‰ and most of the results were within 1σ ($n = 33$). Raw data and a statistical evaluation are given in the Supplementary File S2.2 and Table S2.2, respectively.

4.1 Wadi Musjah (HTR, SIMS)

The $\delta^{18}O_{PO4}$ values measured by HTR ($n = 12$) have a range from 16.6 ‰ to 18.8 ‰ (Table 2.1), which is within the range of $\delta^{18}O$ values for the SIMS measurements ($n = 28$) from analogous specimens of 15.5 ‰ to 19.4 ‰ (Figures 2.4, 2.5A). The analysed layers had overlapping $\delta^{18}O_{PO4}$ and $\delta^{18}O$ values, except for the most basal level (WMJ-7C, Table 2.1, Figure 2.4). The mean $\delta^{18}O$ values differ between samples before and after the SSB for both techniques. Middle to late Smithian samples (below UAZ-3, Figures 2.4, 2.5A) have an average value of 16.9 ±0.2 ‰ ($n = 7$) measured by HTR and of 16.3 ±0.5 ‰ ($n = 18$) by SIMS. In contrast, late Smithian to early Spathian specimens (UAZ-3 upwards) have mean values of 18.5 ±0.2 ‰ ($n =$

5; HTR) and 18.6 ±0.4 ‰ ($n = 10$, SIMS). Statistical tests (Student's *t*-test, One-way ANOVA) to compare $\delta^{18}O$ values measured by HTR *vs* SIMS (Table S2.2) and late Smithian to early Spathian results were well correlated between both techniques (*t* test: t(13) = 0.3216, p > 0.75, Table S2.2) (Figure 2.4). However, middle to late Smithian samples are statistically different (*t* test: t(23) = 2.878, p < 0.00084). Most of this dataset is represented by ramiform elements of ellisonids (Figure 2.4, Table S2.1). Student *t* test using only the late Smithian layer with platform (P_1) elements available for both techniques (Table 2.1: *Sc.* ex gr. *milleri* WMJ-2C 4–7 samples) gives no significant difference between values (*t* test: t(4) = 0.3288, p > 0.758, Table S2.2). More details about how the selection of platform or ramiform elements can influence the $\delta^{18}O$ values are explained below (5.1 section). Finally, *Sc.* ex gr. *milleri* specimens from Wadi Musjah have average $\delta^{18}O_{PO4}$ values of 16.9 ±0.2 ‰ ($n = 3$) and 17.0 ±0.2 ‰ by HTR and SIMS respectively. These values overlapped with the $\delta^{18}O$ of the conodont in-house standard used for this study (TM-SM: 17.1 ‰), that is from the same geochronological range (*Anasibirites* Zone, late Smithian) but from Timor (File S2.2).
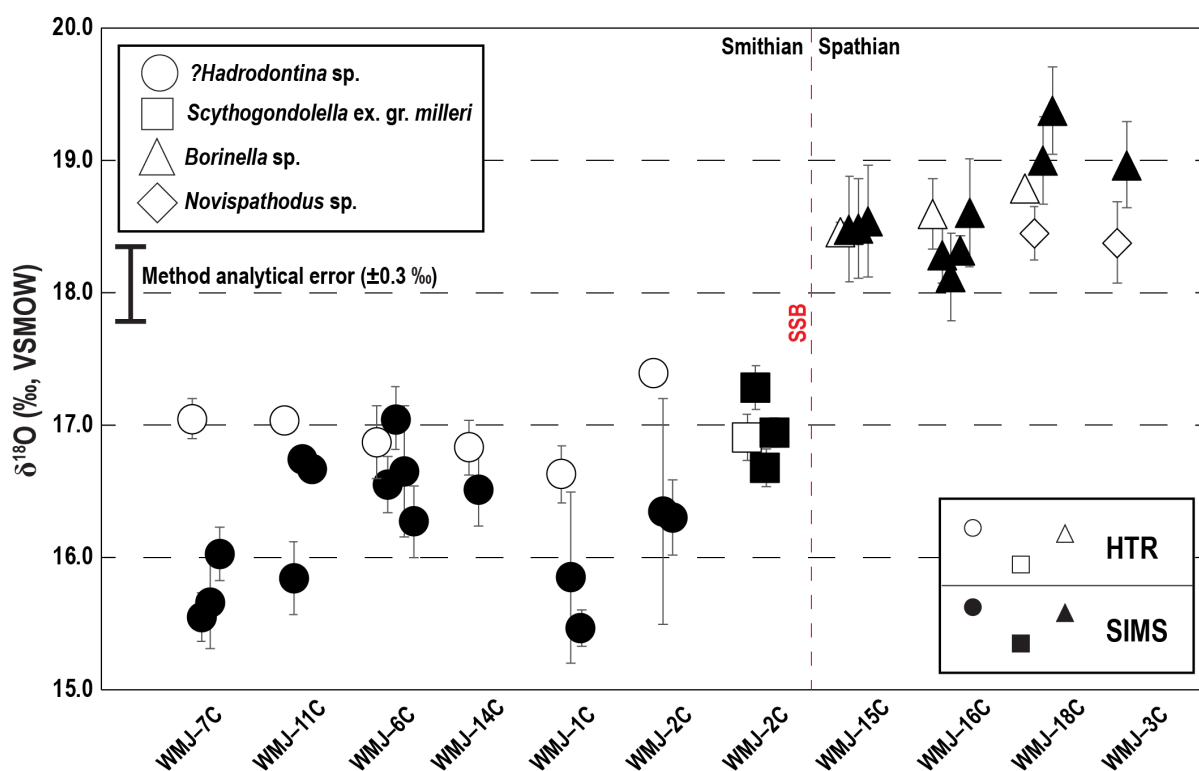
Figure 2.4. Comparison between the $\delta^{18}O$ values from Wadi Musjah in stratigraphic order from left to right across the SSB, measured in different taxa (upper left) by different methods: silver phosphate analysed by High-Temperature Reduction (HTR: white) and Secondary Ion Mass Spectrometry (SIMS: black). Note the about 2 ‰ increase of $\delta^{18}O$ values across the SSB and that ellisonid (*?Hadrodontina* sp.) SIMS results are slightly lower than analogous specimens analysed by HTR.
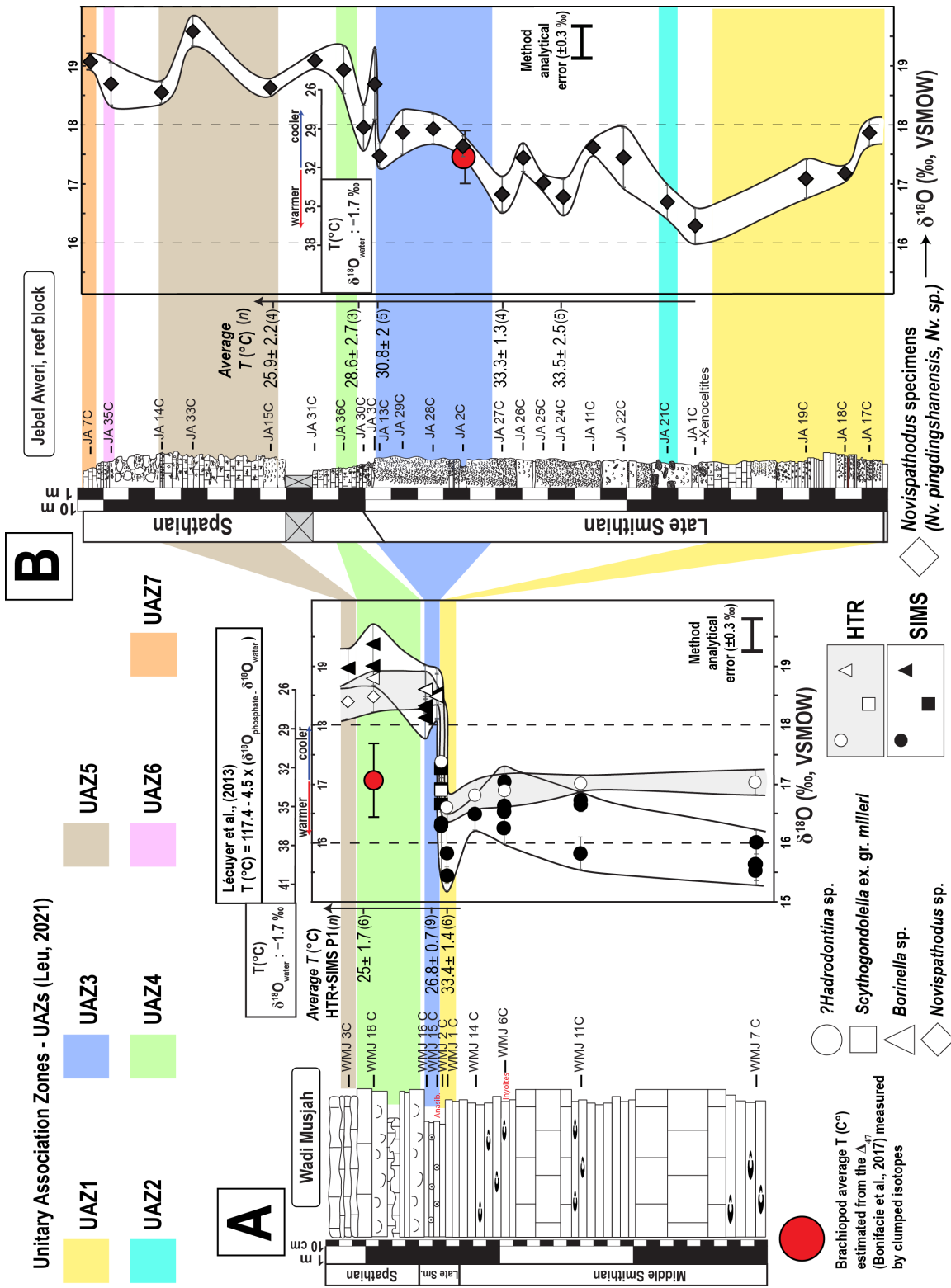
Figure 2.5. Compilation of the unitary association zones (UAZs – upper left) (Leu, 2021) and oxygen isotope values measured from (**A**) Wadi Musjah and (**B**) Jebel Aweri. Paleotemperature bars from $\delta^{18}O$, red circles, Table 2.3) are based on the equation of Lécuyer et al., (2013) [T (°C) = 117.4 - 4.5 x ($\delta^{18}O^{PO4}$ - $\delta^{18}O_w$)]. Brachiopod average palaeotemperatures and plotted error (Δ_{47}, red circles, Table 2.3) were estimated using the equation of Bonifacie et al. (2017). At the left of each oxygen isotope plots, the average temperatures of some intervals of the SSB are given, starting from the Smithian thermal maximum. For Wadi Musjah the averages are from HTR $\delta^{18}O_{PO4}$ and P_1-elements SIMS $\delta^{18}O$ values. The higher sedimentation rate of Jebel Aweri supports a much more gradual cooling along the SSB.

4.2 Jebel Aweri (SIMS)

The $\delta^{18}O$ values from specimens analysed by SIMS ($n = 24$) have a range between 16.3 ‰ and 19.6 ‰ (Table 2.2, Figure 2.5B). The $\delta^{18}O$ averages are also different between samples of below and above the SSB, but the values have an oscillating pattern (Figure 2.5B) relative to their stratigraphic position. Isotopic excursions are noted within the UAZs 1 to 3 below the SSB, and these are different from the uniform change towards more positive $\delta^{18}O$ values measured for the Wadi Musjah specimens (Figure 2.5A). The $\delta^{18}O$ average of *Novispathodus pingdingshanensis* specimens have a more negative range from the UAZ-1 up to the JA-27C layer at the base of UAZ-3 (17.1 ±0.5 ‰, $n = 11$). From the UAZ-3, the $\delta^{18}O$ values gradually change to more positive values. The average $\delta^{18}O$ within this UAZ is in between the mean $\delta^{18}O$ values of samples below and above this interval (17.7 ±0.2 ‰, $n = 4$). From the first layer above the UAZ-3 (i.e., above the SSB) upwards, the average $\delta^{18}O$ is higher with a mean value of 18.8 ±0.4 ‰ ($n = 9$). Statistical tests (One-way ANOVA, Tukey's pairwise, Kruskal-Wallis) using these three datasets discussed above were done and results have confirmed that their average isotopic compositions are significantly different (ANOVA: $F = 39.90$, $p < 0.01$, Table S2.2).

The oxygen isotopic compositions were compared to $\delta^{13}C_{carbonate}$ values measured for Wadi Musjah and Jebel Aweri (Leu, 2021) and to the $\delta^{18}O_{PO4}$ and $\delta^{13}C_{carbonate}$ values measured for the additional Omani sites of Radio Tower and Wadi Bani Khalid (Chen et al., 2019, 2021) (Figure S2.3).

4.3 Brachiopods clumped isotopes

Δ_{47}-derived temperatures for brachiopods and micrites are clearly different (Table 2.3), with micritic carbonate samples preferentially yielding higher temperatures, suggesting that the analysed brachiopods preserve near-primary palaeotemperature information (complete information in Table S2.3). Temperature estimates for brachiopod samples from Jebel Aweri have a range between 28 °C and 35 °C (mean: 31 ±2 °C, 95% Confidence interval - CI) and for bulk micrite, between 40 °C and 59 °C (mean: 52 ±10 °C, 95% CI). In Wadi Musjah samples, $\Delta47$ temperatures are between 27 °C and 36 °C (mean: 33 ±3 °C, 95% CI) in brachiopods and between 52 °C and 83 °C (mean: 68 ±10 °C, 95% CI) in micrite. These Δ_{47} temperature estimates for brachiopods equate to calculated mean $\delta^{18}O_w$ values of -1.6 ±0.7 ‰ (range: -0.65 ‰ to -3.22 ‰) for Jebel Aweri and a mean value of -1.9 ±1 ‰ for Wadi Musjah (range: -0.22 ‰ to -3.12 ‰) using the calcite-water oxygen isotope fractionation relationship proposed by Coplen (2007). In contrast, much higher $\delta^{18}O_w$ values are obtained using the equation of Kim and O'Neil (mean values of 0.2 ±0.7 ‰ for Jebel Aweri and -0.1 ±1 ‰ for Wadi Musjah). The

$\delta^{18}O_w$ values calculated based on Coplen (2007) are used as these are more compatible with assumed values for open ocean waters in an ice-free world. Consequently, from both localities, a mean $\delta^{18}O_w$ value of -1.7 ±0.8 ‰ can be estimated for Smithian–Spathian seawater and is subsequently used to calculate temperatures from $\delta^{18}O$ measurements in bioapatites.

Table 2.3. Brachiopods $\delta^{18}O$ and $\delta^{13}C$ values and clumped isotopes palaeotemperatures based on the Δ_{47} (Bonifacie et al., 2017). The complete version is given as Supplementary Table S2.3. CI = Confidence interval; ETF = Empirical transfer function.

Sample ID	Locality	Texture	$\delta^{13}C$ VPDB	$\delta^{18}O$ VPDB Calcite	$\delta^{18}O$ VSMOW Calcite	Final Δ_{47-90} ETF-Cc	Δ_{47} T (°C)	Avg. T (°C)	$\delta^{18}O_w$ Coplen (2007)	Avg.	95% CI
C2 BM	Jebel Aweri	Micrite	4.24	-4.51	26.26	0.556	*40*		-1.03		
C2 C	Jebel Aweri	Micrite	5.70	-3.18	27.63	0.511	*58*	52	3.33	2.0	2.4
C2 M	Jebel Aweri	Micrite	7.27	-3.01	27.80	0.509	*59*		3.63		
C2	Jebel Aweri	Transcluscent shell calcite	5.71	-2.71	28.12	0.593	*28*		-1.52		
C2 R1	Jebel Aweri	Transcluscent shell calcite	5.46	-3.84	26.95	0.592	*28*		-2.61		
C2 R2	Jebel Aweri	Transcluscent shell calcite	4.00	-2.74	28.09	0.586	*30*		-1.11		
C2 R3	Jebel Aweri	Transcluscent shell calcite	7.36	-2.83	27.99	0.583	*31*	31	-1.07	-1.6	0.7
C2 R4	Jebel Aweri	Transcluscent shell calcite	3.69	-5.57	25.16	0.574	*34*		-3.22		
C2 R5	Jebel Aweri	Transcluscent shell calcite	5.66	-3.17	27.64	0.574	*34*		-0.80		
C2 R6	Jebel Aweri	Transcluscent shell calcite	5.69	-3.27	27.54	0.570	*35*		-0.65		
W18 M1	Wadi Musjah	Micrite	3.45	-3.18	27.63	0.525	*52*		2.40		
W18 M2	Wadi Musjah	Micrite	3.54	-4.97	25.79	0.459	*83*		5.23		
W18 M2	Wadi Musjah	Micrite	3.54	-5.00	25.76	0.510	*59*	68	1.57	3.4	1.1
W18X B	Wadi Musjah	Micrite	6.34	-4.40	26.37	0.481	*72*		4.17		
W18 PV	Wadi Musjah	Micrite	5.89	-5.72	25.01	0.472	*76*		3.48		
W18	Wadi Musjah	Transcluscent shell calcite	3.25	-3.78	27.01	0.593	*27*		-2.63		
W18 R1	Wadi Musjah	Transcluscent shell calcite	4.17	-4.30	26.47	0.583	*31*		-2.48		
W18 R2	Wadi Musjah	Transcluscent shell calcite	5.65	-5.66	25.08	0.571	*35*	33	-3.12	-1.9	1.0
W18 R3	Wadi Musjah	Transcluscent shell calcite	4.36	-3.68	27.12	0.568	*36*		-0.97		
W18 R4	Wadi Musjah	Transcluscent shell calcite	4.30	-2.95	27.87	0.568	*36*		-0.22		

5. Discussion

5.1 Wadi Musjah δ¹⁸O values (HTR *vs* SIMS) and implications for palaeoclimatic studies

Conodont $\delta^{18}O_{PO4}$ values measured by HTR have a similar average value compared to those of the SIMS technique, but with an expected larger overall variability in $\delta^{18}O$ for the single elements analysed by *in-situ* SIMS (Figures 2.4, 2.5A). Furthermore, $\delta^{18}O$ values from P_1 elements for both methods are similar. In contrast, the middle to late Smithian ramiform elements of ellisonids have lower average $\delta^{18}O$ values for the SIMS measurements compared to whole conodont measurements by HTR (*t* test: $t(19) = 3.5529$, $p < 0.00212$, Table S2.2). No such differences in average or variability of $\delta^{18}O$ values has been noted for the platform elements of the late Smithian from Jebel Aweri (segminate P_1, *Novispathodus pingdingshanensis*, Figure 2.5B, Tables 2.1, 2.2). The $\delta^{18}O$ values of these Jebel Aweri specimens are also similar (*t* test: $t(12) = 0.51353$, $p > 0.61691$, Table S2.2) to the three platform elements (segminiplanate P_1, *Scythogondolella* ex. gr. *milleri*) analysed for the late Smithian of Wadi Musjah (WMJ-2, Figure 2.4). In a detailed study of different conodont tissues from *Scythogondolella* ex. gr. *milleri* of Timor, Chapter I), it was concluded that the $\delta^{18}O_{PO4}$ values of bulk analyses using the HTR and from *in-situ* analyses from the hyaline crown are generally similar, but critically depend on textural features of the particular biogenic tissues analysed. The lower average $\delta^{18}O$ values measured by the SIMS method for ellisonid ramiform elements from Wadi Musjah are likely related to irregular bioapatite textures and resulting poor polishing qualities because of the textural features of the albid crown (a.k.a. 'white matter', Sweet, 1988). This tissue is more cancellate and porous (e.g., Trotter et al., 2007; Zhang et al., 2017), a feature that may affect the sample texture and final topography of the analytical surface exposed to the SIMS measurements, both of which are known sources of analytical artefacts for SIMS analysis (Kita et al., 2009; Shirley et al., 2020; Chapter I). Hence, we have focussed on preparing the samples for SIMS measurements such that only the lower part of the crown is exposed for analyses, once the albid tissue commonly grows within the denticles, located above this basal portion (e.g., Donoghue, 1998). This is a difficult task though, as it has been shown that the microstructure of different type of elements (e.g., ramiform *vs* platform) can be complex and also taxa specific (Donoghue, 2001; Jones et al., 2012; Murdock et al., 2013; Martinez-Pérez et al., 2014, 2016) and that the conodont crown can be composed of a combination of lamellar hyaline tissue with the albid tissue (Donoghue et al., 1998).

The use of ellisonid ramiform elements for *in-situ* oxygen isotope studies have to be done with caution, as their converted $\delta^{18}O$ values may yield higher temperatures than what they

really were, as if for example, this study used only Smithian ramiform elements. While a more detailed microstructural and chemical composition investigation of these conodont elements is necessary to fully address their morphological aspects and relevance for a further discussion on changes in the oxygen isotope compositions, several important points to be noted for potential changes across the SSB remain valid irrespective of the inclusion or exclusion of the data from ellisonid ramiform elements (Figures 2.4, 2.5):

1. The δ^{18}O values of conodonts from the middle to late Smithian are relatively low compared to those of the early to middle Spathian for both profiles of Wadi Musjah and Jebel Aweri, irrespective of the method used for the analyses.

2. During the middle to late Smithian, there is a general trend towards higher δ^{18}O values in both profiles, although the higher resolution profile of Jebel Aweri suggests cyclic changes in values with approach to the SSB.

3. The early to middle Spathian is characterised by higher δ^{18}O values in both profiles of Wadi Musjah and Jebel Aweri, but where again the higher resolution profile in Jebel Aweri suggests a more gradual, potentially cyclic change towards higher values.

5.2 Palaeotemperature estimates of conodont species and brachiopods

Conodonts are considered to be nektonic and to have lived in different water depths, as a reflection of their ecological niche (e.g., Trotter et al., 2008; 2015; Joachimski et al., 2012; Goudemand et al., 2019). A classification for the different conodont species was recently proposed, where ellisonids (e.g., *Platyvillosus*, *Pachycladina*, *Parachirognathus*) are acknowledged as a group with a habitat in the uppermost parts of the water column. This means that their δ^{18}O values could represent sea surface temperatures (SST). Neospathodids (e.g., *Neospathodus*, *Novispathodus*) have a δ^{18}O offset of +0.7 ‰ compared to ellisonids, implying that they may have lived in deeper, colder waters (Goudemand et al., 2019). Finally, neogondolellids (e.g., *Neogondolella*, *Scythogondolella*, *Borinella*) have a positive isotopic offset (+1.1 ‰), which in the absence of a vital effect for different conodonts would characterise them as living in even colder parts of the water column. Given this ecological divergence between conodont species, Goudemand et al. (2019) suggested an additional correction in order to relate measured δ^{18}O values to temperature and/or differences in water depths of the habitat.

For two brachiopods, one from the late Smithian of Jebel Aweri and the other from the early Spathian of Wadi Musjah, distinct growth layers were analysed for their clumped isotope compositions (Table 2.3, Figure 2.5). Some layers that texturally appear to have preserved original growth structures, but also other layers clearly recrystallised with coarse-grained

carbonate crystals, gave reproducible palaeotemperatures of 31 ±3 °C (JA-2C) and 33 ±3.7 °C (WMJ-18C) and. Using also the $\delta^{18}O$ values of these layers, these temperatures allow for an estimate of the water $\delta^{18}O$ values, calculated to be about -1.7 ±0.8 ‰. While the exact timing of the recrystallized zones is unclear, given the good agreement with some "primary" growth zones in terms of temperature of the clumping, this would support an early diagenetic recrystallization in the presence still of seawater. A value of the seawater of -1.7 ‰ in conjunction with the measured $\delta^{18}O$ values of conodonts suggests slightly warmer temperatures for the *Novispathodus* sp. specimens (segminate P_1 elements, WMJ-18C, 3C avg: 27 ±0.2 °C, *n* = 2, Figure 2.5A), but slightly lower temperatures for converted $\delta^{18}O$ values of segminiplanate P_1 elements of the conodont *Borinella* sp. (WMJ-18C, 3C avg: 24 ±1 °C, *n* = 4, Figure 2.5A) from Wadi Musjah. The combination of the clumped isotope measurements on the brachiopods and the conodont-based $\delta^{18}O$ values for palaeotemperatures could be interpreted with the brachiopod carbonate O-isotope composition representing early diagenetic conditions in the presence of seawater, but where the diagenesis did not affect the phosphate conodont $\delta^{18}O$ value. For the late Smithian of Jebel Aweri where clumped isotope compositions of brachiopods give temperatures similar to those of the conodonts for a seawater composition of -1.7 ‰, one could argue that both original environmental and early diagenetic temperatures were similar at about 31 ±3 °C (Figure 2.5).

On average, the estimated temperatures measured for the clumped isotope compositions of the micrites within the brachiopod-bearing layers is higher for Wadi Musjah than Jebel Aweri (68 *vs* 52 °C, Table 2.3). Possibly, an early exchange of the Wadi Musjah brachiopod with the diagenetic fluids may have biased the pristine cooler temperature expected for the early Spathian, as it has been experimentally demonstrated to happen on biogenic calcites (e.g., Cisneros-Lazaro et al., 2022). Nonetheless, if the interaction occurs early during diagenesis, one can assume that the environmental conditions may not have been much different from the first carbonate precipitation. Hence, we consider the $\delta^{18}O_w$ value of -1.7 ‰ to be a feasible assumption for the Early Triassic seawater.

Since no platform elements or additional taxa of ellisonids were available for layers where neospathodids or neogondolellids were recovered, the additional habitat-correction proposed by Goudemand et al. (2019) was not applied here. Moreover, in the only layer (WMJ-2C) where ellisonids were found with neogondolellids segmiplanate P_1 elements (*Scythogondolella* sp.), the $\delta^{18}O$ from HTR and SIMS analyses overlapped within the error range (±0.3 ‰) (Figures 2.4, 2.5A). Therefore, the $\delta^{18}O$ data measured from neospathodids and neogondolellids will also be considered as a proxy of SST.

5.3 Jebel Aweri *vs* Wadi Musjah converted $\delta^{18}O$: a gradual climatic cooling

Oxygen isotope values from the Wadi Musjah and Jebel Aweri are similar for the same UAZ's and hence also give similar trends from the middle Smithian to the early Spathian (Figure 2.5). The $\delta^{18}O_{PO4}$ measured from bioapatites can then be related to their temperature of formation (e.g., Longinelli and Nuti, 1973a; Kolodny et al., 1983), given knowledge of the $\delta^{18}O_w$ values. The latter was estimated via the clumped isotope compositions of brachiopods. Through this method, the $\delta^{18}O_w$ can be estimated to be about -1.7 ±0.8 ‰ for both sites, a value within error similar to that assumed for open ocean waters for an ice-free world (-1 ‰, e.g., Fischer et al., 2013; Trotter et al., 2015; Leuzinger et al., 2015; Grossman and Joachimski, 2020). As conodont bioapatites have rarely been analysed from marine sections, the $\delta^{18}O$ values measured from the Omani localities may well represent a pristine record of palaeotemperatures for the Smithian–Spathian climatic transition. The carbonate block from Jebel Aweri is of particular interest due to its high sedimentation rates and hence high temporal resolution for the late Smithian–early Spathian. This is well illustrated by the number of layers from where conodont elements could be recovered per UAZ for this locality (Figure 2.5). For example, close to the SSB (i.e., within the UAZ's 1–3) Wadi Musjah is represented only by 4 samples, while Jebel Aweri provides more than 10 layers over the same period (UAZ's).

During the Smithian (middle to late), sea water temperatures from Wadi Musjah (HTR, SIMS P_1 elements) have a range from 26 to 35 ºC, while in Jebel Aweri they have a range between 25.8 to 36.6 ºC. Towards the Spathian the temperatures clearly decreased, with a range between 22.6 to 27.1 ºC in Wadi Musjah and from 21.8 to 26.4 ºC in Jebel Aweri. The palaeotemperature decrease has concluded within the latest Smithian in both sections (UAZ-3). Although both exotic blocks represent marine mounds, the sedimentary facies suggest a deeper water depositional setting for Wadi Musjah compared to Jebel Aweri (Leu, 2021). The similarity in calculated temperatures for the conodonts measured from these two sites likely suggests that conodonts lived under similar conditions in both localities. Isotopic compositions reported from other studies (Sun et al., 2012; Romano et al., 2013; Goudemand et al., 2019) are also compatible with a positive shift of $\delta^{18}O$ values at the SSB (change of about +2 ‰), interpreted as a large cooling event with temperatures decreasing in the order of about 8 ºC. The high temporal resolution of Jebel Aweri now illustrates that the transition towards cooler conditions was rather gradual and the SIMS analyses on a number of individual conodonts could also support climatic oscillations towards the SSB (Figure 2.5B). While a higher number of analysis per layer are necessary to confirm if these oscillations are indeed correct, it is tempting to speculate that the cooling during this period was not really abrupt. In the late Smithian from the base of the

UAZ-1, sea water temperatures increased by about 7 ºC, reaching a thermal maximum of 36.6 ±1.4 ºC (i.e., Late Smithian Thermal Maximum) between UAZs 1 and 2 (JA-1C, Figure 2.5B). From this layer upwards until the base of UAZ-3, the climate is relatively stable and the average temperature was not yet typical of cold conditions (32.8 ±1.7 ºC, $n = 7$). Progressively, at the base of the UAZ-3 the palaeotemperatures started to decrease and the average value calculated for this zone is 29.9 ±0.9 ºC ($n = 4$). After that, the palaeotemperatures reached the 'cold range' (25.3 ±2 ºC) that prevailed towards the early Spathian (Figure 2.5B).

This is the first time that a high-resolution section of the SSB has its oxygen isotope compositions analysed and it complements the understanding of the biotic crisis at this interval. The gradual SSB climatic cooling shown in Jebel Aweri would also suggest that rapid temperature changes were not the sole trigger for the late Smithian secondary consumer extinction, neither a limiting factor for species diversification (Goudemand et al., 2019). The onset of the biotic crisis precedes the cooling event (Goudemand et al., 2019; Widmann et al., 2020), and here apparently the temperatures decreased further during the latest Smithian (Figure 2.5B). The faunal extinction is likely to be a more complex expression of changes in global partial pressures of atmospheric CO_2 and its feedback mechanisms on the environment and on potentially forcing climatic changes (c.f., Leu, 2021). Other effects like transgressive-regressive cycles, changes in primary productivity and the efficiency of the biological pump should also play a role in the secondary consumers' biotic crisis across the SSB (Romano et al., 2013; Goudemand et al., 2019; Widmann et al., 2020).

5.4 Comparisons of the O-isotope records

To compare our isotopic data with that from contemporaneous sections from China (Sun et al., 2012) and Pakistan (Romano et al., 2013; Goudemand et al., 2019), an interdisciplinary calibration combining chemostratigraphy, lithostratigraphy and the biozonation of conodonts and ammonoids was used (Leu, 2021). A comparison of the data is shown in Figure 2.6. As the following discussion is focused on the chemostratigraphy, information about the biozonation correlations with the UAZs is given in a larger figure in the Supplements (Figure S2.4). In general, all sections show similar trends for their changes in the isotopic compositions but have some differences with regard to both their absolute $\delta^{13}C$ and $\delta^{18}O$ values. High-precision U-Pb ages measured for zircons are available from additional South China sites (Shanggang, Qiakong and Laren: Widmann et al., 2019, 2020; Leu, 2021). While a precise dating at the Omani sections remains challenging due to the absence of ash layers of volcanic origin, the approximate age and duration of the C- and O-isotope excursions have been estimated through

the multidisciplinary intercalibration of Leu (2021). We also extrapolated the age correlation to the comparative South China and Pakistani sites (Figure 2.6).

The CIEs for the Omani and South China sections are similar in trend (Leu, 2021; Figure 2.6), but their amplitudes of the $\delta^{13}C$ excursions also vary between localities, being about 3 ‰ in Zuodeng, about 4 ‰ in Jebel Aweri and about 6 ‰ in all other profiles. The excursions in oxygen isotope compositions of conodonts are also synchronous for the applied UAZ biochronologic constraints (Figure 2.6). From the middle to half of the late Smithian (i.e., up to UAZ-2 of Oman / UAZ-7 South China), $\delta^{18}O$ values from Tethyan coastal sections (15.6 ‰ to 18.2 ‰) have a comparable range to those measured in Oman (16.3 ‰ to 17.8 ‰). Slightly lower values were measured in Pakistan (15.6 ‰ to 17.2 ‰) and higher in Zuodeng and Jinya (South China, 16.9 ‰ to 18.2 ‰). Among the factors that control the $\delta^{18}O$, the relatively small difference in average values between the Omani sections and the additional Tethyan localities is probably linked to distinct freshwater influence and/or evaporative conditions on the shelf-sequences, giving rise to slightly different $\delta^{18}O_w$ values (e.g., Kocsis et al., 2007; Carrillo-Briceno et al., 2019). Calculated temperatures over 35–36 °C are close to the tolerance limit for multicellular animals (38 to 40 °C, Brock, 1985; Rothschild and Mancinelli, 2001; Fischer et al., 2013) , and it is unlikely that conodonts lived under such conditions. Hence, if indeed the $\delta^{18}O$ values have been preserved, the low $\delta^{18}O_{PO4}$ values would indicate the existence of brackish-like conditions (e.g., Kocsis et al., 2007; Fischer et al., 2013; Leuzinger et al., 2015; Carrillo-Briceno et al., 2019). This would suggest that some conodonts analysed from Pakistan (well-preserved, CAI value of 1 - Romano et al., 2013; Goudemand et al., 2019) were not formed under fully marine settings, if their respective calculated palaeotemperatures are over 35 °C (middle to late Smithian, Figure 2.6). In contrast, palaeotemperatures calculated for Zuodeng and Jinya are cooler (29 °C to 34 °C) compared to the general warm range estimated for analogous late Smithian layers from other coastal localities (32 °C to 40 °C), thus supporting these samples as representing close to pristine temperatures. In contrast, the calculated temperatures for South China sites are rather feasible to biological life only if the $\delta^{18}O_w$ value of -1.7 ‰ is used as well as the updated palaeotemperature equation of Lécuyer et al. (2013).
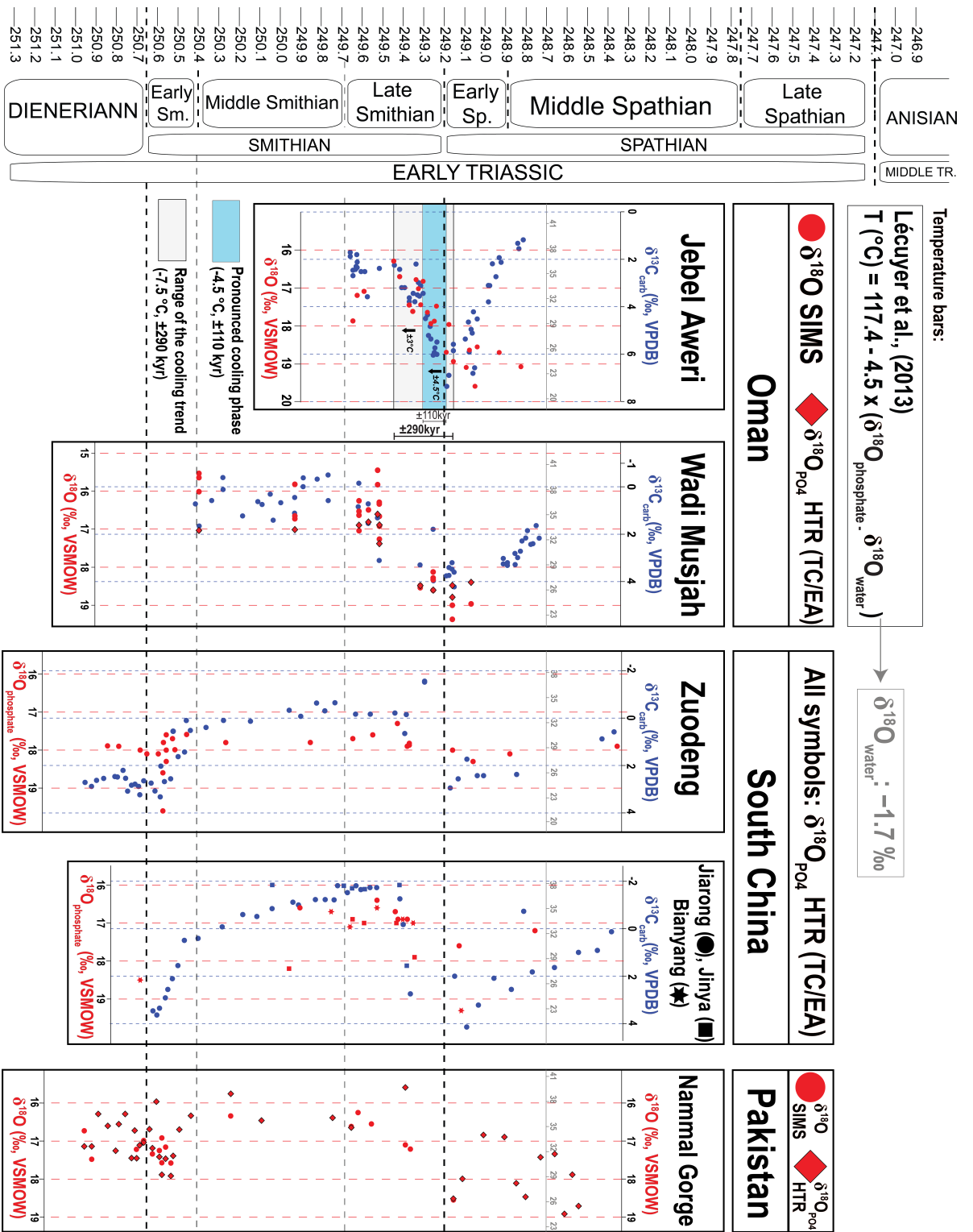
Figure 2.6. At the leftmost column, the intercalibrated U-Pb ages (Widmann et al., 2020; Leu, 2021; Figure S4) are plotted against the δ¹³C$_{carb}$ and δ¹⁸O records (right) for: Jebel Aweri, Wadi Musjah (this study), Zuodeng, Jinya, Bianyang (Sun et al., 2012), and Nammal Gorge (Romano et al., 2013, Goudemand et al., 2019). Timing of Early Triassic is taken from the Bayesian age depth model of Widmann et al. (2020). For the section of Jebel Aweri, the relative duration of the SSB climatic oscillation is marked (shaded gray-blue area). Modified after Leu (2021).

In contrast, as of the early Spathian the $\delta^{18}O$ values are all higher by about 1.7 to 2.0 ‰, which for the same O-isotope compositions of seawater would clearly reflect a global cooling at the SSB. For the Omani, Pakistan and Bianyang (South China) sections the increase of 1.7 to 2.0 ‰ in $\delta^{18}O$ would correspond to a temperature cooling of about 7.5 to 8 °C cooling. Changes are somewhat smaller for Zuodeng, Jinya and Jiarong increase in $\delta^{18}O$ values of 1 to 1.5 ‰, that would still suggest a cooling of about 5 to 6 °C (Figure 2.6). Differences in the $\delta^{18}O$ for Chinese and Pakistani or also Omani sections may well be related to relatively small salinity contrasts between the localities (local, regional freshwater influence or evaporative conditions), linked to the varying depositional palaeoenvironment (coastal *vs* marine).

Through the intercalibration based on the combined UAZ's and bio- as well as chemostratigraphy of the Omani sections and those in the larger Tethyan realm, it is possible to assess the relative timing and also duration of the cooling measured across the SSB (Figures 2.6, 2.7). This is made possible because of the recent U-Pb dating of a sequence of ash beds within the Chinese sections and their synchroneity with respect to the C-isotope stratigraphy and respective UAZ's (Widmann et al., 2020; Leu, 2021). Furthermore, the progression of average temperature changes can now be evaluated in detail across the SSB because of the high-resolution section from Jebel Aweri. From the onset until its conclusion, an approximate duration of ±290 kyr is suggested for the SSB climatic cooling (Figures 2.6, 2.7B, C). This span is similar to estimates based on the CIE of South China (Shaggang: 251 ±143 kyr, Laren: 296 ±161 kyr, Qiakong: 423 ±137 kyr) (Widmann et al., 2020), validating the feasibility of this approach. Sea water temperatures apparently decreased by about 3 °C just after the Late Smithian Thermal Maximum (±130 kyr) (Figures 2.5B, 2.7). In succession, a more intense cooling occurred (by another 4.5 °C over ±110 kyr), and the temperatures reached the cold range that persisted during the early Spathian (max temperatures of about 26 °C Figure 2.7C). Although climatic cycles are noted within Smithian and Spathian layers, more analyses as well as higher isotopic resolutions are necessary to confirm if the oscillating aspect firstly measured here is pristine.

Through the intercalibration based on the combined UAZ's and bio- as well as chemostratigraphy of the Omani sections and those in the larger Tethyan realm, it is possible to assess the relative timing and also duration of the cooling measured across the SSB (Figures 2.6, 2.7). This is made possible because of the recent U-Pb dating of a sequence of ash beds within the Chinese sections and their synchroneity with respect to the C-isotope stratigraphy and respective UAZ's (Widmann et al., 2020; Leu, 2021). Furthermore, the progression of average temperature changes can now be evaluated in detail across the SSB because of the

high-resolution section from Jebel Aweri. From the onset until its conclusion, an approximate duration of ±290 kyr is suggested for the SSB climatic cooling (Figures 2.6, 2.7B, C). This span is similar to estimates based on the CIE of South China (Shaggang: 251 ±143 kyr, Laren: 296 ±161 kyr, Qiakong: 423 ±137 kyr) (Widmann et al., 2020), validating the feasibility of this approach. Sea water temperatures apparently decreased by about 3 °C just after the Late Smithian Thermal Maximum (±130 kyr) (Figures 2.5B, 2.7). In succession, a more intense cooling occurred (by another 4.5 °C over ±110 kyr), and the temperatures reached the cold range that persisted during the early Spathian (max temperatures of about 26 °C Figure 2.7C). Although climatic cycles are noted within Smithian and Spathian layers, more analyses as well as higher isotopic resolutions are necessary to confirm if the oscillating aspect firstly measured here is pristine.

Figure 2.7. A detailed profile of the Smithian–Spathian boundary (SSB) and changes in the δ18O values of conodonts from Jebel Aweri. At the left, the age and timing of the SSB (Widmann et al., 2020) are given. **(A)** Average paleotemperatures across the SSB are based on the equation of Lécuyer et al (2013) [T (°C) = 117.4 - 4.5 x (δ18O$_{PO4}$ - δ18O$_w$)] and δ18O$_w$ value of -1.7 ‰. At the middle **(B)**, the δ18O values are plotted with their individual standard deviations. At the right **(C)**, estimates for the approximate duration of the SSB cooling and its relative intensity are given.

6. Conclusions

Oxygen isotope compositions of 64 conodonts from two distinct Early Triassic marine carbonate sections in Oman were measured using conventional analytical methods as well as an *in-situ* SIMS method. This allowed for a high-resolution sampling of conodont dental elements that can be assigned to Unitary Association Zones corresponding to the Smithian-Spathian boundary (Leu, 2021), also allowing for a detailed comparisons with other Tethyan sections from Oman, Pakistan, and China, where the latter sections have also been well dated through ash beds and U/Pb dating (Widmann et al., 2020). The high-resolution marine sedimentary records of the new Omani profiles, in particular, allow for the following conclusions to be drawn on changes in climate across the SSB:

– After the Smithian thermal maximum, sea water temperatures gradually decreased and at the earliest Spathian palaeotemperatures were about 7 to 8 °C lower than during the late Smithian. The decrease in temperature was more pronounced during the latest Smithian. Similar trends in $\delta^{18}O$ values and hence temperature are noted for other localities during the same period. In parallel with major changes in the carbon budget, this cooling event could have influenced the secondary consumers' extinction.

– Oxygen and carbon isotope excursions from marine Omani localities are similar in overall magnitude compared to other nearshore or coastal Tethyan sections. Smaller differences in the absolute isotopic compositions are a reflection of the varying depositional palaeoenvironments (e.g., salinity) between the localities.

– Using the results from clumped isotope measurements in brachiopods, the value of -1.7 ‰ for the $\delta^{18}O_{water}$ translates to feasible temperatures for biological life for Oman and South China (26 to 37 °C). The Early Triassic recovery was hence less impacted than previously interpreted by the adverse temperature conditions.

– An approximate duration of about 290 kyr is hypothesised for the SSB climatic oscillations that are indicated by the high-resolution SIMS analyses of conodonts. Additional sampling and methods may reveal if the temperature variations can be related to the Milankovitch orbital cycles.

High-resolution sampling of additional layers' representative of the Smithian–Spathian intervals are necessary to further corroborate the above conclusions. It must be remarked that in some cases, only a higher temporal resolution can reveal the full impact of climate change, such as lagged effects caused by temperature changes (e.g., Bartlett et al., 2015). Careful *in-situ* measurements of isotopic compositions may have the potential to provide a sufficiently high resolution and hence allow for a more detailed visualisation of changes in palaeoclimate and/or

palaeoenvironmental conditions.

7. Research Data and Supplementary Material

Research data associated with this article can be found in the Supplementary Material. All suplements were uploaded to a Data Repository (https://doi.org/10.5281/zenodo.7301728). The Supplementary Material table of contents to the current chapter is:

File S2.1 Profilometer images and output files of sample preparation.

File S2.2 Raw oxygen isotope data and normalisation.

Table S2.1 Referred Omani bioapatites and the different techniques used to investigate them.

Table S2.2 Statistical tests of conodont oxygen isotope data.

Table S2.3 Clumped isotopes measurements complete table. Palaeotemperatures are based on the Δ_{47}, Bonifacie et al. (2017). CI = Confidence interval; ETF = Empirical transfer function.

Figure S2.1 Wadi Musjah stratigraphic log, associated conodont taxonomy and biochronology. Modified after Leu (2021).

Figure S2.2 Jebel Aweri stratigraphic log, associated conodont taxonomy and biochronology. Modified after Leu (2021).

Figure S2.3 Carbon and oxygen isotope compositions from Omani sites (Wadi Bani Khalid and Radio Tower isotope values were measured by Chen et al., 2019, 2021). Modified after Leu (2021).

Figure S2.4 Full figure of the multiple proxy intercalibration done using the chemostratigraphy, lithology, biochronology and unitary association zones (UAZs) for Omani, Pakistani and South China sites. Modified after Leu (2021).

"We are going to die, and that makes us the lucky ones. Most people are never going to die because they are never going to be born. The potential people who could have been here in my place but who will in fact never see the light of day outnumber the sand grains of Sahara...

... How dare we whine at our inevitable return to that prior state from which the vast majority have never stirred?"

- Richard Dawkins

CHAPTER III

Brackish settings in the Panthalassa realm during the Early Triassic (Smithian–Spathian) suggested by oxygen isotopes from conodonts

Author contributions:

Zoneibe Luz, conceptualisation, data curation, formal analysis and investigation, methodology, visualisation, original draft writing, review and editing.

Marc Leu, methodology, resources, validation, visualisation, draft review and editing.

Franziska Blattmann, data investigation, validation, draft review and editing.

Hugo Bucher, conceptualisation, funding acquisition, methodology, resources, supervision, draft writing, review and editing.

Torsten Vennemann, conceptualisation, funding acquisition, methodology, resources, supervision, validation, draft review and editing.

Christian Vérard, resources, validation, visualisation, draft review and editing.

Brackish settings in the Panthalassa realm during the Early Triassic (Smithian–Spathian) suggested by oxygen isotopes from conodonts

Zoneibe Luz[a,*], Marc Leu[b], Franziska Blattmann[a], Hugo Bucher[b], Torsten Vennemann[a], Christian Vérard[c]

[a] Institut des Dynamiques de la Surface Terrestre, Université de Lausanne, Rue de la Mouline, 1015 Lausanne, Switzerland

[b] Palaeontological Institute and Museum, University of Zürich, Karl-Schmid-Strasse 4, 8006 Zürich, Switzerland

[c] Section of Earth and Environmental Sciences, University of Geneva, Rue des Maraîchers 13, 1205 Geneva, Switzerland

*Corresponding author: zoneibe.luz@gmail.com (Zoneibe Luz)

Abstract

The Smithian–Spathian boundary represents one of several intra-Triassic recovery cycles and its associated extinction is thought to rival even that of the Permian-Triassic mass extinction, an event that eliminated more than 90 % of all marine organisms. In order to investigate the seawater chemistry on the past environmental changes following this important period of recovery, the stable oxygen isotope compositions ($\delta^{18}O$) of conodonts were analysed from selected sections that represent mid to high palaeolatitudes from the Tethys and Panthalassa oceans. Although separated by a large time-window, some aspects of the modern oceans resemble those of the Triassic, such as the upwelling of western waters in the Panthalassa and Pacific oceans. The values measured from Panthalassa coastal conodonts are about 2 to 3 ‰ lower than values from Tethyan marine conodonts. The reason for the low $\delta^{18}O$ values is continental freshwater runoff and longshore currents descending polar waters depleted in ^{18}O towards lower latitudes. By assuming similar habitats and temperatures for the same conodont species sampled from high palaeolatitudes as their Tethyan counterparts, seawater $\delta^{18}O_w$ values of -4.5 ‰ are calculated, which compares to low-latitude, marine $\delta^{18}O_w$ values of about -1.7 ‰. This gradient of about 2.5 ‰ is similar to that for modern seawater $\delta^{18}O$ values between low- and high- latitudinal surface waters. These findings suggest a strong influence and regional forcing over fully marine geochemical compositions, but also explain Early Triassic nearshore anoxic events that may have been triggered by the continental freshwater runoff.

Keywords: Oxygen isotopes, SIMS, conodonts, Smithian–Spathian, seawater chemistry

1. Introduction

The Earth's seawater chemistry is closely related to climatic and environmental changes resulted from major biotic crises (e.g., Turchyn and DePaolo, 2019). With about 70 % of Earth covered by oceans, marine as well as coastal ecosystems play an essential role in Earth's nutrient cycle and for life (Gordon, 1986; Horne, 1999; Tamburini et al., 2003; Gruber, 2011). Partly driven by circulation patterns (i.e., thermohaline circulation, Gordon, 1986; Wunsch, 2002), marine plankton during active bioproductivity act as effective oceanic carbon sinks of atmospheric CO_2 (IPCC, 2019) and a compromise of their normal, steady-state functioning endangers the stability of the carbon cycle in marine systems. Another example of a natural phenomenon influencing both marine and coastal waters are the upwelling zones, where deep cold waters ascend and boost the primary productivity at the surface as nutrients are introduced to support life also for small to large vertebrates (e.g., Kämpf and Chapman, 2016; Mohan et al., 2018; Narvekar et al., 2021; Barlow et al., 2021). Closer to the terrestrial realm, rivers are also important for a net input of essential nutrients, not only helping to maintain life near estuaries as feeding grounds and nurseries, but also being the most important source for nutrients to the oceans at large, and where the nutrients are derived by terrestrial chemical weathering and continental erosion (e.g., Amazon basin: McClain and Naiman, 2008; Weber et al., 2017; Goulding et al., 2019).

Directly and indirectly, oceans influence and are influenced by unicellular and multicellular organisms and most importantly: they can counterbalance impacts of the current climate change (Beerling, 2008; Arnesen, 2017; Roberts and Mannion, 2019; Buesseler et al., 2020). Hence, it is important to understand the seawater chemistry over geologic time. Both of the phenomena cited above, upwelling and river input, can be estimated by means of stable oxygen isotopes ($\delta^{18}O$) in phosphates, valuable assets for past seawater reconstruction (e.g., Fischer et al., 2013; Joachimski and Lambert, 2015; Goudemand et al., 2019). Bioapatites are known proxies' archives which interact and exchange with the oceanic chemical components *in-vivo*, as well as during fossilization (e.g., Trueman and Tuross, 2002; Kohn, 2008). The $\delta^{18}O$ values measured in bioapatites are environmental proxies of relative sea surface temperatures but also depend on the $\delta^{18}O$ values of water and hence salinity of the marine waters (Luz et al., 1984, Trotter et al., 2008; Sun et al., 2012; Romano et al., 2013; Goudemand et al., 2019; Chapter II).

Along the geological past, the extinction events are of particular interest as these may represent periods of relatively rapid environmental changes, similar to those that can be expected for today (e.g., intervals with relatively rapid changes in CO_2 concentrations; Payne

and Clapham, 2012; Goudemand et al., 2019; Fordham et al., 2020). A better understanding of the past seawater chemistry thus not only complements the knowledge about past biotic crises, but it also allows for an evaluation of the interplay between environmental and temperature changes with time.

This study concentrates on the Early Triassic period (about 252 to 247 Ma., Widmann, 2019), that is the interval which succeeds the greatest extinction event in Earth's history: the Permian–Triassic boundary mass extinction (PTBME). Current thinking is that this crisis was closely related to the consequences of the magmatic activity associated with the Siberian Traps, which may have added significant levels of greenhouse gases into the atmosphere (e.g., MacLeod, 2013). More than 90 % of all marine fauna perished (MacLeod, 2014) and harsh environmental conditions were thought to have persisted for over 5 Ma, delaying the ecological recovery during the Early Triassic (e.g., Joachimski et al., 2012; Sun et al., 2012; Grasby et al., 2016). While the benthic fauna lingered to recover after the PTBME, secondary consumers (e.g., ammonoids, conodonts) had short-term cycles of diversification-extinction periods (Orchard, 2007; Galfetti et al., 2007b, 2008; Brühwiler et al., 2010; Ware et al., 2011; Romano et al., 2013; Hautmann et al., 2015; Jattiot et al., 2018; Leu et al., 2019; Zhang et al., 2019; Goudemand et al., 2019; Widmann et al., 2020). These cycles were likely controlled by equally short-term climatic oscillations with locally variable environmental impacts (e.g., bottom-water anoxia) (Song et al., 2011; Leu et al., 2019; Goudemand et al., 2019; Widmann et al., 2020). However, at the Smithian–Spathian boundary (SSB, 249.29 to 249.11 Ma, Widmann, 2019) the nektonic organisms suffered a major biodiversity loss, commonly thought to be even higher in magnitude compared to that of the PTBME (Orchard, 2007; Brühwiler et al., 2010). Numerous independent proxies (e.g., bioapatites, carbonate rocks, fossilised pollen) support cycles of rapid environmental changes at planetary level (Hermann et al., 2011; Romano et al., 2013; Hochuli et al., 2016; Hammer et al., 2019; Goudemand et al., 2019; Widmann et al., 2020). The reasons behind these intra-Triassic extinctions are still debated, but it has recently been suggested that volcanic and unilateral temperature cycles (warming/cooling) may have alternately been the main drivers for these cycles (Hammer et al., 2019; Goudemand et al., 2019; Widmann et al., 2020). Carbon isotope compositions of organic and inorganic carbon support global increases of atmospheric CO_2 and associated increase in the continental weathering and erosion of silicates as a subsequent mitigation as a cause for this cyclicity (Zhang et al., 2018; Goudemand et al., 2019; Schneebeli-Hermann et al., 2020; Widmann et al., 2020). These processes suggest that eutrophication may have been common in coastal zones due to an increased nutrient input from the continents (Payne and Kump, 2007; Meyer et al., 2016; Goudemand et al., 2019). This is

further corroborated by an abundance of black shales, typical geological indicators of bottom-water anoxia, in many continental sections worldwide over this period (Grasby et al., 2013; Wignall et al., 2016; Zhang et al., 2018; Song et al., 2014, 2019).

During the Early Triassic the eastern part of the Tethys apparently had restricted circulation towards the East of the Pangea continental mass (Figure 3.1), with poor deep water (below 2000 m) regeneration (Arnesen, 2017). Upwelling was possible though in the Panthalassic sea at the western margin of Pangea, in a similar fashion to that of the modern Pacific Ocean at the western margin of North and South America (Figure 3.1) (Martindale et al., 2014; Arnesen, 2017; Grasby et al., 2020; Brookfield et al., 2020). During the onset of the SSB crisis, geochemical proxies (e.g., $\delta^{13}C_{org}$, P and N in sediments) have indicated that the transfer of nutrients to the sea surface was, however, also compromised in the Panthalassa realm (e.g., Grasby et al., 2020).
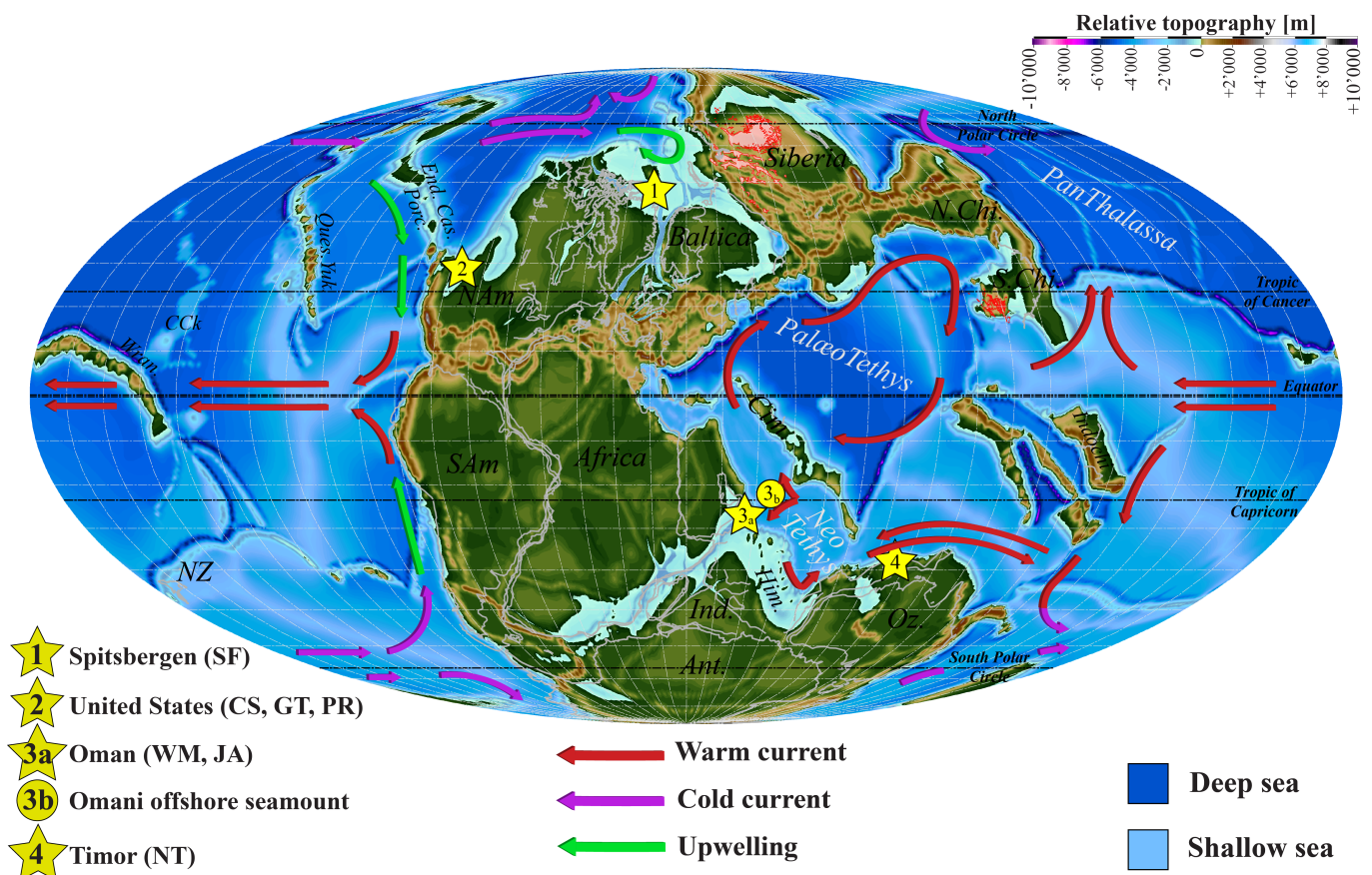
Figure 3.1. A preliminary version of the PANALESIS palaeogeographical map (Vérard et al., 2019) with palaeopositions (symbols) of the sample sites; **(1)** Stensiöfjellet (SF) in Spitsbergen, **(2)** Crittenden Springs (CS), Georgetown (GT) and Palomino Ridge (PR) in United States, **(3)** Wadi Musjah (WM) and Jebel Aweri (JA) in Oman, and **(4)** Noe Tobe in Timor. The stars represent the modern location of the sites, while the circle for Oman **(3b)** is the location of the marine seamount during the Early Triassic. The map corresponds to the preliminary version of PANALESIS (Vérard, 2019), where global plate tectonic maps are converted into palaeo-DEMs (Digital Elevation Models or 3D surface maps) following the method described in Vérard et al. (2015). Palaeocurrents (coloured arrows) are based on Late Permian (Brookfield et al., 2019) and Late Triassic (Martindale et al., 2014) palaeogeographies.

To further constrain the seawater chemistry from the Smithian–Spathian boundary, a number of relatively well-preserved conodont bioapatites (Conodont Alteration Index – CAI – between 1 to 3.5) were analysed for their stable oxygen isotope compositions ($\delta^{18}O$). Conodonts are extinct, eel-like marine vertebrates that are commonly used both as index fossils as well as for their oxygen isotope compositions for the Palaeozoic and early Mesozoic (Luz et al., 1984; Wenzel et al., 2000; Sun et al., 2012; Joachimski et al., 2012; Rigo et al., 2012; Romano et al., 2013; Trotter et al., 2008; 2016a; Chen et al., 2016; Goudemand et al., 2019; Chapter II). The same species of conodonts from distinct palaeolatitudes and locations within the Early Triassic oceans were used. Locations include subtropical sites (United States, Oman, West Timor) and sites from the boreal realm (Svalbard, Spitsbergen) (Figure 3.1). Studies on temperature and/or seawater chemistry proxies (e.g., O-isotope compositions of carbonates, alkenones, long-chained hydrocarbons) are also often hindered by secondary alteration, as well as by possible regional effects (e.g., continental runoff) that may superimpose the primary signal of open ocean marine conditions. However, to overcome possible regional influences, three of the studied sites (two in Oman, one in West Timor) were formed under marine conditions (Figure 3.1). As their rocks were deposited farther from the coast, they should better represent the Early Triassic pristine seawater chemistry. Some of the sites have a low abundance of conodonts only and hence bulk sampling geochemical techniques for O-isotope analyses cannot be used. This required the use of secondary ion mass spectrometry (SIMS), which we calibrated using a more conventional method of bulk sampling and high temperature reduction (HTR) analysis (Mine et al., 2017; Chapter I). In addition, phosphorus (P) concentrations in sediments from Spitsbergen were measured in a parallel contribution (Blattmann et al., in prep), as an environmental proxy for the nutrient supply and bioproductivity and where the phosphorous is largely derived through an influx of riverine, continental systems. Comparisons between P concentrations and the $\delta^{18}O$ values of concurrent conodonts can hence help to interpret the relative changes in continental runoff.

2. Material and Methods

2.1 Study area and material

Conodont dental elements from seven sites were used (Figure 3.1). Geological descriptions about the study areas are summarised in the Supplementary File (File S3.1), with references for more detailed information on the sedimentology and stratigraphy. From the Tethys realm, samples were taken from exotic carbonate blocks that represent marine seamounts for three sections: Noe Tobe (NT) (Timor), Wadi Musjah (WM) and Jebel Awari (JA) (Oman).

Palaeogeographically, they were located at sub-tropical palaeolatitudes at the eastern Pangea margin (Figure 3.1). Geochronologically the Omani localities span layers that range from the middle Smithian to the early Spathian (including *Owenites*, *Anasibirites* and *Glyptophiceras–Xenoceltites* ammonoid beds) while only one horizon was sampled from Timor (*Anasibirites* bed) (Table 3.1). From the Panthalassa realm, samples were obtained from carbonates deposited under coastal settings at four sections (Table 3.2): Georgetown (GT), Crittenden Springs (CS) and Palomino Ridge (PR) (USA) and Stensiöfjellet (SF) (Spitsbergen). The USA sites are located in the western Pangea margin at sub-tropical palaeolatitudes (Figure 3.1). Geochronologically they represent early to late Smithian layers (*Preflorianites*, *Owenites–Inyolites* and *Wasatchites* ammonoid beds). Stensiöfjellet was deposited in the boreal realm at the northern part of Pangea with layers ranging from early Smithian to early Spathian (*Arctoceras*, *Euflemingites*, *Wasatchites* and *Bajarunia* beds). Dental elements were sampled from the collection of the Palaeontological Institute and Museum of the University of Zürich. Rock samples were treated in acetic acid (10 %), sieved and screen washed (0.5 mm, 1 mm, 2 mm) for subsequent picking of conodonts using a stereomicroscope.

Most bioapatites used have a CAI of 1 (burial temperatures $[T] \leq 80$ ºC). For experimental purposes, specimens apparently more altered from CS (CAI 2.5–3, $T \leq 200$ ºC) and PR (CAI 3–3.5, $T \leq 245$ ºC) were used. Taxonomic identification is based on references of Early Triassic species (e.g., Orchard, 2005, 2007; Maekawa et al., 2018, Leu, 2021). Segminate (blade-like) and segmniplanate (platform-like) P_1 elements (family Gondolellidea [Lindström, 1970]) were preferred for more accurate taxonomic identification, since they are the best studied and have relatively high evolutionary rates in morphological diversity and are morphologically less heterogeneous on the species-level than other parts. Exceptions in using platform or blade-like elements for the investigation include more angulate-shaped P_1 and ramiform specimens belonging to the family Ellisonidae (Clark, 1972) recovered for WM and PR localities; and 5 coniform/ramiform S-elements of *N. pindingshanensis* from JA (Table S3.1). A large number of specimens could be recovered from WM and NT, therefore they could be analysed *in-situ* and using bulk sampling techniques, which requires 1 mg of sample powder per analysis. Only very few specimens could be recovered for the American localities, JA and SF, hence the use of SIMS for the oxygen isotope analyses (Tables 3.1, 3.2).

Table 3.1. Conodont $\delta^{18}O$ values analysed by HTR (TC/EA) (gray-shaded) and SIMS (white-shaded) from the Tethyan realm (Timor and Oman). For HTR analysis, the *n* refers to the number of silver capsules analysed for each sample. For SIMS analysis, the *n* refers to the number of sample spots per conodont. All specimens have a Conodont Alteration Index of 1.

Sample ID	Taxon	Origin	Age / Ammonoid biozone	$\delta^{18}O$ (VSMOW)	$\delta^{18}O$ Std dev.	*n*
TM2	*Scythogondolella* ex gr. *milleri*	Noe Tobe/ Timor	late Smithian / *Anasibirites multiformis*	17.0	0.2	10
TM5				17.0	0.2	4
TM6				17.0	0.2	4
TM7				16.9	0.3	4
TM8				17.3	0.2	3
TM9				16.9	0.2	4
TM10				17.0	0.2	3
TM11				17.4	0.5	4
TM12				17.4	0.1	4
TM15				17.3	0.4	7
TM16				16.5	0.3	7
TM17				17.1	0.3	8
TM18				17.3	0.4	8
TM–Nv1	*Novispathodus* sp.			17.0	0.2	2
TM–Nv1				16.6	0.2	2
TM-HTR	*Scythogondolella* ex gr. *milleri*			17.3	0.4	7
WMJ-7C 1	?*Hadrodontina* sp.	Wadi Musjah/ Oman	middle Smithian	17.0	0.2	3
WMJ-7C 2				15.5	0.2	4
WMJ-7C 3				15.6	0.4	4
WMJ-7C 4				16.0	0.2	4
WMJ-11C 1			middle Smithian / *Owenites koeneni*	17.0	0.1	3
WMJ-11C 2				15.8	0.3	3
WMJ-11C 3				16.7		1
WMJ-11C 4				16.7	0.1	2
WMJ-6C 1			late Smithian	16.9	0.3	4
WMJ-6C 2				16.5	0.2	4
WMJ-6C 3				17.0	0.2	4
WMJ-6C 4				16.6	0.5	4
WMJ-6C 5				16.3	0.3	4
WMJ-14C 1				16.8	0.2	3
WMJ-14C 2				16.5	0.3	4
WMJ-1C 1			late Smithian / *Anasibirites* beds	16.6	0.2	3
WMJ-1C 2				15.8	0.6	4
WMJ-1C 3				15.5	0.1	4
WMJ-2C 1				17.4	0.0	2
WMJ-2C 2				16.3	0.9	2
WMJ-2C 3				16.3	0.3	4
WMJ-2C 4	*Scythogondolella* ex gr. *milleri*			16.9	0.2	3

WMJ-2C 5				17.3	0.2	3
WMJ-2C 6				16.7	0.1	3
WMJ-2C 7				16.9	0.1	4
WMJ-15C 1	*Borinella* sp.		late Smithian	18.5	0.1	3
WMJ-15C 2				18.5	0.4	2
WMJ-15C 3				18.5	0.4	4
WMJ-15C 4				18.5	0.4	4
WMJ-16C 1				18.6	0.3	3
WMJ-16C 2				18.3	0.2	4
WMJ-16C 3				18.1	0.3	4
WMJ-16C 4				18.3	0.1	4
WMJ-16C 5				18.6	0.4	4
WMJ-18C 1			early Spathian	18.8	0.0	3
WMJ-18C 2				19.0	0.3	4
WMJ-18C 3				19.4	0.3	4
WMJ-18C 4	*Novispathodus* sp.			18.5	0.2	3
WMJ-3C 1				18.4	0.3	3
WMJ-3C 2	*Borinella* sp.			19.0	0.3	4
JA-17C	*Novispathodus pindingshanensis*	Jebel Aweri/ Oman	late Smithian	17.8	0.2	4
JA-18C				17.2		1
JA-19C				17.1	0.3	4
JA-1C			late Smithian / *Xenoceltites*	16.3	0.3	3
JA-21C			late Smithian	16.7	0.3	6
JA-22C				17.5	0.5	2
JA-11C				17.6		1
JA-24C				16.8	0.3	2
JA-25C				17.0		1
JA-26C				17.4	0.2	7
JA-27C				16.8	0.3	3
JA-2C				17.6	0.2	2
JA-28C				17.9	0.2	8
JA-29C				17.9	0.4	4
JA-13C				17.5	0.2	4
JA-3C	*Novispathodus* sp.			18.7	0.6	6
JA-30C	*Novispathodus* nov. sp.			18.0	0.4	4
JA-36C	*Novispathodus* sp.		early Spathian	18.9	0.4	4
JA-31C				19.1		1
JA-15C				18.6	0.1	4
JA-33C				19.6	0.2	4
JA-14C				18.5	0.2	4
JA-35C				18.7	0.4	4
JA-7C				19.0	0.1	4

Table 3.2. Conodont $\delta^{18}O$ values measured only by the SIMS method from the Panthalassa realm (United States and Spitsbergen).

Sample ID	Taxon	Origin	Age / Ammonoid biozone	CAI	$\delta^{18}O$ (VSMOW)	$\delta^{18}O$ Std dev.	*n*
GT14-1	*Scythogondolella* ex gr. *milleri*	Georgetown/ USA	late Smithian / *Wasachites tardus*	1	15.4	0.2	3
GT14-2					15.0		1
CS34N-1		Crittenden Springs/USA		2.5-3	15.0	0.6	4
CS34N-2					15.4	0.3	4
CS34N-3					15.9	0.3	4
CS34N-4					15.6	0.1	4
CS34B-1	undifferentiated ramiform		middle/late? Smithian		14.8	0.1	3
CS34B-2					13.5	0.5	3
CS34B-3					13.5	0.5	3
PLR30-1		Palomino Ridge/USA	middle Smithian		13.9	0.3	3
PLR30-2				3-3.5	14.7		1
PLR27-1			middle Smithian / *Owenites/Inyoites*		15.2	0.3	4
PLR27-2					13.4	0.2	3
PLR12-1					15.8	0.2	3
PLR12-2					13.4	0.2	2
PLR12-3					13.7	0.1	2
PLR20-1			middle Smithian / *Preflorianites toulai*		14.4	0.1	3
PLR20-2					15.3	0.4	4
PLR9					13.8	0.3	3
STC4Ng-1	*Neogondololella* nov. sp. D	Stensiöfjellet C/ Spitsbergen	early Spathian / *Bajarunia*	1	15.9	0.3	4
STC4Sc/ Bo-1	*Sc. mosheri/Borinella* aff. *buurensis*				16.6		1
STC4Nv-1	*Novispathodus* sp.				14.8	0.1	2
STC4Nv-2					14.9	0.1	2
STC4Nv-3					14.3	0.1	3
STC1-1	*Scythogondolella mosheri*		late Smithian / *Wasachites tardus*		14.3	0.2	2
STC1-2					14.3	0.2	4
STC3-1	*Scythogondolella* ex gr. *milleri*		late Smithian / *Euflemingites*		14.4	0.2	3
STC3-2					14.4	0.1	2
STC3-3					14.4	0.2	4
STC15-1			late Smithian		14.3	0.3	2
STC15-2					14.2		1
STC15-3	Neogondolellid				13.5	0.3	3
STC15-4					14.0	0.4	4
STC13-1					14.0	0.4	3
STC16-1			middle Smithian		17.1		1
STC16-2					16.4	0.2	2
STC10-1					14.4	0.2	4

The three main identified groups were: ellisonids (*Hadrodontina*), neospathotids (*Novispathodus*) and neogondollelids (*Neogondolella*, *Scythogondolella*, *Borinella*). Because many teeth from *Scythogondolella* ex gr. *milleri* were available for both methods selected (bulk and *in-situ*) from almost all localities (exception: PR), the genus *Scythogondolella* was selected as reference taxon. This species is widely used for conodont biostratigraphy and is overlapping with the *Anasibirites/Wasatchites distractus* ammonoid zone (Leu et al., 2019, Goudemand et al., 2019). *Scythogondolella* ex gr. *milleri* had a relatively short occurence in the fossil record (~200 ky) but can be found in late Smithian deposits around the world (e.g., Orchard and Zonneveld, 2009; Leu et al., 2019). Numerous well-preserved (CAI 1) conodonts of *Scythogondolella* ex gr. *milleri* were collected from the exotic carbonate block from NT (Table 3.1). Their preservation state and abundance represented a good tool to establish our analytical protocol for SIMS measurements (Chapter I). A complete list of samples analysed (Table S3.1), and as well as additional information on material and methods is given in the Supplementary Material.

2.2 Stable oxygen isotope analyses in phosphate (HTR, SIMS)

The methods used in this chapter to the HTR and SIMS measurements are the same described in the first chapter (section 3.2.3). Only specific methods details and standards related to the conodonts investigated to this chapter are reported below. Analytical details regarding both evaluation methods (e.g., raw data, treatment, etc.) can be verified in the Supplementary File S3.2.

2.2.1 Bulk sampling and High-Temperature Reduction analysis (HTR)

Measurements were corrected to in-house and international Ag_3PO_4 phosphate standards (LK-2L: 12.1‰, LK-3L: 17.9‰, USGS80: 12.5 ‰, USGS81: 34.7 ‰) that had better than ±0.3‰ (1σ) standard deviations during measurements (Vennemann et al., 2002). The NIST SRM 120c phosphorite reference material had an average value of 21.6‰ ±0.3‰ (*n* = 22).

2.2.2 *In-situ* analysis by Secondary-Ion Mass Spectrometry (SIMS)

In-situ measurements were made, where possible, on the hyaline tissue (Chapter I). Longitudinal cross sections done at the lower part of the conodont crown (oriented to expose the basal view) were mounted in an epoxy resin. Overall, conodont samples had a relief of about

2 µm (File S3.3). Oxygen isotope measurements were made during seven different sessions (from December 2018 to February 2021). In order to calibrate the measurements, two crystals of Durango standard and an in-house conodont standard (TM-SM) were used to normalise the $\delta^{18}O$ values (Chapter I; File S3.2). The standard deviation was ±0.3 ‰ (1σ) for the Durango and between ±0.2 to ±0.4 ‰ for the TM-SM (File S3.2). Durango apatite $\delta^{18}O$ values were determined by laser fluorination (first crystal: 8.7 ±0.1 ‰, $n = 2$; second crystal: 9.0 ±0.1 ‰, $n = 4$) (Vennemann et al., 2002). Each run was normalised with their respective Durango batch (File S3.2). The $\delta^{18}O$ value for the conodont standard (17.1 ‰) is based in HTR (TC/EA) measurements ($n = 7$, about 400 specimens) and SIMS analyses ($n = 13$) (Vennemann et al., 2002; Chapter I).

3. Results

The $\delta^{18}O$ values of 118 bioapatites have a range from 13.4 ‰ to 19.6 ‰ (Tables 3.1, 3.2, Figures 3.2, 3.3). Conodonts analysed by HTR ($n = 13$) have a range of 2.2 ‰ and a reproducibility of individual values of ±0.3 ‰ (1σ). The range in $\delta^{18}O$ values measured for individual conodonts by SIMS ($n = 105$) is 6.2 ‰ and most of the results were within the 1σ reproducibility of 0.3 ‰ ($n = 74$). Raw data and a statistical evaluation are given in the Supplements (File S3.2, Table S3.2).

3.1 Tethys Ocean – Oman and Timor (HTR, SIMS)

Eighty conodonts were analysed from Tethys localities, 64 from Oman and 16 from Timor. From WM, the HTR $\delta^{18}O_{PO4}$ values have a range from 16.6 ‰ to 18.8 ‰ ($n = 12$), overlapping with analogous conodonts analysed by SIMS (15.5 ‰ to 19.4 ‰, $n = 28$) (Table 3.1, Figure 3.2). Only ramiform elements of ellisonids from basal layers (WM-7C to WM-2C) had contrasting values between both techniques, with SIMS $\delta^{18}O$ values lower than HTR and statistically different (*t* test: $t(23) = 2.878$, p < 0.00084). For JA, *Novispathodus* sp. P_1 elements (exceptions: JA-18C, 19C, 1C) were mainly measured ($n = 24$) and the $\delta^{18}O$ values were between 16.3 ‰ to 19.6 ‰. This dataset has a similar range with the HTR results from WM, but with an oscillating pattern (Figure 3.2). Middle to basal late Smithian $\delta^{18}O$ values average at 16.9 ±0.2 ‰ ($n = 7$, HTR) and 16.3 ±0.5 ‰ ($n = 18$, SIMS) for WMJ and 17.1 ±0.5 ‰ for JA ($n = 11$). In contrast, upper late Smithian to early Spathian samples have an average $\delta^{18}O$ of 18.5 ±0.2 ‰ ($n = 5$, HTR), 18.6 ±0.4 ‰ ($n = 10$) for WMJ, and of 18.5 ±0.4 ‰ for JA ($n = 13$).
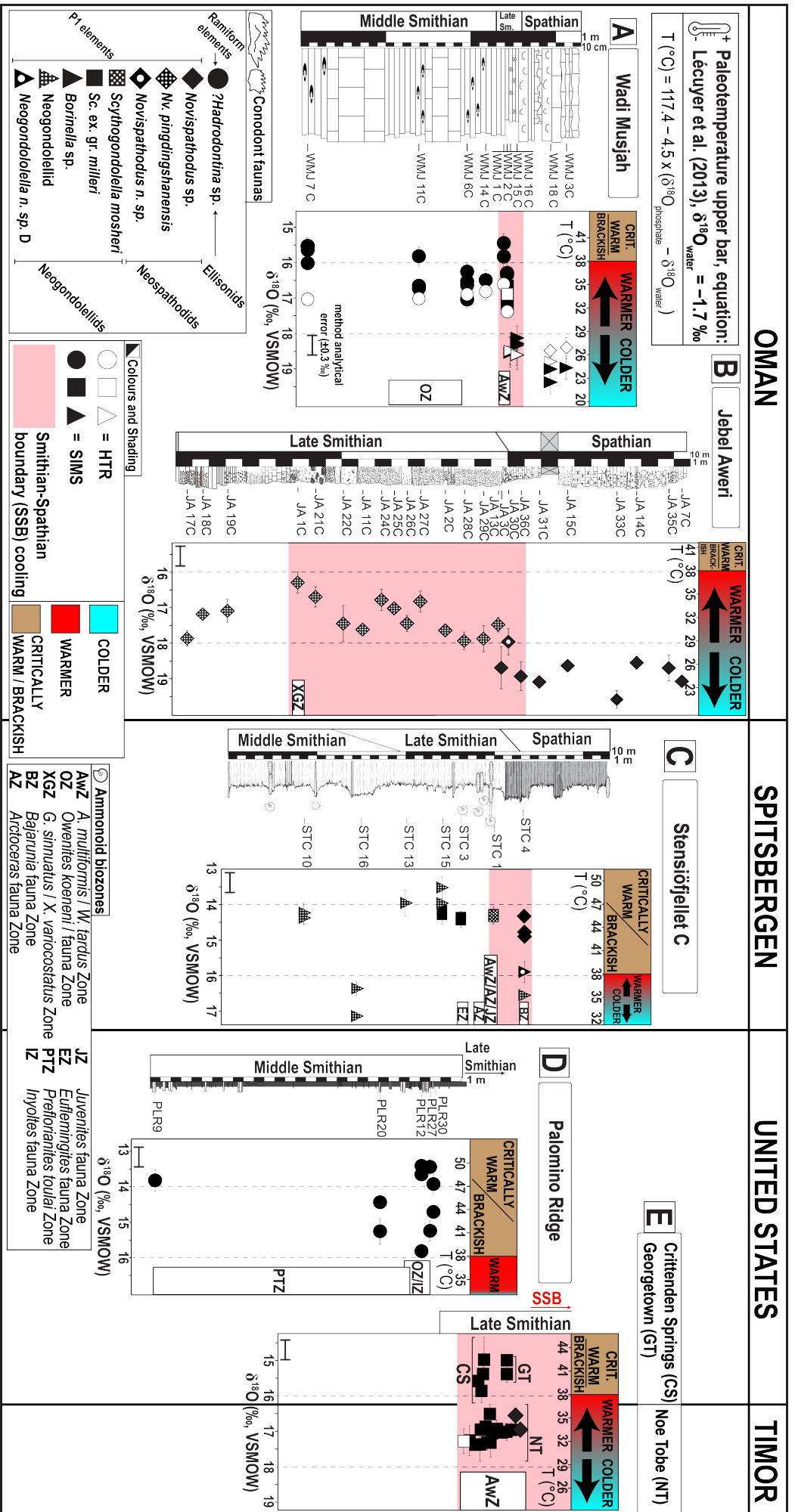
Figure 3.2. Oxygen isotope compositions and a simplistic representation of the stratigraphic succession for **(A)** Wadi Musjah, **(B)** Jebel Aweri, **(C)** Stensiöfjellet, **(D)** Palomino Ridge. Values from **(E)** Crittenden Springs, Georgetown and Noe Tobe come are predominantly from *Sc. ex. gr. milleri* of the same layer; the δ¹⁸O values are all plotted for better visualisation of the scatter. The Smithian–Spathian boundary (SSB) cooling event is marked for each locality (red-shaded area). Captions at the top/bottom of the figure summarise information about conodont dental elements and faunas (symbols) and respective method for analysis of the δ¹⁸O values (filled symbol), associated ammonoid biozones (white squares) and for palaeotemperatures (upper *x*-axis).
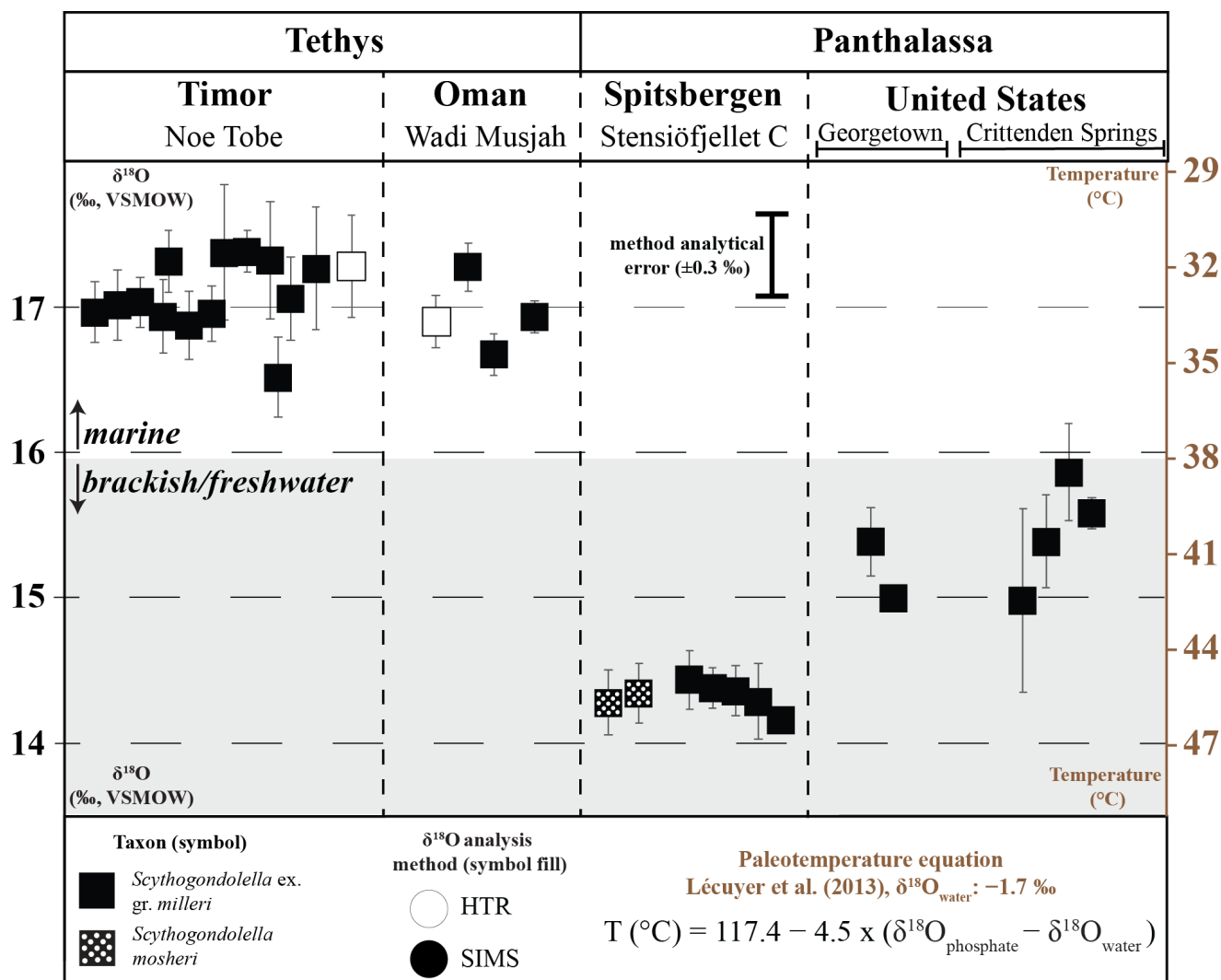
Figure 3.3. The δ18O values (left) and palaeotemperatures (right) of *Scythogondolella* (symbols) from the Tethyan and Panthalassic realms. Data is mainly from *Sc.* ex. gr. *milleri*, a cosmopolitan late Smithian species. The lower δ18O values measured in Panthalassa (below the horizontal, grey-shaded area) indicate that bioapatites formed under low-salinity conditions.

The dataset from NT (*n* = 16) is primarily composed by P_1 elements of *Sc.* ex. gr. *milleri*, except for two *Novispathodus* sp. that due to their small size, were measured only *in-situ* (TM-Nv1, 2). The average $\delta^{18}O_{PO4}$ value of *Sc.* ex. gr. *milleri* analysed by HTR is 17.3 ±0.4 ‰ (7 sample splits used), while the SIMS δ18O values have a range between 16.5 ‰ to 17.4 ‰ (*n* = 15). This dataset is statistically indistinguishable from *Sc.* ex. gr. *milleri* from WMJ (WMJ-2C, Figure 3.2) and with geochronologically analogous specimens from JA (JA-17C to 27C, Figure 3.2) (ANOVA: *F* = 0.35, *p* = 0.7034).

3.2 Panthalassa Ocean – USA and Spitsbergen (SIMS)

Thirty-eight specimens were analysed *in-situ* (SIMS) from the Panthalassa Sea, half being from the USA and the other half from Spitsbergen. The δ18O values from the USA (GT, CS, PR) have a range from 13.4 ‰ to 15.9 ‰ (Table 3.2, Figure 3.2). The dataset from GT and CS mainly includes *Sc.* ex. gr. *milleri* P_1 elements with a small variability of their isotopic

composition (15.4 ±0.3 ‰, $n = 6$). However, values measured in three ramiform elements from CS with a CAI of 2.5–3 have lower $\delta^{18}O$ values averaging 13.9 ±0.7 ‰ ($n = 3$). From PR, only ramiform elements could be used and similar to CS and WM, slightly lower $\delta^{18}O$ values with a higher variance were measured (14.4 ±0.9 ‰, $n = 10$). While some outliers can be related to the state of preservation (specimens with CAI 5, Table 3.2), well-preserved ramiform elements from WM also have low values when evaluated by the SIMS (more details below).

Analyses from SF ($n = 19$) were all made on P_1 elements and the $\delta^{18}O$ values reproduce to better than ±0.3 ‰ (1σ), except for two samples (STC13-1, STC15-4: ±0.4 ‰). The $\delta^{18}O$ values have a range between 13.5 ‰ to 17.1 ‰ (avg: 14.8 ±1 ‰), but most were 14.3 ±0.3 ‰ ($n = 15$). The higher limit of the $\delta^{18}O$ values measured is found in four neogondolellids samples (16.5 ±0.5 ‰), that should represent real environmental changes at their occurring intervals (middle Smithian for STC16-1, 2; early Spathian for STC-4Ng, Bo.).

Considering only the $\delta^{18}O$ values of *Scythogondolella* from both palaeo-oceans (*Sc.* ex. gr. *milleri*) from the late Smithian of the USA have a mean $\delta^{18}O$ value of 15.4 ±0.3 ‰ ($n = 6$), somewhat higher than the average $\delta^{18}O$ of *Sc.* from the late Smithian of Spitsbergen (14.4 ±0.1 ‰, $n = 7$). However, both are below the mean $\delta^{18}O$ value of *Sc.* ex gr. *milleri* from Timor and Oman (statistically undistinguishable: 17.1 ±0.2 ‰, $n = 18$). Statistical tests using these three datasets (USA *vs* Spitsbergen *vs* Oman and Timor) have shown significant differences between their isotopic compositions (ANOVA: $F = 340.1$, $p < 0.01$).

4. Discussion

The oxygen isotope compositions of bioapatite from both palaeo-oceans follow similar trends during the Smithian–Spathian climatic upheavals, albeit with different absolute $\delta^{18}O$ values. Tethyan conodonts have similar $\delta^{18}O$ values irrespective of the analytical technique used; an exception is given for Omani ellisonid ramiform elements analysed by SIMS, that have about 1 to 1.5 ‰ lower values compared to analogous specimens analysed as bulk samples (HTR, Table 3.1, Figure 3.2A). Similar results were measured for samples from the USA where ellisonid ramiform SIMS $\delta^{18}O$ values are scattered, but specimens have similar $\delta^{18}O$ values as of *Sc.* ex. gr. *milleri* P_1 elements (Table 3.2, Figure 3.2D, E). While from some localities (e.g., PR) they had a CAI of 3.5 that can explain the higher variance in $\delta^{18}O$ measured, analogous specimens from WM have a CAI of 1 and similarly low values were found as noted for American P_1 *vs* ramiform elements. This further indicates that ellisonid ramiform element $\delta^{18}O$ values must be interpreted with caution as palaeoenvironmental proxies (Chapter II), but the combination of stable isotope oxygen techniques can help to constrain and interpret reliable

$\delta^{18}O$ results (Figure 3.2A).

4.1 Tethyan *vs* Panthalassa oxygen isotope compositions

Both Omani sections have a positive oxygen isotope excursion (OIE) of 1.5 to 1.8 ‰ characteristic of the SSB cooling (Figure 3.2A, B) and absolute $\delta^{18}O$ values for *Sc.* ex. gr. *milleri* are similar to those from Timor (WM and NT, Figure 3.2A, E), the other Tethyan site. The SSB positive isotope excursion is also given by P_1 elements from Spitsbergen, but the $\delta^{18}O$ values are about 2 to 3 ‰ lower compared to Tethyan P_1 elements (Figure 3.2A, B, C). For Spitsbergen the OIE is particularly marked by the $\delta^{18}O$ values from early Spathian neogondolellids, conodont taxa which are assumed to have a deeper/colder water habitat (Goudemand et al., 2019; Chapter II). Early Spathian neospathodids (*Novispathodus*) $\delta^{18}O$ values, in contrast, do overlap with those of the late Smithian neogondolellids (Figure 3.2C). Based on depth preferences of conodont species, these are likely to have about 0.4 ‰ lower values (i.e., about 1.2 °C warmer) compared to the neogondolellids (Goudemand et al., 2019), but here are in fact about 1 ‰ higher. In addition, the $\delta^{18}O$ values of *Sc.* ex. gr. *milleri* from USA are slightly higher than the late Smithian *Sc.* ex. gr. *milleri* from Spitsbergen (Figures 3.2C, E; 3.3), probably indicative of a regional or even a palaeolatitudinal offset between these localities (more details below in the **4.2**).

To fully understand the nature of the conodont oxygen isotope compositions, the two factors controlling the $\delta^{18}O_{PO4}$ value from a given bioapatite during its formation must be taken into consideration: temperature and the $\delta^{18}O$ of the water ($\delta^{18}O_w$). Open-ocean waters are generally homogeneous in isotopic composition (modern seawater is close to 0‰), while all meteoric waters are eventually derived from marine waters by evaporation, which fractionates the isotopic composition of the H_2O molecules such that freshwater typically has lower $\delta^{18}O_w$ values compared to seawater (Longinelli and Nuti, 1973a, b; Kolodny et al., 1983). For this reason, marine organisms which form their bioapatite in waters near coastal environments may have lower $\delta^{18}O_{PO4}$ values for the same temperature of formation if there was an important influx of meteoric waters from the adjacent continental runoff (e.g., Klug et al., 2010; Fischer et al., 2013; Leuzinger et al., 2015; Kocsis et al., 2007, 2015; Carrillo-Briceño et al., 2019). As an influx of meteoric water will also cause a lower salinity of the marine waters, conodont $\delta^{18}O$ values may also reflect palaeosalinity patterns (i.e., evaporative or freshwater conditions, c.f. Buggisch et al., 2008; Sun et al., 2012; Joachimski and Lambert, 2015). This could be argued to be the case for the low $\delta^{18}O$ measured for conodonts from American sites and Spitsbergen in this study (Table 3.2, Figure 3.2).

For the Omani sites a $\delta^{18}O_w$ value of -1.7‰ can be estimated based on brachiopod clumped isotope compositions (Chapter II; Edward et al., in prep.) for the Early Triassic seawater. Given such a value for water, the measured $\delta^{18}O$ values for Omani and Timor P_1-element conodonts correspond to calculated palaeotemperatures between 26 to 37 °C (Figure 3.2), which are feasible for biological life. However, using the same seawater $\delta^{18}O_w$ value of -1.7 ‰, the low ^{18}O values measured for Panthalassic P_1 and ramiform-elements would correspond to palaeotemperatures over 40 °C (> 45 °C for Spitsbergen). These values are higher than the tolerance limit of 38 °C for multicellular life (e.g., Brock, 1985; Rothschild and Mancinelli, 2001) and hence it is unlikely that conodonts lived in such conditions. However, if the $\delta^{18}O_w$ values were lower than those of -1.7 ‰ estimated for time-equivalent Tethian waters, lower temperatures would be calculated. Hence, rather than representing differences in the temperatures of biomineralization the differences between the average Tethyan and Panthalassic $\delta^{18}O$ values could be related to different $\delta^{18}O_w$ values, within the distinct depositional settings from where the conodonts formed.

Conodonts from the Panthalassa realm are from geological sections deposited in coastal settings, which is different from conodonts of the Tethyan realm that were deposited in a marine setting. As such, the coastal settings for the Panthalassa localities may have had a lower $\delta^{18}O_w$ value compared to the Tethyan sections. Palaeogeographically, both Panthalassa palaeobasins are also interpreted to have been in a relatively shallow basins with a likely epicontinental sea aspect (Figure 3.1), hence emphasizing a possible effect by continental runoff. Additionally, during the Permian-Triassic transition, smaller sedimentary systems started to prograde from Greenland into Svalbard that at the time was part of the Barents Sea Basin (Mørk et al., 1982; Wignall et al., 1998; Haug Eide et al., 2018). Coincidently in the latest Permian and earlist Triassic, a rifting of the western Norwegian-eastern Greenland margins happened (e.g., Faleide et al., 2008; Stoker et al., 2016), possibly due to a dynamic rift-shoulder uplift (c.f. ten Brink and Stern, 1992; Daradich et al., 2003). Such changes led to increased topography, which caused the erosion rates and sediment supply to increase, further supporting an epicontinental sea palaeoenvironment in Spitsbergen. A similar geologic situation but for the North American Midcontinent Sea (NAMS) was recently modelled for a range of different continental runoff scenarios using an isotope-enabled Community Earth System Model by Mararewich et al. (2021). Their model predicted $\delta^{18}O_w$ values for this American epicontinental sea that was estimated to have been up to 3 ‰ lower relative to the open ocean at the time, depending on different palaeotopographic features for the source terrain of the continental runoff. These models were in good agreement with actual measurements for $\delta^{18}O_{PO4}$ values from conodonts

measured from shales within the time-equivalent sequences of the American Midcontinental Sea (Joachimski and Lambert, 2015) and for which large salinity differences have also been postulated.

Generally, continental runoff processes may also support an increase in the primary productivity near coastal areas and, by extension, may also lead to regional anoxia and given relatively high sedimentation rates too, a good preservation of organic matter in the near-shore sediments (e.g., Zhang et al., 2018; Goudemand et al., 2019), but an absence thereof for marine deposits (Leu, 2021; Chapter II). Continental freshwater input into the Panthalassic basins seems to have been continuous, given that the oxygen isotope compositions are relatively low during the entire Smithian and even after the SSB. The $\delta^{18}O$ values from the USA while more scattered and representing a shorter period of sedimentation (middle to late Smithian only), have average $\delta^{18}O$ values about 1 ‰ higher than the Spitsbergen equivalent conodont tissues (Figure 3.2D, E), compatible too with an epicontinental sea setting (Figure 3.1A, B).

For both basins (USA and Spitsbergen) the change towards higher $\delta^{18}O$ values noted for the SSB has also been noted for the Timor, Oman and indeed sections in South China and Pakistan (see Goudemand et al., 2019). This change, at least in part, may thus be related to a global cooling, but for the USA and Spitsbergen sections may indeed also support a decrease in the freshwater influence to the coastal or epicontinental seas. An earlier positive OIE recorded at the middle Smithian for the Spitsbergen sections, where the $\delta^{18}O$ values of neogondolellids increased by about 2 ‰, may also be related to a brief period of cooling, by analogy to the changes noted for the SSB (STC-16, Figure 3.2C). However, in contrast to the changes noted for the SSB, this brief period of possible cooling, has not been noted elsewhere and indeed the middle Smithian is thought to be an overall warm period, much as the late Smithian (e.g., Romano et al., 2013; Zhang et al., 2018; Goudemand et al., 2019). Hence, in the case of Spitsbergen, this brief "cooling" may simply equate to a brief period characterised by a reduction in the continental runoff and hence decreased influence on the $\delta^{18}O_w$. The western margin of the Panthalassa has also been subject to upwelling events (e.g., Beauchamp and Baud, 2002; Grasby et al., 2020), where the arrival of open-ocean waters into the more brackish waters of Spitsbergen would certainly also have increased the local $\delta^{18}O_w$ values. Preliminary elemental phosphorus data, however, has shown that the P concentrations have not changed at all during this middle Smithian O-isotope excursion (Blattmann et al., in prep). As such, a reduction of freshwater input may remain the preferred interpretation for this brief peak.

A reduction of upwelling may be expected during the middle–late Smithian. This interval supports the presence of a thermal maximum, and the warming of the ocean surface can with

time increase thermal stratification (Gruber, 2011; García-Reyes et al., 2015). Such phenomena limits the upwelling depth, thus disrupting the amount of nutrient input into the euphotic zone (Chhak and Di Lorenzo, 2007; Jacox and Edwards, 2011; Jacox et al., 2015; García-Reyes et al., 2015). Nitrogen isotopes also suggest productivity disturbances in the Panthalassa during the Early Triassic (Grasby et al., 2016; Grasby et al., 2020). Consequently, the nutrient input brought by continental runoff becomes even more important for mediating biological activity (García-Reyes et al., 2015), during intervals where upwelling events are limited by climatic changes.

Another explanation for the increase in the $\delta^{18}O$ values in the middle Smithian of Spitsbergen, a factor that is not easily interpreted only with geochemical proxies, can be considered: the palaeoecological features of neogondolellid conodonts. Geological evidence shows that there was a palaeoenvironmental change at the layer (STC-16) where the early positive OIE was measured, with carbonates having a larger grain size and suggestive of a change in the sedimentary facies. Facies characterization describe these rocks as being deposited under higher energy conditions compared to adjacent layers, also implying an increase in sea level at this time, something also corroborated by additional independent proxies (c.f. Paull and Paull, 1997; Haq et al., 2018; Brayard et al., 2020). Transgressive episodes would offer a higher water column for conodonts to inhabit at the Spitsbergen shallow–water basin, thus reducing possible interactions of the deeper–water neogondolellids (Goudemand et al., 2019) with depleted $\delta^{18}O_w$ from surface freshwater input. These findings highlight that conodont ecological features may prevail over the expected climatic isotopic excursions, being also possible that their $\delta^{18}O_{PO4}$ values reflect the depositional characteristics from where they are recovered.

4.2 A palaeogeographical oxygen seawater map

The current dataset and interpretation are largely based on specimens of the *Scythogondolella* genus from the late Smithian for Panthalassa as well as Tethyan sites (Figure 3.3). Tethyan conodonts from sections deposited in marine settings (i.e., without freshwater influence) may be used to estimate 'pristine' global seawater $\delta^{18}O_w$ values (Figures 3.2, 3.3) and/or palaeotemperatures. Given $\delta^{18}O_w$ values of about -1.7 ‰ (see above reference to measurements of the clumped isotope compositions), palaeotemperatures for $\delta^{18}O$ values of *Sc.* ex gr. *milleri* (late Smithian, *Anasibirites/Wasatchites* beds) from these localities are between 32 to 35 °C, with a mean temperature of 33 ±1.1 °C. This average is clearly lower than the tolerance limit for biological life (≤ 38 °C) and it also corresponds to the global average temperature proposed for 250 Ma (about 33 °C) from the recent Phanerozoic palaeotemperature

model compiled by Scotese et al. (2021). The $\delta^{18}O$ values of *Scythogondolella* from the USA and Spitsbergen should not be used for palaeothermometry, but instead their oxygen isotope composition can be used as a proxy for assessing the $\delta^{18}O_w$. This assumes that Panthalassic specimens lived in a similar thermal regime compared to their Tethyan counterparts. Conodonts are animals that lived until the end of the Triassic. However, since the Cambrian they survived a number of extinctions (e.g., Orchard, 2007; Joachimski et al., 2009; Trotter et al., 2016a), and one of the probable reasons for this is the pelagic nature of these aquatic vertebrates. Modern fish species usually adapt to a preferential habitat and water depth or thermal regime in order to optimise their biological processes, moving towards a deeper profile if surface waters become warmer than their tolerance (e.g., sharks, Ebert et al., 2013; Papastamatiou et al., 2015). Also, the cosmopolitan taxon *Sc.* ex. gr. *milleri* is found in both boreal realms as well as tropical to sub-tropical realms (Orchard, 2007; Leu et al., 2019). Climatic events such as the Smithian Thermal Maximum could have further influenced their migration towards higher latitudes, while they were temporarily absent in the tropics (Leu, 2021). Hence, it is likely too that animals of this group could have adapted to habitats of similar thermal regimes that are optimal for their biological processes and survival. Strategies like vertical movements in the water column as suggested earlier for the neogondolellids from Spitsbergen and horizontal migrations towards higher latitudes possibly assured their ecological success during adverse conditions.

Given the above assumptions, the $\delta^{18}O_w$ values can be calculated for the Panthalassic localities by using an average temperature of 33 ±1.1 °C from Tethyan specimens (details in Table S3.3) in the palaeotemperature equation (Lécuyer et al., 2013). The $\delta^{18}O_w$ values are of -3.4 ‰ to -4.5 ‰ for the USA and Spitsbergen sites, respectively (Figure 3.4). The about 1 ‰ offset between these could be related to regional drainage basin characteristics from each locality. However, it is also possible that the noted difference reflects a palaeolatitudinal isotopic offset. To demonstrate this latter hypothesis, we plotted the assessed $\delta^{18}O_w$ on the Early Triassic palaeogeographic map presented in Figure 3.1 (Vérard et al., 2015; Vérard, 2019) (Figure 3.5). For comparative purposes, we also calculated the $\delta^{18}O_w$ values for previous oxygen isotope studies where conodonts were recovered from coastal depositional settings (Sun et al., 2012; Romano et al., 2013; Goudemand et al., 2019). Here too *Scythogondolella* specimens from Pakistan and analogous late Smithian specimens from South China (*Glyptophiceras* and *Wasachites* ammonoid zones) were used (Table S3.3).
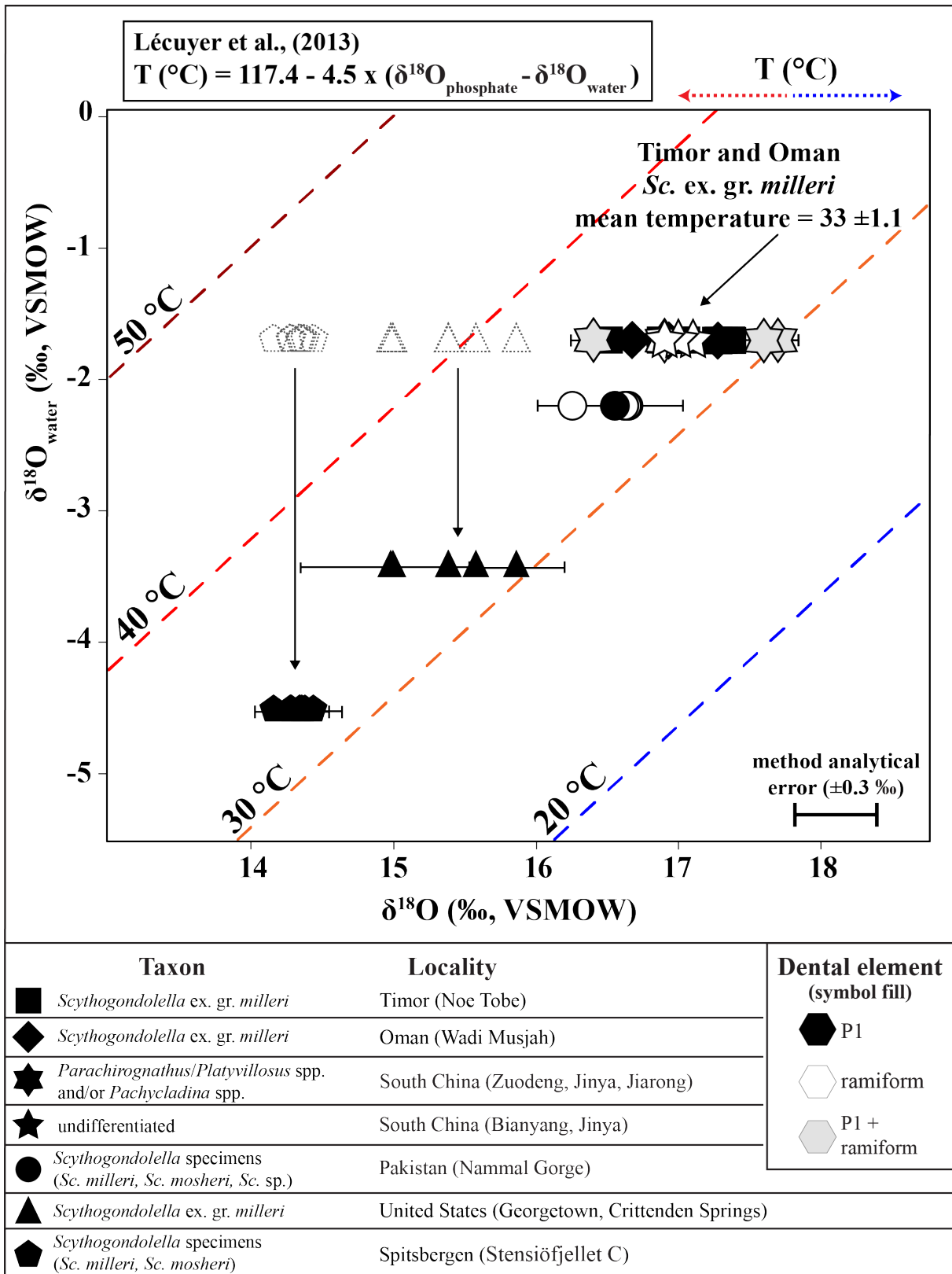
Figure 3.4. Oxygen isotope compositions and their relationship as a function of the oxygen isotopic composition of water and temperature for *Scythogondolella* (this research, Romano et al., 2013; Goudemand et al., 2019) and analogous late Smithian specimens (symbols) (Sun et al., 2012). Dashed lines are isotherms calculated using the phosphate oxygen-water temperature relation of Lécuyer et al. (2013). Using a temperature of 33 °C, the $\delta^{18}O_w$ values from coastal sections can be estimated. Note that for coastal sections studied in this research (USA, Spitsbergen), traced symbols are mainly over the 40 °C isotherm if the marine/tropical $\delta^{18}O_w$ value is used (-1.7 ‰).
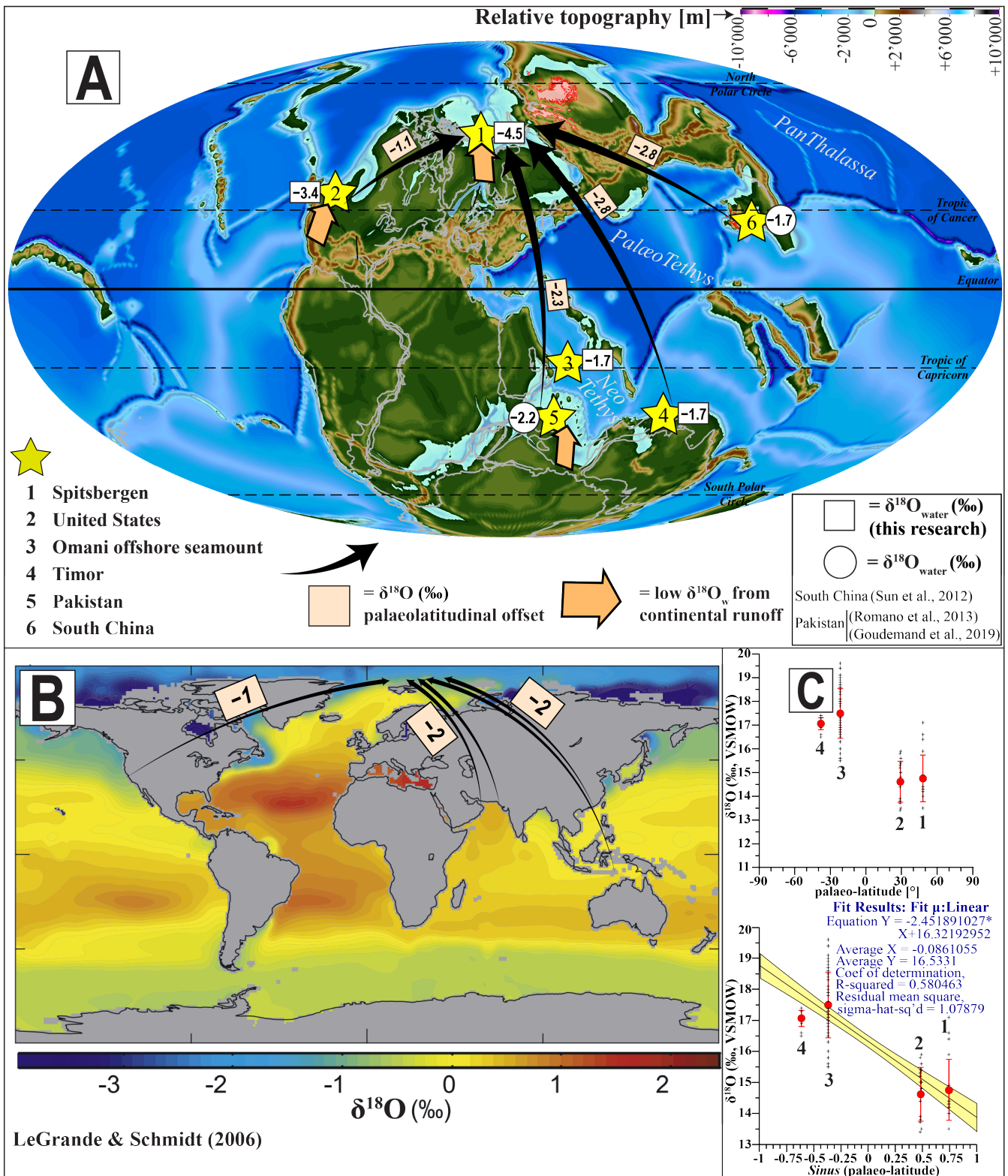
Figure 3.5. (A) Compilation of the PANALESIS palaeogeographic map and calculated $\delta^{18}O_w$ values for conodonts studied here (white squares, Timor, Oman, Spitsbergen, USA) and previously (circles, South China – Sun et al., 2012; Pakistan – Romano et al., 2013; Goudemand et al., 2019). Localities where the continental runoff possibly influenced the conodont $\delta^{18}O$ values are indicated (orange arrow). A palaeolatitudinal $\delta^{18}O$ offset of about 2.5 ‰ is noted between low (and the marine realm) to high -palaeolatitudes in Panthalassa (black arrows and ivory squares). **(B)** A similar $\delta^{18}O$ latitudinal offset is recognised between current-day localities and the boreal realm (LeGrande and Schmidt, 2006). In **(C)**, the relationship between the palaeolatitudes and the $\delta^{18}O$ values measured in this study is shown (linear regression: $R^2 = 0.580463$). A larger version of this subimage is available as Supplementary Figure S3.1.

The reconstitution of $\delta^{18}O_w$ for the oceans shown in Figure 3.5A indicates a $\delta^{18}O_w$ offset between the western Pangea margin subtropical and the boreal realm during the Triassic similar to that for modern seawater between the western USA subtropical and high-latitudinal waters (LeGrande and Schmidt, 2006; Figure 3.5B). This is compatible with a similar meteoric water cycle, continental constellation and present-day geography/topography. For the low values in Spitsbergen and in the USA, both a "continental" and "palaeolatitude" and possibly also "palaeoaltitude" effect (see the mountain range in Figure 3.5A, east of Spitsbergen and west of USA) can be combined to account for the low $\delta^{18}O_w$ and hence $\delta^{18}O$ values measured (c.f., Rozanski et al., 1993; Macarewich et al., 2021). Meanwhile in the Tethyan realm, the $\delta^{18}O_w$ values can be estimated to be -1.7 ‰ and -2.2 ‰ for South China and Pakistan, respectively (Figures 3.4, 3.5; Table S3.3). Remarkably, it can be noted that the $\delta^{18}O_w$ value for the tropics (i.e., South China) is very similar to the $\delta^{18}O_w$ from the marine realm at the subtropics. This implies that the $\delta^{18}O_w$ value of -1.7 ‰ estimated from clumped isotope measurements of brachiopods may well represent the global $\delta^{18}O_w$ average during the Triassic. The lower $\delta^{18}O_w$ from Pakistan is coherent with its coastal setting, being more susceptible to the influence of freshwater input.

Numerical modelling experiments are currently being developed by Ragon et al. (personal communication), with the modelling being conducted using the Massachusetts Institute of Technology General Circulation Model (MITgcm, Marshall et al., 1997a, b), which is a three-dimensional (3D) system where the full coupling between atmosphere, ocean and sea ice is taken into account (c.f., Brunetti and Vérard, 2018; Brunetti et al., 2015, 2019, for details). Preliminary results have shown that the modelled meteoric precipitation estimates match the lower salinity outlined for the boreal and Panthalassa realm (Ragon et al., personal communications, February 2022). Thus, the modelled findings would further support a freshwater input as a means of lowering the $\delta^{18}O_w$ for the USA and Spitsbergen in a setting of an epicontinental basin. The contrasting $\delta^{18}O_w$ values between the subtropics of both palaeo-oceans can be accounted for by a regional influence of the continental runoff, by their respective palaeogeographic settings and possibly precipitation (c.f., Martindale et al., 2014; Arnesen, 2017; Brookfield et al., 2019; Grasby et al., 2020). The $\delta^{18}O_w$ offsets for the late Smithian are very similar to modern $\delta^{18}O_w$ offsets between the current localities and the boreal realm (Figure 3.5B), and a freshwater input can also account for the low $\delta^{18}O_w$ values from Panthalassic and Pakistani conodonts.

5. Conclusions

Stable oxygen isotope analyses of 118 conodonts from the Early Triassic of both Tethyan

marine tropical/sub-tropical sites as well as Panthalassa marine/coastal sites of the boreal realm can be interpreted in terms of regional differences of the seawater oxygen isotope chemistry. In part, this was possible through advances in the analytical techniques used, such SIMS measurements for the $\delta^{18}O$ values of rare specimens from sections of the Panthalassa ocean. While the Smithian–Spathian cooling event is recorded in both palaeo-oceans by an increase in the $\delta^{18}O$ values of about 1.5 to 1.8 ‰, this is with contrasting absolute values between Tethyan marine and Panthalassa "coastal" sections. The $\delta^{18}O$ values from well-preserved (CAI of 1) conodonts of the Tethys are interpreted as primary isotopic compositions, and for given estimates of Smithian–Spathian seawater values of -1.7 ‰, palaeotemperatures of 26 to 37 °C can be estimated, that is temperatures that are feasible for biologic life. However, the 2 to 3 ‰ lower $\delta^{18}O$ values from Panthalassa sites of Spitsbergen and the USA, require $\delta^{18}O_w$ values strongly influenced by continental runoff. Runoff processes also support the increase of the primary productivity near coastal areas and may have ultimately also caused regional anoxia for these sites. A change towards higher $\delta^{18}O$ values for both the boreal as well as the tropical/ sub-tropical sites is interpreted to be related to global cooling and for the boreal sites may also imply a reduced continental runoff.

Based on the assumption that a cosmopolitan species (*Scythogondolella milleri*, late Smithian) lived in the same palaeotemperature range in both palaeo-oceans, the $\delta^{18}O_w$ values were estimated on a global scale and a palaeolatitudinal and palaeogeographic offset in $\delta^{18}O$ values of water can be noted. The difference of about 2.5 ‰ between low (-1.7 ‰) and high (-4.5 ‰) palaeolatitude waters is similar to that noted for the oceans today. Moreover, Tethyan marine and low latitude $\delta^{18}O_w$ values are similar, but $\delta^{18}O$ and geochemical analyses from coastal sections may be biased by regional processes and hence, must be interpreted with caution. Stable oxygen isotope analysis of additional conodont specimens/species from different palaeolatitudes and depositional settings are necessary to quantify and constrain these propositions further. Nonetheless, the first views of Early Triassic palaeoceans have similar aspects compared to modern oceans and hence changes in oceanography related to climatic changes may be studied by analogy.

6. Research Data and Supplementary Material

Research data associated with this article can be found in the Supplementary Material. All suplements were uploaded to a Data Repository (https://doi.org/10.5281/zenodo.7301728). The Supplementary Material table of contents to the current chapter is:

File S3.1 General geological description for the sites where conodont samples were recovered.

File S3.2 Raw oxygen isotope data and normalisation.

File S3.3 Profilometer output files with sample topography.

Table S3.1 Complete list of all referred conodont bioapatites and oxygen isotope technique used.

Table S3.2 Statistical tests of conodont oxygen isotope data.

Table S3.3 Estimations of the $\delta^{18}O_w$ based on conodont oxygen isotope data.

Figure S3.1 Enlarged image of the relationship between the palaeolatitudes and the $\delta^{18}O$ values measured in this study, originally presented in Figure 3.5C.

References

Arnesen, E. 2017. On the Late Permian thermohaline circulation. A study of the oceanic circulation and its relation to the Permian–Triassic Extinction. *M.Sc.-dissertation*, University of Oslo, Norway. 102 p.

Aguilera, O.; Luz, Z.; Carrillo-Briceño, J. D.; Kocsis, L.; Vennemann, T.; Toledo, P. M. et al. 2017. Neogene sharks and rays from the Brazilian "Blue Amazon". *PLoS One*. **12**, e0182740.

Bagherpour, B.; Bucher, H.; Vennemann, T.; Schneebeli-Hermann, E.; Yuan, D.; Leu, M. et al. 2019. Are Late Permian carbon isotope excursions of local or of global significance? *GSA Bulletin*, **132**(3–4), 521–544.

Barlow, D. R.; Klinck, H.; Ponirakis, D.; Garvey, C. and Torres, L. G. 2021. Temporal and spatial lags between wind, coastal upwelling, and blue whale occurrence. *Scientific Reports*, **11**, 6915.

Barnes, C. R. and Fahreus, L. E. 1975. Provinces, communities, and the proposed nektobenthic habit of Ordovician conodontophorids. *Lethaia*, **8**, 133–149.

Baud, A.; Béchennec, F.; Krystyn, L.; Le Métour, J.; Marcoux, J.; Maury, R. and Richoz, S. 2001. Permo–Triassic Deposits: from the Platform to the Basin and Sea-mounts. Conference on the Geology of Oman. Field guide-book, Excursion A01. In *Conference on the Geology of Oman, Field guidebook, Excursion A01*. 1–54.

Baud, A.; Richoz, S.; Beauchamp, B.; Cordey, F.; Grasby, S.; Henderson, C. M. et al. 2012. The Buday'ah Formation, Sultanate of Oman: A Middle Permian to Early Triassic Oceanic Record of the Neotethys and the late Induan microsphere bloom. *Journal of Asian Earth Sciences*, **43**, 130–144.

Beauchamp, B. and Baud, A. 2002. Growth and demise of Permian biogenic chert along northwest Pangea: evidence for end-Permian collapse of thermohaline circulation. *Palaeogeography, Palaeoclimatology, Palaeoecology*, **184**, 37–63.

Béchennec, F. 1992. Explanatory notes to the Geological map of Al Ashkharah. *Sultanate of Oman, Ministry of Petroleum and Minerals, Directorate of Minerals, Bureau de Recherches Geologiques et Minieres*, Or. pp. Sheet-N.

Beerling, D. 2008. The Emerald Planet: How Plants Changed Earth's History. *Oxford University Press*, 1 ed. 304 p.

Bernasconi, S. M.; Müller, I. A.; Bergmann, K. D.; Breitenbach, S. F. M.; Fernandez, A.; Hodell, D. A. et al. 2018. Reducing uncertainties in carbonate clumped isotope analysis through consistent carbonate-based standardization. *Geochemistry, Geophysics, Geosystems*, **19**, 2895–2914.

Bernasconi, S. M.; Daëron, M.; Bergmann, K. D.; Bonifacie, M.; Meckler, A. N.; Affek, H. P. et

al. 2021. InterCarb: A community effort to improve interlaboratory standardization of the carbonate clumped isotope thermometer using carbonate standards. *Geochemistry, Geophysics, Geosystems*, **22**, e2020GC009588.

Bonifacie, M.; Calmels, D.; Eiler, J. M.; Horita, J.; Chaduteau, C.; Vasconcelos, C. et al. 2017. Calibration of the dolomite clumped isotope thermometer from 25 to 350 °C, and implications for a universal calibration for all (Ca, Mg, Fe) CO_3 carbonates. *Geochimica et Cosmochimica Acta*, **200**, 255-279.

Bottjer, D. J. 2012. Life in the Early Triassic Ocean. *Science*, **338**, 336.

Boyd, P. W. 2015. Toward quantifying the response of the oceans' biological pump to climate change. *Frontiers in Marine Science*, **2**: 77.

Brand, U.; Azmy, K.; Bitner, M.; Logan, A.; Zuschin, M.; Came, R. and Ruggiero, E. 2013. Oxygen isotopes and $MgCO_3$ in brachiopod calcite and a new paleotemperature equation. *Chemical Geology*, **359**, 23-31.

Brayard, A.; Olivier, N.; Vennin, E.; Jenks, J. F.; Bylund, K. G.; Stephen, D. A. et al. 2020. New middle and late Smithian ammonoid faunas from the Utah/Arizona border: new evidence for calibrating Early Triassic transgressive-regressive trends and paleobiogeographical signals in the western USA basin. *Global and Planetary Change*, **192**(179), 103251.

Briggs, D. E. G.; Clarkson, E. N. K. and Aldridge, R. J. 1983. The conodont animal. *Lethaia*, **16**(1), 1–14.

Brock, T. D. 1985. Life at high temperatures. *Science*, **230**, 132–138.

Brookfield, M. E.; Stebbins, A. G.; Williams, J. C.; Wolbach, W. S.; Hannigan, R. and Bhat, G. M. 2020. Palaeoenvironments and elemental geochemistry across the marine Permo-Triassic boundary section, Guryul Ravine (Kashmir, India) and a comparison with other North Indian passive margin sections. *The Depositional Record*, **6**, 75–116.

Brosse, M.; Bucher, H.; Baud, A.; Frisk, Å. M.; Goudemand, N.; Hagdorn, H. et al. 2019. New data from Oman indicate benthic high biomass productivity coupled with low taxonomic diversity in the aftermath of the Permian–Triassic Boundary mass extinction. *Lethaia*, **52**(2), 165–187.

Brühwiler, T.; Goudemand, N.; Galfetti, T.; Bucher, H.; Baud, A.; Ware, D. et al. 2009. The Lower Triassic sedimentary and carbon isotope records from Tulong (South Tibet) and their significance for Tethyan palaeoceanography. *Sedimentary Geology*, **222**(3), 314–332.

Brühwiler, T.; Bucher, H.; Brayard, A. and Goudemand, N. 2010. High-resolution biochronology and diversity dynamics of the Early Triassic ammonoid recovery: the Smithian faunas of the Northern Indian Margin. *Palaeogeography, Palaeoclimatology, Palaeoecology*, **297**(2), 491–501.

Brühwiler, T.; Bucher, H.; Goudemand, N. and Galfetti, T. 2012. Smithian (Early Triassic) ammonoid

faunas from Exotic Blocks from Oman: taxonomy and biochronology. *Palaeontographica Abteilung – Palaozoologie-Stratigraphie*, **296**(1–4), 3–107.

Brunetti, M. and Vérard, C. 2018. How to reduce long-term drift in present-day and deep-time simulations? *Climate Dynamics*, **50**, 4425–4436.

Brunetti, M.; Vérard, C. and Baumgartner, P. O. 2015. Modeling the Middle Jurassic ocean circulation. *Journal of Palaeogeography*, **4**(4), 373–386.

Brunetti, M.; Kasparian, J. and Vérard, C. 2019. Co-existing climate attractors in a coupled aquaplanet. *Climate Dynamics*, **53**, 6293–6308.

Buesseler, K. O.; Boyd, P. W.; Black, E. E. and Siegel, D. A. 2020. Metrics that matter for assessing the ocean biological carbon pump. *Proceedings of the National Academy of Sciences*, **117**(18), 9679–9687.

Buggisch, W.; Joachimski, M. M.; Sevastopulo, G. and Morrow J. R. 2008. Mississippian $\delta^{13}C_{carb}$ and conodont apatite $\delta^{18}O$ records—Their relation to the Late Palaeozoic glaciation. *Palaeogeography, Palaeoclimatology, Palaeoecology*, **268**, 273–292.

Buggisch, W.; Joachimski, M. M.; Lehnert, O.; Bergström, S. M.; Repetski, J. E. and Webers, G. F. 2010. Did intense volcanism trigger the first Late Ordovician icehouse? *Geology*, **38**(4), 327–330.

Cappetta, H. 2012. Chondrichthyes II: Mesozoic and Cenozoic Elasmobranchii teeth. In Schultze, H. P. (ed.). *Handbook of Paleoichthyology 3E. Verlag Dr. Friedrich Pfeil. München, Germany*, 512 p.

Cardoso, C. N.; Sanz-López, J.; Blanco-Ferrera, S.; Lemos, V. B. and Scomazzon, A. K. 2015. Conodont color alteration index and upper Paleozoic thermal history of the Amazonas Basin, Brazil. *Journal of South American Earth Sciences*, **64**(1), 139–151.

Carlson, S. J. 1990. Vertebrate dental structures. In Carter, J. G. (ed.). *Skeletal Biomineralization: Patterns, Processes and Evolutionary Trends. Van Nostrand Reinhold, New York*, pp. 531–556.

Carrillo-Briceño, J. D.; Luz, Z.; Hendy, A.; Kocsis, L.; Aguilera, O. and Vennemann, T. 2019. Neogene Caribbean elasmobranchs: diversity, paleoecology and paleoenvironmental significance of the Cocinetas Basin assemblage (Guajira Peninsula, Colombia). *Biogeosciences*, **16**, 33–56

Carpenter, K. E.; Abrar, M.; Aeby, G.; Aronson, R. B.; Banks, S.; Bruckner, A. et al. 2008. One-third of reef-building corals face elevated extinction risk from climate change and local impacts. *Science*, **321**, 560–563.

Carr, T. R.; Paull, R. K. and Clark, D. L. 1984. Conodont paleoecology and biofacies analysis of the Lower Triassic Thaynes Formation in the Cordilleran Miogeocline. In Clark D. L. (ed.). *Geological Society of America Special Papers*, **196**, 283–294.

Chen, Y.; Jiang, H.; Lai, X.; Yan, C.; Richoz, S.; Liu, X. et al. 2015. Early Triassic conodonts of Jiarong, Nanpanjiang Basin, southern Guizhou Province, South China. *Journal of Asian Earth Sciences*,

105, 104–121.

Chen, Y.; Neubauer, T. A.; Krystyn, L. and Richoz, S. 2016. Allometry in Anisian (Middle Triassic) segminiplanate conodonts and its implications for conodont taxonomy. *Palaeontology*, **59**(5), 597–751.

Chen, Y.; Richoz, S.; Krystyn, L. and Zhang, Z. 2019. Quantitative stratigraphic correlation of Tethyan conodonts across the Smithian–Spathian (Early Triassic) extinction event. *Earth-Science Reviews*, **195**, 37–51.

Chen, Y.; Joachimski, M. M.; Richoz, S.; Krystyn, L.; Aljinović, D.; Smirčić, D. et al. 2021. Smithian and Spathian (Early Triassic) conodonts from Oman and Croatia and their depth habitat revealed. *Global and Planetary Change*, **196**, 103362.

Chew, D. M.; Babechuk, M. G.; Cogné, N.; Mark, C.; O'Sullivan, G. J.; Henrichs, I. A. et al. 2016. (LA,Q)-ICPMS trace-element analyses of Durango and McClure Mountain apatite and implications for making natural LA-ICPMS mineral standards. *Chemical Geology*, **435**, 35–48.

Chhak, K. and Di Lorenzo, E. 2007. Decadal variations in the California Current upwelling cells. *Geophysical Research Letters*, **34**, L14604.

Clark, D. L. 1972. Early Permian crisis and its bearing on Permo–Triassic taxonomy. *Geologica et Paleontologica*, **1**, 147–158.

Clarkson, M. O.; Richoz, S.; Wood, R. A.; Maurer, F.; Krystyn, L.; McGurty, D. J. and Astratti, D. 2013. A new high-resolution δ^{13}C record for the Early Triassic: insights from the Arabian Platform. *Gondwana Research*, **24**(1), 233–242.

Clarkson, M. O.; Kasemann, S. A.; Wood, R. A.; Lenton, T. M.; Daines, S. J.; Richoz, S. et al. 2015. Ocean acidification and the Permo–Triassic mass extinction. *Science*, **348**(6231), 229–232

Clarkson, M. O.; Wood, R. A.; Poulton, S. W.; Richoz, S.; Newton, R. J.; Kasemann, S. A. et al. 2016. Dynamic anoxic ferruginous conditions during the end-Permian mass extinction and recovery. *Nature Communications*, **7**(1), 1–9.

Coplen, T. B. 2007. Calibration of the calcite-water oxygen-isotope geothermometer at Devils Hole, Nevada, a natural laboratory. *Geochimica et Cosmochimica Acta*, **71**, 3948–3957.

Daculsi, G. and Kerebel, L. M. 1980. Ultrastructural study and comparative analysis of fluoride content of enameloid in sea-water and fresh-water sharks. *Archives of Oral Biology*, **25**(3), 145–151.

Dauphin, Y. and Williams, C. T. 2004. Diagenetic trends of dental tissues. *Comptes Rendus Palevol*, **3**(6), 583–590.

Donoghue, P. C. J. 1998. Growth and patterning in the conodont skeleton. *Philosophical Transactions of the Royal Society B*, **353**, 633–666.

Donoghue, P. C. J. 2001. Microstructural variation in conodont enamel is a functional adaptation.

References

Philosophical Transactions of the Royal Society B, **268**, 1691–1698.

Donoghue, P. C. J. and Purnell, M. A. 1999. Growth, function and the conodont fossil record. *Geology*, **27**, 251–254.

Donoghue, P. C. J.; Purnell, M. A.; Aldridge, R. J. and Zhang, S. 2008. The interrelationships of 'complex' conodonts (Vertebrata). *Journal of Systematic Palaeontology*, **6**(2), 119–153.

Drewicz, A. E.; Trayler, R. B.; Holloway, M. E.; Harrigan, C. O. and Kohn, M. J. The interpretability of stable hydrogen isotopes in modern herbivore tooth enamel. *Geochimica et Cosmochimica Acta*, **270**, 84–94.

Ebert, D.; Fowler, S.; Compagno, L. J. V. and Dando, M. 2013. Sharks of the world. *Wild Nature Press Plymouth*. 528 p.

Eiler, J. M. 2011. Paleoclimate reconstruction using carbonate clumped isotope thermometry. *Quaternary Science Reviews*, **30**, 3575–3588.

Eiler, J. M. and Schauble, E. 2004. $^{18}O^{13}C^{16}O$ in Earth's atmosphere. *Geochimica et Cosmochimica Acta*, **68**, 4767–4777.

Elliott, J. 2002. Calcium phosphate biominerals. In Kohn, M. J.; Rakovan, J. and Hughes, J. M. (eds.). Review in Mineralogy and Geochemistry. *Mineralogical Society of America Reviews in Mineralogy and Geochemistry*, **48**, pp. 427–454.

Enax, J.; Prymak, O.; Raabe, D. and Epple, M. 2012. Structure, composition, and mechanical properties of shark teeth. *Journal of Structural Biology*, **178**, 290–299.

Enax, J.; Janus, A. M.; Raabe, D.; Epple, M. and Fabritius, H.-O. 2014. Ultrastructural organization and micromechanical properties of shark tooth enameloid. *Acta Biomaterialia*. **10**, 3959–3968.

Epstein, S.; Buchsbaum, R.; Lowenstam, H. A. and Urey, H. C. 1953. Revised carbonate-water isotopic temperature scale. *Geological Society of America Bulletin*, **64**, 1315–1326.

Epstein, A. G.; Epstein, J. B. and Harris, L. D. 1977. Conodont color alteration – an index to organic metamorphism. *US Geological Survey Professional Papers*, **995**. 27 p.

Fischer, J.; Voigt, S.; Franz, M.; Schneider, J. W.; Joachimski, M.; Tichomirowa, M. et al. 2012. Palaeoenvironments of the late Triassic Rhaetian Sea: implications from oxygen and strontium isotopes of hybodont shark teeth. *Palaeogeography Palaeoclimatology Palaeoecology*, **353–355**, 60–72.

Fischer, J.; Schneider, J. W.; Voigt, S.; Joachimski, M.; Tichomirowa, M.; Tütken, T. et al. 2013. Oxygen and strontium isotopes from fossil shark teeth: environmental and ecological implications for late Palaeozoic European basins. *Chemical Geology*, **342**, 44–62.

Fordham, D. A.; Jackson, S. T.; Brown, S. C.; Huntley, B.; Brook, B. W.; Dahl-Jensen, D. et al. (2020). Using paleo-archives to safeguard biodiversity under climate change. *Science*, **369**(6507), 1072.

Francillon-Vieillot, H.; de Buffrénil, V.; Castanet, J.; Géraudie, J.; Meunier, F. J.; Sire, J. Y. et al. 1990. Microstructure and mineralization of vertebrate skeletal tissues. In Carter, J. G. (ed.). *Skeletal Biomineralization: Patterns, Processes and Evolutionary Trends. Van Nostrand Reinhold, New York*. pp. 471–530.

Galfetti, T.; Bucher, H.; Ovtcharova, M.; Schaltegger, U.; Brayard, A.; Brühwiler T. et al. 2007a. Timing of the Early Triassic carbon cycle perturbations inferred from new U-Pb ages and ammonoid biochronozones. *Earth and Planetary Science Letters*, **258**, 593–604.

Galfetti, T.; Bucher, H.; Brayard, A.; Hochuli, P. A.; Weissert, H.; Guodun, K. et al. 2007b. Late Early Triassic climate change: insights from carbonate carbon isotopes, sedimentary evolution and ammonoid paleobiogeography. *Palaeogeography Palaeoclimatology Palaeoecology*, **243**(3–4), 394–411.

Galfetti, T.; Bucher, H.; Martini, R.; Hochuli, P. A.; Weissert, H.; Crasquin-Soleau, S. et al. 2008. Evolution of Early Triassic outer platform paleoenvironments in the Nanpanjiang Basin (South China) and their significance for the biotic recovery. *Sedimentary Geology*, **204**(1–2), 36–60.

García-Reyes, M.; Sydeman, W. J.; Schoeman, D. S.; Rykaczewski, R. R.; Black, B. A.; Smit, A. J. et al. 2015. Under pressure: climate change, upwelling, and eastern boundary upwelling ecosystems. *Frontiers in Marine Sciences*, **2**, 109.

Ghosh, P.; Adkins, J.; Affek, H.; Balta, B.; Guo, W.; Schauble, E. A. et al. 2006. ^{13}C-^{18}O bonds in carbonate minerals: a new kind of paleothermometer. *Geochimica et Cosmochimica Acta*, **70**, 1439–1456.

Gordon, A. L. 1986. Interocean exchange of thermocline water. *Journal of Geophysical Research*, **91**(4), 5037–5046.

Goudemand, N.; Orchard, M. J.; Urdy, S.; Bucher, H. and Tafforeau, P. 2011. Synchrotron-aided reconstruction of the conodont feeding apparatus and implications for the mouth of the first vertebrates. *Proceedings of the National Academy of Sciences*, **108**(21), 8720–8724.

Goudemand, N.; Romano, C.; Leu, M.; Bucher, H.; Trotter, J. A. and Williams, I. S. 2019. Dynamic interplay between climate and marine biodiversity upheavals during the early Triassic Smithian–Spathian biotic crisis. *Earth-Sciences Reviews*, **195**, 169–178.

Goulding, M.; Venticinque, E.; Ribeiro, M. L. B.; Barthem, R. B.; Leite, R. G.; Forsberg, B. et al. 2019. Ecosystem-based management of Amazon fisheries and wetlands. *Fish and Fisheries*, **20**, 138–158.

Grasby, S. E.; Beauchamp, B.; Embry, A. F. and Sanei, H. 2013. Recurrent Early Triassic ocean anoxia. *Geology*, **41**, 175–178.

Grasby, S. E.; Beauchamp, B. and Knies, J. 2016. Early Triassic productivity crises delayed recovery from world's worst mass extinction. *Geology*, **44**(9), 779–782.

References

Grasby, S. E.; Knies, J.; Beauchamp, B.; Bond, D. P. G.; Wignall, P. and Sun, Y. 2020. Global warming leads to Early Triassic nutrient stress across northern Pangea. *GSA Bulletin*, **132**(5–6), 943–954.

Grossman, E. L. and Joachimski, M. M. 2020. Oxygen Isotope Stratigraphy. In *Geologic Time Scale 2020. Elsevier*, 279–307.

Gruber, N. 2011. Warming up, turning sour, losing breath: ocean biogeochemistry under global change. *Philosophical Transactions of the Royal Society A*, **369**, 1980–1996.

Guex, J. and Davaud, E. 1984. Unitary associations method: use of graph theory and computer algorithm. *Computers and Geosciences*, **10**(1), 69–96.

Guinotte, J. M. and Fabry, V. J. 2008. Ocean acidification and its potential effects on marine ecosystems. *Annals of the New York Academy of Sciences*, **1134**, 320–342.

Hammer, Ø.; Jones, M. T.; Schneebeli-Hermann, E.; Hansen, B.-B. and Bucher, H. 2019. Are Early Triassic extinction events associated with mercury anomalies? A reassessment of the Smithian/ Spathian boundary extinction. *Earth-Science Reviews*, **195**, 179–190.

Haq, B. U. 2018. Triassic eustatic variations reexamined. *GSA Today*, **28**, 4–9.

Hauser, M.; Martini, R.; Matter, A.; Krystyn, L.; Peters, T.; Stampfli, G. and Zaninetti, L. 2002. The break-up of East Gondwana along the northeast coast of Oman: evidence from the Batain basin. *Geological Magazine*, **139**(2), 145–157.

Hautmann, M.; Bagherpour, B.; Brosse, M.; Frisk, Å.; Hofmann, R.; Baud, A. et al. 2015. Competition in slow motion: the unusual case of benthic marine communities in the wake of the end-Permian mass extinction. *Palaeontology*, **58**(5), 871–901.

Helser, T. E.; Kastelle, C. R.; McKay, J. L.; Orland, I. J.; Kozdon, R. and Valley, J. W. 2018. Evaluation of micromilling/conventional isotope ratio mass spectrometry and secondary ion mass spectrometry of $\delta^{18}O$ values in fish otoliths for sclerochronology. *Rapid Communications in Mass Spectrometry*, **32**(20), 1781–1790.

Hermann, E.; Hochuli, P. A.; Méhay, S.; Bucher, H.; Brühwiler, T.; Ware, D. et al. 2011. Organic matter and palaeoenvironmental signals during the Early Triassic biotic recovery: The Salt Range and Surghar Range records. *Sedimentary Geology*, **234**, 19–41.

Hochuli, P. A.; Sanson-Barrera, A.; Schneebeli-Hermann, E. and Bucher, H. 2016. Severest crisis overlooked—Worst disruption of terrestrial environments postdates the Permian–Triassic mass extinction. *Scientific Reports*, **6**, 28372.

Hofmann, M. and Schellnhuber, H-J. 2009. Oceanic acidification affects marine carbon pump and triggers extended marine oxygen holes. *Proceedings of the National Academy of Sciences*, **106**(9), 3017–3022.

Horne, D. J. 1999. Ocean Circulation modes of the Phanerozoic: implications for the antiquity of deep-

sea benthonic invertebrates. *Crustaceana*, **72**(8), 999–1018.

Hughes, J. M. and Rakovan, J. F. 2015. Structurally Robust, Chemically Diverse: Apatite and Apatite Supergroup Minerals. *Elements*, **11**, 165–170.

Hull, P. M. and Darroch, S. A. F. 2013. Mass extinctions and the structure and function of ecosystems. In Bush, A. M.; Pruss, S. B. and Payne, J. L. (eds.). *Ecosystem Paleobiology and Geobiology. The Paleontological Society Papers*, **19**, pp. 115–156.

Iacumin, P.; Bocherens, H.; Mariotti, A. and Longinelli, A. 1996. Oxygen isotope analyses of co-existing carbonate in biogenic apatite: a way to monitor diagenetic bone phosphate? *Earth and Planetary Science Letters*, **142**, 1–6.

Immenhauser, A. M.; Schreurs, G.; Peters, T.; Matter, A.; Hauser, M. and Dumitrica, P. 1998. Stratigraphy, sedimentology and depositional environments of the Permian to uppermost Cretaceous Batain Group. *Eclogae Geologicae Helvetiae*, **91**(2), 217–236.

Intergovernmental Panel on Climate Change. 2019. IPCC Special Report on the Ocean and Cryosphere in a Changing Climate. [Pörtner, H.-O.; Roberts, D. C.; Masson-Delmotte, V.; Zhai, P.; Tignor, M.; Poloczanska, E. et al. (eds.)]. *Cambridge University Press, Cambridge, UK and New York, NY, USA*. 755 p.

Isozaki, Y. 1997. Permo–Triassic boundary superanoxia and stratified superocean: records from lost deep sea. *Science*, **276**(5310), 235–238.

Jacox, M. G. and Edwards, C. A. 2011. Effects of stratification and shelf slope on nutrient supply in coastal upwelling regions. *Journal of Geophysical Research Atmospheres*, **116**(3), C03019.

Jacox, M. G.; Bograd, S. J.; Hazen, E. L. and Fiechter, J. 2015. Sensitivity of the California Current nutrient supply to wind, heat, and remote ocean forcing. *Geophysical Research Letters*, **42**(14), 5950–5957.

Jattiot, R.; Bucher, H.; Brayard, A.; Monnet, C.; Jenks, J. F. and Hautmann, M. 2015. Revision of the genus *Anasibirites* Mojsisovics (Ammonoidea): an iconic and cosmopolitan taxon of the late Smithian (Early Triassic) extinction. *Papers in Palaeontology*, **2**(1), 155–188.

Jattiot, R.; Brayard, A.; Bucher, H.; Vennin, E.; Caravaca, G.; Jenks, J. F. et al. 2018. Palaeobiogeographical distribution of Smithian (early Triassic) ammonoid faunas within the western USA basin and its controlling parameters. *Palaeontology*, **61**, 881–904.

Jeppson, L. 1979. Conodont element function. *Lethaia*, **12**, 153–171.

Joachimski, M. M. and Lambert, L. 2015. Salinity contrast in the US Midcontinent Sea during Pennsylvanian glacio-eustatic highstands: Evidence from conodont apatite δ^{18}O. *Palaeogeography Palaeoclimatology Palaeoecology*, **433**, 71–80.

Joachimski, M. M.; Breisig, S.; Buggisch, W.; Talent, J. A.; Mawson, R.; Gereke, M. et al. 2009.

References

Devonian climate and reef evolution: Insights from oxygen isotopes in apatite. *Earth and Planetary Science Letters*, **284**, 599–609.

Joachimski, M. M.; Lai, X. L.; Shen, S. Z.; Jiang, H. S.; Luo, G. M.; Chen, B. et al. 2012. Climate warming in the latest Permian and the Permian–Triassic mass extinction. *Geology*, **40**(3), 195–198.

Jones, D.; Evans, A. R.; Rayfield, E. J.; Siu, K. K. W. and Donoghue, P. C. J. 2012. Testing microstructural adaptation in the earliest dental tools. *Biology Letters*, **8**, 952–955.

Jones, G. L. 1992. Irish Carboniferous conodonts record maturation levels and the influence of tectonism, igneous activity and mineralization. *Terra Nova*, **4**(2), 238–244.

Kämpf, J. and Chapman, P. 2016. The Functioning of Coastal Upwelling Systems. In Upwelling systems of the world. *Springer International Publishing Switzerland*. pp. 31–66.

Katvala, E. C. and Henderson, C. 2012. Chemical element distributions within conodont elements and their functional implications. *Paleobiology*, **38**(3), 447–458.

Kiessling, W.; Raja, N. B.; Roden, V. J.; Turvey, S. T. and Saupe, E. E. 2019. Addressing priority questions of conservation science with palaeontological data. *Philosophical Transactions of the Royal Society B*, **374**, 20190222.

Kim, S.-T. and O'Neil, J. R. 1997. Equilibrium and nonequilibrium oxygen isotope effects in synthetic carbonates. *Geochimica et Cosmochimica Acta*, **61**, 3461–3475.

Kirsanow, K.; Makarewicz, C. and Tuross, N. 2008. Stable oxygen (δ^{18}O) and hydrogen (δD) isotopes in ovicaprid dentinal collagen record seasonal variation. *Journal of Archaeological Science*, **35**(12), 3159–3167.

Kita, N. T.; Ushikubo, T.; Fu, B. and Valley, J. W. 2009. High precision SIMS oxygen isotope analysis and the effect of sample topography. *Chemical Geology*, **264**, 43–57.

Klug, S.; Tütken, T.; Wings, O.; Hans-Ulrich, P. and Martin, T. 2010. A Late Jurassic freshwater shark assemblage (Chondrichthyes, Hybodontiformes) from the southern Junggar Basin, Xinjiang, Northwest China. *Palaeobiodiversity and Palaeoenvironments*, **90**, 241–257.

Knoll, A. H.; Bambach, R. K.; Payne, J. L.; Pruss, S. and Fischer, W. W. 2007. Paleophysiology and end-Permian mass extinction. *Earth and Planetary Science Letters*, **256**(3–4), 295–313.

Koch P. L.; Tuross N. and Fogel M. L. 1997. The effects of sample treatment and diagenesis on the isotopic integrity of carbonate in biogenic hydroxylapatite. *Journal of Archaeological Science*, **24**, 417–429.

Kocsis, L. 2011. Geochemical compositions of marine fossils as proxies for reconstructing ancient environmental conditions. *Chimia*, **65**(10), 787–791.

Kocsis, L.; Vennemann, T. and Fontignie, D. 2007. Migration of sharks into freshwater systems during

the Miocene and implications for Alpine paleoelevation. *Geology*, **35**, 451–454.

Kocsis, L.; Gheerbrant, E.; Mouflih, M.; Cappetta, H.; Yans, J. and Amaghzaz, M. 2014. Comprehensive stable isotope investigation of marine biogenic apatite from the late Cretaceous-early Eocene phosphate series of Morocco. *Palaeogeography Palaeoclimatology Palaeoecology*, **394**, 74–88.

Kocsis, L.; Vennemann, T. W.; Ulianov, A. and Brunnschweiler, J. M. 2015. Characterizing the bull shark *Carcharhinus leucas* habitat in Fiji by the chemical and isotopic compositions of their teeth. *Environmental Biology of Fishes*, **98**(6), 1609-1622.

Kohn, M. J. 2008. Models of diffusion-limited uptake of trace elements in fossils and rates of fossilisation. *Geochimica et Cosmochimica Acta*, **72**, 3758–3770.

Kohn, M. J. and Cerling, T. E. 2002. Stable isotope compositions of biological apatite. In Kohn, M. J.; Rakovan, J. and Hughes, J. M. (eds.). *Review in Mineralogy and Geochemistry*, **48**, pp. 455–488.

Kohn, M. J.; Schoeninger, M. J. and Barker, W. W. 1999. Altered states: effects of diagenesis on fossil tooth chemistry. *Geochimica et Cosmochimica Acta*, **63**, 2737–2747.

Kolodny, Y. and Luz, B. 1991. Oxygen isotopes in phosphates of fossil fish—Devonian to recent. In Taylor, H. P.; O'Neil, J. R. and Kaplan, I. R. (eds.). *Stable Isotope Geochemistry: A Tribute to Samuel Epstein. Geochemical Society, Washington, D.C.*, pp. 65–76.

Kolodny, Y.; Luz, B. and Navon, O. 1983. Oxygen isotope variations in phosphate of biogenic apatites, I. Fish bone apatite—rechecking the rules of the game. *Earth and Planetary Science Letters*, **64**, 398–404.

Krystyn, L.; Richoz, S.; Baud, A. and Twitchett, R. J. 2003. A unique Permian–Triassic boundary section from the neotethyan Hawasina basin, Central Oman Mountains. *Palaeogeography Palaeoclimatology Palaeoecology*, **191**(3–4), 329–344.

Latif, M.; Böning, C.; Willebrand, J.; Biastoch, A.; Dengg, J.; Keenlyside, et al. 2006. Is the thermohaline circulation changing? *Journal of Climate*, **19**, 4631–4637.

Lécuyer, C. 2004. Oxygen Isotope Analysis of Phosphate. In Groot, P. (ed.). Handbook of Stable Isotope Analytical Techniques. *Elsevier*, chapter 22, pp. 482–499.

Lécuyer, C.; Picard, S.; Garcia, J-P.; Sheppard, S. M. F.; Grandjean, P. and Dromart, G. 2003. Thermal evolution of Tethyan surface waters during the Middle-Late Jurassic: Evidence from δ^{18}O values of marine fish teeth. *Paleoceanography*, **18**(3), 1076.

Lécuyer, C.; Balter, V.; Martineau, F.; Fourel, F.; Bernard, A.; Amiot, R. et al. 2010. Oxygen isotope fractionation between apatite-bound carbonate and water determined from controlled experiments with synthetic apatites precipitated at 10–37 °C. *Geochimica et Cosmochimica Acta*, **74**, 2072–2081.

Lécuyer, C.; Amiot, R.; Touzeau, A. and Trotter, J. 2013. Calibration of the phosphate δ^{18}O thermometer

with carbonate-water oxygen isotope fractionation equations. *Chemical Geology*, **347**, 217–226.

LeGeros, R. Z. 1981. Apatites in biological systems. *Progress in Crystal Growth and Characterization of Materials*, **4**(1-2), 1–45.

LeGrande, A. and Schmidt, G. 2006. Global gridded data set of the oxygen isotopic composition in seawater. *Geophysical Research Letters*, **33**, L12604.

Leonhard, I.; Shirley, B.; Murdock, D. J. E.; Repetski, J. and Jarochowska, E. 2021. Growth and feeding ecology of coniform conodonts. *PeerJ*, **9**(4), e12505.

Leu, M. 2021. Conodont taxonomy, quantitative biochronology and evolutionary trends during the Smithian–Spathian interval (Early Triassic). *PhD-thesis*. University of Zurich, Switzerland.

Leu, M.; Bucher, H. and Goudemand, N. 2019. Clade-dependent size response of conodonts to environmental changes during the late Smithian extinction. *Earth-Science Reviews*. **195**, 52–67.

Leuzinger, L.; Kocsis, L.; Billon-Bruyat, J.-P.; Spezzaferri, S. and Vennemann, T. 2015. Stable isotope study of a new chondrichthyan fauna (Kimmeridgian, Porrentruy, Swiss Jura): an unusual freshwater-influenced isotopic composition for the hybodont shark *Asteracanthus*. *Biogeosciences*, **12**, 6945–6954.

Li, Y.; Tang, G. Q.; Liu, Y.; He, S.; Chen, B.; Li, Q. L. and Li, X. H. 2021. Revisiting apatite SIMS oxygen isotope analysis and Qinghu-AP reference material. *Chemical Geology*, **582**, 120445.

Lindström, M. 1970. A suprageneric taxonomy of the conodonts. *Lethaia*, **3**(4), 427–445.

Linzmeier, B.; Tobin, T.; Ward, P.; Orland, I. J.; Assing, D.; Kitajima, K. et al. 2020. High spatial-resolution assessment of diagenesis and primary isotopic variability in Maastrichtian molluscan carbonates from Antarctica. *Microscopy and Microanalysis*, **26** (S2). 300–301.

Longinelli, A. and Nuti, S. 1973a. Revised phosphate-water isotopic temperature scale. *Earth and Planetary Science Letters*, **19**, 373–376.

Longinelli, A. and Nuti, S. 1973b. Oxygen isotope measurements of phosphate from fish teeth and bones. *Earth and Planetary Science Letters*, **20**, 337–340.

Luz, B.; Kolodny, Y. and Kovach, J. 1984. Oxygen isotope variations in phosphate of biogenic apatites, III. Conodonts. *Earth and Planetary Science Letters*, **69**, 255–262.

Macarewich, S. I.; Poulsen, C. J. and Montañez, I. P. 2021. Simulation of oxygen isotopes and circulation in a late Carboniferous epicontinental sea with implications for proxy records. *Earth and Planetary Science Letters*, **559**, 116770.

MacLeod, N. 2013. The Great Extinctions: What Causes Them and How They Shape Life. *The Natural History Museum, London*, 208 p.

MacLeod, N. 2014. The geological extinction record: History, data, biases, and testing. In Keller, G. and Kerr, A. C. (eds.). Volcanism, Impacts, and Mass Extinctions: Causes and Effects. *Geological*

Society of America Special Paper, **505**, 1–28.

Maekawa, T.; Komatsu, T. and Koike, T. 2018. Early Triassic conodonts from the Tahogawa Member of the Taho Formation, Ehime Prefecture, Southwest Japan. *Paleontological Research*, **22**(s1), 1–62

Marin-Carbonne, J.; Kiss, A.; Bouvier, A.-S.; Meibom, A.; Baumgartner, L.; Bovay, T. et al. 2022. Surface analysis by secondary ion mass spectrometry (SIMS): principles and applications from Swiss laboratories. *Chimia*, **76**, 26–33.

Marshall, J.; Adcroft, A.; Hill, C.; Perelman, L. and Heisey, C. 1997a. A finite-volume, incompressible Navier Stokes model for studies of the ocean on parallel computers. *Journal of Geophysical Research*, **102**, 5753–5766.

Marshall, J.; Hill, C.; Perelman, L. and Adcroft, A. 1997b. Hydrostatic, quasi-hydrostatic, and nonhydrostatic ocean modeling. *Journal of Geophysical Research*, **102**, 5733–5752.

Marshall, P. A. and Baird, A. H. 2000. Bleaching of corals of the Great Reef Barrier: differential susceptibilities among taxa. *Coral Reefs*, **19**, 155–163.

Martindale, R. C.; Corsetti, F. A.; James, N. P. and Bottjer, D. J. 2014. Paleogeographic trends in Late Triassic reef ecology from northeastern Panthalassa. *Earth-Science Reviews*, **142**, 18–37.

Martínez-Pérez, C.; Plasencia, P.; Jones, D.; Kolar-Jurkovšek, T.; Sha, J.; Botella, H. and Donoghue, P. C. J. 2014. There is no general model for occlusal kinematics in conodonts. *Lethaia*, **47**, 547–555.

Martínez-Pérez, C.; Rayfield, E. J.; Botella, H. and Donoghue, P. C. J. 2016. Translating taxonomy into the evolution of conodont feeding ecology. *Geology*, **44**(4), 247–250.

McClain, M. E. and Naiman, R. J. 2008. Andean Influences on the Biogeochemistry and Ecology of the Amazon River. *BioScience*, **58**(4), 325–338.

McConnell, D. 1973. Apatite: Its Crystal Chemistry, Mineralogy, Utilization, and Geologic and Biologic Occurrences. *Springer-Verlag, New York.* 111 p.

Meyer, K. M.; Yu, M.; Jost, A. B.; Kelley, B. M. and Payne, J. L. 2011. $\delta^{13}C$ evidence that high primary productivity delayed recovery from end-Permian mass extinction. *Earth and Planetary Science Letters*, **302**(3–4), 378–384.

Meyer, K. M.; Ridgwell, A. and Payne, J. L. 2016. The influence of the biological pump on ocean chemistry: implications for long-term trends in marine redox chemistry, the global carbon cycle, and marine animal ecosystems. *Geobiology*, **14**, 207–219.

Michener, R. and Lajtha, K. 2007. Stable isotopes in ecology and environmental science. *Oxford, Blackwell Scientific Publications*, 316 p.

Mine, A. H.; Waldeck, A.; Olack, G.; Hoerner, M. E.; Alex, S. and Colman, A. S. 2017. Microprecipitation

References

and δ^{18}O analysis of phosphate for paleoclimate and biogeochemistry research. *Chemical Geology*, **460**, 1–14.

Mohan, J. A.; Miller, N. R.; Herzka, S. Z.; Sosa-Nishizaki, O.; Kohin, S.; Dewar, H. et al. 2018. Elements of time and place: manganese and barium in shark vertebrae reflect age and upwelling histories. *Proceedings of the Royal Society B*, **285**(1890), 20181760.

Murdock, D. J. E.; Dong, X.-P.; Repetski, J. E.; Marone, F.; Stampanoni, M. and Donoghue, P. C. J. 2013. The origin of conodonts and of vertebrate mineralized skeletons. *Nature*, **502**, 546–549.

Narvekar, J.; Chowdhury, R. R.; Gaonkar, D.; Dinesh Kumar, P. K. and Prasanna Kumar, S. 2021. Observational evidence of stratification control of upwelling and pelagic fishery in the eastern Arabian Sea. *Scientific Reports*, **11**, 7293.

Orchard, M. J. 1995. Taxonomy and correlation of Lower Triassic (Spathian) segminate conodonts from Oman and revision of some species of *Neospathodus*. *Journal of Paleontology*, **69**(1), 110–122

Orchard, M. J. 1996. Conodont fauna from the Permian–Triassic boundary: observations and reservations. *Permophiles*, **28**, 29–35.

Orchard, M. J. 2005. Multielement conodont apparatuses of Triassic Gondolelloidea. *Special Papers in Paleontology*, **73**, 73–101.

Orchard, M. J. 2007. Conodont diversity and evolution through the latest Permian and Early Triassic upheavals. *Palaeogeography Palaeoclimatology Palaeoecology*, **252**(1), 93–117.

Orchard, M. J. 2008. Lower Triassic conodonts from the Canadian Arctic, their intercalibration with ammonoid-based stages, and a comparison with other North American Olenekian faunas. *Polar Research*, **27**(3), 393–412.

Orchard, M. J. and Zonneveld, J.-P. 2009. The Lower Triassic Sulphur Mountain Formation in the Wapiti Lake area: lithostratigraphy, conodont biostratigraphy, and a new biozonation for the lower Olenekian (Smithian). *Canadian Journal of Earth Sciences*, **46**, 757–790.

Orland, I. J.; Kozdon, R.; Linzmeier, B.; Wycech, J.; Śliwiński, M. G.; Kitajima, K. et al. 2015. Enhancing the accuracy of carbonate δ^{18}O and δ^{13}C measurements by SIMS. *AGU Fall 2015 Meeting, (San Francisco, USA)*, Paper number: PP52B-03.

Papastamatiou Y. P.; Watanabe, Y. Y.; Bradley, D.; Dee, L. E.; Weng, K.; Lowe, C. G. et al. 2015. Drivers of Daily Routines in an Ectothermic Marine Predator: Hunt Warm, Rest Warmer? *PLoS ONE*, **10**(6): e0127807.

Passow, U. and Carlson, C. A. 2012. The biological pump in a high CO_2 world. *Marine Ecology Progress Series*, **470**, 249–271.

Paull, R. K. and Paull, R. A. 1997. Transgressive conodont faunas of the early Triassic: an opportunity for correlation in the Tethys and the circum-Pacific. In Dickins, J. M.; Zunyi, Y.; Hongfu, Y.;

Lucas, S. G. and Acharyya, S. K. (eds.). Late Palaeozoic and Early Mesozoic circum-Pacific events and their global correlation. *World and Regional Geology*, **10**, *Cambridge University Press, New York*, pp. 158-167.

Payne, J. L.; Lehrmann, D. J.; Wei, J. Y.; Orchard, M. J.; Schrag, D. P. and Knoll, A. H. 2004. Large perturbations of the carbon cycle during recovery from the end-Permian extinction. *Science*, **305**, 506–509.

Payne, J. L. and Kump, L. R. 2007. Evidence for recurrent early Triassic massive volcanism from quantitative interpretation of carbon isotope fluctuations. *Earth and Planetary Science Letters*, **256**(1), 264–277.

Payne, J. L. and Clapham, M. T. 2012. End-Permian Mass Extinction in the Oceans: An Ancient Analog for the Twenty-First Century? *Annual Review of Earth and Planetary Sciences*, **40**, 89–111.

Pereira, A. L. and Benedito, E. 2007. Isótopos estáveis em estudos ecológicos: métodos, aplicações e perspectivas. *Revista Biociências*, **13**(1–2), 16–27.

Peters, T.; Al-Battashy, M.; Bläsi, H.; Hauser, M.; Immenhauser, A.; Moser, L. and Al-Rajhi, A. 2001. Geological map of Sur and Al Ashkharah, Sultanate of Oman Ministry of Commerce and Industry, *Directorate General of Minerals*. Sheet NF 40–8F and Sheet NF 40–12C, Scale 1: 100,000, Explanatory Notes.

Pietzner, H.; Vahl, J.; Werner, H. and Ziegler, W. 1968. Zur chemischen Zusammensetzung und Mikromorphologie der Conodonten. *Palaeontographica, Abteilung A, Palaozoologie-Stratigraphie*, **128**, 115–152.

Posner, A. S.; Blumenthal, N. C. and Betts, F. 1984. Chemistry and structure of precipitated hydroxyapatites In Nriaga, J. O. and Moore, P. B. (eds.). *Phosphate Minerals. Springer Verlag, Berlin*, pp. 330–350.

Pucéat, E.; Joachimski, M.; Bouilloux, A.; Monna, F.; Bonin, A.; Montreuil, S. et al. 2010. Revised phosphate-water fractionation equation reassessing paleotemperatures derived from biogenic apatite. *Earth and Planetary Science Letters*, **298**, 135–142.

Purnell, M. A. and Jones, D. 2012. Quantitative analysis of conodont tooth wear and damage as a test of ecological and functional hypotheses. *Paleobiology*, **38**(4), 605–626.

Raiswell, R. 1997. A geochemical framework for the application of stable sulphur isotopes to fossil pyritization. *Journal of the Geological Society*, **154**, 343–356.

Rakovan, J. 2002. Growth and surface properties of apatite. In Kohn, M. J.; Rakovan, J. and Hughes, J. M. (eds.). Phosphates: geochemical, geobiological, and materials importance. *Reviews in Mineralogy and Geochemistry, Mineralogical Society of America, Washington*. pp. 51–86.

Richoz, S. 2006. Stratigraphie et variations isotopiques du carbone dans le Permien supérieur et le Trias

inférieur de quelques localités de la Néotéthys (Turquie, Oman et Iran). *Mémoires de Géologie, Société Académique Vaudoise, Lausanne*. **46**, 251 p.

Richoz, S.; Baud, A.; Krystyn, L.; Twitchett, R. and Marcoux, J. 2005. Permo–Triassic deposits of the Oman Mountains: from basin and slope to the shallow platform. In *24th IAS regional Meeting. International Association of Sedimentologists*. Muscat, Oman. 58 p.

Richoz, S.; Krystyn, L.; Baud, A.; Brandner, R.; Horacek, M. and Mohtat-Aghai, P. 2010a. Permian–Triassic boundary interval in the Middle East (Iran and N. Oman): Progressive environmental change from detailed carbonate carbon isotope marine curve and sedimentary evolution. *Journal of Asian Earth Sciences*, **39**(4), 236–253.

Richoz, S.; Krystyn, L.; Weidlich, O.; Baud, A.; Beauchamp, B.; Bernecker, M. et al. 2010b. The Permian–Triassic transition in the Oman Mountains: Transect of the Tethyan margin from shallow to deepwater deposits. In Baud, A. and Bernecker, M. (eds.). *IGCP 572 Field Guide Book 2*. vol. 572. 109 p.

Richoz, S.; Baud, A.; Beauchamp, B.; Grasby, S. E.; Henderson, C. M. and Krystyn, L. 2014. Khuff Margin: Slope to Oceanic Deposits (Permian–Triassic Allochthons and Exotics, Oman). In Pöppelreiter, M. (ed.). Permo–Triassic Sequence of the Arabian Plate. *EAGE Publisher*. Chap. 4, 55–76.

Riebesell, U.; Zondervan, I.; Rost, B.; Tortell, P. D.; Zeebe, R. E. and Morel, F. M. M. 2000. Reduced calcification of marine plankton in response to increased atmospheric CO_2. *Nature*, **407**, 364–367.

Rigo, M.; Trotter, J. A.; Preto, N. and Williams, I. S. 2012. Oxygen isotopic evidence for Late Triassic monsoonal upwelling in the northwestern Tethys. *Geology*, **40**(6), 515–518.

Roberts, G. and Mannion, P. D. 2019. Timing and periodicity of Phanerozoic marine biodiversity and environmental change. *Scientific Reports*, **9**, 6116.

Roger, J.; Béchennec, F.; Janjou, D.; Le Métour, J.; Wyns R. and Beurrier, M. 1991. Geological map of Ja'alan. *Directorate General of Minerals, Ministry of Petroleum and Minerals*. Sheet NF 40–08E, scale 1:100.000, with Explanatory Notes.

Rollion-Bard, C. and Marin-Carbonne, J. 2011. Determination of SIMS matrix effects on oxygen isotopic compositions in carbonates. *Journal of Analytical Atomic Spectrometry*, **26**, 1285–1289.

Romano, C.; Goudemand, N.; Vennemann, T. W.; Ware, D.; Schneebeli-Hermann, E.; Hochuli, P. A. et al. 2013. Climatic and biotic upheavals following the end-Permian mass extinction. *Nature Geoscience*, **6**(1), 57–60.

Rothschild, L. and Mancinelli, R. 2001. Life in extreme environments. *Nature*, **409**, 1092–1101.

Rozanski, K.; Araguas-Araguas, L. and Gonfiantini, R. 1993. Isotopic patterns in modern global

precipitation. In Swart, P. K.; Lohmann, K. C.; McKenzie, J. and Savin, S. (eds.). Climate change in continental isotopic records. *Geophysical Monograph*, **78**. *American Geophysical Union*, 1–37.

Schmidtko, S.; Stramma, L. and Visbeck, M. 2017. Decline in global oceanic oxygen content during the past five decades. *Nature*, **542**, 335–339.

Schneebeli-Hermann, E.; Bagherpour, B.; Vennemann, T.; Leu, M. and Bucher, H. 2020. Sedimentary organic matter from a cored Early Triassic succession, Georgetown (Idaho, USA). *Swiss Journal of Palaeontology*, **139**(5), 1–16.

Scotese, C. R.; Song, H.; Mills, B. J. W. and van de Meer, D. G. 2021. Phanerozoic paleotemperatures: The earth's changing climate during the last 540 million years. *Earth-Science Reviews*, **215**, 103503.

Shen, J.; Algeo, T. J.; Planavsky, N. J.; Yu, J.; Feng, Q.; Song, H. et al. 2019. Mercury enrichments provide evidence of Early Triassic volcanism following the end-Permian mass extinction. *Earth-Science Reviews*, **195**, 191–212.

Shirley, B.; Grohganz, M.; Bestmann, M. and Jarochowska, E. 2018. Wear, tear and systematic repair: testing models of growth dynamics in conodonts with high-resolution imaging. *Proceedings of the Royal Society B*, **285**, 20181614.

Shirley, B.; Bestmann, M. and Jarochowska, E. 2020. The cono-dos and cono-dont's of phosphatic microfossil preparation and microanalysis. *Micron*, **138**, 102924.

Sisma-Ventura, G.; Tütken, T.; Peters, S. T. M.; Bialik, O. M.; Zohar, I. and Pack, A. 2019. Past aquatic environments in the Levant inferred from stable isotope compositions of carbonate and phosphate in fish teeth. *PLoS One*, **14**(7): e0220390.

Skinner, W. C. H. and Jahren, A. H. 2007. Biomineralization. In Holland, H. D. and Turekian, K. K. (eds.). *Treatise on Geochemistry*, chapter 8.04, pp. 1–69.

Śliwiński, M. G.; Kitajima, K.; Spicuzza, M. J.; Orland, I. J.; Ishida, A.; Fournelle, J. H. and Valley, J. W. 2018. SIMS bias on isotope ratios in Ca-Mg-Fe carbonates (Part III): δ^{18}O and δ^{13}C matrix effects along the magnesite-siderite solid-solution series. *Geostandards and Geoanalytical Research*, **42**(1), 49–76.

Song, H.; Tong, J. and Chen, Z. Q. 2011. Evolutionary dynamics of the Permian–Triassic foraminifer size: evidence for Lilliput effect in the end-Permian mass extinction and its aftermath. *Palaeogeography Palaeoclimatology Palaeoecology*, **308**(1), 98–110.

Song, H.; Wignall, P. B.; Chu, D.; Tong, J.; Sun, Y.; Song, H. et al. 2014. Anoxia/high temperature double whammy during the Permian-Triassic marine crisis and its aftermath. *Scientific Reports*, **4**, 4132.

References

Song, H.; Du, Y.; Algeo, T. J.; Tong, J.; Owens, J. D.; Song, H. et al. 2019. Cooling-driven oceanic anoxia across the Smithian/Spathian boundary (mid-Early Triassic). *Earth-Science Reviews*, **195**, 133–146.

Souquet, L. and Goudemand, N. 2020. Exceptional basal-body preservation in some Early Triassic conodont elements from Oman. *Palaeogeography Palaeoclimatology Palaeoecology*, **549**, 109066.

Stolper, D. A. and Eiler, J. M. 2015. The kinetics of solid-state isotope-exchange reactions for clumped isotopes: A study of inorganic calcites and apatites from natural and experimental samples. *American Journal of Science*, **315**, 363–411.

Sturrock, A. M.; Trueman, C. N.; Darnaude, A. M. and Hunter, E. 2012. Can otolith elemental chemistry retrospectively track migrations in fully marine fishes? *Journal of Fish Biology*, **81**, 766–795.

Sun, Y.; Joachimski. M. M.; Wignall, P. B.; Yan, C.; Chen, Y.; Jiang, H. et al. 2012. Lethally hot temperatures during the Early Triassic greenhouse. *Science*, **338**(6105), 366–370.

Sun, Y.; Wiedenbeck, M.; Joachimski, M. M.; Beier, C.; Kemner, F. and Weinzierl, C. 2016. Chemical and oxygen isotope composition of gem-quality apatites: Implications for oxygen isotope reference materials for secondary ion mass spectrometry (SIMS). *Chemical Geology*, **440**, 164-178.

Sweet, W. C. 1988. The Conodonta: Morphology, Taxonomy, Paleoecology, and Evolutionary History of a Long-Extinct Animal Phylum. *Oxford Monographs on Geology and Geophysics*, **10**. Clarendon Press, New York. 212 p.

Sweet, W. C. and Bergström, S. M. 1984. Conodont provinces and biofacies of the Late Ordovician. In Clark D. L. (ed.). Conodont biofacies and provincialism. *Geological Society of America Special Paper*, **196**, 69–87.

Sweet, W. C. and Donoghue, P. C. J. 2001. Conodonts: Past, Present and Future. *Journal of Palaeontology*, **75**, 1174–1184.

Tamburini, F.; Föllmi, K.; Adatte, T.; Bernasconi, S. M. and Steinmann, P. 2003. Sedimentary phosphorus record from the Oman margin: New evidence of high productivity during glacial periods. *Paleoceanography*, **18**(1), 1015.

Trotter, J. A. and Eggins, S. M. 2006. Chemical systematics of conodont apatite determined by laser ablation ICPMS. *Chemical Geology*, **233**, 196–216.

Trotter, J. A.; Fitz Gerald, J. D.; Kokkonen, H. and Barnes, C. R. 2007. New insights into the ultrastructure, permeability, and integrity of conodont apatite determined by transmission electron microscopy. *Lethaia*, **40**, 97–110.

Trotter, J. A.; Williams, I. S.; Barnes, C. R.; Lécuyer, C. and Nicoll, R. S. 2008. Did cooling oceans trigger Ordovician biodiversification? Evidence from conodont thermometry. *Science*, **321**,

550–554

Trotter, J. A.; Williams, I. S.; Nicora, A.; Mazza, M. and Rigo, M. 2015. Long-term cycles of Triassic climate change: a new δ^{18}O record from conodont apatite. *Earth and Planetary Science Letters*, **415**, 165–174.

Trotter, J. A.; Williams, I. S.; Barnes, C. R.; Männik, P. and Simpson, A. 2016a. New conodont δ^{18}O records of Silurian climate change: Implications for environmental and biological events. *Palaeogeography Palaeoclimatology Palaeoecology*, **443**, 34–48.

Trotter, J. A.; Barnes, C. R. and McCracken, A. D. 2016b. Rare earth elements in conodont apatite: Seawater or pore-water signatures? *Palaeogeography Palaeoclimatology Palaeoecology*, **462**, 92–100.

Trueman, C. N. and Tuross, N. 2002. Trace elements in recent and fossil bone apatite. In Kohn, M. J.; Rakovan, J. and Hughes, J. M. (eds.). Phosphates: Geochemical, Geobiological and Materials Importance. *Mineralogical Society of America Reviews in Mineralogy and Geochemistry*, **48**, pp. 489–521.

Turchyn, A. V. and DePaolo, D. J. 2019. Seawater Chemistry Through Phanerozoic Time. *Annual Review of Earth and Planetary Sciences*, **47**, 197–224.

Turner, S.; Burrow, C. J.; Schultze, H.-P.; Blieck, A.; Reif, W.-E.; Rexroad C. B. et al. 2010. False teeth: conodont vertebrate phylogenetic relationships revisited. *Geodiversitas*, **32**, 545–594.

Tütken, T. and Vennemann, T. 2011. Fossil bones and teeth: Preservation or alteration of biogenic compositions? *Palaeogeography Palaeoclimatology Palaeoecology*, **310**, 1–8.

Twitchett, R. J.; Krystyn, L.; Baud, A.; Wheeley, J. R. and Richoz, S. 2004. Rapid marine recovery after the end-Permian mass-extinction event in the absence of marine anoxia. *Geology*, **32**(9), 805–808.

Van Dover, C. L. 2007. Stable isotope studies in marine chemoautotrophically based ecosystems: An update. In Michener, R. and Lajtha, K. (eds.). Stable Isotopes in Ecology and Environmental Science. *Blackwell Publishing*. pp. 202–237.

Vennemann, T. and Hegner, E. 1998. Oxygen, strontium, and neodymium isotope composition of fossil shark teeth as a proxy for the palaeoceanography and palaeoclimatology of the Miocene northern Alpine Parathethys. *Palaeogeography Palaeoclimatology Palaeoecology*, **310**(3–4), 107–121.

Vennemann, T.; Hegner, E.; Cliff, G. and Benz, G. W. 2001. Isotopic composition of recent shark teeth as a proxy for environmental conditions. *Geochimica et Cosmochimica Acta*, **65**, 1583–1599.

Vennemann, T.; Fricke, H. C.; Blake, R. E.; O'Neil J. R. and Colman A. 2002. Oxygen isotope analysis of phosphates: a comparison of techniques for analysis of Ag_3PO_4. *Chemical Geology*, **185**, 321–336.

References

Vérard, C.; Hochard, C.; Baumgartner, P. O. and Stampfli, G. M. 2015. 3D palaeogeographic reconstructions of the Phanerozoic versus sea-level and Sr-ratio variations. *Journal of Palæogeography*, **4**(1), 64–84.

Vérard, C. 2019. PANALESIS: Towards global synthetic palaeogeographies using integration and coupling of manifold models. *Geological Magazine*, **156**(2), 320–330.

Ware, D.; Jenks, J. F.; Hautmann, M. and Bucher, H. 2011. Dienerian (Early Triassic) ammonoids from the Candelaria Hills (Nevada, USA) and their significance for palaeobiogeography and palaeoceanography. *Swiss Journal of Palaeontology*, **104**, 161–181.

Weber, S. C.: Carpenter, E. J.; Coles, V. J.; Yager, P. L.; Goes, J. and Montoya, J. P. 2017. Amazon River influence on nitrogen fixation and export production in the western tropical North Atlantic. *Limnology and Oceanography*, **62**, 618–631.

Wenzel, B.; Lécuyer, C. and Joachimski, M. M. 2000. Comparing oxygen isotope records of Silurian calcite and phosphate—$\delta^{18}O$ compositions of brachiopods and conodonts. *Geochimica et Cosmochimica Acta*, **64**(11), 1859–1872.

Wheeley, J. R.; Smith, M. P. and Boomer, I. 2012. Oxygen isotope variability in conodonts: implications for reconstructing Palaeozoic palaeoclimates and palaeoceanography. *Journal of the Geological Society of London*, **169**, 239–250.

Widmann, P. 2019. Improved CA-ID-TIMS U-Pb protocol applied to a temporal calibration and quantification of Early Triassic climate disturbances. *PhD-thesis*. University of Geneva, Switzerland.

Widmann, P.; Bucher, H.; Leu, M.; Vennemann, T.; Bagherpour, B.; Schneebeli-Hermann, E. et al. 2020. Dynamics of the largest carbon isotope excursion during the Early Triassic biotic recovery. *Frontiers in Earth Science*, **8**, 196.

Wignall, P. B. and Twitchett, R. J. 2002. Extent, duration, and nature of the Permian-Triassic superanoxic event. In Koeberl, C. and MacLeod, K. C. (eds.). Catastrophic Events and Mass Extinctions: Impacts and Beyond. *Geological Society of America Special Paper*, **356**, 395–413.

Wignall, P. B.; Bond, D. P.; Sun, Y.; Grasby, S. E.; Beauchamp, B.; Joachimski, M. M. et al. 2016. Ultra-shallow-marine anoxia in an early Triassic shallow-marine clastic ramp (Spitsbergen) and the suppression of benthic radiation. *Geological Magazine*, **153**(2), 316–331.

Wilmers, J.; Waldron, M. and Bargmann, S. 2021. Hierarchical microstructure of tooth enameloid in two Lamniform shark species, *Carcharias taurus* and *Isurus oxyrinchus*. *Nanomaterials*, **11**, 969.

Wolf-Gladrow, D. A.; Riebesell, U.; Burkhardt, S. and Jelle, B. 1999. Direct effects of CO_2 concentration on growth and isotopic composition of marine plankton. *Tellus*, **51B**, 461–476.

Wudarska, A.; Wiedenbeck, M.; Slaby, E.; Lempart-Drozd, M.; Harris, C.; Joachimski, M. M. et al.

2022. Inter-laboratory characterisation of apatite reference materials for oxygen isotope analysis and associated methodological considerations. *Geostandards and Geoanalytical Research*, **46**(2), 277–306.

Wunsch, C. 2002. What Is the Thermohaline Circulation? *Science*, **298**, 1179.

Wyns, R.; Béchennec, F.; Le Métour, J.; Roger, J. and Chevrel, S. 1992. Geological map of Sur. Muscat, Directorate General of Minerals. *Ministry of Petroleum and Minerals*. Sheet NF 40–08, scale 1: 250 000.

Yirmiya, R.; Goshen, I.; Bajayo, A.; Kreisel, T.; Feldman, S.; Tam, J. et al. 2006. Depression induces bone loss through stimulation of the sympathetic nervous system. *Proceedings of the National Academy of Sciences*, **103**(45), 16876–16881.

Zazzo, A.; Lécuyer, C. and Mariotti, A. 2004a. Experimentally-controlled carbon and oxygen isotope exchange between bioapatites and water under inorganic and microbially-mediated conditions. *Geochimica et Cosmochimica Acta*, **68**, 1–12.

Zazzo, A.; Lécuyer, C.; Sheppard, S. M. F.; Grandjean P. and Mariotti A. 2004b. Diagenesis and the reconstruction of paleoenvironments: a method to restore original $\delta^{18}O$ values of carbonate and phosphate from fossil tooth enamel. *Geochimica et Cosmochimica Acta*, **68**, 2245–2258.

Zhang, L.; Cao, L.; Zhao, L.; Algeo, T. J.; Chen, Z-Q.; Li, Z. et al. 2017. Raman spectral, elemental, crystallinity, and oxygen-isotope variations in conodont apatite during diagenesis. *Geochimica et Cosmochimica Acta*, **210**, 184–207.

Zhang, F.; Romaniello, S. J.; Algeo, T. J.; Lau, K. V.; Clapham, M. E.; Richoz, S. et al. 2018. Multiple episodes of extensive marine anoxia linked to global warming and continental weathering following the latest Permian mass extinction. *Science Advances*, **4**(4), p.e1602921.

Zhang, L.; Orchard, M. J.; Brayard, A.; Algeo, T. J.; Zhao, L.; Chen, Z. Q. and Lyu, Z. 2019. The Smithian/Spathian boundary (late Early Triassic): a review of ammonoid, conodont, and carbon-isotopic criteria. *Earth-Science Reviews*, **195**, 7–36.

Žigaitė, Ž. and Whitehouse, M. 2014. Stable oxygen isotopes of dental biomineral: differentiation at the intra- and inter-tissue level of modern shark teeth. *GFF*, **136**(1), 337–340.

GENERAL
CONCLUSIONS

General conclusions

Oxygen isotope analyses were performed for the first time in the studied geological sections, complementing in the understanding of their respective palaeoenvironments. The analytical protocol tested in the 1st Chapter, of cross sectioning conodonts at the lower part of the crown, as well as of verify sample porosity, should serve to further prepare specimens from other localities for palaeoclimatic investigations. The heterogeneity in the elemental concentrations of the studied bioapatites apparently have not influenced significantly the stable oxygen isotopic measurements, instead, sources of $\delta^{18}O$ variation seems more related to analytical and sample preparation issues (sample texture). Conodonts analysed by the *in-situ* technique (secondary ion mass spectrometry – SIMS) presented a higher $\delta^{18}O$ variability in ramiform dental elements and in mixed biomineralogical tissues (e.g., albid + hyaline crown). In contrast, analysis in the hyaline crown of P_1 dental elements have a good reproducibility (±0.3 ‰) and well correlated with analogously used bulk sampling (high-temperature reduction – HTR). The hyaline crown is further corroborated as a reliable tissue for *in-situ* stable isotope analysis, but mainly because of its smaller pore sizes (hundreds of nanometers) compared to the albid tissue pore sizes (up to 5 μm).

Through the analysis of the hyaline tissue, we measured the 1.5 to 1.8 ‰ positive oxygen isotope excursion characteristic of the Smithian–Spathian boundary (SSB) climatic cooling in the Panthalassa and Tethys oceans. However, the absolute $\delta^{18}O$ values between Tethyan and Panthalassa conodonts are different. The well–preserved (CAI 1) marine conodonts of the Tethys are interpreted as pristine, and their $\delta^{18}O$ values reflect palaeotemperatures that are biologically feasible (≤ 38 °C) and not lethally hot, further indicating that the climate was not uniformly adverse as first theorized. Also, the SSB climatic cooling was gradual at the beginning, taking a strong turn by the latest Smithian. Sea water temperatures decreased progressively by about 3 °C at the initial phase, but by the latest Smithian the cooling was more pronounced, being of about 4.5 °C in a shorter time interval. At the earliest Spathian, palaeotemperatures were about 8 °C lower. The same drop in the $\delta^{18}O$ values is measured in coastal conodonts from Spitsbergen, but the absolute values from these and from American conodonts (middle to late Smithian) are about 2 ‰ to 3 ‰ lower. These low $\delta^{18}O$ values are translated in palaeotemperatures over > 40 °C, indicating that the oxygen isotope compositions from Panthalassa were instead affected by coastal processes, thus depleting the environmental $\delta^{18}O_{water}$. Given the palaeogeographic features of the Panthalassa realm, possible reasons for the low $\delta^{18}O$ values include continental freshwater input, a mid to high palaeolatitudinal $\delta^{18}O$ offset or even a palaeoaltitude effect (e.g.,

rain with low $\delta^{18}O$ from mountains).

Similar to previous stable oxygen isotope investigations, in some cases no $\delta^{18}O$ offset was measured between species expected to live in different environments, but the contrary was also found, and it was essential to note some environmental changes. For example, it was the $\delta^{18}O$ values of neogondolellids, species that inhabited deep in the water column, which recorded the SSB cooling in Spitsbergen. In contrast, $\delta^{18}O$ data from species that lived at upper water depths overlap with the $\delta^{18}O$ values from Smithian layers. The compilation of the measured oxygen isotope compositions with results from climate models may improve the understanding of the interplay between carbon cycle sinks (i.e., river discharge) and temperature changes. More analyses of stable oxygen isotopes in additional conodont specimens/species from other sections, and comparison with other proxies (e.g., phosphorus concentrations) are necessary to quantify and constrain these hypotheses further. Nonetheless, the products of this thesis should both complement in future interpretations about the Early Triassic climatic context and contribute with reliable $\delta^{18}O$ data to the quantification of climatic changes for the METECO – Sinergia investigation.

APPENDIX I

Co-authored publications linked to this thesis (abstracts)

Neogene sharks and rays from the Brazilian 'Blue Amazon'

Orangel Aguilera, Zoneibe Luz, Jorge D. Carrilo–Briceño, László Kocsis, Torsten W. Vennemann, Peter Mann de Toledo, Afonso Nogueira, Kamilla Borges Amorim, Heloísa Moraes-Santos, Marcia Reis Polck, Maria de Lourdes Ruivo, Ana Paula Linhares, Cassiano Monteiro-Neto

The lower Miocene Pirabas Formation in the North of Brazil was deposited under influence of the proto-Amazon River and is characterized by large changes in the ecological niches from the early Miocene onwards. To evaluate these ecological changes, the elasmobranch fauna of the fully marine, carbonate-rich beds was investigated. A diverse fauna with 24 taxa of sharks and rays was identified with the dominant groups being carcharhiniforms and myliobatiforms. This faunal composition is similar to other early Miocene assemblages from the proto-Carribbean bioprovince. However, the Pirabas Formation has unique features compared to the other localities; being the only Neogene fossil fish assemblage described from the Atlantic coast of Tropical Americas. Phosphate oxygen isotope composition of elasmobranch teeth served as proxies for paleotemperatures and paleoecology. The data are compatible with a predominantly tropical marine setting with recognized inshore and offshore habitats with some probable depth preferences (e.g., *Aetomylaeus* groups). Paleohabitat of taxa particularly found in the Neogene of the Americas (†*Carcharhinus ackermannii*, †*Aetomylaeus cubensis*) are estimated to have been principally coastal and shallow waters. Larger variation among the few analyzed modern selachians reflects a larger range for the isotopic composition of recent seawater compared to the early Miocene. This probably links to an increased influence of the Amazon River in the coastal regions during the Holocene.

Neogene Caribbean elasmobranchs: diversity, paleoecology and paleoenvironmental significance of the Cocinetas Basin assemblage (Guajira Peninsula, Colombia)

Jorge D. Carrilo–Briceño, <u>Zoneibe Luz</u>, Austin Hendy, László Kocsis, Orangel Aguilera, Torsten W. Vennemann

The Cocinetas Basin is located on the eastern flank of the Guajira Peninsula, northern Colombia (southern Caribbean). During the late Oligocene through the Pliocene, much of the basin was submerged. The extensive deposits in this area suggest a transition from a shallow marine to a fluvio-deltaic system, with a rich record of invertebrate and vertebrate fauna. The elasmobranch assemblages of the early Miocene to the late Pliocene succession in the Cocinetas Basin (Jimol, Castilletes and Ware formations, as well as the Patsúa Valley) are described for the first time. The assemblages include at least 30 taxa of sharks (Squaliformes, Pristiophoriformes, Orectolobiformes, Lamniformes and Carcharhiniformes) and batoids (Rhinopristiformes and Myliobatiformes), of which 24 taxa are reported from the Colombian Neogene for the first time. Paleoecological interpretations are based on the feeding ecology and on estimates of the paleohydrology (relative salinity, temperature) using stable isotope compositions of oxygen in the bioapatite of shark teeth. The isotopic composition of the studied specimens corroborates paleoenvironmental settings for the studied units that were previously estimated based on the sedimentology and biology of the taxa. These Neogene elasmobranch assemblages from the Cocinetas Basin provide new insights into the diversity the sharks and rays inhabiting the coastal and estuarine environments of the northwestern margin of South America, both during the existence of the gateway between the Atlantic and Pacific oceans and following its closure.

Life and reproduction of titanosaurians: Isotopic hallmark of mid–palaeolatitude eggshells and its significance for body temperature, diet, and nesting

Léa Leuzinger, Stefano M. Bernasconi, Torsten W. Vennemann, Zoneibe Luz, Pierre Vonlanthen, Alexey Ulianov, Claudia Baumgartner-Mora, E. Martín Hechenleitner, Lucas E. Fiorelli, Pablo H. Alasino

Eggshells represent an important part of the fossil record of Titanosauria (Dinosauria – Neosauropoda) and their stable isotope compositions are valuable palaeoenvironmental proxies. A new set of conventional (δ^{18}O and δ^{13}C) and clumped (Δ_{47}) stable isotope compositions of titanosaurian eggshells is presented, together with that of a bone and a single associated tooth, sampled in three Late Cretaceous nesting sites from La Rioja Province, NW Argentina. The preservation state of the fossils was first evaluated using optical and analytical techniques, such as transmitted light and optical cathodoluminescence (CL) microscopy, energy dispersive X-ray spectroscopy (EDX), and laser ablation-inductively coupled plasma-mass spectrometry (LA-ICP-MS). The isotopic compositions of the fossils were then compared to those of associated carbonate rocks and nodules, hydrothermal calcite and quartz, and those reported for eggshells from other nesting sites worldwide. This large, combined sample set allows us to define an isotopic hallmark ($\delta^{13}C_{VPDB}$ = −15 to −11‰; $\delta^{18}O_{VSMOW}$ = 27 to 33‰) typical for well-preserved mid-palaeolatitude titanosaurian eggshells. This hallmark is intended to identify the oological specimens best suited for palaeoenvironmental reconstructions, for instance in museum collection samples that may lack associated abiogenic materials such as host rocks. In addition, our isotopic data support that titanosaurians were animals with an elevated body temperature, mainly feeding on C3 plants, and reproducing under conditions more arid than the long-term average. The data are in excellent agreement with the isotopic data reported from other mid-palaeolatitude nesting sites around the world, indicating that titanosaurians needed similar environmental conditions to reproduce, regardless of the palaeogeographic location of their habitat. Finally, we raise the question whether titanosaurians experienced reproduction-related fasting, as noted for several extant vertebrates, and discuss the complexity of interpreting Δ_{47}-derived temperatures, despite very consistent bulk isotopic data.

A bone to pick: stable isotope compositions as tracers of food sources and paleoecology for notosuchians in the Brazilian Upper Cretaceous Bauru Group

Carolina Klock, Léa Leuzinger, Rodrigo Miloni Santucci, Agustín G. Martinelli, André Marconato, Thiago S. Marinho, Zoneibe Luz, Torsten W. Vennemann

Notosuchia is a highly diverse group of crocodyliforms that peaked during the Cretaceous period. Their taxonomic abundance and morphological disparity in the Upper Cretaceous Bauru Group (Bauru Basin, Brazil) is remarkable, with over 20 species reported. The stable carbon and oxygen isotope composition of notosuchian bioapatite from two sites (i.e., the Ponto 1 do Price and Fazenda Três Antas) in west Minas Gerais State was analyzed to evaluate differences in feeding habits among the taxa found in both localities. Possible environmental stressors are examined, in parallel to sedimentological, paleopedological, and paleontological studies, which indicate a semi-arid to arid climate for the Bauru Group. Multiple tissues of notosuchian crocodyliforms were included in our study, as well as a testudines carapace fragment, lepisosteiform fish teeth and scales, and host rocks. The mineral textures, X-ray diffraction and stable isotope data support preservation of tooth enamel and scale ganoin bioapatite. The $\delta^{13}C$ results point to different feeding habits between two terrestrial, carnivore notosuchians, namely a terrestrial source diet for *Uberabasuchus terrificus* and an aquatic source diet for *Campinasuchus dinizi*. The $\delta^{18}O_w$ for the crocodyliform data was calculated and compared to other Upper Cretaceous sites. Values support dry conditions during the formation of the bioapatite for the Fazenda Três Antas site and point to the Hateg Basin in Romania, yet likely younger, as a good paleoclimatic analogue.

An expanded Smithian-Spathian (Early Triassic) boundary from a reefal build-up record in Oman: Implications for conodont taxonomy, high-resolution biochronology, and the carbon isotope record

Marc Leu, Hugo Bucher, Aymon Baud, Torsten W. Vennemann, Zoneibe Luz, Michael Hautmann, Nicolas Goudemand

Some 2.7 Ma after the Permian-Triassic boundary mass extinction (PTBME), a stepwise extinction of the nekton (ammonoids and conodonts) ended at the Smithian-Spathian boundary (SSB) during an episode of climate cooling. SSB records from continental shelves are usually affected by an unconformity, suggesting a forced regression of glacio-eustatic origin. Here, we document a new 30 m thick SSB section from Jebel Aweri (Batain Plain, Oman) that provides an exceptionally complete and expanded record preserved in an exotic block. Most of this SSB section consists of metazoan reefal build-ups that formed in shallow water on an offshore sea mount. In Wadi Musjah (Hawasina nappes, Oman), another exotic block records the SSB in a deeper water setting represented by Hallstatt-type facies. These two sections provide a unique perspective on the early Spathian rapid re-diversification of conodonts. They led to a thorough revision of conodont taxonomy around the SSB and to the construction of the highest resolution biochronological scheme for this time interval in the Tethys. A total of five SSB sections from Oman representing both offshore sea mounts and lower slope deposits were included in a high-resolution, quantitative Unitary Associations analysis. The resulting 8 conodont biozones are intercalibrated with ammonoid zones and with the carbonate carbon isotope record ultimately placing the SSB in the interval of separation between UAZ-3. and UAZ-4. Only the association of *Nv. pingdingshanensis* with *Ic. crassatus* can be used to unambiguously characterize the base of the Spathian.

Latest Maastrichtian middle- and high-latitude mosasaurs and fish isotopic composition: carbon source, thermoregulation strategy and thermal latitudinal gradient

Léa Leuzinger, László Kocsis, Zoneibe Luz, Torsten W. Vennemann, Alex Ulianov, Marta Fernández

Here we report high-palaeolatitude stable isotope compositions of Maastrichtian fossil fish and marine reptiles (mainly mosasaurs) from Antarctica (64 °S) and compare them with mid-palaeolatitude samples from Argentine Patagonia (54 °S). Disparities between the $\delta^{13}C$ values of bony fish and marine reptiles correspond to differences in the foraging ground (distance from the shore and depth), while dramatically higher $\delta^{13}C$ values (by 18 ‰) in shark enameloid cannot be explained through ecology and are here imputed to biomineralisation. Comparison with extant vertebrates suggest that the diet alone can explain the offset observed between bony fish and mosasaurs, however breath holding due to a diving behaviour in mosasaurs may have had a some impact on their $\delta^{13}C$ values as previously suggested. The $\delta^{18}O_{PO4}$ values of the remains confirm a relatively stable, elevated body temperature for marine reptiles, meaning that they were thermoregulators. We calculated a water temperature of ~8 °C for Antarctica from the fish $\delta^{18}O_{PO4}$ values, warmer than present temperatures and consistent with the absence of polar ice sheet during the latest Maastrichtian. Our fish data greatly extend the latitudinal range of Late Cretaceous fish $\delta^{18}O_{PO4}$ values, and result in a thermal latitudinal gradient of 0.4 °C / ° latitude when compiled with literature data, *i.e.* well in line with previous studies.

APPENDIX II

List of conferece abstracts

List of conference abstracts

As first author:

Luz, Z.; Leu, M.; Bucher, H. and Vennemann, T. 2019. Characterizing conodont biophosphate from the Early Triassic: an analytical and paleoclimatological approach. In *Geophysical Research Abstracts (Vol. 21), EGU General Assembly 2019*.

Luz, Z.; Leu, M.; Baumgartner, L. P.; Bucher, H. and Vennemann, T. 2020. New insights for studying phosphate stable oxygen isotopes in bioapatites interpreted from their geochemistry. In *EGU General Assembly 2020, Online, EGU2020-20624*. DOI: 10.5194/egusphere-egu2020-20624

Luz, Z.; Leu, M.; Edward, O.; Baumgartner, L. P.; Bucher, H. and Vennemann, T. 2020. Deciphering the Early Triassic paleocean using stable oxygen isotopes in conodont bioapatite. In *Goldschmidt Virtual 2020*. DOI: 10.46427/gold2020.1665

Luz, Z.; Leu, M.; Bucher, H. and Vennemann, T. 2020. Evaluation of sea surface temperature gradient during the Smithian-Spathian (Early Triassic) using oxygen isotopes in conodont bioapatite. In *18th Swiss Geoscience Meeting (SGM)*, Zurich, Switzerland.

Luz, Z.; Leu, M.; Blattmann, F.; Bucher, H.; Vérard, C. and Vennemann, T. 2022. Early Triassic paleoclimate estimated through the oxygen isotope compositions of inshore *vs* offshore conodonts. In *Arbeitskreistreffen Wirbeltierpaläontologie*, Mainz, Germany.

Luz, Z.; Leu, M.; Edward, O.; Baud, A.; Bucher, H. and Vennemann, T. 2022. Climate cooling event in the Early Triassic subtropics. In *20th Swiss Geoscience Meeting (SGM)*, Lausanne, Switzerland.

As co-author:

Carrillo-Briceño, J. D.; Luz, Z.; Hendy, A.; Jaramillo, C.; Vennemann, T.; Kocsis, L. and Sánchez-Villagra, M. R. 2016. Colombian fossil elasmobranchs from the "last days" of the Central America Seaway and their environmental significance. In *14th Swiss Geoscience*

Meeting (SGM), Geneva, Switzerland.

Vennemann, T.; Edward, O.; <u>Luz, Z.</u> and Bucher, H. 2020. Tracing temperature and oxygen isotope compositions of Early Triassic seawater with clumped isotope thermometry. In *Goldschmidt Virtual 2020*. DOI: 10.46427/gold2020.2674

Edward, O.; <u>Luz, Z.</u>; Bucher, H. and Vennemann, T. 2020. Carbonate clumped isotope thermometry in deep time: insights from Early Triassic brachiopods and bulk carbonates. In *Goldschmidt Virtual 2020*. DOI: 10.46427/gold2020.646

Blattmann, F.; <u>Luz, Z.</u>; Vennemann, T.; Bucher, H.; Schneebeli-Hermann, E. and Magill, C. 2022. Early Triassic Pyrogenic Carbon Cycling in High Latitudes. *EGU General Assembly 2022*.

Acknowledgements

To my supervisor Torsten Vennemann for his fantastic support and guidance. From the moment I arrived in Lausanne his assistance has been substantial in several aspects. I will carry his shared experiences and conversations with me for life.

To the researchers also involved in the scientific construction of this research, and as well to my personal development: Dr. Hugo Bucher for the patience, significant instruction and insights in geology, palaeontology and about the Early Triassic period; Dr. Lukas Baumgartner for the valuable lessons about the secondary ion mass spectrometry method at the UNIL; Dr. László Kocsis, that again gave me indispensable counselling in several aspects during key moments; Dr. Léa Leuzinger for the unique debates about science and life, as well as for the invitation to do scientific collaborations; M.Sc. Heloísa Maria Moraes Santos, Dr. Orangel Aguilera, Dr. Jorge Carrillo-Briceño, Dr. Stephan Spiekman, Dr. Benita Pulitz, Dr. Torsten Scheyer and Dr. Emilia Jarochowska also for inviting me to do scientific contributions, as well as to the fruitful discussions that were very relevant for my comprehension about biominerals.

To my family who unconditionally supported me since my decision to change country, and during all these years which were sometimes painful without their company. This work is also dedicated to them: my father Raimundo, my mother Sirlei, my sisters Suzyanne and Suzylei, my niece Sophia and my brother–in–law Claudio.

I am also very grateful to my family members who continue to be an important part of my life, and who will always have a place in my heart: Gregorio, Nair, Maze, Lucilano, Lucas, Thessy, Nora, Eddie, Junior, Izabel, Augusta and Logan.

To my Brazilian friends that even from far were by many times meaningful in facing the discoveries of living abroad: Marcio, Vitor, Daniel, Mariana, Desirée, Laís, Raiza, Renata, Danilo, Diego, Erick, Gabriela, Dan, Nando, Artur, Renato, Lucas A., Lucas, Luiz, Samyr, Juan, Igor, Igor S., Henrique, Magno, Rafael, Vargas, Mateus, Lin(s), Alex G., Marco, Larissa, Lidyanne, Dulci, Ramses, Luan, Renato, Andre, L. Felipe, Madson, Yuri, Felipe, Anderson, Gabriel, Alex, Carol, Bianca, Juliana, Mayanna, André, Oswaldo, Angelo, Darren, Antonio, Sue, Ana P. and Magda; and a special thanks to the long-time friends from the best comic discussion forum ever (DC vs Marvel vs ETC): Thiago N., Renato, Marcelo, Yuri, Pedro, Vinicius, Du, Thiago M., Caio P., Francisco, Max, Otavio, Douglas, Felipe, Thiago, Rafael, Valter, Luiz, André Ca., André Co., André, Rui, Caio, Douglas Co., Vicente,

Pablo and Samuel.

To the friends that I knew during my academic stay at UNIL, which have shown me how lovely this world can receive you: Eric, Anaël, John, Dey, Shannon, Marc, Morgane, Christian, Vjeran, Gabriel, Mike, Franziska, Olu, Ignes, Clémence, Joanne, Gustavo, Marie–Noelle, Dylan, Ghislan, Filipe, Alex, Bruno, Vitor, Heitor, Otavio, Linus, Juliana, Steve, Morisnky, Javier, Marceline, Federico, Laurent, Sébastian, Giulia, Ste, Franscesco, Martin, Nico, Natalie, Benjamin, Magali, Gilles, Elisa, Elfie, Josh, Vitor, Lorena, Dafne, Remi, Gaëtan, Francesc, Lorenzo, Pierre, Christophe, Dominic, Camille, Jared, Inigo, Lara, Louis, Elsa, Borhan, Jeanne, Patricia and Solene.

A special paragraph is required to the people from the UNIL association that runs the Géopolis bar: Zelig! The moments that I was with you were some of the most incredible in my time around, and you always will be in my memories: Gabriel, Chris, Selim, Xavier, Giona, Yan, Pierre, Schafter, Irina, Marta, Chloe, Abel, A. Paris, Olivia, Bobby, Océane, Roxane, Arnaud M., Maude, Pit, Bastien, Emilyn, David, Vincent, Younous, Arnaud G., Amin, Yassin, Joelle, Ophelie, Sam, Elise, Mattia, Sara, Coco, Mylène, Jay, Jonas(s), Valentin, Sacha, Simon(s) and Joris.

And last but not least, to the friends that I have made doing my preferred hobby: online games. I can assure that memorable and unique moments came along the last two years, that were necessary during these hard times. A notable mention for the 'Spiters': Zampa, Isra, Tuwz, Morf, Nona, Baba, Naksh, Nobio, Obri, Alonzo, Iron, Sulfury, Yorgen, Derekk, Izyon, Nordax, Primal, Drowna, Panta, Rytnek, Brain, DrGreen, Tauril, Konoro, Chuntz, Nivi, Kouzu, Greg, Apo, Hudg, Insx, Natu, Vujnz, Sbjctd, Vingo, Fa, Uvo, Smorc, Zycs and Gotts; and also to Ob, Arcadias, Zaelix, Shamy, Moto, Sozaone, Illusion, Style, Saumon, Magstah and Smough.

PhD in Earth Sciences

I aim to apply my scientific and technical skills in addressing the problems of the modern world. For achieving such, I'm motivated to learn new methodologies and practices that will expand my skills and competencies. I am personally inspired to make scientific language more accessible to the public to reinforce concepts related to the environment and the importance of biodiversity.

AREAS OF EXPERTISE

Topics
- Life and environmental sciences
- Palaeontology
- Science education
- Climate change

Know-how
- Management of natural history museum collections
- Research projects and fieldwork activities of natural science disciplines
- Evaluation of analytical protocols and scientific data
- Educational practices for secondary school and graduation students, and to the public
- Sample preparation in chemistry/geology/biology laboratories

PROFESSIONAL EXPERIENCE

Scientific collaborator (intern) at the Research Institute of Organic Agriculture (FiBL), Switzerland   2022 - now
- Intelectual (research) and fieldwork support to the project 'Agroforestry' - contributing to the implementation of Ramial Chipped Wood (RCW) with Swiss farmers

Conservator-restorer (intern) to the Service de la culture - 'Section Collections' des Musées cantonaux du Valais, Switzerland   2021 - 2022
- Support to the 'Chantier des collections' for the Museum of Nature - conservation and cataloguing activities in objects that were prepared to be moved to a new building

PhD assistant at the University of Lausanne (UNIL), Switzerland   2016 - 2021
Laboratory assistant
- Sub-responsible of the inorganic preparation room to the Stable Isotope Laboratory; analysed samples for private requests; use of gas chromatography mass spectrometers
Teaching assistant
- 'General geochemistry' (bachelor, French) at UNIL; 'Biomineralisation' (bachelor/master, English) at the Ecole Polytechnique Fédérale de Lausanne (EPFL)

Research assistant at the Museu Paraense Emilio Goeldi (MPEG), Brazil   2008 - 2013
- Support to scientific mediation activities about regional fossils; Assistant in the MPEG palaeontological collection (survey, preparation, catalog and identification)

FORMATIONS

PhD in Earth Sciences	2017-2022
At the Université de Lausanne (UNIL), Switzerland	
Master in Environmental Sciences	2014-2016
At the Universidade Federal do Pará (UFPA), Brazil	
Bachelor in Biological Sciences	2007-2010
At the Centro Universitário do Estado do Pará (CESUPA), Brazil	

LANGUAGES

English	Level C1	**Spanish**	Level B1
French	Level B2	**Portuguese**	Native language

Zoneibe LUZ

CONTACT

En Lèvremont, 13
1143 Apples

+41 79 520 96 34
zoneibe.luz@gmail.com

DETAILS

Born on the 27.10.1989
Brazilian

INFORMATICS

MS Office, LaTeX;
Illustrator, Photoshop, InDesign;
InShot, MovieMaker

COMPLEMENTARY EDUCATION

PRODUCTION

PARTICIPATION IN EVENTS

cf. Annex to the CV

ics*Curriculum Vitae*

COMPLEMENTARY EDUCATION

Short-term course in Molecular Biology (BNF, Switzerland) - RNA Extraction (QIAGEN) and PCR techniques	2021
Special student in Quaternary Climate Changes (UFPA, Brazil); Paleontology in Tropical America (UFPA, Brazil); Introduction to Geology (UFPA, Brazil)	2012
Short-term course in Paleontology in Tropical America (MPEG, Belém, Brazil)	2011
Short-term course in Marine Biogeography and Evolution of Crustaceans (CESUPA, Brazil); Paleoclimatology applied to Oceanography (UFPA, Brazil); Environmental Impacts at the Coastal Zone (UFPA, Brazil); Collections Management of Museum Collections (MPEG, Brazil)	2010
Short-term course in Zooarchaeology (Sociedade de Arqueologia Brasileira – SAB, Brazil)	2009

PRODUCTION

Articles published in scientific journals

KLOCK C.; LEUZINGER L.; SANTUCCI R.; MARTINELLI A.; MARCONATO A.; MARINHO T.; **LUZ Z.** et al. A bone to pick: stable isotope compositions of food sources and paleoecology for notosuchians in the Brazilian Upper Cretaceous Bauru Group. *Cretaceous Research*. [doi: 10.1016/j.cretres.2021.105113]	2022
LEUZINGER L.; BERNASCONI S. M; VENNEMANN T.; **LUZ Z.** et al. Titanosaur life and reproduction: isotopic hallmark of mid-palaeolatitude eggshells and its significance for body temperature, diet, and nesting. *Chemical Geology*. [doi: 10.1016/j.chemgeo.2021.120452]	2021
CARRILLO-BRICEÑO J. D. ; **LUZ Z.** ; et al. Neogene Caribbean elasmobranchs: diversity, paleoecology and paleoenvironmental significance of the Cocinetas Basin assemblage (Guajira Peninsula, Colombia). *Biogeosciences*. [doi : 10.5194/bg-16-33-2019]	2019
AGUILERA O. ; **LUZ Z.** et al. Neogene sharks and rays from the Brazilian Blue Amazon. *PLoS ONE*. [doi : 10.5194/bg-16-33-2019]	2017
COSTA S. A. R. F. ; **LUZ Z.** et al. Contribuição à Zooarqueologia do Sambaqui do Moa : novos vestígios ictiológicos. *Revista do Museu de Arqueologia e Etnologia*. [doi : 10.11606/issn.2448-1750.revmae.2012.106687]	2012

Reviewed articles

MAYER, G. B. et al. South Brazil pre-colonial sharks: Insights into biodiversity and species distribution. *Journal of Fish Biology*. [doi : 10.1111/jfb.14998]

Chapters published in books

PEIXOTO L. A. W.; HOLANDA G. M.; LAGE M. R.; **LUZ Z.** et al. Informações sobre etnoictiologia. *In*: *Diversidade biológica das áreas de proteção ambiental: Ilhas do Combu e Algodoal - Maiandeua, Pará, Brasil*.1 ed.Belém, Pará: Museu Paraense Emilio Goeldi, v.1, p. 147-168.	2009

Other productions

Interview to the section 'A Palaeontologist Abroad' to the <*Palaeontological Association*> newsletter. Available in: https://www.palass.org/publications/newsletter/archive/106/newsletter-no-106	2021

PARTICIPATION IN EVENTS (LAST 5 YEARS)

Presentation (Virtual) in the EGU2020 - Sharing Geoscience Online: New insights for studying phosphate stable oxygen isotopes in bioapatites interpreted from their geochemistry	2020
Presentation (Virtual) in the Goldschmidt Virtual: Deciphering the Early Triassic Paleocean Using Stable Oxygen Isotopes in Conodont Bioapatite	
Presentation (Virtual) in the Swiss Geoscience Meeting: Evaluation of sea surface temperature gradient during the Smithian-Spathian (Early Triassic) using oxygen isotopes in conodont bioapatite	
Presentation (Poster) in the EGU General Assembly: Characterizing conodont biophosphate from the Early Triassic: an analytical and paleoclimatological approach.	2019
Presentation (Oral) in the 14th Swiss Geoscience Meeting: Colombian fossil elasmobranchs from the "last days" of the Central America Seaway and their environmental significance.	2016